CENTRO DE ASTROBIOLOGÍA (INTA-CSIC)
Departamento de Astrofísica
UNIVERSIDAD AUTÓNOMA DE MADRID
Departamento de Física Teórica, Facultad de Ciencias

Accretion and circumstellar properties of Herbig Ae/Be stars

PhD dissertation submitted by
Ignacio Mendigutía Gómez
for the degree of Doctor in Physics

Supervised by
Dr. Benjamín Montesinos Comino
Dr. Alcione Mora Fernández

Academic advisor
Dr. Carlos Eiroa de San Francisco

Madrid, November 2011

A Carmina. A mis padres y hermanos.

Agradecimientos

Agradezco a todos aquellos que de manera más o menos directa han contribuido a que este trabajo haya sido posible.

A las personas con las que he colaborado más estrechamente, por dejarme aprender de ellos y dedicar tiempo y esfuerzos en esta tesis. En primer lugar, a Benjamín Montesinos, por darme la oportunidad, y estar siempre dispuesto a prestar su inestimable ayuda. Agradezco profundamente la confianza depositada desde el principio y la manera en que me ha guiado. A Alcione Mora, por sus siempre atinados consejos. Espero haberme contagiado entre otras cosas de su rigurosidad en el método. A Carlos Eiroa, por compartir su amplia experiencia y hacerme ver las cosas con perspectiva, y por ponerse al frente cuando las cosas se pusieron difíciles. A James Muzerolle, por darme la oportunidad de visitar Baltimore durante dos meses y poder aprender de él. A Rene Oudmaijer, Gwendolyn Meeus, Bruno Merín y Nuria Calvet, por su apoyo, ánimo y paciencia, y por ayudarme compartiendo sus conocimientos.

A los pioneros del máster de Astrofísica, juntos dimos nuestros primeros pasos en este mundillo. A todos los investigadores con los que he tenido la oportunidad de conversar en diversos congresos, conferencias y charlas. A aquellos con los que he compartido largas e inolvidables noches de observación. A Jesús Maldonado, por venir a ayudarme con mis observaciones en Calar Alto, y por compartir el camino desde hace ya tanto tiempo. Al personal técnico y administrativo de INTA, CAB, UAM, UCM, STScI, ESO y de los observatorios de Canarias y Calar Alto, por facilitar tanto las cosas.

A mis compañeros que trabajan o han trabajado en el LAEFF (ahora parte del departamento de Astrofísica del CAB) y he tenido la suerte de conocer, por todos estos años, y por prestarme su ayuda en uno u otro momento en diversos aspectos relacionados con esta tesis.

A los buenos amigos, los nuevos, y los "de siempre", por su apoyo e interés, por estar ahí y disfrutar juntos de tantos buenos momentos.

Finalmente, a mis hermanos, Ana y Carlos, por devolverme a la realidad cuando el nivel de "frikismo" llega demasiado lejos, por escucharme. A mis padres, porque son mi modelo a seguir. A mi padre, por contagiarme desde pequeño su inquietud por conocer, y por las largas discusiones sobre muchos aspectos de esta tesis. A mi madre, porque su infinita dedicación y amor a todos sus hijos no puede medirse. A Carmina, por convertirse en toda una experta en discos protoplanetarios, probablemente sin haberlo buscado. Por enseñarme tantísimo sobre lo verdaderamente importante, y por lo que fuimos, somos y seremos. A todos ellos, por ser mi referencia.

Ignacio Mendigutía Gómez
Madrid, 17 de Noviembre de 2011

Abstract

This work focuses on the massive counterparts of classical T-Tauri stars, the so-called Herbig Ae/Be (HAeBe) stars. These are the most massive objects to experience an optically visible pre-main sequence (PMS) phase, bridging the transition between low and high-mass young stars. Our knowledge about the HAeBe properties is much more limited than that for lower-mass objects. The main reason is the comparatively small sample, caused by the fast evolution of massive objects to the main-sequence, and by the fact that star formation process shows favour for the less-massive objects, as the shape of the initial-mass function suggests.

The general aim of this thesis is to contribute to our knowledge of HAeBe stars, in particular, the behaviour of the circumstellar atomic gas, the accretion properties, and the evolution and physical mechanisms driving the star-disk interaction. This research is mainly based on multi-epoch optical spectra and simultaneous optical-near infrared (nIR) photometry of a representative sample of 38 HAeBe stars, as well as on their stellar parameters and spectral energy distributions. The main achievements of this work are summarized as follows:

- We have carried out the most complete characterization to date of the circumstellar behaviour of HAeBe stars in the optical, analysing multi-epoch (intervals of hours-days-months) and averaged spectra in Hα, [OI]6300, NaID and HeI5876. These spectra, and the simultaneous photometry, have allowed us to estimate line fluxes and to assess whether the observed equivalent-width variations are caused by changes in the stellar continuum or by variations of the circumstellar gas itself. These data constitute one of the largest existing sets to study some of the variability properties of intermediate-mass PMS stars, which led us to find significant differences between the variability behaviour of HAe and HBe stars, as well as between HAeBes and classical T-Tauri stars.

- We have applied magnetospheric-accretion shock modelling to reproduce the observed Balmer excess from multi-epoch Johnson's UB photometry, deriving the most reliable estimates of the accretion rates for a wide sample of HAeBe stars to date. We provided empirical expressions relating the accretion and the Hα, [OI]6300 and Brγ luminosities, being the first time that these calibrations are accurately obtained for the HAeBe regime. In contrast, we found that the Hα line width at 10% of peak intensity is not a valid accretion tracer for the HAeBes, unlike for lower mass stars. In addition, the accretion-rate changes from multi-epoch Balmer excess measurements seem to be uncorrelated to the simultaneous variability of the Hα and [OI]6300 lines. This led us to suggest that the origin of the empirical calibrations between the accretion and line luminosities could not be driven by the influence of accretion on the emission lines, but by a common dependence on the stellar luminosity.

- Finally, we have looked for trends relating the accretion rates with several stellar and disk properties. We have estimated inner gas dissipation timescales for the HAeBe regime, and report similar correlations than those for lower mass T Tauri stars. In particular, we find trends relating the mass accretion rate with the nIR excess and disk mass that point to simple viscous disk models explaining them. However, we find slightly faster inner gas dissipation timescales for our sample, and indications suggesting that a different physical process -such as photoevaporation- plays a major role dissipating disks around HAeBes.

Resumen

Este trabajo se centra en las contrapartidas masivas de las estrellas T Tauri clásicas, las denominadas estrellas Herbig Ae/Be (HAeBe). Estos son los objetos más masivos capaces de experimentar una fase pre-secuencia principal (PMS) visible en el óptico, sirviendo de nexo entre las estrellas jóvenes de baja y alta masa. Nuestro conocimiento sobre las propiedades de las estrellas HAeBe es mucho más limitado que el de los objetos menos masivos. La razón fundamental es el comparativamente pequeño tamaño de la muestra, debido a la rápida evolución de los objetos masivos hacia la secuencia principal, y al hecho de que el proceso de formación estelar favorece a las estrellas menos masivas, tal como sugiere la función inicial de masas.

El objetivo principal de esta tesis es contribuir al conocimiento de las estrellas HAeBe, en concreto, al comportamiento del gas atómico circunestelar, las propiedades de acreción, y la evolución y mecanismos físicos que dirigen la interacción estrella-disco. Este estudio se basa fundamentalmente en espectros ópticos multi-época y fotometría simultánea en el óptico-infrarrojo cercano (nIR) de una muestra representativa de 38 estrellas HAeBe, así como en sus parámetros estelares y distribuciones espectrales de energía. Los principales logros de este trabajo se resumen a continuación:

- Hemos llevado a cabo la caracterización mas completa hasta la fecha del comportamiento circunestelar de estrellas HAeBe en el óptico, analizando espectros multi-época (intervalos de horas-dias-meses) y promediados en Hα, [OI]6300, NaID y HeI5876. Estos espectros, y la fotometría simultánea, nos han permitido estimar flujos de línea y evaluar en qué casos las variaciones de la anchura equivalente son causadas por cambios en el contínuo estelar o por variaciones del propio gas circunestelar. Esta base de datos es una de las más extensas para estudiar algunas de las propiedades de variabilidad de las estrellas PMS de masa intermedia, la cual nos llevó a encontrar diferencias significativas entre el comportamiento variable de las estrellas HAe y las HBe, así como entre las HAeBe y las T Tauri clásicas.

- Hemos aplicado un modelado de acreción magnetosférica para reproducir los excesos de Balmer observados a partir de fotometría multi-época UB de Johnson, derivando las estimaciones mas fiables hasta la fecha de la tasa de acreción de una muestra amplia de estrellas HAeBe. Proporcionamos expresiones empíricas que relacionan las luminosidades de acreción con las de Hα, [OI]6300 y Brγ, siendo la primera vez que este tipo de calibraciones son obtenidas de manera precisa para el régimen HAeBe. Por contra, encontramos que la anchura Hα al 10% de la máxima intensidad no es un trazador válido de acreción para las HAeBes, a diferencia de las estrellas de menor masa. Además, los cambios en la acreción a partir de medidas multi-época del exceso de Balmer parecen no correlacionar con la variabilidad simultánea de las líneas Hα y [OI]6300. Esto nos llevó a sugerir que el origen de las calibraciones empíricas entre las luminosidades de acreción y de línea podría no estar dirigida por la influencia de la acreción sobre las líneas de emisión, sino por una dependencia común en la luminosidad estelar.

- Finalmente, Hemos buscado tendencias relacionando las tasas de acreción con varias propiedades estelares y del disco. Hemos estimado escalas temporales de disipación del gas interno para el régimen HAeBe, documentando correlaciones similares a las de las estrellas T Tauri. En particular, encontramos tendencias relacionando la tasa de acreción de masa con el exceso nIR y con la masa del disco que podrían ser explicables

a partir de modelos simples de discos viscosos. Sin embargo, encontramos escalas temporales de disipación del gas interno ligeramente más rápidas para nuestra muestra, e indicaciones que sugieren que un proceso físico diferente -como la fotoevaporación- juega un papel principal a la hora de disipar discos alrededor de las HAeBes.

Contents

List of Figures

List of Tables

Chapter 1

Introduction

This chapter introduces general theoretical and observational aspects related to this thesis -specific introductory sections are included at the beginning of chapters 3, 4 and 5-, and outlines its structure. Section 1.1 summarizes the current understanding of the stellar and planetary formation. The specific properties of the type of stars studied in this work are detailed in Sect. 1.2. Accretion processes in pre-main sequence stars are described in Sect. 1.3. The goals and structure of this thesis are in Sect. 1.4. A brief summary of additional work is in Sect. 1.5.

1.1 Star and planet formation

Star formation comprises different stages whose timescales depend on physical processes that, in turn, depend on the properties of the central object and environment conditions (Palla & Stahler 1999). According to the current paradigm (Lada 1987; Shu et al. 1987), the formation process for a typical solar-like star can be roughly divided into four phases. These can be observationally characterized from the shape of the spectral energy distribution (SED), in particular, from the α parameter, defined as the slope of the log λF_λ distribution against log λ, longwards 2 μm. Figure 1.1 shows an overview of the star -and planet- formation processes, along with the corresponding SEDs. Stellar formation starts when a dense core ($\alpha > 0$; Class 0 and I) in a molecular cloud collapses, probably influenced by external sources such a supernovae explosion or strong winds from surrounding massive stars. Physical mechanisms such as accretion, winds or photo-evaporation, make the envelope to dissipate on timescales of 10^5 - 10^6 yr. In addition, angular momentum conservation implies that infalling matter tends to adopt a circumstellar (CS) disk structure (Terebey et al. 1982), from which planets are expected to be formed. The so-called pre-main sequence (PMS) phase (Classes II and III, for which -2 $< \alpha <$ 0 and $\alpha <$ -2, respectively) starts once the SED is that of an optically visible central object plus an infrared (IR) excess coming from the dust in the disk. The PMS phase involves important CS gas and dust dissipation, and is the period when planetesimals are eventually grouped into planets (Ruden 1999). After several Myr, the star can be surrounded by a planetary system and reaches the main-sequence (MS), when hydrogen burns through p-p reactions.

The combination of recent observational and theoretical efforts makes this rough view more complex than pictured above. As an example, the Spitzer observatory has revealed a wide variety of PMS SEDs, most probably reflecting different evolutionary patterns (see e.g. Cieza 2008); the so-called transition objects show IR excesses above $\sim$ 10 μm, indicating

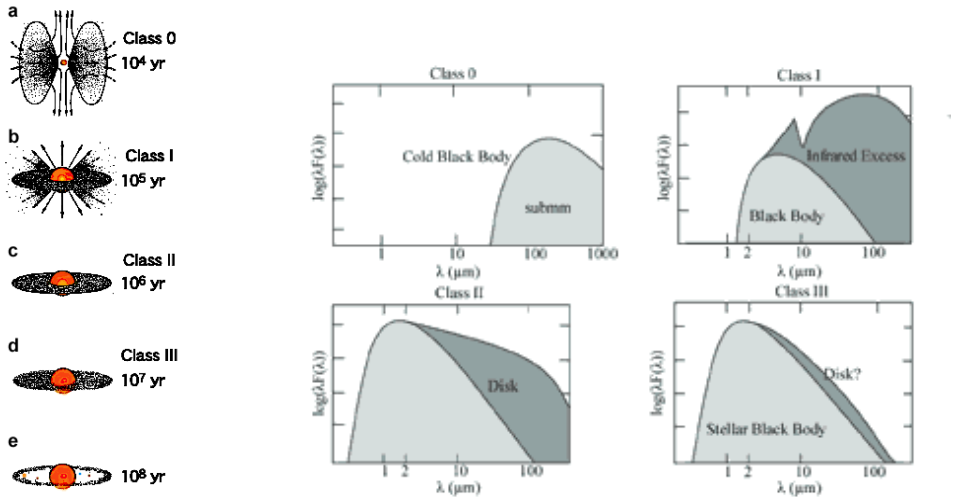

Figure 1.1: Classical view of the formation of a solar-like star surrounded by a planetary system (left) and the corresponding SEDs (right). The PMS phase is that when the SED reflects a stellar photosphere plus an IR excess from the dust of the circumstellar disk.

important inner dust disk dissipation. This can be caused from different physical processes, being planetary formation one of the most attractives (e.g. Huélamo et al. 2011). In addition, the α parameter is indicative not only of an evolutionary stage, but it is also associated to different inclinations to the line of sight (Robitaille et al. 2006).

Alternatively, the star formation process can be studied in terms of the evolution of the mass accretion rate onto the central object. That is shown in Fig. 1.2 for an isolated low-mass star, as derived from a combination of theory and observations (Hartmann 2009). Three stages can be clearly differenciated: accretion influenced from the contribution of the infalling envelope, accretion dominated by viscous dissipation of the disk, and very low accretion rate when the disk dissipates. The first stage occurs for Class 0–I objects when mass is still falling onto the disk from the protostellar envelope. At the same time, the disk accretes onto the central object, sometimes showing brief FU Ori outbursts caused by strong disk accretion. EXor-type increases of the mass accretion rate could also be observed. Once the protostellar envelope dissipates, PMS stars show disk-to-star accretion (Sect. 1.3) at an almost steady rate, which tends to slowly decay until accretion ceases over a period of a few million years. This may be indicating the formation of giant planets, which could clear the inner parts of the disk and accrete material otherwise destined for the central star.

This point of view is again rather simplistic: there are strong star to star differences, the timescale when accretion ceases is very uncertain, and strong influences most probably come from the presence of stellar companions and from environmental conditions.

1.2 Herbig Ae/Be stars

Most of our knowledge about star and planet formation is based on observations of low-mass PMS objects, the so-called T-Tauri stars ($0.1 \leq M_*/M_\odot \leq 2$; spectral types F, G K and M). These are divided according to the presence or absence of accretion signatures (Classical and Weak T-Tauri; CTT, WTT). Herbig (1960) firstly characterized the higher-mass (2-10 $M_\odot$)

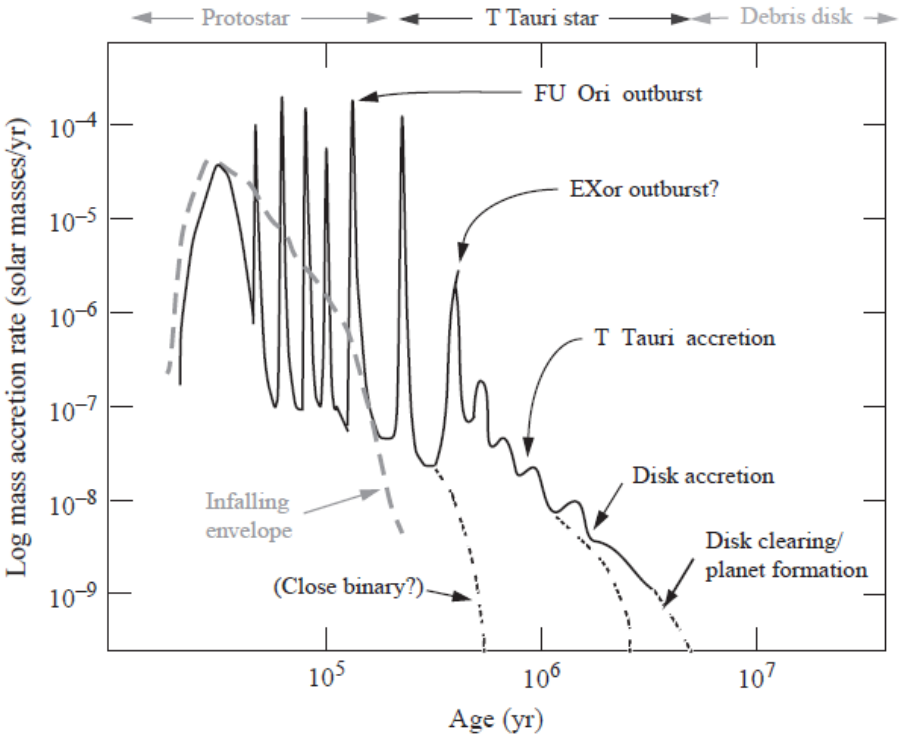

Figure 1.2: Evolution of the mass accretion rate during the formation of a typical isolated low-mass (solar-type) star (Figure from Hartmann 2009).

analogs of CTTs from the analysis of 26 objects, which were described as stars with spectral types A or B and emission lines (Ae/Be), located in a obscured region and illuminating a bright nebulosity in its immediate vicinity. This characterization did not consider isolated Herbig Ae/Be (HAeBe) objects, whereas classical Be stars could be included as members of the group. Nowadays, the properties defining a HAeBe star include spectral types A or B with emission lines, IR excess due to hot/cool CS dust, and luminosity class III to V (Waters & Waelkens 1998). The initial sample of Herbig (1960) was soon increased (see e.g. Finkenzeller & Mundt 1984; Herbig & Bell 1988; Thé et al. 1994; Carmona et al. 2010), and $\sim$ 100 bona-fide spectroscopically characterized HAeBe stars have been well identified to date (Thé et al. 1994). This list could be extended up to $\sim$ 150 members within the nearby Gould belt region, if Fe stars and other objects with uncertain spectral types or without emission lines are included. The scarcity of HAeBes results from the shape of the initial-mass function (Salpeter 1995), which favours the formation of lower-mass objects. In addition, high-mass stars are expected to be formed on a shorter timescale (Tayler 1994), making difficult their observation in the PMS phase.

The dividing line between the T-Tauri and the HAeBe regimes originates at $T_* \sim 8000$ K ($M_* \sim 2$ $M_\odot$), which separates MS stars with convective or radiative sub-photospheres (Simon et al. 2002). However, the validity of this limit within the PMS phase is not well established (see e.g. Finkenzeller & Mundt 1984). Moreover, recent works indicate that surface convection operates efficiently in stars about twice as massive as the Sun (Antoci et al. 2011). The group of stars called intermediate-mass T-Tauri (IMTT; F-G spectral types and 1-4 $M_\odot$, Calvet et al. 2004) can be considered as a link between the CTTs and the HAes. In addition, HAes and HBes show significant differences (see e.g. Waters 2006,

for a summary), which will be remarked from the results of this thesis. On the other hand, CTTs and HAeBes share many common observational characteristics, such as the presence of emission lines in their spectra, the photometric and spectroscopic variability and the variety of shapes in their SEDs. In this respect, the classification of Meeus et al. (2001) divides HAeBes into groups I and II according to the increasing or flattening IR excess between 10 and 60 μm. This SED classification is now preferred against others (see e.g. Hillenbrand et al. 1992) since it could be reflecting different disk shapes (Meeus et al. 2001; Dullemond 2002; Dullemond & Dominik 2004), photopolarimetric behaviours (Dullemond et al. 2003), strength of the polycyclic aromatic hydrocarbons (PAHs) features (Acke & van den Ancker 2004), and evolutionary phases (Acke et al. 2004).

Despite the relatively low number of observational and theoretical studies on the HAeBe regime, compared to the T Tauri one, several facts make that group worth of a detailed investigation:

- Different observational and theoretical works (Johnson et al. 2007; Kennedy & Kenyon 2008; Boss 2011) indicate that the formation of planets could be more efficient around stars more massive than the Sun.

- Given the similarity in mass and spectral type, HAeBes are the possible precusors of most older Vega-like stars surrounded by debris disks (see e.g. the case of β Pic in Barrado y Navascués et al. 1999). These non-primordial disks are again the perfect candidates hosting planetary bodies (Kalas et al. 2005).

- HAeBes fill the gap between low and high-mass PMS stars. They link the objects with fully convective subphotospheres with those reaching the MS phase before accretion ceases and the contracting envelope dissipates (Palla & Stahler 1999). Therefore, HAeBe stars can be considered as an interface regime whose study should reveal possible differences between the physical processes driving PMS evolution at different stellar masses.

1.2.1 Variability. The UXOr subsample

A defining characteristic of PMS stars is the photometric, polarimetric and spectroscopic variability on different timescales. Herbst et al. (1994) established a classification according to the photometric behaviour. The UXOr-type variability affects a wide number of early-type CTTs and HAeBes (Herbst et al. 1994; Herbst & Shevchenko 1999), and takes its name from the prototypical HAe star UX Ori (Grinin et al. 1994). UXOrs show sudden decreases of the stellar brightness -up to 3-4 magnitudes in V, on weeks- accompanied by polarimetric increase and simultaneous reddening, which could switch to blueing in very deep minima. This behaviour was explained by Grinin et al. (1988) from opaque clouds in the CS disk that intersect our line of sight. These dusty screens would cause the stellar brightness to decrease and the polarization and stellar reddening to increase. The contribution of the scattered light from the disk would dominate when the stellar brightness decrease is more pronounced, causing the blueing effect. This explanation implies that disks surrounding UXOrs are seen close to edge-on. Alternatives to this view proposed that the UXOr-type variability was caused by changes in the accretion luminosity (Herbst & Shevchenko 1999). However, multi-epoch observations revealed that the variability in the equivalent width of spectroscopic lines shown by several UXOr stars comes from the contrast between an almost constant line flux and a variable continuum (see e.g. Grinin et al. 1994; Rodgers et al. 2002; Mendigutía et al.

2010), supporting the obscuration model. Those observations exemplify the importance of a simultaneous characterization of the line equivalent widths and the stellar continuum.

Several authors (Grady et al. 1996; de Winter et al. 1999) suggested that the objects screening the stellar light in UXOr stars were infalling cometary-bodies, in a similar way to the observed behaviour in β Pic. This interpretation directly linked HAeBes and Vega-type stars through the UXOr phase (Grady et al. 2000). However, this view was ruled out by Natta et al. (1997) and Mora et al. (2002, 2004), who did not find significant differences between UXOrs and the remaining HAeBes, apart from their specific orientation to our line of sight.

It is important to point out that most of the monitoring efforts devoted to PMS stars are photometric, and multi-epoch spectroscopy has been focused mainly on individual objects or small samples.

1.3 Accretion in the pre-main sequence phase

Most of the mass of PMS stars in their evolution to the MS is acquired by accretion from the disks. In addition, the disk lifetime -and therefore the timescale over which planets could be formed- is mainly determined by its gas content, since this is the main constituent (typically adopted to be 100 times more abundant than dust, though recent estimates provide lower values, see e.g. Thi et al. 2010). However, direct measurements of molecular gas, specially H_2, are very difficult to achieve (Richter et al. 2002). In this way, an indirect gas tracer such as the mass accretion rate (e.g. Fedele et al. 2010) becomes a key parameter to understand and constraint.

From a classical perspective (Lynden-Bell & Pringle 1974), CS disks would extend up to the stellar surface, where part of the gravitational energy would be released as accretion luminosity through a hot thin boundary layer. This view explained the UV excess and spectroscopic veiling shown by CTTs (see e.g. Basri & Bertout 1989; Bertout et al. 1993). However, "boundary layer" models predicted infall velocities of a few km s^{-1}, since the material was supposed to slow-down from the disk to the star. Those velocities are much lower than the ones inferred from the observation of redshifted absorption components in several spectral lines (hundreds of km s^{-1}; Edwards et al. 1993). In addition, many CTT stars lack strong near infrared (nIR) excesses, which cannot be explained from a disk that extends up to the stellar surface. Finally, boundary layer models failed to explain why CTTs are usually slow rotators ($\sim$ 10 km s^{-1}) whereas the fast rotating material just above the photosphere ($\sim$ 200 km s^{-1}) should spin-up the central object.

Nowadays the consensus is that accretion in CTT stars is magnetically driven. According to the magnetospheric accretion (MA) paradigm (Uchida & Shibata 1985; Camenzind 1990; Koenigl 1991; Shu et al. 1994) the inner disk is truncated at a few stellar radii, between the stellar surface and the co-rotation radius. The ionized material then follows the magnetic field lines at free-fall velocities and impacts the stellar surface generating hot accretion shocks (Fig. 1.3). In this way, redshifted absorption components and other line profiles can be reproduced from material at close to free-fall velocities and MA models (Edwards et al. 1994; Hartmann et al. 1994; Muzerolle et al. 1998a,b, 2001), the inner part of the disk is now depleted of material, accounting for the variety of nIR excesses observed (Meyer et al. 1997), and the low stellar rotational velocities reflect the disk velocity at the truncation radius (the so-called disk-braking; Edwards et al. 1993; Hartmann 2002). In addition, strong magnetic fields are measured in CTTs (Valenti & Johns-Krull 2004), winds are naturally explained from the MA paradigm (e.g. Kurosawa et al. 2006, and references therein), and there are evidences of hot

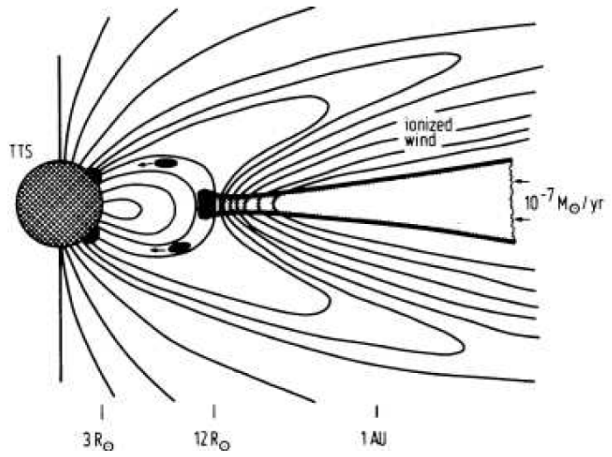

Figure 1.3: Geometrical scheme of the magnetospheric accretion scenario (figure from Camenzind 1990)

accretion spots in accreting T Tauri stars (Bouvier et al. 1995). These have been modelled, explaining the continuum excess and veiling shown by CTTs (Calvet & Gullbring 1998). The accretion rates derived from this method correlate with the strength of several emission lines, which are used as empirical accretion tracers (see e.g. Herczeg & Hillenbrand 2008; Fang et al. 2009; Rigliaco et al. 2011, and references therein).

The relative position of T-Tauri stars with transition disks in the mass accretion rate-disk mass plane has been used to analyse the physical process dominating disk dissipation (Alexander & Armitage 2007; Najita et al. 2007). As an example, large disk masses and low accretion rates, compared to those typically shown by non-transition disks, are expected if jovian planets are formed: a large reservoir of material is necessary to form such type of planets, at the same time that the inner gas content -and therefore the accretion rate- is strongly diminished. On the opposite, the accretion rates of stars with transition disks where grain growth dominates should be similar to those with non-transition disks. Photoevaporated disks should show both low masses and accretion rates.

The situation is not that clear for HAeBe stars. The appearance of several high-velocity redshifted absorption profiles cannot be easily explained from a boundary layer model, but a first requirement for MA to operate is the existence of strong enough magnetic fields, whereas these are in principle not expected for stars with a radiative sub-photosphere (Sect. 1.2). However, different evidences suggest that MA could also be valid at least for the HAeBes with late spectral types. Magnetic fields are detected in these objects (Wade et al. 2007; Hubrig et al. 2009), spectropolarimetric measurements point to MA acting in HAe stars (Vink et al. 2002, 2003; Mottram et al. 2007), and several observational properties of prototypical HAeBe stars are consistent with the MA scenario (Muzerolle et al. 2004; Brittain et al. 2009; Grady et al. 2010). The low level of optical continuum excess and spectroscopic veiling in these objects was explained by Muzerolle et al. (2004) from the similar temperature that characterizes the stellar photosphere and the accretion shocks. These were modelled by Calvet et al. (2004) for a sample of IMTTs, who found that the correlation between the Brγ and the accretion luminosities can be extended to that regime.

Whether MA can be applied to HAeBe stars and how the accretion rates could be derived for these objects is object of active debate (see e.g. Muzerolle et al. 2004; Donehew & Brittain 2011), and a central topic of this thesis. In addition, the comparison between the accretion

rate estimates for a wide sample of HAeBe stars and several stellar and disk parameters could shed light on the physics of the star-disk interaction and the processes driving disk dissipation.

1.4 Objectives and structure of this thesis

The general goal of this thesis is to provide additional insight into the circumstellar and accretion properties of a sample of 38 pre-main sequence Ae, late-type Be and intermediate-mass F-G stars, representative of the HAeBe regime. This work is mainly based on the analysis of multi-epoch optical spectroscopy and simultaneous optical-nIR photometry.

Specific objectives are:

- Analyse and quantify the optical spectroscopic variability of HAeBe stars. Analyse possible origins of these variations.
- Analyse the star-disk interaction in HAeBe stars and the possible application of MA to this regime to derive accretion rates. Identify possible correlations between these and spectroscopic tracers to simplify the estimate of the accretion rates in this type of objects. Study the accretion rate variability.
- Relate the accretion rates with several stellar and disk properties guided by the analogous correlations for T Tauris, aiming to shed light on the timescale and physical mechanisms driving circumstellar dissipation in intermediate-mass stars.
- Identify analogies and differences between HAe and HBe stars, and between HAeBe and T Tauri stars.

The main results of this thesis have been published in two refereed papers in Astronomy & Astrophysics, and a third one will soon be submitted. The structure of this work is the following:

- Chapter 2 describes the multi-epoch spectra and simultaneous photometry analysed, as well as the properties of the sample of HAeBe stars studied.
- Chapter 3 includes the analysis and results on the optical spectroscopic variability (Mendigutía et al. 2011a).
- Chapter 4 includes the analysis and results on the accretion rates and accretion tracers (Mendigutía et al. 2011b).
- Chapter 5 includes the analysis and results on the accretion rates in relation with several stellar and disk properties (Mendigutía et al. 2012).
- Chapter 6 summarizes the main results and conclusions of this thesis and suggests future research lines.
- Appendices A, B, C, and D include part of the data generated from this thesis.

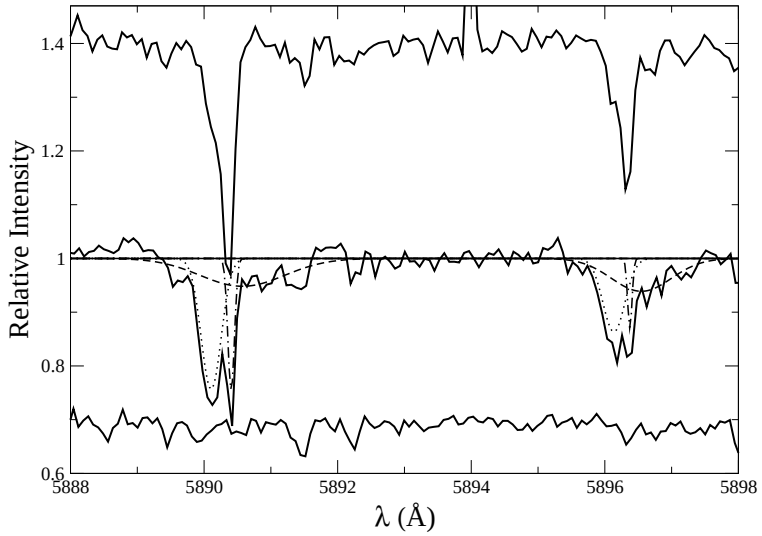

Figure 1.4: NaI doublet of the HAeBe object HD 35929 (at the centre of the graph) and two control standard stars in a similar line of sight but located closer (bottom, HIP 25187) and farther (top, HIP 24828). An interstellar component is detected in HD 35929 and in the farther object. The Gaussian curves which best fit the NaID profile of the target star are shown. Each NaI line can be divided into three components: photospheric (dashed line), interstellar (dot-dashed line) and stable circumstellar (at the radial velocity of the star -13 km s^{-1}- dotted line).

1.5 Additional work not presented in this thesis

Apart from the work presented here, other research line in the same framework was started. However, despite of the expectations and large effort put on its development, it did not provided conclusive results. Since it has helped the author of this work to gain experience in several important astronomical tools, we would like to summarize briefly what we did. The goal was to detect cold atomic gas in CS disks of a wide sample of HAeBe and Vega-like stars from high-resolution spectra, looking for an expression for the expected decline in time. This would have then been related with the dust content from the SEDs of the sources. The method was to compare several absorption features of each target star with those of MS stars with similar spectral types, located along similar lines of sight, and with shorter and longer distances than that of the target star. In this way, the contribution from the interstellar medium and from the stellar photosphere could be identified and subtracted, and the CS atomic gas contribution measured. This method seemed to be promising and was used by Redfield (2007) to estimate the gas content of the Vega-like star HD 32297. Although we succeeded detecting atomic gas in a few stars (see e.g. Fig. 1.4), these results were scarce compared with the amount of observing time and data analysis required: we obtained time in the Calar Alto and La Palma observatories, observing hundreds of stars and reducing the corresponding echelle spectra, whose analysis included calculations such as radial velocities and multi-Gaussian fitting of several line profiles.

In addition, the author of this thesis collaborates in GASPS (GAS in Protoplanetary Systems, PI Bill Dent), a Herschel observatory Open Time Key Programme. The final aim of that project is to study the gas evolution in protoplanetary disks from direct detections of molecular gas tracers in a wide sample of PMS stars in different star-forming regions. The author has been involved as co-I in observing proposals and campaigns for ancillary data in La Palma and Tenerife observatories, and as co-author in several GASPS papers (Meeus et

al. 2010; Thi et al. 2010; Pinte et al. 2010; Mathews et al. 2010; Tilling et al. 2011) and others in progress.

Both research lines described above exemplify different paths and parallel investigations that, although not included, somehow have had an influence on the final results reported in this thesis.

Chapter 2

Data and sample

Almost all the analysis and results in this thesis are based on EXPORT data. Several general characteristics of the EXPORT observations and related results are included in Sect. 2.1. The multi-epoch optical spectra and simultaneous optical-nIR photometry used in this thesis are described in Sect. 2.2. Some properties and caveats about the sample of HAeBe stars analysed are outlined in Sect. 2.3.

2.1 The EXPORT data

The EXPORT (EXo Planetary Observational Research Team) consortium obtained International Time in the Canary Islands' Telescopes, making observations in 1998 and 1999 (Eiroa et al. 2000). This observing time and facilities were devoted to monitor a sample of 74 objects during four observing runs. Most of the stars showed IR excess attributed to CS disks, as well as photometric and spectroscopic variability. 56% were HAeBe and IMTT objects, being the remaining CTTs (16%), Vega-type (11%), Post T-Tauri, A-shell (8%) and MS stars for calibrations (9%). The multi-epoch observations included medium and high resolution spectroscopy, optical photopolarimetry, nIR photometry and optical CCD images. All observations were scheduled to be simultaneous, as far as possible, which is essential to derive accurate fluxes and properties of variable stars. The multi-epoch and simultaneous character of the observations is a defining feature of the EXPORT data and make them unique in this respect.

This observational effort generated a vast amount of data, whose analysis has been published in a series of papers and PhD theses. The most relevant for this work are those on the nIR observations of PMS stars (Eiroa et al. 2001), on their spectral classification and projected rotational velocities (Mora et al. 2001), on their optical photometry and polarimetry (Oudmaijer et al. 2001), on their simultaneos optical and nIR photometric variability (Eiroa et al. 2002), and on the stellar parameters of HAeBe stars (Montesinos et al. 2009), as well as the PhD theses of Merín (2004) and Mora (2004).

Despite the wide exploitation of the EXPORT data, the analysis of the multi-epoch mid-resolution optical spectra of the HAeBe sub-sample was still pending. This thesis is mainly based on its study, also considering the simultaneous optical and nIR photometry.

2.2 The data analysed in this work

Apart from the information provided in the following two sections, further details on the optical spectroscopy, optical photometry and nIR-photometry can be obtained in Mora et al. (2001), Oudmaijer et al. (2001) and Eiroa et al. (2001), respectively.

2.2.1 Mid resolution optical-spectroscopy

The spectra were taken with the Intermediate Dispersion Spectrograph (IDS) attached to the 2.5 m Isaac Newton Telescope (INT), La Palma observatory, during four observing campaings: 14-17 May, 28-31 July, 24-28 October 1998 and 29-31 January 1999. This distribution of dates provided a spectroscopic monitoring on timescales from hours to days-months. Two different instrumental setups were used. An EEV CCD was used in the May 1998 run ($\lambda\lambda$ 5854-6728 $\mathring{A}$, R $\sim$ 4500). An upgraded EEV CCD was used during the other three observing runs ($\lambda\lambda$ 5712-6812 $\mathring{A}$, R $\sim$ 6600). The slit width was 1.0 arcsec projected on the sky.

2.2.2 Optical and near-infrared photometry

The optical photometry was taken using the Turpol UBVRI polarimeter/photometer mounted on the the 2.5 m Nordic Optical Telescope (NOT), La Palma. The data were obtained simultaneously in the UBVRI bands (with effective wavelengths of 0.36, 0.44, 0.53, 0.69 and 0.83 μm). All runs used a 10 arcsec diaphragm, but in July 1998 a 7.5 arcsec diaphragm was employed. The typical (mean) uncertainty is around 0.05 magnitudes for all filters.

JHK photometry was obtained at the Teide Observatory, Tenerife, with the 1.5 m Carlos Sanchez Telescope (CST) under two different instrumental setups. A single channel nIR photometer with a 15 arcsec beam was used in May and October 1998. During the July 1998 and January 1999 runs CAIN, a 2D nIR camera equipped with a NICMOS 256 $\times$ 256 HgCdTe array, was used. The typical uncertainties are $\leq$ 0.02 magnitudes with the single-detector photometer and around 0.05 magnitudes for the nIR images.

The optical-nIR photometry used in this thesis is mainly that taken on the same nights as the spectroscopy, obtained with a time delay of less than 2-3 hours.

2.3 The sample of stars

Table 2.1 shows in Col. 1 the 38 stars selected from the EXPORT sample and analysed in this thesis. Cols. 2, 3, 4, 5, 6 and 7 show the spectral type, the stellar effective temperature, mass, luminosity, age and projected rotational velocity. Most of these stellar parameters were obtained using EXPORT data (Mora et al. 2001; Merín 2004; Montesinos et al. 2009), and will be used along this work. Most of the stars are HAe and late-type HBe stars, but there are also a few IMTTs. The sample is representative of the HAeBe regime, including almost all such type of objects in the northern hemisphere (from the catalogue of Thé et al. 1994, see also Sect 1.2). The evolutionary stage of 51 Oph is not clear, showing characteristics typical of both an HBe star and a MS star with a gas-rich debris disk (van den Ancker et al. 2001; Stark et al. 2009). The UXOr-type variability is shown by $\sim$ 40 % of the stars (Col. 8), pointing to a specific photo-polarimetric behaviour and inclination to the line of sight. Some caveats about the properties of the stars in the sample and their stellar parameters are outlined in the following.

Information on the possible binarity (angular separation, spectral type of the companions and K-brightness difference) is included in Cols. 9, 10 and 11 of Table 2.1. Stellar companions

Table 2.1: Sample of stars and parameters

Star	Spt	T_* (K)	M_* ($M_\odot$)	L_* ($L_\odot$)	Age (Myr)	$v \sin i$ (km s^{-1})	UXOr	d_{comp}(Spt) (")	ΔK (mag)	Ref. comp
HD 31648	A5 Vep	8250	2.0	21.9	6.7	102		...	...	...
HD 34282	A3 Vne	9550^A	$<2.1^A$	5.13^A	$> 7.8^A$	129		...	...	...
HD 34700	G0 IVe	6000^B	2.4^B	20.0^B	3.4^B	46		5.2(M1-2)	3.3	(1)
								9.2(M2-3)	4.2	(1)
HD 58647	B9 IVep	10500	6.0	911	0.4	118		>0.5(?)	?	(2)
HD 141569	B9.5 Vev	9550^A	2.2^A	22.9^A	6.7^A	258		7.6(M2)	1.8^{KS}	(3)
								9.0(M4)	2.4^{KS}	(2)
HD 142666	A8 Ve	7590^A	2.0^A	17.0^A	5.1^A	72		...	...	...
HD 144432	A9 IVev	7410^A	2.0^A	14.8^A	5.3^A	85		1.4(K5Ve)	2.4	(4,5)
HD 150193	A2 IVe	8970	2.2	36.1	5.0	100^C		1.1(F9Ve)	2.2	(4,6)
HD 163296	A1 Vepv	9250	2.2	34.5	5.0	133		...	...	...
HD 179218	A0 IVe	9500	2.6	63.1	3.3	72^D		2.5(?)	6.6	(7,8)
HD 190073	A2 IVev	9500	5.1	471	0.6	20^E		...	...	...
AS 442	B8 Ve	11000	3.5	207	1.5	(?)		?(?)	?	(9)
VX Cas	A0 Vep	10000	2.3	30.8	6.4	179	$\surd$	5.3(?)	4.8	(8)
BH Cep	F5 IIIev	6460^A	1.7^A	8.91^A	8.2^A	98	$\surd$	...	...	...
BO Cep	F5 Ve	6610^A	1.5^A	6.61^A	8.2^A	(?)		...	...	...
SV Cep	A2 IVe	10250	2.4	37.5	5.2	206	$\surd$	...	...	...
V1686 Cyg	A4 Ve	6170^A	$>3.5^A$	257^A	$< 0.2^A$	(?)		...	...	...
R Mon	B8 IIIev	12020^A	$>5.1^A$	2690^A	$< 0.01^A$	(?)		0.7(K1V)	$6.0^{K'}$	(10)
VY Mon	A5 Vep	12020^A	$>5.1^A$	15800^A	$< 0.01^A$	(?)	$\surd$	...	...	...
51 Oph	B9.5 IIIe	10250	4.2	312	0.7	256		...	...	...
KK Oph	A8 Vev	7590^A	2.2^A	25.7^A	3.9^A	177	$\surd$	1.5(G6Ve)	2.5	(4,6)
T Ori	A3 IVev	9750	2.4	50.2	4.0	175		7.7	>4.5	(11)
BF Ori	A2 IVev	8970	2.6	61.6	3.2	37	$\surd$	...	...	...
CO Ori	F7 Vev	6310^A	$>3.6^A$	100^A	$< 0.1^A$	65		2.0(?)	3.2^H	(12)
HK Ori	G1 Ve	8510^A	3.0^A	77.6^A	1.0^A	(?)	$\surd$	0.4(K3)	2.30	(11,13)
NV Ori	F6 IIIev	6750^F	2.2^F	21.2^F	4.4^F	81		...	...	...
RY Ori	F6 Vev	6310^A	2.5^A	28.2^A	1.8^A	66	$\surd$	...	...	...
UX Ori	A4 IVe	8460	2.3	36.8	4.5	215	$\surd$	$\geq$ 0.02(?)	?	(12)
V346 Ori	A2 IV	9750	2.5	61.4	3.5	(?)		...	...	...
V350 Ori	A2 IVe	8970	2.2	29.3	5.5	(?)		0.3(?)	3.2	(8)
XY Per	A2 IV	9750	2.8	85.6	2.5	217		1.2(?)	0.0	(6)
VV Ser	A0 Vevp	13800	4.0	336	1.2	229	$\surd$	...	...	...
CQ Tau	F5 IVe	6800^B	1.5^B	5^B	7.7^B	105	$\surd$	...	...	...
RR Tau	A0 IVev	10000	5.8	781	0.4	225	$\surd$	?(?)	?	(7)
RY Tau	F8 IIIev	5770^F	1.3^F	2.30^F	6.5^G	55	$\surd$	...	...	...
PX Vul	F3 Ve	6760^A	1.5^A	5.25^A	14^A	(?)		...	...	...
WW Vul	A2 IVe	8970	2.5	50.0	3.7	220	$\surd$	...	...	...
LkHa 234	B5 Vev	12900^A	$>5.3^A$	4680^A	$< 0.01^A$	(?)	$\surd$	2.7(?)	> 5.20	(11)

Notes. Unless stated different, the stellar effective temperatures, masses, luminosities, and ages are from Montesinos et al. (2009); the spectral types and $v \sin i$ values from Mora et al. (2001). ^{A}Manoj et al. (2006), ^{B}Alonso-Albi et al. (2009), ^{C}Glebocki et al. (2000), ^{D}Guimãraes et al. (2006), ^{E}Hoffleit & Jascheck (1982) ^{F}Merín (2004), ^{G}Siess et al. (1999). Uncertainties can be found in some of the references, being around $\pm$ 150 K, 12%, 40%, 35% and 6% for the stellar temperature, mass, luminosity, age and $v \sin i$, respectively. UXOrs are classified from Oudmaijer et al. (2001), except SV Cep, UX Ori, VV Ser and CQ Tau (Rodgers 2003). The last three columns refer to possible stellar companions. HD 34700 is a triple visual system, being the brightest object a spectroscopic binary (Sterzik et al. 2005); HD 141569 is triple system (Weinberger et al. 2000). ^{KS} refers to the K_s filter, $^{K'}$ to K' and ^{H} to the Hipparcos H_p magnitude. (1): Sterzik et al. (2005), (2): Baines et al. (2006), (3): Weinberger et al. (2000), (4): Carmona et al. (2007), (5): Pérez et al. (2004), (6): Pirzkal et al. (1997) (7): Wheelwright et al. (2010), (8): Thomas et al. (2007), (9): Corporon & Lagrange (1999), (10): Close et al. (1997), (11): Leinert et al. (1997), (12): Bertout et al. (1999), (13): Smith et al. (2005).

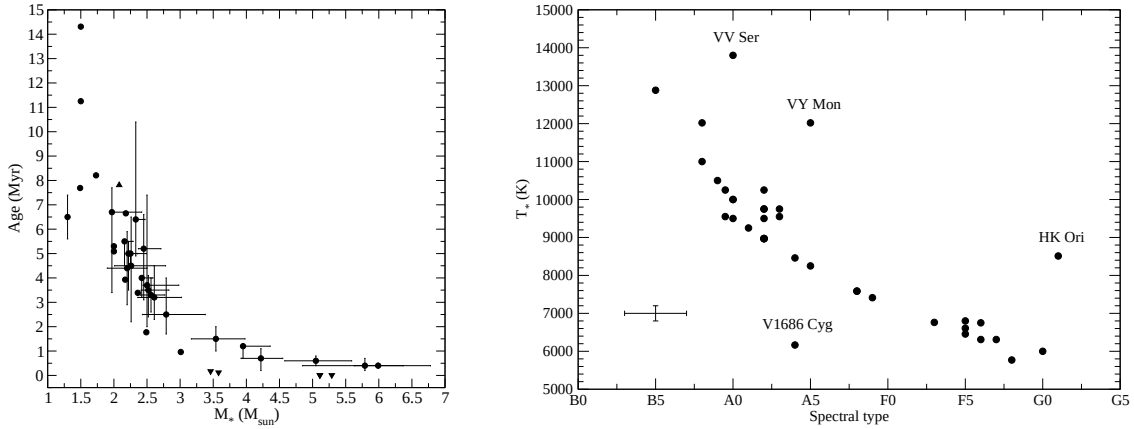

Figure 2.1: (Left): Stellar age against stellar mass for the stars in the sample. Triangles indicate upper and lower limits for the ages -lower and upper limits for the masses-. (Right): Stellar effective temperature against spectral type for the stars in the sample. Typical error bars are indicated. The objects labelled have spectral type uncertainties up to 5 spectral sub-types (see text).

have been reported for 47 % of the stars in the sample. This percentage is lower than that obtained in the most recent survey looking for multiplicity in HAeBe stars (74%; Wheelwright et al. 2010). The interpretation of the spectroscopy must account for the influence of stellar companions when the separation is lower than 1". Since the photometric data were taken with an aperture up to 14", they include the contribution of the companions. However, this tends to be much fainter at optical wavelengths (see e.g. the references in Wheelwright et al. 2010).

Figure 2.1 (left) shows the age of the stars against the stellar mass. The clear decline of the stellar age with the mass of the central object not only characterizes this sample but it is generally observed in the HAeBe regime (see e.g. van Boekel et al. 2005; Garcia Lopez et al. 2006). Following van Boekel et al. (2005), the lack of old HAeBes around 3-6 $M_{\odot}$ stars is likely caused by their faster evolution to the MS. The scarce number of young HAeBes around 1-3 $M_{\odot}$ stars is most probably explained by the fact that they become optically visible later in their evolution, since their envelopes are dissipated later. It is also more likely that, for a given age, the less massive stars escape to optical detection since they are also less luminous. The trend in Fig. 2.1 (left) directly affects part of our results (chapters 4 and 5).

Figure 2.1 (right) shows the stellar effective temperatures against the spectral types. These were derived by Mora et al. (2001) from the same spectra analysed in this work. Accurate determinations of the stellar temperatures were derived by Montesinos et al. (2009), using also EXPORT data and additional resources. We will use the spectral type and the stellar temperature indistincly, given that obviously they reflect each other in almost all sources. However, the four stars labelled in the right panel of Fig. 2.1 show large uncertainties in the spectral type (up to five subtypes, Mora et al. 2001). These uncertainties come from binary contamination (HK Ori), strong line variability (V1686 Cyg and VV Ser) or circumstellar/interstellar lines contaminating the spectrum (VY Mon). The stellar temperatures in Table 2.1 will be used instead of the spectral types in chapter 4.

Chapter 3

Optical spectroscopic variability of Herbig Ae/Be stars

This chapter is adapted from 2011, A&A, 529, A34, by Mendigutía, I.; Eiroa, C.; Montesinos, B.; Mora, A.; Oudmaijer, R. D.; Merín, B. and Meeus, G.

Abstract:
Aims: In order to gain insights into the variability behaviour of the circumstellar (CS) atomic gas, we have analysed 337 multi-epoch optical spectra of 38 Herbig Ae/Be (HAeBe) stars.
Methods: Equivalent widths (EWs) and line fluxes of the Hα, [OI]]6300, HeI5876 and NaID lines were obtained for each spectrum; the Hα line width at 10% of peak intensity (W_{10}) and profile shapes were also measured and classified. The mean line strengths and relative variabilities were quantified for each star. Simultaneous optical photometry was used to estimate the line fluxes.
Results: We present a homogeneous spectroscopic database of HAeBe stars. The lines are variable in practically all stars and timescales, although 30 % of the objects show a constant EW in [OI]6300, which is also the only line that shows no variability on timescales of hours. The HeI5876 and NaID EW relative variabilities are typically the largest, followed by those in [OI]6300 and Hα. The EW changes can be larger than one order of magnitude for the HeI5876 line, and up to a factor 4 for Hα. The [OI]6300 and Hα EW relative variabilities are correlated for most stars in the sample. The Hα mean EW and W_{10} are uncorrelated, as are their relative variabilities. The Hα profile changes in $\sim$ 70 % of the objects. The massive stars in the sample ($M_* > 3$ $M_\odot$) usually show more stable Hα profiles with blueshifted self-absorptions and less variable 10% widths.
Conclusions: Our data suggest multiple causes for the different line variations, but the [OI]6300 and Hα variability must share a similar origin in many objects. The physical mechanism responsible for the Hα line broadening does not depend on the amount of emission; unlike in lower-mass stars, physical properties based on the Hα luminosity and W_{10} would significantly differ. Our results provide additional support to previous works that reported different physical mechanisms in Herbig Ae and Herbig Be stars. The multi-epoch observations we present are a useful tool for understanding the origin of the CS lines and their variability, and to establish distinctions in the physical processes operating in pre-main sequence stars.

Keywords: Stars: pre-main sequence - Stars: activity - circumstellar matter - Astronomical data bases - planetary systems: protoplanetary disks -

3.1 Introduction

Herbig Ae and Be (HAeBe) stars are intermediate mass, pre-main sequence (PMS) objects, which are considered as the possible progenitors of Vega-like stars surrounded by circumstellar (CS) debris disks and, eventually, planets. The spectroscopic monitoring of some sources (see e.g. Praderie et al. 1986; Pogodin 1994; Rodgers et al. 2002; Mora et al. 2002, 2004) revealed that the spectra of HAeBe objects are not only characterized by the presence of emission lines, but also by the complex variations observed in both the emission and absorption features. This variability is also characteristic of T-Tauri stars (see e.g. Johns & Basri 1995; Schisano et al. 2009, and references therein).

The optical spectra of PMS stars show several important features that have been related to

different physical processes. Magnetospheric accretion models have succeeded in reproducing the profiles and strengths of the Hα and NaID lines (Hartmann et al. 1994; Muzerolle et al. 1998a,b, 2001, 2004). Despite the unknown nature of the magnetic fields in HAeBe stars (see e.g. Wade et al. 2005; Alecian et al. 2007; Wade et al. 2007; Hubrig et al. 2009), magnetospheric accretion has been shown to act in several HAe objects (Muzerolle et al. 2004; Mottram et al. 2007). The Hα line has also been associated with winds (Cabrit et al. 1990) or with combined magnetopheric accretion-wind models (Kurosawa et al. 2006). The Hα line width at 10% of peak intensity is used to estimate accretion rates in lower-mass PMS stars (see e.g. White & Basri 2003; Natta et al. 2004; Jayawardhana et al. 2006). The [OI]6300 line has been associated with accretion-powered outflows and winds (Finkenzeller 1985; Böhm & Catala 1994; Böhm & Hirth 1997; Corcoran & Ray 1997, 1998), and with the stellar UV-luminosity and disk-shape (Acke et al. 2005; van der Plas et al. 2008). The high temperature close to the stellar surface, which is generated in the accretion shock, has been suggested to be responsible for the HeI5876 line (Tambovtseva et al. 1999; Grinin et al. 2001). NaID lines seen in absorption describe the complex gas motions characterizing the CS medium around PMS stars (Mora et al. 2002, 2004).

Most spectroscopic studies are based on isolated spectra of different sources or have been focused on particular objects. The different approaches explaining the physical origin of the lines can profit from multi-epoch spectroscopic data. The EXPORT consortium (Eiroa et al. 2000) monitored a large number of intermediate-mass PMS stars, allowing for an extensive and homogeneous study of their spectroscopic variability. In this paper we analyse EXPORT multi-epoch optical spectra of HAeBe stars, specifically the lines Hα, [OI]6300, HeI5876, NaI $D_2$5890 and $D_1$5896. The photometric and spectroscopic variability of those objects requires simultaneous measurements to obtain accurate values for the line fluxes. These are derived using the already published simultaneous optical photometry of the stars in our sample (Oudmaijer et al. 2001). We will present a dataset comprised of multi-epoch line equivalent widths, fluxes, Hα profiles and widths, which is provided as a valuable observational legacy of the spectroscopic behaviour of HAeBe stars. We analyse and quantify the observed changes in the different lines and look for general trends, mainly focused on the equivalent width variability. A more specific analysis will be made in subsequent papers.

Sect. 3.2 describes the sample and spectra. Sect. 3.3 presents our results. They are analysed in Sect. 3.4, which describes the spectroscopic variability shown by the different lines (Sect. 3.4.1 for Hα, Sect. 3.4.2 for [OI]6300, Sect. 3.4.3 for HeI5876, Sect. 3.4.4 for NaID and Sect. 3.4.5 for a compendium of the spectroscopic characterization). Sect. 3.5 discusses the results and Sect. 3.6 includes a brief summary and conclusions.

3.2 Sample properties and observations

Table 3.1 (left side) shows the 38 stars in the sample. Cols. 1 to 3 indicate the name of the star, the spectral type, and the stellar mass. While most of the objects are HAeBe stars (covering almost all these objects in the Northern hemisphere from the catalogue of Thé et al. 1994), 10 of them have spectral types ranging from F3 to G1. The stellar masses range between $\sim$ 1– 6 $M_\odot$. As a selection criterion, all objects show the Hα line in emission. The sample span the 1 – 15 Myr age-range (Manoj et al. 2006; Montesinos et al. 2009), which is the period of the evolution from protoplanetary to young debris disks and the epoch of planet formation. There is a good balance between variable and non-variable objects, according to their simultaneous photopolarimetric behaviour (Oudmaijer et al. 2001; Eiroa et al. 2001, 2002).

The spectra were obtained by the EXPORT consortium (Eiroa et al. 2000) with the long slit Intermediate Dispersion Spectrograph (IDS) on the 2.5 m Isaac Newton Telescope (INT). The typical spectral resolution is R $\sim$ 5500, covering the wavelength range $\lambda\lambda$ 5800–6700 Å. The slit width was 1" projected on the sky (i.e. narrow enough to avoid confusion in most binaries of the sample; see e.g. Wheelwright et al. 2010, and references therein). Details of the observations and data reduction are given by Mora et al. (2001). The stars were observed over one or more of the four EXPORT runs. The right side of Table 3.1 shows the log of the observations, illustrating the monitoring timescales: from days to months in general, and for a few stars even hours. A total of 337 spectra were obtained, ranging from 3 to 18 per star, typically 6–10 spectra per object. In order to study the non-photospheric contribution (see Sect. 3.3), additional spectra of 28 spectroscopic standard MS stars were also taken in the same campaigns and with the same configuration.

3.3 Results

The contribution of the CS component to the spectra of the PMS sample was estimated from the spectra of the standard MS stars with similar spectral types. These were rotationally broadened using the projected rotational velocities derived by Mora et al. (2001) for the PMS objects. The non-photospheric contribution is given by the residuals obtained from the subtraction of the broadened standard spectra from the observed PMS spectra. The results refer to the normalized non-photospheric spectra.

Table A.1 (Appendix A) gives estimates of the equivalent widths (EWs) of the Hα, [OI]6300, HeI5876, $NaID_2$ and $NaID_1$ lines for all spectra of our sample. The Hα widths at 10% of peak intensity (W_{10}) and profile types (see below) are also listed. As usual, positive and negative EW values correspond to absorption and emission features, respectively. When a spectral line is seen partly in absorption and partly in emission, only the strongest component (i.e., that with the largest |EW|) is included. This double contribution appears mainly in the HeI5876 line, which usually shows both a redshifted absorption and a blueshifted emission. Although a specific analysis of this behaviour is beyond the scope of this work, it probably indicates the presence of hot infalling gas close to the stellar surface. In addition, the HeI5876 and NaID lines change from absorption to emission in several objects.

Conservative EW uncertainties were estimated by determining the maximum and minimum EW values from two different continuum levels that are located below and above unity ($\sim 1 \mp 1.5\sigma$), respectively. Both continuum levels bracket the adjacent noise to each spectral line. Typical median uncertainties are 3%, 8%, 10%, 20% and 30% of the EW values in the Hα, $NaID_2$, $NaID_1$, HeI5876 and [OI]6300 lines, respectively. Typical EW-uncertainties are larger than, or similar to, the typical strength of telluric absorption lines (see e.g. Caccin et al. 1985; Lundström et al. 1991; Reipurth et al. 1996). Telluric variability is also in general negligible compared with that reported for the lines (see below). Uncertainties for W_{10} are typically $\sim$ 1% of its value.

We follow the two-dimensional scheme by Reipurth et al. (1996) to classify the observed Hα profiles: type I are symmetric with no or very weak dips; type II are double-peaked profiles with the secondary peak higher than half the strength of the primary; type III have a secondary peak less than half the strength of the primary and type IV are P Cygni-type profiles. The scheme incorporates the designations "R" or "B" to indicate if the secondary peak is redshifted or blueshifted with respect to the primary. If both peaks have equal strengths, only the profile type is indicated. For type IV, the letters indicate a P-Cygni profile ("B") or inverse P Cygni ("R"). The letter "m" is added when more than one absorption

Table 3.1: Sample of stars and log of the INT/IDS spectra analysed.

Star	Spectral type	M_*	1998 May				1998 Jul				1998 Oct					1999 Jan			Ntot
		($M_\odot$)	14	15	16	17	28	29	30	31	24	25	26	27	28	29	30	31	
HD 31648	A5 Vep	2.0	...	...	...	...	...	...	...	...	1	...	1	1	1	1	1	1	7
HD 34282	A3 Vne	$<2.1^A$	...	...	...	...	...	...	...	...	1	1	1	1	1	1	1	1	8
HD 34700	G0 IVe	2.4^B	...	...	...	...	...	...	...	...	1	1	1	1	...	1	1	1	7
HD 58647	B9 IVep	6.0	...	...	...	...	...	...	...	...	...	...	...	...	...	1	1	1	3
HD 141569	B9.5 Vev	2.2^A	1	1	1	1	...	1	1	1	...	...	...	...	...	1	1	1	10
HD 142666	A8 Ve	2.0^A	1	1	1	1	1	1	1	1	...	...	...	...	...	1	1	1	11
HD 144432	A9 IVev	2.0^A	1	1	1	1	1	1	1	1	...	...	...	...	...	1	1	1	11
HD 150193	A2 IVe	2.2	...	1	1	1	...	...	...	...	...	...	...	...	...	...	...	...	3
HD 163296	A1 Vepv	2.2	1	1	1	1	1	2	2	2	...	...	...	...	...	...	...	...	11
HD 179218	A0 IVe	2.6	...	1	1	1	...	...	...	...	...	...	...	...	...	...	...	...	3
HD 190073	A2 IVev	5.1	1	1	1	1	1	1	1	1	...	...	...	...	...	...	...	...	8
AS 442	B8 Ve	3.5	...	1	1	1	1	1	...	...	...	...	...	...	...	...	...	...	5
VX Cas	A0 Vep	2.3	...	...	...	...	1	1	1	1	1	1	1	1	1	...	1	1	11
BH Cep	F5 IIIev	1.7^A	...	1	1	1	1	1	1	1	2	2	2	2	1	...	1	...	17
BO Cep	F5 Ve	1.5^A	...	1	1	1	1	1	1	1	1	1	1	1	1	...	...	1	13
SV Cep	A2 IVe	2.4	1	1	1	1	1	1	1	1	1	1	1	1	1	1	...	...	14
V1686 Cyg	A4 Ve	$>3.5^A$	1	1	1	...	1	1	1	1	1	1	1	1	1	...	...	...	12
R Mon	B8 IIIev	$>5.1^A$	...	...	...	...	...	...	...	...	...	...	...	...	...	1	1	1	3
VY Mon	A5 Vep	$>5.1^A$	...	...	...	...	...	...	...	...	...	...	...	...	...	1	1	1	3
51 Oph	B9.5 IIIe	4.2	1	1	1	1	1	1	1	1	...	...	...	...	...	...	...	...	8
KK Oph	A8 Vev	2.2^A	1	1	1	3	1	1	1	1	...	...	...	...	...	...	...	...	10
T Ori	A3 IVev	2.4	...	...	...	...	...	...	...	...	1	1	...	1	1	1	1	1	7
BF Ori	A2 IVev	2.6	...	...	...	...	...	...	...	...	1	1	1	1	1	1	1	2	9
CO Ori	F7 Vev	$>3.6^A$	...	...	...	...	...	...	...	...	1	1	1	1	1	1	1	1	8
HK Ori	G1 Ve	3.0^A	...	...	...	...	...	...	...	...	1	1	1	1	1	1	1	1	8
NV Ori	F6 IIIev	2.2	...	...	...	...	...	...	...	...	1	1	1	1	1	1	1	1	8
RY Ori	F6 Vev	2.5^A	...	...	...	...	...	...	...	...	...	1	1	1	1	1	1	1	7
UX Ori	A4 IVe	2.3	...	...	...	...	...	...	...	...	1	2	2	2	1	1	2	4	15
V346 Ori	A2 IV	2.5	...	...	...	...	...	...	...	...	1	1	1	1	1	1	1	1	8
V350 Ori	A2 IVe	2.2	...	...	...	...	...	...	...	...	1	...	1	1	1	1	1	1	7
XY Per	A2 IV	2.8	...	...	...	...	1	1	1	1	...	1	1	1	1	1	1	1	11
VV Ser	A0 Vevp	4.0	...	1	1	1	1	3	3	3	1	1	1	1	1	...	...	...	18
CQ Tau	F5 IVe	1.5^B	...	...	...	...	...	...	...	...	1	1	1	1	1	1	1	1	8
RR Tau	A0 IVev	5.8	...	...	...	...	...	...	...	...	1	1	1	1	1	1	1	1	8
RY Tau	F8 IIIev	1.3^C	...	...	...	...	...	...	...	...	1	1	1	1	...	1	1	...	6
PX Vul	F3 Ve	1.5^A	...	...	...	...	1	1	1	1	1	1	1	1	1	...	...	...	9
WW Vul	A2 IVe	2.5	1	1	1	1	1	1	1	1	1	1	1	1	1	...	...	...	13
LkHa 234	B5 Vev	$>5.3^A$	...	...	...	...	1	1	1	1	1	1	1	1	1	...	...	...	9

Notes. Left side: spectral types are from Mora et al. (2001). The non-flagged stellar masses are from Montesinos et al. (2009) and references therein. Flagged numbers are from ^{A}Manoj et al. (2006), ^{B} Alonso-Albi et al. (2009), ^{C}Merín (2004). Uncertainties for the stellar mass can be found in some of the references and are around 12%. Right side: The number of spectra per star is given for each observing day. The last column indicates the total number of spectra per object.

appears, and also when small dips are apparent in the type I profiles.

An object is considered as 'variable' in the EW of a line when its value differs in two or more spectra, taking into account the individual uncertainties. We use the relative variability $|\sigma(\mathrm{EW})/<\mathrm{EW}>|$ as a reliable measurement of the strength of the EW-changes, where σ is the standard deviation from the individual EW measurements of a given star[1] and <EW> is the mean line equivalent width. Johns & Basri (1995) used an equivalent parameter to characterize the variability of the Hα intensity in several T-Tauri stars. The non-variable objects tend to show the lowest values of $|\sigma(\mathrm{EW})/<\mathrm{EW}>|$; in these stars this ratio only contains information about the precision of the measurements. $\sigma(\mathrm{W_{10}})/<\mathrm{W_{10}}>$ and $\sigma(\mathrm{L})/<\mathrm{L}>$ are used to assess the relative variability of the Hα line width and that of the line luminosities.

Table 3.2 gives the mean line equivalent widths and their relative variabilities. Mean values and relative variabilities of $\mathrm{W_{10}}$(Hα) are also given, as well as the number of spectra displaying the corresponding Hα profiles. Uncertainties are listed for the non-variable stars in a given spectral line.

Table A.2 (Appendix A) shows the line fluxes for the spectra with simultaneous optical photometry (Oudmaijer et al. 2001). They were estimated using the EWs in Table A.1, and the V and R magnitudes obtained during the same night, taken within a time span of less than 2-3 hours. Fluxes are derived for 137 spectra (i.e. 41% of the initial 337 spectra) of 36 stars (the initial sample excluding AS 442 and R Mon). We used the expression $\mathrm{F} = \mathrm{F_0} \times |\mathrm{EW}|/10^{0.4m}$, with $\mathrm{F_0}$ the zero-magnitude fluxes (Bessell 1979) and m the V (for the NaID and HeI5876 lines) or R (for the Hα and [OI]6300 lines) magnitudes. We also computed fluxes for the NaID and HeI5876 lines that showed positive EWs, meaning the stellar flux absorbed by the lines. These fluxes are related to the amount of gas in the line of sight, traced by these species.

Table 3.3 shows the typical (mean) line luminosities of each star, obtained by averaging the fluxes in Table A.2 and assuming spherical symmetry. The distances considered are indicated in Col. 3. The line luminosity relative variabilities are also given, although the statistics is poorer than for the EWs, because of the lower number of spectra with simultaneous photometry (given in Col. 2).

The reddening towards the objects is low for most stars, with very few exceptions ($E(B\text{-}V) \leq 0.1$ for almost half of the objects, and $E(B\text{-}V) \sim 1$ for the most reddened sources -V1686 Cyg and LkHa 234-, Merín 2004). The fact that our multi-epoch line fluxes and luminosities are not de-reddened avoids introducing additional uncertainties and does not affect the analysis and discussion in the following sections.

[1] i.e. for N spectra, $\sigma = [\frac{1}{N-1} \cdot \sum_{i=1}^{N} (\mathrm{EW}_i - <\mathrm{EW}>)^2]^{1/2}$

Table 3.2: Mean equivalent and line widths, relative variabilities, and Hα profiles.

Star	<EW> Hα (Å)	<W_{10}> Hα (km/s)	Profile type ($N_{spectra}$) Hα	<EW> [OI]6300 (Å)	<EW> HeI5876 (Å)	<EW> $NaID_2$ (Å)	<EW> $NaID_1$ (Å)
HD 31648	-19.4 [0.10]	>557 [0.19]	IIIB(7)	...	-0.41 [0.34]	-0.64 [0.16]	-0.61 [0.15]
HD 34282	-5.0 [0.22]	>628 [0.19]	IIIR(3) IIIB(3) IIIRm(2)	...	0.18 [0.28]	0.10 [0.20]	0.06 [0.33]
HD 34700	-2.4 [0.12]	355 [0.06]	I(6) IIIR(1)	...	...	0.09 [0.22]	0.08 ± 0.01
HD 58647	-11.4 ± 0.3	616 ± 6	IIR(3)	-0.06 [0.50]	-0.13^f ± 0.04	0.15 [0.20]	0.13 ± 0.02
HD 141569	-6.0 ± 0.1	>641 [0.02]	IIR(10)	-0.14 [0.21]	...	0.1 [0.30]	0.1 [0.50]
HD 142666	-4.0 [0.25]	540 [0.24]	IIIR(4) IIIRm(4) IIB(1) IIR(1)	-0.010* ± 0.009	0.19 [0.47]	0.21 [0.19]	0.18 [0.22]
HD 144432	-11.8 [0.10]	>441 [0.23]	IIIB(11)	-0.013* ± 0.006	-0.29^f [0.55]	(-0.27 [0.63])	-0.26* [0.46]
HD 150193	-13.8 [0.06]	>481 [0.11]	IIIB(3)	...	-0.21^f ± 0.07	-0.36 ± 0.06	-0.28 ± 0.06
HD 163296	-22.8 [0.08]	690 [0.09]	IIIB(8) I(3)	-0.03* [0.67]	(0.54 [0.93])	-0.47 [0.36]	-0.46 [0.33]
HD 179218	-13.6 [0.05]	475 [0.02]	I(3)	-0.03 [0.33]	(0.04 [1.75])	-0.05 ± 0.01	-0.03 [0.67]
HD 190073	-25.6 [0.05]	391 [0.03]	IVB(5) I(3)	-0.03* [1.00]	-0.47^f [0.13]	-1.02 [0.04]	-0.85 ± 0.02
AS 442	-32.7 [0.12]	646 [0.05]	IIIB(5)	-0.09 ± 0.02	0.19 [0.37]	0.76 [0.22]	0.63 [0.19]
VX Cas	-22.1 [0.51]	650 [0.15]	IIR(7) IIB(3) IIIR(1)	-0.21 [0.76]	0.61 [0.41]	0.53 [0.53]	0.47 [0.45]
BH Cep	-6.2 [0.37]	700 [0.09]	IIR(5) IIIR(5) IIIBm(4) IIRm(2) IIBm(1)	-0.03* [0.67]	0.36 [0.53]	0.44 [0.36]	0.37 [0.38]
BO Cep	-7.5 [0.21]	645 [0.12]	IIR(7) IIIRm(2) IIIR(2) IIB(1) IIRm(1)	-0.17 ± 0.02	0.31 [0.64]	0.26 [0.35]	0.21 [0.33]
SV Cep	-11.7 [0.08]	705 [0.07]	IIR(7) IIB(5) IIIR(2)	-0.13 ± 0.01	0.47 [0.45]	0.31 [0.39]	0.26 [0.38]
V1686 Cyg	-22.7 [0.42]	>458 [0.10]	IIIB(7) IIIBm(5)	-0.30 [0.77]	(0.25* [0.88])	1.57 [0.47]	0.86 [0.69]
R Mon	-114 ± 2	832 [0.01]	Im(3)	-5.0 ± 0.1	1.2^f ± 0.2	-0.15 ± 0.02	-0.47 ± 0.06
VY Mon	-41 ± 1	711 [0.03]	IIIB(3)	-1.9 ± 0.1	...	2.32 ± 0.07	1.53 [0.05]
51 Oph	-3.3 ± 0.1	521 [0.03]	IIB(8)	...	-0.1 [0.30]	(-0.06* [0.83])	(-0.14 [0.57])
KK Oph	-74.1 [0.15]	607 [0.08]	I(3) Im(3) IIR(3) IIB(1)	-2.41 [0.22]	(0.46 [0.56])	(-0.4 [1.12])	(-0.22 [1.68])
T Ori	-21.5 [0.27]	675 [0.05]	IIR(7)	-0.13 [0.31]	0.58 [0.28]	0.42 [0.40]	0.30 [0.40]
BF Ori	-9.9 [0.06]	752 [0.09]	IIR(7) IIB(2)	-0.04 [0.25]	0.67 [0.31]	0.60 [0.33]	0.50 [0.30]
CO Ori	-21.1 [0.11]	549 [0.06]	I(5) Im(3)	-0.29 [0.24]	0.07* [1.14]	0.31 [0.55]	0.27 [0.41]
HK Ori	-57.6 [0.27]	582 [0.06]	IIB(4) IIR(3) I(1)	-1.29 [0.26]	0.40* [0.48]	(0.35 [0.80])	(0.34 [0.65])
NV Ori	-4.0 [0.05]	608 [0.11]	IIIR(3) IIR(3) Im(1) IIB(1)	-0.012* ± 0.006	0.20* [0.50]	(-0.21 [0.86])	(-0.22 [0.73])
RY Ori	-15.8 [0.23]	611 [0.06]	IIR(6) IIB(1)	-0.12 [0.50]	0.59 [0.44]	0.98 [0.30]	1.01 [0.30]
UX Ori	-9.3 [0.33]	>659 [0.14]	Im(8) IIIRm(3) IIRm(2) IIBm(1) IVR(1)	-0.05 ± 0.01	(0.27 [0.78])	(-0.25 [0.92])	(-0.13 [1.23])
V346 Ori	-3.8 [0.24]	908 ± 55	IIIRm(5) IIIBm(3)	...	...	(0.15 [0.80])	(0.11 [0.73])
V350 Ori	-12.3 [0.17]	722 [0.06]	IIR(4) IIIR(2) IIIRm(1)	-0.13 [0.31]	0.43 [0.37]	0.71 [0.18]	0.60 [0.27]
XY Per	-9.8 [0.11]	726 [0.02]	IIB(6) IIR(3) IIRm(1) IIBm(1)	-0.04* [0.75]	0.23 [0.43]	0.55 [0.16]	0.44 [0.11]
VV Ser	-49.7 [0.05]	695 [0.04]	IIR(8) IIB(8) II(2)	-0.54 [0.11]	(0.57 [0.47])	0.83 [0.19]	0.71 [0.24]
CQ Tau	-4.8 [0.31]	>531 [0.24]	IIIR(5) IIR(2) Im(1)	-0.06 [0.50]	0.10* [1.00]	0.39 [0.26]	0.33 [0.24]
RR Tau	-25.6 [0.34]	683 [0.02]	IIR(5) IIB(3)	-0.39 [0.23]	0.43 [0.18]	0.76 [0.21]	0.66 [0.20]
RY Tau	-15.3 [0.19]	680 [0.12]	IIB(3) IIIB(1) IIBm(1) IIR(1)	-0.75 ± 0.05	(-0.24 [1.12])	(0.48 [0.90])	(0.41 [0.98])
PX Vul	-14.4 [0.08]	626 [0.05]	IIIB(5) Im(2) IIB(2)	-0.08 [0.25]	0.19* [0.74]	0.17 [0.23]	0.16 [0.19]
WW Vul	-19.1 [0.10]	744 [0.06]	IIB(9) IIR(4)	-0.09 [0.22]	0.69 [0.35]	0.66 [0.35]	0.50 [0.44]
LkHa 234	-69.9 [0.07]	762 [0.04]	IIB(6) IIIB(3)	-0.57 [0.12]	0.81 [0.23]	(-0.39 [2.51])	(-0.22 [3.30])

Notes. Values from the data in Table A.1. Numbers in brackets are the EW relative variabilities. Typical uncertainties are $\delta(|\sigma/<EW>|) \sim 0.03$, 0.15, 0.16, 0.14 and 0.12 for the Hα, [OI]6300, HeI5876 and $NaID_2$ and D_1 lines, respectively. $\delta(\sigma/<W_{10}>) \sim 0.01$. Propagated uncertainties (±) are indicated for the non-variable objects. Values in parentheses indicate those lines shown both in absorption and emission. Only the values of the most frequent absorption/emission behaviour are considered in these cases to derive the mean values. * indicates that there is at least one spectrum not showing the line. "..." indicates that the line is not detected. ^{f} indicates that the HeI5876 line has only one component (absorption or emission) in all spectra.

Table 3.3: Mean line luminosities.

Star	$N_{spectra}$	d	<L> Hα	<L> [OI]6300	<L> HeI5876	<L> $NaID_2$	<L> $NaID_1$
		(pc)	($\times10^{31}$ erg s^{-1})	($\times10^{29}$ erg s^{-1})	($\times10^{30}$ erg s^{-1})	($\times10^{30}$ erg s^{-1})	($\times10^{30}$ erg s^{-1})
HD 31648	3	146	10.4 [0.15]	...	2.35 [0.45]	3.91 [0.21]	3.86 [0.15]
HD 34282	2	164[1]	0.50±0.08	...	*0.195* [0.27]	*0.100* [0.36]	*0.0644* [0.50]
HD 34700	1	336[4]	2.0±0.3	...	...	*0.7*±0.2	*0.6*±0.2
HD 58647	1	543	179±10	81±30	22±9	*31*±4	*26*±4
HD 141569	4	99[1]	2.51±0.09	6±1	...	*0.47*±0.05	*0.481* [0.47]
HD 142666	3	145[1]	0.81±0.08	...	*0.37*±0.07	*0.470* [0.15]	*0.40*±0.04
HD 144432	3	145[1]	4.79 [0.11]	0.4*±0.4	0.860 [0.53]	0.928 [0.68]	1.0±0.1
HD 150193	2	203	6.2±0.3	...	0.9±0.2	1.4±0.2	1.1±0.2
HD 163296	3	130	21.3 [0.05]	1.50* [1.73]	*5.68* [0.41]	2.96 [0.39]	3.13 [0.48]
HD 179218	1	201	18±1	4±1	*0.7*±0.2	0.6±0.1	0.3±0.1
HD 190073	1	767	360±12	82±10	68±10	*146*±10	*128*±10
VX Cas	6	619	4.88 [0.18]	3.83 [0.16]	*1.69* [0.62]	*1.11* [0.41]	*1.02* [0.40]
BH Cep	7	450[1]	1.26 [0.16]	0.784 [0.60]	*0.537* [0.61]	*0.669* [0.38]	*0.578* [0.53]
BO Cep	5	400[1]	1.11 [0.24]	2.6±0.5	*0.464* [0.55]	*0.277* [0.51]	*0.232* [0.46]
SV Cep	5	596	6.52 [0.08]	7±1	*2.46* [0.41]	*1.48* [0.49]	*1.21* [0.42]
V1686 Cyg	6	980[1]	6.19 [0.44]	7.85 [0.35]	(*0.471* [0.90])	*2.64* [0.81]	*1.47* [0.97]
VY Mon	1	800[1]	8.2±0.2	39±4	...	*1.5*±0.1	*1.02*±0.08
51 Oph	3	142	23±2	...	8±2	2.49* [1.06]	8±2
KK Oph	3	160[1]	1.03±0.03	3.54 [0.09]	(*0.0630* [0.42])	(*0.0227* [0.31])	(*0.0282* [0.28])
T Ori	3	472	12.6 [0.13]	7.49 [0.27]	*1.972* [0.22]	*2.18* [0.30]	*1.52* [0.34]
BF Ori	4	603	14.8±0.6	8±1	*9.86* [0.57]	*9.66* [0.49]	*9.38* [0.23]
CO Ori	5	450[1]	5.27 [0.07]	6.58 [0.22]	*0.0573** [2.24]	*0.469* [0.94]	*0.397* [0.72]
HK Ori	5	460[1]	9.98 [0.41]	23.9 [0.4]	*0.590** [0.68]	(*0.565* [0.20])	(*0.566* [0.27])
NV Ori	5	450[2]	3.5±0.2	0.457* [2.24]	*1.22** [0.68]	1.75 [0.16]	1.71 [0.21]
RY Ori	4	460	1.99 [0.12]	1.43 [0.44]	*0.460* [0.22]	*0.993* [0.33]	*1.01* [0.33]
UX Ori	5	517	10.8 [0.21]	6±1	(*2.73* [0.65])	(2.36 [0.30])	(1.08 [0.69])
V346 Ori	3	586	3.2±0.4	...	...	(*1.55* [0.42])	(*1.18* [0.43])
V350 Ori	2	735	4.8±0.2	5±1	*1.3*±0.2	*2*±1	*2.6*±0.2
XY Per	4	347	9.00 [0.28]	4.37* [0.87]	*2.35* [0.41]	*4.51* [0.19]	*3.58* [0.14]
VV Ser	7	614	17.3 [0.06]	19.8 [0.18]	*1.28* [0.25]	*1.67* [0.20]	*1.41* [0.26]
CQ Tau	5	130[3]	0.501 [0.19]	0.49±0.08	*0.10**±0.02	*0.409* [0.18]	*0.316* [0.11]
RR Tau	5	2103	169 [0.18]	253 [0.14]	*24.4* [0.41]	*42.4* [0.33]	*37.7* [0.33]
RY Tau	5	134[2]	0.850 [0.09]	4.4±0.3	(0.0694 [0.26])	(0.0993 [0.47])	(0.103 [0.50])
PX Vul	5	420[1]	2.76±0.09	1.71 [0.28]	*0.210* [0.62]	*0.227* [0.27]	*0.218* [0.22]
WW Vul	6	696	15.3 [0.07]	8.13 [0.22]	*5.83* [0.29]	*6.00* [0.42]	*4.79* [0.50]
LkHa 234	4	1250[1]	43.9±0.6	36±3	*2.71* [0.19]	1.18 [0.62]	0.8±0.2

Notes. Values from the data in Table A.2. Numbers in brackets are the line luminosity relative variabilities. Typical uncertainties are $\delta(\sigma/<L>) \sim 0.06$, 0.1, 0.2, and 0.1 for the Hα, [OI]6300, HeI5876 and NaID lines, respectively. Propagated uncertainties (±; distance errors not considered) are indicated for the non-variable objects. Italic numbers refer to lines seen in absorption and values in parentheses are those lines shown both in absorption and emission. Only the values of the most frequent absorption/emission behaviour are considered in these cases to derive the mean values. * indicates that there is at least one spectrum not showing the line. "..." indicates that the line is not detected. The distances are from Montesinos et al. (2009) by default, the remaining ones are taken from [1]Manoj et al. (2006), [2]Blondel et al. (2006), [3]Garcia Lopez et al. (2006), [4]Acke et al. (2005).

3.4 Analysis

3.4.1 The Hα line

Our data show that the Hα emission line remains constant, at least on timescales of days-months, for HD 141569 and 51 Oph, based on 8 and 10 spectra, respectively. In addition, Hα is non-variable in HD 58647, R Mon and VY Mon; however, there are only three spectra per object, so that variability at timescales longer than days cannot be excluded. The remaining stars show EW(Hα) variability.

The typical Hα relative variability, $|\sigma/<\mathrm{EW}>|$, is 0.19 (mean) and 0.15 (median)[2]. Hα EW variations up to a factor $\mathrm{EW}_{max}/\mathrm{EW}_{min} \sim 4$ can be observed for individual stars (e.g. V1686 Cyg, VX Cas). The <EW>(Hα) ranges between -2 and -74 Å, with typical values of -19.4 Å (mean) and -14.4 Å (median)

All objects change their W_{10}(Hα) but HD 58647 with only three measurements and V346 Ori with very large uncertainties. The typical relative variability is only $\sigma(\mathrm{W}_{10})/<\mathrm{W}_{10}> =$ 0.09 (mean), 0.07 (median). Some stars show W_{10}(Hα) changes up to a factor ~ 2.5 (e.g. CQ Tau). The $<\mathrm{W}_{10}>$(Hα) ranges from 355 km s^{-1} to 908 km s^{-1} and is typically around 640 km s^{-1}

Changes of both EW and W_{10} are seen on timescales as short as hours from the five objects with more than one spectrum per night. Our data show typical changes of a factor ~ 1.1 in both parameters on this timescale. The strongest variations occur over longer timescales however, i.e. weeks-months, at least in our database.

Variations in the line profile are very frequent –only 18% of the stars display the same type in all spectra– and are common on timescales of days; $\sim$73% show variations from one day to the next one. Some extreme cases are VV Ser, changing from type IIR to type IIB profiles practically from spectrum to spectrum, and UX Ori, BO Cep and BH Cep, which show five different profile types. BH Cep also shows the fastest variation, changing from IIB to IIIB in less than one hour. The high-mass objects in our sample tend to show the same Hα profile type during a given observing run, i.e. on timescales of a week, and all objects showing stable Hα profiles only on shorter timescales have $\mathrm{M}_* < 3\ \mathrm{M}_\odot$.

All Hα profiles classified by Reipurth et al. (1996) are observed in our spectra with a similar distribution (see also Vieira et al. 2003): type II profiles are the most frequent (52% of the observations), followed by type III (32%) and I (13%). P-Cygni type profiles are the least common (less than 3%). "R" and "B" profiles appear almost in the same proportion (44% versus 43%). However, B profiles are mainly shown by the most massive objects in our sample (the stars with $\mathrm{M}_* \geq 3\ \mathrm{M}_\odot$ have "B" profiles in 60% of the spectra; in fact only they show P-Cygni signatures). "R" profiles dominate in the HAe and lower-mass range of our sample (47% of the spectra, against 37% in "B").

3.4.2 The [OI]6300 line

Thirty-two out of the 38 stars show the [OI]6300 emission line. The line is variable in $\sim$70% of the stars; typical values of $|\sigma/<\mathrm{EW}>|$ are 0.51 (mean) and 0.26 (median). The largest EW variations -a factor $\sim$ 7–9- are seen, as for the Hα line, in V1686 Cyg and VX Cas. [OI]6300 variability is not detected on timescales of hours. For seven objects, the line is seen only in several spectra. The emission is very faint in these stars and their $|\sigma/<\mathrm{EW}>|$ values should be taken with caution. They could be affected by telluric variability or by artefacts

[2]In order to improve the reliability of the typical values and ranges derived, the 33 objects with 5 or more spectra are usually taken as a reference.

from the telluric emission subtraction. Higher SNR spectra of the objects with the weakest [OI]6300 line would be necessary to better estimate their line relative variability. Typical <EW([OI]6300)> values are −0.29 Å (mean) and −0.12 Å (median). The difference between the mean and median values comes from the few objects showing |<EW([OI]6300)>| >> 1 Å.

Most of the stars display a single-peaked almost symmetric low-velocity component. For the few objects with profiles different from single-peaked, the emission tends to be faint and the SNR low, probably distorting their profiles.

3.4.3 The HeI5876 line

Only 4 out of the 38 stars do not show the HeI5876 line in any of their spectra. The line is present in the rest of the stars, although five objects do not show it in all their spectra. In seven stars the line appears either in absorption or in emission, depending on the observing date. In most cases, 84% of the objects, the line is present either fully in absorption, or the absorption is dominant. All objects show variations in the EW of the line, with the exception of HD 150193, HD 58647, and R Mon. There are only three spectra available for each object, thus we cannot exclude that this result is due to the comparatively poor spectroscopic coverage.

Changes in EW(HeI5876) take place in all timescales. The relative variability range is $0.12 < |\sigma/<\text{EW}>| < 1.22$, with a typical value of 0.53 (mean) and 0.46 (median). The variability is larger in those objects where the line is dominated by absorption. Line EW variations up to a factor $\text{EW}_{max}/\text{EW}_{min} \sim 13$ can be observed in these cases (e.g. BO Cep), compared to a factor ~ 6 for the objects showing the line emission (e.g. HD 144432). The typical mean and median value of |<EW(HeI5876)>| is 0.38 $\mathring{A}$, ranging between $-0.47 \leq$ <EW(HeI5876)> ≤ 0.81 $\mathring{A}$.

3.4.4 The NaID lines

NaID lines are seen in absorption for most of the cases ($\sim$ 70 % of the stars). The NaID absorption lines can have a non-negligible interstellar contribution owing to clouds in the line of sight of our objects (see e.g. Redfield 2007). Therefore, several EWs given in Tables A.1 and 3.2 should be considered as upper limits to the CS absorption. The timescale variability of the interstellar absorption is, however, much longer than that covered by our spectra (see e.g. Lauroesch & Meyer 2003). Thus, the observed variability of the NaID lines is caused by the CS gas component.

There are seven objects with a constant EW in the NaID lines. Again, apart from HD 34700 and HD 190073, only three spectra are available for each one. The remaining objects show EW variability. As expected, the relative variability is equal in both NaID lines ($\sim$ 0.50), within the uncertainties. As for the HeI5876 line, the smallest $\text{EW}_{max}/\text{EW}_{min}$ factors are shown by the objects with NaID in emission (up to a a factor ~ 4 in e.g. HD 163296, against a factor ~ 6 for objects with the lines in absorption such as CO Ori). NaID EWs do not usually change in hours. The only exception is HD 163296; its NaID emission changed a factor ~ 2 in one night (29-Jul-1998), but no variations were detected the two following nights. We note that variations on timescales of hours have been reported for UX Ori using higher resolution spectra (Mora et al. 2002). The typical <EW(NaID)> in our sample is $\sim$ 0.40 Å.

The NaID ratio is a good indicator of the optical thickness at these wavelengths (e.g. Mora et al. 2002, 2004). Changes in the optical depth of the CS medium in the line of sight

are observed in almost all objects, however, averaged values indicate optically thick media for most of the stars ($<EW(NaID_2)/EW(NaID_1)> \sim 1$).

3.4.5 Compendium of the EW variability

Table 3.4 summarizes typical values for the equivalent widths and their relative variabilities, the minimum and maximum values, the percentage of objects showing line variations, and the number of objects with variability on a timescale of hours. We remark that this one refers only to a sample of five stars with that spectroscopic timescale coverage. The percentage of objects where the corresponding line is undetected is also given. The values in the last three rows of the bottom panel are derived considering both NaID lines.

Table 3.4: Summary of the typical equivalent and line widths and their relative variability.

	EW(Hα) ($\AA$)	$\lvert\sigma/<EW(H\alpha)>\rvert$	W_{10}(Hα) (km s^{-1})	$\sigma/<W_{10}(H\alpha)>$
mean	19.4	0.19	627	0.09
median	14.4	0.15	646	0.07
range	2 – 74	0.05 – 0.51	355 – 908	0.02 – 0.24
% var		94		97
N_{stars} var (hours)		3		4

	EW([OI]6300) ($\AA$)	$\lvert\sigma/<EW([OI]6300)>\rvert$	EW(HeI5876) ($\AA$)	$\lvert\sigma/<EW(HeI5876)>\rvert$
mean	0.29	0.51	0.38	0.53
median	0.12	0.26	0.38	0.46
range	0.01 – 2.41	0.11 – 1.41	−0.47 – 0.81	0.12 – 1.22
% var		69		100
N_{stars} var (hours)		0		3
% no detection		15		9

	EW(NaID2) ($\AA$)	$\lvert\sigma/<EW(NaID_2)>\rvert$	EW($NaID_1$) ($\AA$)	$\lvert\sigma/<EW(NaID_1)>\rvert$
mean	0.40	0.53	0.38	0.57
median	0.47	0.37	0.33	0.41
range	−1.02 – 1.57	0.15 – 2.51	−0.85 – 1.01	0.13 – 3.27
% var		100		
N_{stars} var (hours)		1		
% no detection		0		

In general, CS absorption features show a larger EW variability than the emission lines. The EW relative variability is significantly higher for the HeI5876, NaID and [OI]6300 lines than for Hα. In addition, approximately 30 % of the objects show a constant [OI]6300 equivalent width, but the remaining lines are variable in practically all stars in which these are detected. Considering the short timescale variations, the number of variable stars is similar for the HeI5876 and Hα lines, a small percentage seems to present NaID variability, while no star shows changes in [OI]6300.

Finally, when simultaneous EWs and line fluxes are compared, the relative variability of the EWs tends to be equal to or an upper limit of that of the line fluxes for most of the stars.

3.5 Discussion

The described results indicate that the physical conditions in the line-forming regions are highly complex and variable on practically any timescale, and that the use of individual EW or line flux measurements could lead to biased conclusions. Averaged EW values are likely more representative, which might be specially true for the absorption component of the HeI5876 line, where the variations can be larger than one order of magnitude. Our sample shows that there is no significant correlation between the mean strengths and their relative variabilities, therefore, both are necessary to completely characterize the line behaviour of the stars.

Although a detailed study of the physical origin of the lines and their variations is beyond the scope of this work, the observed differences between the typical variabilities of the features, both in strength and in timescale, suggest multiple causes for the different line variations. In addition, our results show that there are no clear correlations among the relative variabilities of the different lines, excluding the obvious relation between the $NaID_2$ and D_1 changes, and the one between Hα and [OI]6300. Figure 3.1 shows the Hα and [OI]6300 EW relative variabilities of the sources with a clear detection of the [OI] line in all their spectra (this avoids possible telluric/instrumental effects; see Sect. 3.4.2). The Spearman's probability of false correlation (see e.g. Conover 1980) is only 0.19%. Although $|\sigma/<\mathrm{EW}>|$([OI]6300) tends to be larger than $|\sigma/<\mathrm{EW}>|$(Hα), the strength of the corresponding EW variations are coupled in many stars. This suggests that the EW variations share a common origin. One possibility is that Hα and [OI]6300 are affected by accretion-wind variability (see below and e.g. Corcoran & Ray 1997, 1998). Variability in the UV radiation would have influence on the strength of the [OI]6300 emission (Acke et al. 2005). Changes in the stellar continuum level could also affect the EW variations of both lines simultaneously, as we outline below.

Line EWs change because the conditions in the CS gas vary (producing variations in the line luminosity) and/or because there are changes in the continuum level. Most objects with significant V-band variability ($\Delta V \geq 0.4$) increase their Hα and [OI]6300 EWs as the stellar brightness decreases, leaving the corresponding line luminosities almost constant or even decreasing (see e.g. RR Tau on the left panel of Fig. 3.2, and also Rodgers et al. 2002). This behaviour has been explained as due to the coronographic effect caused by dusty clouds that occult the stellar surface (Grinin et al. 1994; Rodgers et al. 2002). The EW enhancement would result from the contrast between the continuum dimming and the almost constant line luminosity. This explanation has been suggested for stars showing the UXOr behaviour, but we note that objects such as V1686 Cyg, which is not classified as an UXOr from its simultaneous optical photopolarimetry (Oudmaijer et al. 2001), show a similar pattern in the Hα and [OI]6300 lines (see right panel of Fig 3.2).

Continuum changes can be rejected as the origin of the EW variability in other cases. Several examples are given in Fig. 3.3, where the remarkable line variations are not accompanied by significant changes in the simultaneous optical brightness (Oudmaijer et al. 2001). The main spectroscopic features shown by HK Ori during two consecutive nights are plotted in the top panels. The appearance of redshifted NaID emission lines is accompanied by a decrease of the absorption component of the HeI5876 line. Simultaneously, the [OI]6300 and Hα lines reduce their luminosities by a factor ~ 3. Hα changes from double-peaked to a redshifted single-peaked profile, with W_{10} remaining constant. The corresponding NaID ratios indicate

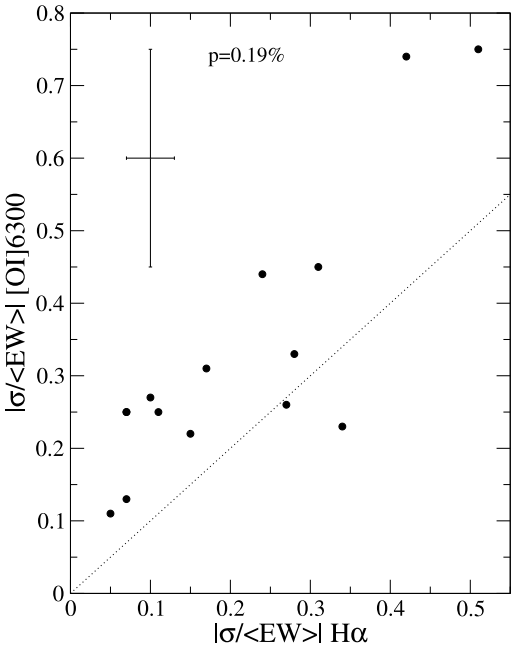

Figure 3.1: Equivalent width relative variability of the [OI]6300 line against that in Hα for the objects showing clear [OI] detections in all their spectra. The dotted line indicates equal values. The typical error bars and the Spearman's probability of false correlation are indicated.

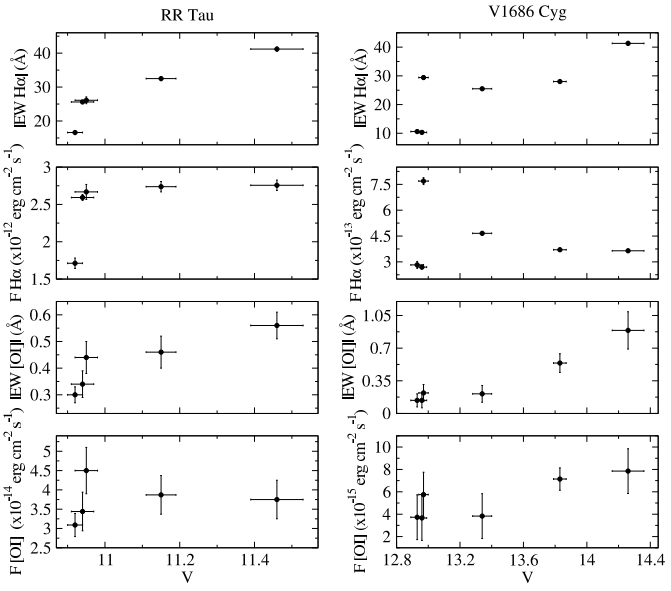

Figure 3.2: Equivalent widths and line fluxes of the Hα and [OI]6300 lines against the simultaneous V magnitude (Oudmaijer et al. 2001) for RR Tau and V1686 Cyg.

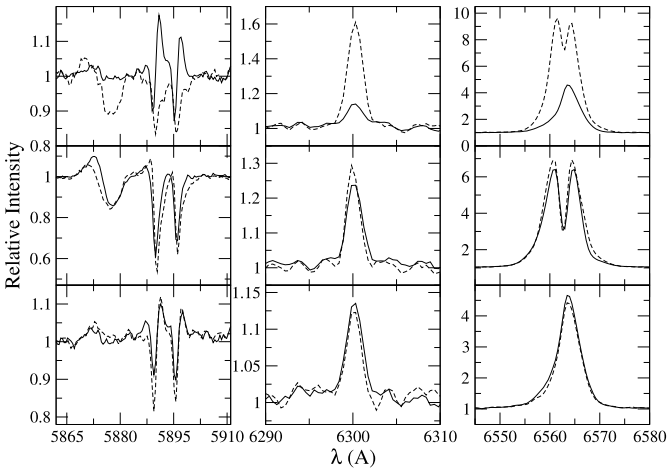

Figure 3.3: NaID and HeI5876 (left panels), [OI]6300 (middle panels) and Hα (right panels) lines shown by HK Ori (top panels, 1998, October 25 and 26), VV Ser (middle panels, 1998, October 24 and 27) and CO Ori (bottom panels, 1998, October 25 and 26). The dashed and solid lines correspond to the first and second night.

that the CS gas changed from optically thick to optically thin at these wavelengths. These findings are difficult to interpret, but obscuring dusty screens in the line of sight are clearly excluded. An alternative could be that the accretion and/or wind rate diminished from one night to the other and produced the decrease of the Hα and [OI] strengths and reduced the gas density, which explains the change to optically thin. This would allow the detection of hot infalling gas very close to the stellar surface, seen in emission. The examples in the middle and bottom panels of Fig. 3.3 show that small variations in the Hα and [OI]6300 lines are again related to each other.

The data show that the main origin for the EW-variability (gas or continuum changes) strictly depends on each star, each line considered and the epoch of observation. The complex behaviour of the lines and the continuum requires their simultaneous characterization to distinguish the origin of the spectroscopic variability.

Regarding the Hα line, its relative variability in W_{10} is twice as low as that in the EW, and we find no significant correlation either between the mean widths and line strengths or between their relative variabilities. Figure 3.4 shows that these parameters have a very high Spearman's probability of false correlation. This suggests that the physical mechanism responsible for the Hα broadening does not depend on the column density of hydrogen atoms. A similar result was found for the [OI]6300 line by Acke et al. (2005). Both the Hα luminosity and W_{10} are used as empirical accretion tracers in lower-mass stars (see e.g. Fang et al. 2009; Jayawardhana et al. 2006, and references therein). Our result indicates that both Hα measurements would typically produce different estimates in HAeBe stars.

Finally, we stress that the Hα behaviour depends on the stellar mass. The more massive objects in our sample tend to have more stable Hα line profiles with blueshifted self-absorptions, which could be indicative of a strong wind contribution (see also e.g. Finkenzeller & Mundt 1984). The less massive stars in our sample are slightly dominated by redshifted self-absorptions in their Hα profiles, which suggests that they are influenced by accretion (Muzerolle et al. 2004). In addition, our multi-epoch data suggest that the strength of the W_{10}(Hα) variability is significantly anti-correlated with the mass of the central object. Figure 3.5 shows our $\sigma/<W_{10}(H\alpha)>$ estimates against the stellar mass. Despite the scatter at low

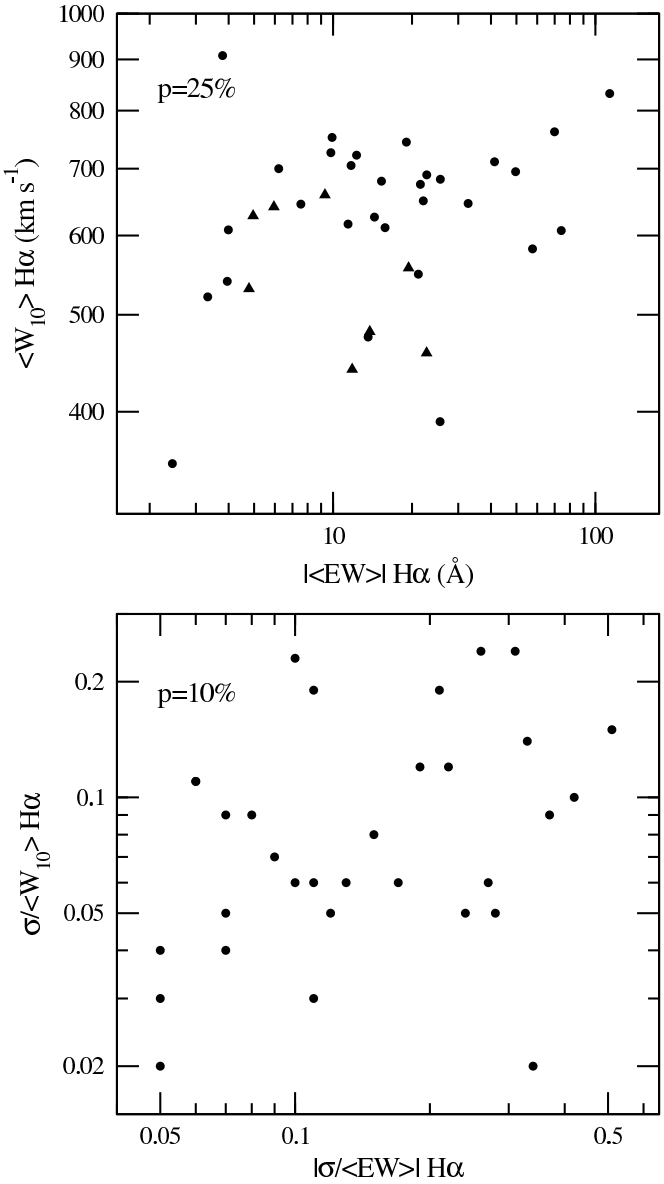

Figure 3.4: Mean value of the width of the Hα line against that of the equivalent width (top) and relative variabilities (bottom). Triangles are lower limits for $<W_{10}(H\alpha)>$. The Spearman's probabilities of false correlation are indicated.

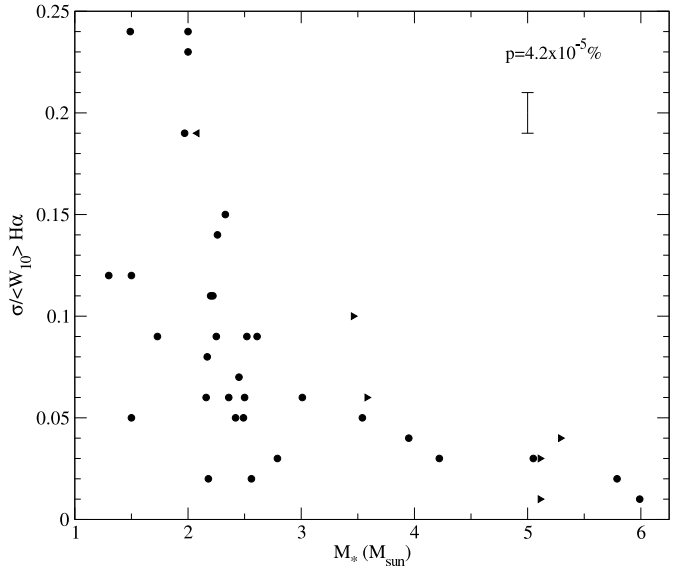

Figure 3.5: Relative variability of the Hα width at 10% of peak intensity against the stellar mass. Triangles are upper and lower limits for M_*. The typical $\sigma/<W_{10}(H\alpha)>$ uncertainty and the Spearman's probability of false correlation are indicated.

masses, almost all stars with $M_* \geq 3.0$ $M_\odot$ show a low $W_{10}(H\alpha)$ relative variability (≤ 0.06). A more extended emitting region could produce more stability in the line width. Preliminary magnetospheric accretion modelling that we are currently applying on HAe stars suggests that changes in the size of the magnetosphere and/or in the gas temperature of this region could induce significant changes in $W_{10}(H\alpha)$ (hundreds of km s^{-1}). The results found point to different physical processes operating in Herbig Ae and Herbig Be stars, which agrees with previous spectropolarimetric studies (see e.g. Vink et al. 2002; Mottram et al. 2007).

3.6 Summary and conclusions

The work presented here shows that multi-epoch spectroscopic observations together with simultaneous photometry are an extremely useful tool to better understand the variability of the circumstellar lines in PMS stars. By means of a large number of optical spectra the variability of the Hα, [OI]6300, HeI5876 and NaID lines has been analysed in a sample of 38 HAeBe stars. These spectra and the simultaneous photometry have allowed us to estimate line fluxes and to soundly assess if the observed EW variations are caused by changes in the stellar continuum or by variations of the circumstellar gas itself. Indeed, the spectra and photometry -and their simultaneous character- on which the analysis is based constitute one of the largest existing data bases to study some of the variability properties in intermediate-mass PMS stars. Several specific results we obtained are:

- The EW variability of the different lines depends on the analysed timescale and is independent of the mean line strength. The HeI587 and NaID lines show the largest EW variations and can be seen either in absorption or in emission. In contrast, [OI]6300 is the only line without variations on timescales of hours and is also the line with variability in a smaller percentage of the stars in the sample.

- There is a correlation between the Hα and [OI]6300 relative variabilities, which suggest

a common origin. In some stars the EW variability of both lines are due to variations of the continuum, but in other objects the EW variability reflects variations of the line luminosities and, consequently, in the CS gas properties.

- Mean values and relative variabilities of the Hα line width W_{10} and EW are uncorrelated in our sample. The lack of correlation between both parameters suggests that Hα broadening does not depend on the column density of hydrogen atoms. Thus, estimates of gas properties, such as accretion rates, based on the Hα W_{10} or EW would differ significantly, unlike in lower mass stars.

- The Hα behaviour differs depending on the stellar mass, which suggests different physical processes for Herbig Ae and Herbig Be stars. The massive stars tend to show stable Hα profiles, mainly dominated by blueshifted self-absorptions. In addition, stars with $M_* \geq 3.0$ $M_\odot$ show very low W_{10}(Hα) relative variabilities (≤ 0.06).

Finally, we point out that in addition to the mean spectra and relative variability distributions available in Appendix B, any of the spectra can be requested from the authors and are also available from Virtual Observatory tools.

Acknowledgements: C. Eiroa, G. Meeus, I. Mendigutía and B. Montesinos are partially supported by grant AYA-2008 01727. We thank Enrique Solano and Mauro López for making the spectra available from VO tools.

Chapter 4

Accretion rates and accretion tracers of Herbig Ae/Be stars

This chapter is adapted from 2011, A&A, 535, A99, by Mendigutía, I.; Calvet, N.; Montesinos, B.; Mora, A.; Muzerolle, J.; Eiroa, C.; Oudmaijer, R.D. and Merín, B.

Abstract:
Context: The scarcity of accretion rate estimates and accretion tracers available for Herbig Ae/Be (HAeBe) stars contrasts with the extensive studies for lower mass objects.
Aims: This work aims to derive accretion rates from the UV Balmer excess for a sample of 38 HAeBe stars. We look for possible empirical correlations with the strength of the Hα, [OI]6300, and Brγ emission lines.
Methods: Shock modelling within the context of magnetospheric accretion (MA) was applied to each star. We obtained the accretion rates from the excess in the Balmer discontinuity, derived from mean values of multi-epoch Johnson's UB photometry. The accretion rates were related to both mean Hα luminosities, Hα 10% widths, and [OI]6300 luminosities from simultaneous spectra, and to Brγ luminosities from the literature.
Results: The typical -median- mass accretion rate is 2×10^{-7} $M_\odot$ yr^{-1} in our sample, 36 % of the stars showing values $\leq 10^{-7}$ $M_\odot$ yr^{-1}, 35% between 10^{-7} and 10^{-6}, and 29% $> 10^{-6}$ $M_\odot$ yr^{-1}. The model fails to reproduce the large Balmer excesses shown by the four hottest stars ($T_* > 12000$ K). When accretion is related to the stellar masses and luminosities ($1 \leq M_*/M_\odot \leq 6$; $2 \leq L_*/L_\odot \leq 10^3$), we derive $\dot{M}_{\rm acc} \propto M_*^5$ and $L_{\rm acc} \propto L_*^{1.2}$, with scatter. Empirical calibrations relating the accretion and the Hα, [OI]6300, and Brγ luminosities are provided. The slopes in our expressions are slightly shallower than those for lower mass stars, but the difference is within the uncertainties, except for the [OI]6300 line. The Hα 10% width is uncorrelated with $\dot{M}_{\rm acc}$, unlike for the lower mass regime. The mean Hα width shows higher values as the projected rotational velocities of HAe stars increase, which agrees with MA. The accretion rate variations in the sample are typically lower than 0.5 dex on timescales of days to months, Our data suggest that the changes in the Balmer excess are uncorrelated to the simultaneous changes of the line luminosities.
Conclusions: The Balmer excesses and Hα line widths of HAe stars can be interpreted within the context of MA, which is not the case for several HBes. The steep trend relating $\dot{M}_{\rm acc}$ and M_* can be explained from the mass-age distribution characterizing HAeBe stars. The line luminosities used for low-mass objects are also valid to estimate typical accretion rates for the intermediate-mass regime under similar empirical expressions. However, we suggest that several of these calibrations are driven by the stellar luminosity.

keywords: Stars: pre-main sequence - Accretion, accretion disks - circumstellar matter - protoplanetary disks - Stars: activity - Line: formation

4.1 Introduction

Most of the stellar mass acquired during the pre-main sequence (PMS) phase comes through accretion from the disk. In addition, estimates of the mass accretion rate are needed to analyse circumstellar gas dissipation, and therefore to quantify the timescale when planets could be formed in protoplanetary disks. Magnetospheric accretion (MA hereafter, Uchida & Shibata 1985; Koenigl 1991; Shu et al. 1994) is the accepted paradigm that explains disk-to-star accretion in classical T-Tauri (CTT) and lower mass stars. In the MA scenario, the

inner disk is truncated at some point between the stellar surface and the co-rotation radius, where matter is accelerated through the magnetic field lines until it reaches the central star. The resulting hot accretion shocks can be modelled, allowing us to explain the continuum excess and the spectroscopic veiling from temperature differences with the stellar photosphere (Calvet & Gullbring 1998). This modelling yields accretion rate estimates, which are found to correlate with the strength of spectroscopic features covering the wavelength range from the UV to the IR (see e.g. Herczeg & Hillenbrand 2008; Fang et al. 2009; Rigliaco et al. 2011, and references therein). Even though the origin of these correlations is not clear, those spectral lines are used as empirical tracers, which simplifies the process of estimating accretion rates.

Herbig Ae/Be (HAeBe) stars are the massive (1-10$M_{\odot}$) counterparts of CTTs. How circumstellar matter accretes on those objects remains an open issue. For instance, MS stars with spectral types earlier than $\sim$ A6 ($M_* \geq 2$ $M_{\odot}$) are not expected to have convective sub-photospheric zones generating the necessary magnetic fields (Simon et al. 2002, and references therein). However, in young stars, convection zones may appear in earlier spectral types than expected (Finkenzeller 1985). In addition, different evidence suggests that MA could be extended to the intermediate-mass regime. Although weak in several cases, magnetic fields have been detected in some HAeBes (Wade et al. 2007; Hubrig et al. 2009). Spectropolarimetric measurements point to MA acting in HAe stars (Vink et al. 2002, 2003; Mottram et al. 2007), and Grady et al. (2010) conclude that the accretion in these objects goes through high-latitude funnels, again suggesting magnetically controlled accretion (see also Brittain et al. 2009). High-velocity redshifted self-absorptions observed in line profiles of several HAeBe stars (Natta et al. 2000; Mora et al. 2002, 2004) point to infalling material at close to free-fall velocities. These can be easily explained from MA and hardly at all from a competing scenario such as the boundary-layer one (see e.g. the review in Alencar 2007).

MA modelling was carried out for a sample of nine intermediate-mass T-Tauri stars by Calvet et al. (2004), showing that the correlation between the accretion and Brγ luminosities can be extended to these objects. The problem of measuring accretion rates for the HAeBe regime was faced by Muzerolle et al. (2004, MDCH04 hereafter). They reproduced the line profiles of UX Ori by assuming the MA geometry. The absence of significant line veiling and optical excess in most HAeBe objects was explained from the similar temperatures characterizing the stellar photosphere and the accretion shocks. The excess in the Balmer discontinuity was shown to be a valid measurement of accretion by MDCH04, providing a calibration between both parameters for a typical HAe star.

The large number of accretion studies for wide samples of low-mass stars contrasts with the lack of accretion rate measurements for HAeBes, which is also reflected in the scarce number of empirical tracers of accretion available for these objects. Accretion rate estimates for a wide sample of HAeBe stars were obtained by Garcia Lopez et al. (2006) from the Brγ line, using the correlation derived by (Calvet et al. 2004) for stars in a lower range of stellar temperatures. The recent accretion rate estimates by Donehew & Brittain (2011) are based on the calibration between the mass accretion rate and the excess in the Balmer discontinuity provided in MDCH04, which was modelled for a specific set of stellar parameters. However, the measurement of accretion requires modelling observed properties for each object individually. The accretion rates can then be compared with spectral diagnostics to establish possible empirical correlations. That comparison could benefit from simultaneous measurements, given the variability characterizing PMS stars (Eiroa et al. 2002; Mendigutía et al. 2011a, Paper I hereafter).

Following MDCH04, in this work we apply shock modelling within the context of MA, aiming to reproduce the strength of mean Balmer excesses derived from multi-epoch pho-

tometry of a wide sample of HAeBe stars. The accretion rates obtained in this way are then related to the mean strength of the Hα and [OI]6300 emission lines from simultaneous spectra, as well as to non-simultaneous Brγ luminosities from the literature. In addition, the simultaneous multi-epoch data allows us to make a first approach on the accretion rate variability and its relation with the spectral lines.

Section 4.2 summarizes the properties of the sample and the data. Section 4.3 describes the shock model (Sect. 4.3.1) and provides the accretion rates estimates (Sect. 4.3.2), which are compared to previous results (Sect. 4.3.2). Section 4.4 relates our accretion luminosities with those of the Hα, [OI]6300, and Brγ lines. The relation between accretion and the Hα 10% width is treated separately in Sect. 4.4.1. The analysis of the accretion rate variability is outlined in Sect. 4.5. The discussion and conclusions are included in Sects. 4.6 and 4.7.

4.2 Sample properties and data

Table 4.1 shows stellar parameters of the 38 stars in the sample. Columns 1 to 9 indicate the name of the star, the stellar mass, luminosity, effective temperature, radius, surface gravity, age, projected rotational velocity ($v \sin i$), and distance. Uncertainties can be found in some of the references given in the caption. Montesinos et al. (2009), from where most of the values are taken, gives around 12%, 40%, $\pm$ 150 K, $\pm$ 0.1 dex and 35% for the stellar mass, luminosity, effective temperature, surface gravity and age, respectively. The low errors, as compared to other methods based on spectral types, arise from a detailed spectroscopic and photometric modelling, based on the comparison to Kurucz synthetic spectra and stellar evolutionary tracks. The typical uncertainty for $v \sin i$ is 6% (Mora et al. 2001). The sample is the same one as was analysed in Paper I. The objects are mainly HAe and late-type HBes, as well as ten intermediate-mass T-Tauri stars with F–G spectral types and 1-4 $M_\odot$. All the stars show IR excess (Merín 2004) indicative of dusty circumstellar environments, and the Hα line in emission, pointing to active accretion.

This work is mainly based on the multi-epoch Hα and [OI]6300 spectra from Paper I, and the multi-epoch UBV photometry from Oudmaijer et al. (2001). The spectra were taken at mid-resolution (R $\sim$ 5500), and the photospheric contribution was subtracted. We selected those spectra and photometry taken on the same nights. Therefore, the results in this paper were derived from (almost) simultaneous spectroscopic and photometric measurements, unless otherwise stated. The slit width of the spectrograph was 1" projected in the sky, which avoids contamination from stellar companions in almost all sources. This is not the case for the photometry, where the aperture was $\sim$ 14". However, most of the stars in our sample with reported multiplicity have much fainter companions in the optical (see e.g. the references in Wheelwright et al. 2010). We assume that their contribution to the emission at short wavelengths is negligible for our purposes.

Table 4.1: Sample of stars.

Star	M_* ($M_\odot$)	L_* ($L_\odot$)	T_* (K)	R_* ($R_\odot$)	g [cm s^{-2}]	Age (Myr)	$v \sin i$ (km s^{-1})	d (pc)	<L(Hα)> [$L_\odot$]	<W_{10}(Hα)> (km s^{-1})	<L([OI]6300)> [$L_\odot$]	<E(B-V)> (mag)	L(Brγ) [$L_\odot$]
HD 31648	2.0	21.9	8250	2.3	4.0	6.7	102	146	-1.42	595	...	0.02	(?)
HD 34282	$<2.1^A$	5.13^A	9550^A	0.8	4.9	$> 7.8^A$	129	164^A	-2.82	487	...	0.19	-4.20^1
HD 34700	2.4^B	20.0^B	6000^B	4.2	3.6	3.4^B	46	336^H	-2.29	334	...	0.01	(?)
HD 58647	6.0	911	10500	9.1	3.3	0.4	118	543	-0.13	619	-2.49	0.13	-2.08^2
HD 141569	2.2^A	22.9^A	9550^A	1.8	4.3	6.7^A	258	99^A	-2.01	646	-3.71	0.09	$-3.99^{1,2}$
HD 142666	2.0^A	17.0^A	7590^A	2.4	4.0	5.1^A	72	145^A	-2.33	483	-4.75	0.26	$-3.53^{1,3}$
HD 144432	2.0^A	14.8^A	7410^A	2.3	4.0	5.3^A	85	145^A	-1.87	421	-4.93	0.06	$-3.29^{1,3}$
HD 150193	2.2	36.1	8970	2.5	4.0	5.0	100^C	203	-1.15	458	...	0.45	-2.64^1
HD 163296	2.2	34.5	9250	2.3	4.1	5.0	133	130	-1.17	726	-4.37	0.03	$-2.77^{1,2,3}$
HD 179218	2.6	63.1	9500	2.9	3.9	3.3	72^D	201	-1.16	464	-3.86	0.08	-2.74^3
HD 190073	5.1	471	9500	8.0	3.4	0.6	20^E	767	0.06	378	-2.49	0.13	(?)
AS 442	3.5	207	11000	4.0	3.8	1.5	(?)	826	-0.15	646	-2.42	0.73	(?)
VX Cas	2.3	30.8	10000	1.9	4.3	6.4	179	619	-1.43	672	-3.48	0.37	(?)
BH Cep	1.7^A	8.91^A	6460^A	2.4	3.9	8.2^A	98	450^A	-2.34	705	-4.25	0.31	(?)
BO Cep	1.5^A	6.61^A	6610^A	2.0	4.0	11.2^A	(?)	400^A	-2.51	685	-3.97	0.13	(?)
SV Cep	2.4	37.5	10250	1.9	4.3	5.2	206	596	-1.33	731	-3.20	0.39	(?)
V1686 Cyg	$>3.5^A$	257^A	6170^A	14	2.7	$< 0.2^A$	(?)	980^A	-0.27	457	-2.80	0.63	-1.77^3
R Mon	$>5.1^A$	2690^A	12020^A	12	3.0	$< 0.01^A$	(?)	800^A	0.34	832	-1.04	0.70	(?)
VY Mon	$>5.1^A$	15800^A	12020^A	29	2.5	$< 0.01^A$	(?)	800^A	-0.65	719	-0.46	1.79	(?)
51 Oph	4.2	312	10250	5.6	3.6	0.7	256	142	-1.23	522	...	0.03	$-2.68^{1,2}$
KK Oph	2.2^A	25.7^A	7590^A	2.9	3.8	3.9^A	177	160^A	-2.28	593	-3.53	0.36	-3.53^1
T Ori	2.4	50.2	9750	2.5	4.0	4.0	175	472	-0.88	680	-2.95	0.54	(?)
BF Ori	2.6	61.6	8970	3.3	3.8	3.2	37	603	-1.24	731	-3.49	0.15	-2.92^3
CO Ori	$>3.6^A$	100^A	6310^A	8.4	3.1	$< 0.1^A$	65	450^A	-0.99	553	-2.77	0.70	(?)
HK Ori	3.0^A	77.6^A	8510^A	4.1	3.7	1.0^A	(?)	460^A	-1.57	573	-2.69	0.37	$-2.92^{1,3}$
NV Ori	2.2^F	21.2^F	6750^F	3.4	3.7	4.4^F	81	450^I	-1.97	583	-4.81	0.08	(?)
RY Ori	2.5^A	28.2^A	6310^A	4.5	3.5	1.8^A	66	460	-1.7	598	-3.74	0.49	(?)
UX Ori	2.3	36.8	8460	2.8	3.9	4.5	215	517	-1.36	677	-3.58	0.17	$-2.80^{1,3}$
V346 Ori	2.5	61.4	9750	2.8	4.0	3.5	(?)	586	-1.87	889	...	0.29	-3.21^3
V350 Ori	2.2	29.3	8970	2.2	4.1	5.5	(?)	735	-1.39	724	-3.26	0.47	-2.62^3
XY Per	2.8	85.6	9750	3.3	3.9	2.5	217	347	-1.12	728	-3.29	0.46	-2.97^3
VV Ser	4.0	336	13800	3.2	4.0	1.2	229	614	-0.06	691	-1.82	1.04	$-1.34^{1,3}$
CQ Tau	1.5^B	5^B	6800^B	1.6	4.2	7.7^B	105	130^1	-2.86	529	-4.54	0.25	$-3.96^{1,3}$
RR Tau	5.8	781	10000	9.3	3.3	0.4	225	2103	0.04	681	-1.47	0.51	-1.58^1
RY Tau	1.3^F	2.30^F	5770^F	1.5	4.2	6.5^G	55	134^I	-1.97	648	-3.43	0.37	(?)
PX Vul	1.5^A	5.25^A	6760^A	1.7	4.2	14^A	(?)	420^A	-1.56	628	-3.71	0.45	-2.80^3
WW Vul	2.5	50.0	8970	2.9	3.9	3.7	220	696	-0.96	754	-3.17	0.36	-2.33^1
LkHa 234	$>5.3^A$	4680^A	12900^A	14	2.9	$< 0.01^A$	(?)	1250^A	0.58	747	-1.60	1.02	(?)

Notes. Surface gravities and line luminosities are on log scale. "..." means non-detections and "(?)" unknown values. Unless otherwise stated, the stellar masses, luminosities, effective temperatures, gravities, ages, and distances are from Montesinos et al. (2009); $v \sin i$ values from Mora et al. (2001), Hα and [OI]6300 mean values, and mean colour excesses from this work. Stellar radius are computed from M_* and log g when they are available in Montesinos et al. (2009), obtaining equal values if derived from L_* and T_*. R_* comes from these parameters for the remaining stars, for which log g is then obtained from M_* and R_*. The photometry for AS 442 and R Mon was taken from SIMBAD (http://simbad.u-strasbg.fr/simbad/). Brγ luminosities are from [1]Garcia Lopez et al. (2006), [2]Brittain et al. (2007) and [3]Donehew & Brittain (2011). [A]Manoj et al. (2006), [B]Alonso-Albi et al. (2009), [C]Glebocki et al. (2000), [D]Guimãraes et al. (2006), [E]Hoffleit & Jascheck (1982), [F]Merín (2004), [G]Siess et al. (1999), [H]Acke et al. (2005), [I]Blondel et al. (2006).

Columns 10, 11, and 12 of Table 4.1 list the dereddened mean Hα luminosities (<L(Hα)>), the mean Hα widths at 10% of peak intensity (<W_{10}(Hα)>), and the dereddened mean [OI]6300 luminosities (<L([OI]6300)>). The mean line luminosities from Paper I were dereddened using the mean colour excesses in Col. 13, a total-to-selective extinction ratio R_V = 5 (Hernández et al. 2004), and the extinction law compiled in Robitaille et al. (2007)[1] from Kim et al. (1994) and Indebetouw et al. (2005). The mean colour excesses were computed using the BV photometry in Oudmaijer et al. (2001) and the corresponding intrinsic colours in Kenyon & Hartmann (1995). Using a different colour to characterize the reddening in the sample (e.g. $E(V-R)$, see Calvet et al. 2004) would not significantly affect our results. <E(B-V)> is consistent with the colour excess applied by Montesinos et al. (2009) to derive most of the stellar parameters used in this work. Regarding the total-to-selective extinction ratio, Hernández et al. (2004) confirmed that $R_V = 5$ is more consistent with the observed properties of HAeBe stars than the typical $R_V = 3.1$ for the interstellar medium. Using a different R_V or extinction law (see e.g. the discussion in Calvet et al. 2004) would not change the major conclusions of this work, given that most objects in the sample are not heavily extincted ($A_V \leq 2.5$ magnitudes for 79% of the stars). It is noted that different values for R_V were used to derive the stellar parameters in Table 4.1 -e.g. $R_V = 3.1$ in Montesinos et al. (2009) and a range $1 \leq R_V \leq 11$ in Manoj et al. (2006)-. Section 4.4 again considers the influence of the R_V value on our results.

Finally. non-simultaneous Brγ luminosities from the literature (see notes to Table 4.1) are given in Col. 14, with mean values adopted for the stars where two or three measurements are available. For an appropriate comparison, the Brγ luminosities were rescaled to the same distances used in Paper I to derive the remaining line luminosities (Col. 9).

4.3 Accretion rates

4.3.1 Description of the model

HAeBe stars show excess of continuum emission compared with MS stars with similar spectral types, in particular, at the Balmer discontinuity region (see below and Garrison 1978; Donehew & Brittain 2011). The Balmer excesses are modelled in this section to provide estimates of the accretion rates. The analysis of the origin and strength of the magnetic fields necessary for driving accretion is beyond the scope of this work. We assume the MA geometry, using shock models similar to those successfully applied for the lower-mass regime. Following Calvet & Gullbring (1998) and MDCH04, the total flux per wavelength unit emerging from the star is

$$F_\lambda = f F_\lambda^{col} + (1-f) F_\lambda^{phot} \tag{4.1}$$

where f is the filling factor that reflects the stellar surface coverage of the accretion columns, F_λ^{phot} the flux from the undisturbed photosphere, and F_λ^{col} the flux from the column. The Kurucz model corresponding to a given T_* and log g (Kurucz 1993) is used to represent F_λ^{phot}[2]. In turn, the total luminosity of the columns is defined from the inward flux of energy carried by the accretion columns ($\mathcal{F}$) and the outward stellar radiation below the accretion

[1]The extinction law can be downloaded from the web-based SED fitting tool in http://caravan.astro.wisc.edu/protostars/

[2]The use of a family of synthetic models different from Kurucz's does not significantly affect our results. The NextGen/PHOENIX models (Hauschildt et al. 1999) provide equal Balmer excesses, within 0.03 magnitudes, for the typical stellar and model parameters used (see text).

shocks (Calvet & Gullbring 1998):

$$L^{col} = F^{col}A = (\mathcal{F} + F^{phot}) \times A = \xi L_{\rm acc} + F^{phot}A \tag{4.2}$$

where $A = f4\pi {\rm R}_*^2$ is the surface area covered by the shocks, $L_{\rm acc} = {\rm GM}_*\dot{M}_{\rm acc}/{\rm R}_*$ is the accretion luminosity; and $\xi = 1$ - ${\rm R}_*/R_i$, with R_i the disk truncation radius. The parameter F_λ^{col} is modelled as the flux from a blackbody at temperature T_{col} (i.e. $F^{col} = \sigma T_{col}^4$). This is justified for the range of stellar temperatures represented here, given that the main contribution to the flux in the optical and near-UV comes from the optically thick, heated photosphere and that the optically thin pre-shock contribution represents less than 1/4 of L^{col} (see MDCH04). For the model parameters used in this work (see below), the blackbody approach improves as ${\rm T}_*$ increases, and including the optically-thin contribution would change our modelled Balmer excesses by less than ~ 0.07 magnitudes for the colder stars, which is accurate enough for our data. Since the total stellar luminosity can also be represented as a blackbody at the stellar temperature, $F^{phot} = \sigma {\rm T}_*^4$, the second and third terms of Eq. 4.2 provide

$$\sigma\, T_{col}^4 = \mathcal{F} + \sigma {\rm T}_*^4. \tag{4.3}$$

Finally, from the third and fourth terms of Eq. 4.2:

$$\mathcal{F} \times f4\pi {\rm R}_*^2 = \left(1 - \frac{{\rm R}_*}{R_i}\right) \frac{{\rm GM}_*\dot{M}_{\rm acc}}{{\rm R}_*}. \tag{4.4}$$

Once $\mathcal{F}$ and R_i are fixed, the blackbody temperature characterizing the flux from the column and the filling factor for a given set of stellar and accreting parameters can be determined from Eqs. 4.3 and 4.4, respectively. We fixed $\mathcal{F} = 10^{12}$ erg cm^{-2} s^{-1}, which mostly provides appropriate filling factors ($f \leq 0.1$; see e.g. Valenti et al. 1993) and reproduces most of the observed Balmer excesses (see Sect. 4.3.2). The use of a different value within the expected interval, $10^{10} \leq \mathcal{F}$(erg cm^{-2} s^{-1}) $\leq 10^{12}$, does not significantly affect the results (see MDCH04). The disk truncation radius should be smaller than the co-rotation one (R_{cor}, see Sect. 4.4.1 and Shu et al. 1994), which decreases with the stellar rotational velocity:

$$R_{cor} = \left(\frac{{\rm GM}_*{\rm R}_*^2}{v_*^2}\right)^{1/3}. \tag{4.5}$$

The $v \sin i$ values from Table 4.1 are used as proxies for v_*. The disk truncation radius was fixed to $2.5{\rm R}_*$, which is the expected value for HAeBe stars (MDCH04), or to R_{cor} if this is smaller than $2.5{\rm R}_*$. The results do not significantly differ if ${\rm R}_*/R_i$ is changed up to a factor 2 (Herczeg & Hillenbrand 2008).

Once T_{col} and f are determined, the expected total flux can finally be obtained from Eq. 4.1. The left-hand panel of Fig. 4.1 shows an example of a photospheric synthetic spectra modified by the contribution of accretion. This contribution causes the total flux to show a filled-in Balmer discontinuity, compared to that of the undisturbed photosphere.

For a given set of stellar and accreting parameters, the modelled excess in the Balmer discontinuity is defined as $\Delta {\rm D}_B = (U-B)_{phot} - (U-B)_{total}$. This is computed by subtracting the U-B colour of the synthetic total flux, which accounts for the influence of accretion, from the corresponding Kurucz photospheric colour, which reflects the naked photosphere. The fluxes were convolved with the U and B transmission curves provided by the Nordic Optical Telescope (left panel of Fig. 4.1), since the photometric observations were carried out with the

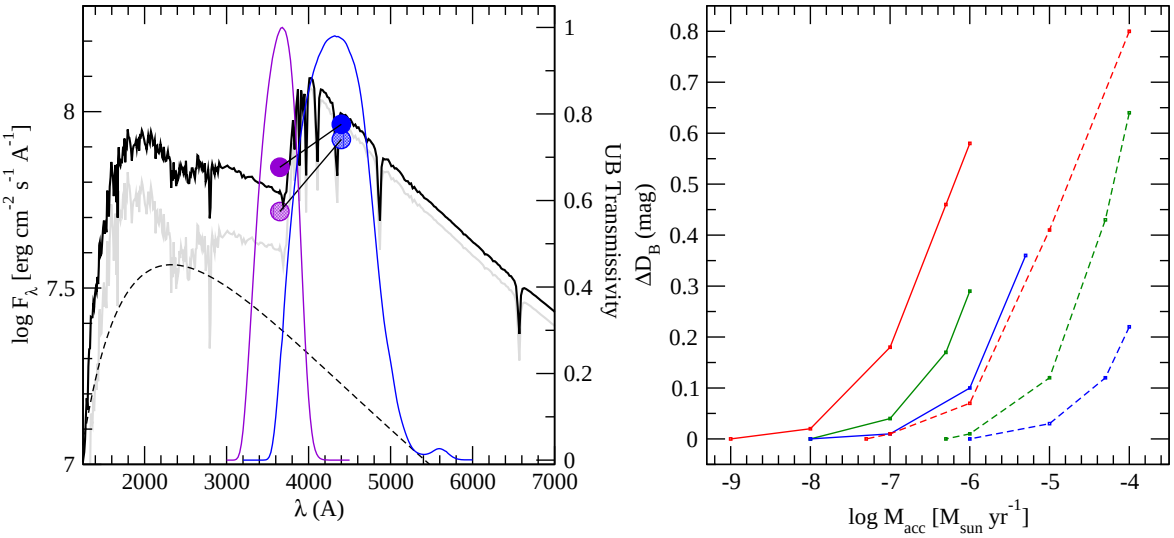

Figure 4.1: (Left): Photospheric flux (grey line), contribution from accretion (fF_λ^{col}, dashed line) and total flux (solid black line) for $M_* = 2.5$ $M_\odot$, $R_* = 2.6$ $R_\odot$, $T_* = 9000$ K, $\mathcal{F} = 10^{12}$ erg cm^{-2} s^{-1} ($T_{col} = 12470$ K) and $R_i = 2.5R_*$. The mass accretion rate is 5×10^{-7} $M_\odot$ yr^{-1}, ($f = 0.084$). All fluxes are computed at the stellar surface. The transmission curves of the U and B filters are plotted in violet and blue, respectively. The convolution of the fluxes with the filter responses provide the synthetic photometric points used to obtain the modelled photospheric and total colours (from the shaded and filled linked circles, respectively). (Right): Predicted excess in the Balmer discontinuity as a function of mass accretion rate for $T_* = 6500$, 9000, and 12500 K (red, green, and blue lines) and log g = 4.0 and 3.0 (solid and dashed lines). $\mathcal{F} = 10^{12}$ erg cm^{-2} s^{-1} and $R_i = 2.5R_*$ for all cases.

instrument TurPol on that telescope (Oudmaijer et al. 2001). That the photometric points are slightly displaced from the spectra is caused by the strong gradients in the fluxes along the transmission bands, specially in U. The difference between the Kurucz colours computed in this way and the intrinsic colours in Kenyon & Hartmann (1995) is ≤ 0.05 magnitudes for the stellar parameters considered here, being typically around 0.01 magnitudes. This accuracy is enough for our purposes and means that the modelled excesses can later be compared to the observed ones, described below. The right-hand panel of Fig. 4.1 shows a representative subset of the ΔD_B–$\dot{M}_{\rm acc}$ calibrations we have modelled. The curves rise with the corresponding filling factors, following Eq. 4.4, and are limited by $f < 1$. There is a strong dependence on the stellar temperature and surface gravity that must be considered when a mass accretion rate is associated to a given ΔD_B value.

From the observational perspective, the mean excess in the Balmer discontinuity for a given star is $<\Delta D_B> = (U-B)_0 - <U-B>_{dered}$, where $(U-B)_0$ is the intrinsic colour from Kenyon & Hartmann (1995), and $<U-B>_{dered}$ the dereddened mean colour, obtained from the observations in Oudmaijer et al. (2001). The dereddening was applied using the <E(B–V)> values in Table 4.1, $R_V = 5$, and the same extinction law mentioned in Sect. 4.2. The top panel in Fig. 4.2 shows the mean observed and intrinsic $B-V$ colours from which the dereddening was applied. The hottest stars in our sample are the most reddened. The bottom panel shows the $<U-B>_{dered}$ and $(U-B)_0$ colours from which the $<\Delta D_B>$ values are obtained. The hottest stars are also the ones showing the largest Balmer excesses. It worth mentioning that a slight variation in the adopted value for the stellar temperature translates into a strong change in $<\Delta D_B>$, for $T_* \leq 6400$ K. This is caused by the steep dependence of both the $U-B$ and $B-V$ intrinsic colours on that range of stellar temperatures

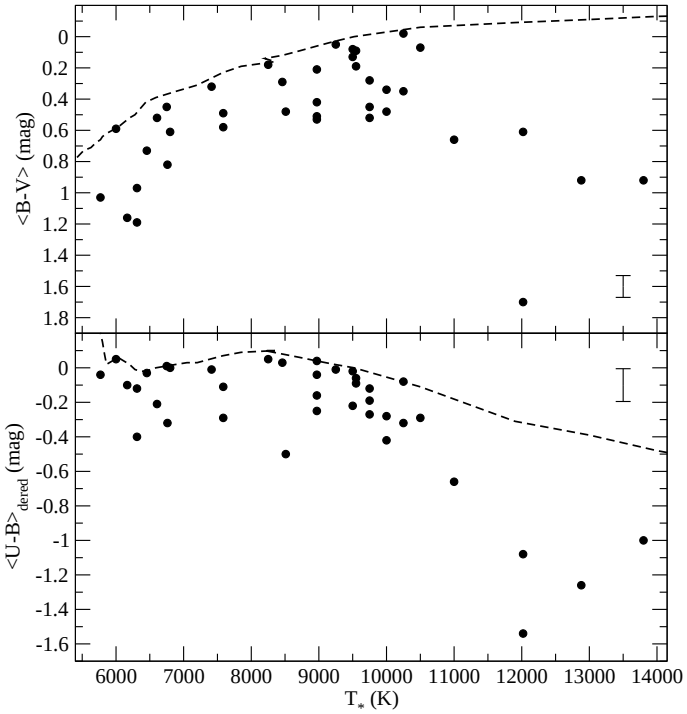

Figure 4.2: Observed mean colours in $B-V$ (top) and $U-B$ (bottom) as a function of the stellar temperature. The colours in the bottom panel are deredenned using the excesses derived from the top panel. The dashed lines indicate the corresponding intrinsic colours from Kenyon & Hartmann (1995). The typical error bars considering the photometric uncertainties are shown.

(e.g. differences up to 0.2 magnitudes for variations of ± 150 K, see Kenyon & Hartmann 1995). In turn, this could significantly change the accretion rate estimate (e.g. a variation of 0.2 magnitudes in the Balmer excess translates into a change up to two orders of magnitude in $\dot{M}_{\rm acc}$ for $T_* = 6500$ K; see right panel of Fig. 4.1). The dependence of the intrinsic colours on T_* is smoother for almost all the stars studied here (Fig. 4.2). The typical uncertainty for $<\Delta D_B>$ is between 0.05 and 0.1 magnitudes in our sample. This was estimated by considering both uncertainties in the photospheric colours, from variations in T_* of ± 150 K, and the photometric uncertainties, which are the dominant contribution for most stars. A typical uncertainty of 0.07 magnitudes is adopted in this paper for $<\Delta D_B>$, but that strictly depends on each star and could increase for the coldest objects in the sample.

Individual calibrations, similar to the examples in the right-hand panel of Fig. 4.1, were constructed for each star from the corresponding M_*, T_*, R_*, and log g parameters in Table 4.1. In this way, a mass accretion rate was assigned to the modelled Balmer excess that matches the observed one. Then $L_{\rm acc}$ was obtained from $\dot{M}_{\rm acc}$, M_*, and R_*. This method does not need distance calibrations since it is based on colour excesses. In addition, the stellar parameters of most stars in the sample were obtained from a distance-independent method (Montesinos et al. 2009). However, distance uncertainties are indirectly introduced through R_* -and log g- when this was derived from a value of L_* based on a distance (e.g. Manoj et al. 2006).

4.3.2 Results

Table 4.2 shows the observed (mean) excesses in the Balmer discontinuity and the accretion rates and best model parameters that reproduce them. The uncertainties for $\dot{M}_{\rm acc}$ were estimated by varying ΔD_B by ± 0.07 magnitudes in the models, which is the typical uncertainty for the observed excess (Sect. 4.3.1). Upper limits are provided when $<\Delta D_B>$ is lower than that value. The uncertainties for $L_{\rm acc}$ also consider the typical error in the M_*/R_* ratios. In addition to the sources of error discussed in these sections, we refer the reader to the broad analysis in Herczeg & Hillenbrand (2008) on how different uncertainties of the stellar and model assumptions could affect the accretion rates estimates.

The high $<\Delta D_B>$ value shown by VV Ser cannot be reproduced using the typical value $\mathcal{F} = 10^{12}$ erg cm^{-2} s^{-1}. Increasing $\mathcal{F}$ by one order of magnitude provides $\dot{M}_{\rm acc} \sim 10^{-4}$ M$_\odot$ yr^{-1}, but the filling factor is almost 100%. Further increases in $\mathcal{F}$ produce lower filling factors, but the corresponding accretion rates also increase. Another possibility is to increase the disk truncation radius to a value significantly higher than the co-rotation one (~ 1.7 R$_*$ for VV Ser). For $R_i = 5.5$ R$_*$ and $\mathcal{F} = 10^{13}$ erg cm^{-2} s^{-1}, the Balmer excess of VV Ser can be reproduced from $\dot{M}_{\rm acc} \sim 5{\times}10^{-5}$ M$_\odot$ yr^{-1} (f = 0.99). Similarly, we find it difficult to reproduce the strong Balmer excesses shown by R Mon, VY Mon, and LkHa 234 from the model used in this work. For the highest accretion rates possible ($\sim 10^{-2}$–10^{-1} M$_\odot$ yr^{-1}, with $\mathcal{F} >> 10^{12}$ erg cm^{-2} s^{-1} and $f \sim 1$), their modelled spectra are featureless and provide Balmer excesses that are $\sim 50\%$ lower than observed. Again, a combination of large disk truncation radius, well above the typical 2.5 R$_*$ for HAeBe stars, $\mathcal{F} \gg 10^{12}$ erg cm^{-2} s^{-1}, and f ~ 1 could reproduce the Balmer excess of these objects from lower accretion rates ($\sim 10^{-5}$ M$_\odot$ yr^{-1}). However, the use of those values would be arbitrary and not supported by theory or observations (see MDCH04). In particular, a disk truncation radius larger than the co-rotation one is in principle not possible in the MA scenario (see e.g. Shu et al. 1994). Temperatures and extinction properties that are different than the ones used in this work would make their Balmer excesses in Table 4.2 wrong, and therefore useless in our fit attempts. However, It is noted that the four problematic objects not only show the highest $<\Delta D_B>$ values in our sample, but are also the hottest ($T_* > 12000$K, i.e. spectral-types earlier than $\sim$ B8) and most heavily extincted sources. There is consensus in the literature that these objects are early-type HAeBe stars (see e.g. the compilation of spectral types in Table 6 of Mora et al. 2001). Our previous results, indicating that the variability of the $H\alpha$ line is clearly lower for the massive early-type HAeBe stars, already pointed to different physical processes operating in their circumstellar environments (see Paper I). The lack of success in reproducing the Balmer excesses could be pointing to a change in the accretion paradigm for the HBe regime (see also Sect. 4.4.1). No result is included in Table 4.2 for the four objects discussed, which would require specific analysis. The calibrations with the line luminosities included in Sect. 4.4 and the stellar parameters used in this work provide mass accretion rates (in M$_\odot$ yr^{-1}) of $\sim 10^{-5}$–$6{\times}10^{-6}$ for VV Ser, $3{\times}10^{-4}$–$3{\times}10^{-5}$ for R Mon, $3{\times}10^{-3}$–$7{\times}10^{-6}$ for VY Mon, and $6{\times}10^{-5}$–$8{\times}10^{-5}$ for LkHa 234. These estimates must be viewed with caution, given the discussion above and their being based on relations derived for colder stars.

The typical (median) accretion rate for the remaining objects is 2×10^{-7} M$_\odot$ yr^{-1}, 36% of the stars showing $\dot{M}_{\rm acc} \leq 10^{-7}$ M$_\odot$ yr^{-1}, 35% between 10^{-7} and 10^{-6} M$_\odot$ yr^{-1}, and 29% larger than 10^{-6} M$_\odot$ yr^{-1}. This distribution is practically the same as predicted from Fig. 8 of MDCH04.

Figure 4.3 (left panel) shows the mass accretion rates against the stellar masses. The

Table 4.2: Observed mean excess in the Balmer discontinuity, accretion rates, and model parameters.

Star	$<\Delta D_B>$ (mag)	log $\dot{M}_{acc}$ [$M_\odot$ yr^{-1}]	log L_{acc} [$L_\odot$]	R_i (R_*)	T_{col} (K)	f (%)
HD 31648	0.05	<-7.23	<0.20	2.5	12215	1.1
HD 34282	0.06	<-8.30	<-0.40	2.5	12695	2.2
HD 34700	0.00	<-8.30	<-1.05	2.5	11730	0.02
HD 58647	0.18	-4.84±0.22	2.47 ±0.23	2.1	13140	12
HD 141569	0.09	-6.89±0.40	0.70 ±0.40	1.5	12695	3.6
HD 142666	0.18	-6.73±0.26	0.69 ±0.27	2.5	12030	3.2
HD 144432	0.06	<-7.22	<0.21	2.5	11990	1.1
HD 150193	0.29	-6.12±0.14	1.33 ±0.15	2.5	12460	13
HD 163296	0.02	<-7.52	<-0.03	2.2	12570	0.61
HD 179218	0.02	<-7.30	<0.14	2.5	12670	0.60
HD 190073	0.22	-5.00±0.25	2.29 ±0.26	2.5	12670	12
AS 442	0.48	-5.08±0.11	2.37 ±0.12	2.5	13405	56
VX Cas	0.22	-6.44±0.22	1.16 ±0.23	2.0	12895	13
BH Cep	0.01	<-8.30	<-0.94	2.4	11800	0.07
BO Cep	0.21	-6.93±0.28	0.45 ±0.29	2.5	11825	2.8
SV Cep	0.24	-6.30±0.20	1.30 ±0.21	1.8	13015	14
V1686 Cyg	0.12	-5.23±0.41	1.66 ±0.41	2.5	11755	0.87
R Mon	0.76	(?)	(?)	...	...	...
VY Mon	1.22	(?)	(?)	...	...	...
51 Oph	0.00	<-7.00	<0.37	1.3	13015	0.11
KK Oph	0.36	-5.85±0.15	1.51 ±0.16	1.6	12030	9.4
T Ori	0.09	-6.58±0.40	0.90 ±0.40	1.8	12780	3.7
BF Ori	0.00	<-8.00	<-0.60	2.5	12460	0.09
CO Ori	0.38	-5.20±0.18	1.93 ±0.19	2.5	11775	4.5
HK Ori	0.57	-5.24±0.12	2.13 ±0.13	2.5	12300	31
NV Ori	0.00	<-8.30	<-0.99	2.5	11850	0.03
RY Ori	0.11	-6.65±0.33	0.59 ±0.33	2.5	11775	0.75
UX Ori	0.05	<-6.77	<0.63	1.5	12285	1.1
V346 Ori	0.25	-5.99±0.17	1.47 ±0.18	2.5	12780	15
V350 Ori	0.20	-6.66±0.24	0.82 ±0.25	2.5	12460	5.0
XY Per	0.16	-5.86±0.20	1.57 ±0.21	1.5	12780	7.5
VV Ser	0.54	(?)	(?)	1.7	...	...
CQ Tau	0.02	<-8.30	<-0.84	2.5	11860	0.21
RR Tau	0.37	-4.11±0.16	3.18 ±0.17	1.3	12895	27
RY Tau	0.24	-7.65±0.17	-0.22±0.18	2.5	11700	0.98
PX Vul	0.33	-6.72±0.16	0.73 ±0.17	2.5	11850	7.2
WW Vul	0.08	-6.38±0.70	1.05 ±0.70	1.5	12460	2.7
LkHa 234	0.88	(?)	(?)	...	...	...

Notes. A typical uncertainty of 0.07 magnitudes is adopted for all $<\Delta D_B>$ values. The symbol (?) refers to the four objects for which strong difficulties are found to reproduce their Balmer excesses from our model.

stars in our sample follow a steeper trend than the lower mass objects, for which $\dot{M}_{\rm acc} \propto {\rm M}_*^2$; (see e.g. Muzerolle et al. 2003, 2005; Mohanty et al. 2005; Natta et al. 2006). We find $\dot{M}_{\rm acc} \propto {\rm M}_*^{5.2}$ for our sample (Pearson's correlation coefficient 0.74). The exponent decreases to 4.6 if the upper limits for the accretion rates are discarded (Pearson's correlation coefficient 0.91). Our data is therefore reasonably well fitted to $\dot{M}_{\rm acc} \propto {\rm M}_*^5$. This trend is driven by the most massive sources and is most probably caused by the mass-age distribution characterizing HAeBe stars (see e.g. van Boekel et al. 2005; Garcia Lopez et al. 2006). This distribution is shown in Fig. 4.4 for our sample. The stars with ${\rm M}_* \geq 2.5{\rm M}_\odot$ are younger than ~ 2 Myr, and the objects with lower stellar masses are older. Following van Boekel et al. (2005), the lack of old HAeBes around 2.5-6 $\rm M_\odot$ stars is likely caused by their faster evolution to the MS, which is supported by observations (Roccatagliata et al. 2011). The scarcity of young HAeBes around 1-2.5$\rm M_\odot$ stars is most probably explained by the fact that they become optically visible later in their evolution. The massive young stars in our sample show the strongest accretion rates, as expected. The mass accretion rates of the less massive older HAeBe stars are orders of magnitude lower. These facts would make the $\dot{M}_{\rm acc}$–$\rm M_*$ trend very steep.

The right-hand panel in Fig. 4.3 shows the accretion luminosities against the stellar ones. The stars in our sample have $0.01{\rm L}_* \leq L_{\rm acc} \leq {\rm L}_*$. Both limits are similar to those reported for lower mass stars (Clarke & Pringle 2006; Tilling et al. 2008). The lower limit is the observational detection threshold for $L_{\rm acc}$. However, although the trend between $L_{\rm acc}$ and $\rm L_*$ shown by low-mass stars ($L_{\rm acc} \propto {\rm L}_*^{1.5}$; see e.g. Tilling et al. 2008) is roughly followed by our sample, our best fit ($L_{\rm acc} \propto {\rm L}_*^{1.2}$) could indicate a decrease in the exponent for the intermediate-mass regime. In fact, a direct visual inspection of the right-hand panel in Fig. 4.3 reveals that there is an apparent decline in the slope of the lower envelope of the $L_{\rm acc}$–$\rm L_*$ trend. That decrease could start at lower stellar luminosities than those analysed in this work, around ${\rm L}_* = {\rm L}_\odot$.

Comparison with previous results

Garcia Lopez et al. (2006) obtained accretion luminosities for a sample of HAeBe stars from the empirical calibration with the Brγ luminosity for intermediate-mass T Tauri stars (log $(L_{\rm acc}/{\rm L}_\odot) = 0.9 \times \log\,({\rm L}_{\rm Br\gamma}/{\rm L}_\odot) + 2.9$; Calvet et al. 2004). The non-photospheric Brγ equivalent widths were transformed to luminosities from the K magnitudes and distances in their Table 1. The mass accretion rates were then derived from their values for $\rm M_*$ and $\rm R_*$, using the same $L_{\rm acc}$–$\dot{M}_{\rm acc}$ expression as in this work (Sect. 4.3.1). Figure 4.5 shows our mass accretion rates against those from Garcia Lopez et al. (2006) for the objects in common. The difference between both determinations decreases once the Brγ luminosities are rescaled to our distances (see Table 4.1) and the correspoding accretion luminosities are transformed into mass accretion rates from our values for $\rm M_*$ and $\rm R_*$. The grey symbols in Fig. 4.5 are obtained in this way, representing the estimates from the method in Garcia Lopez et al. (2006) rescaled to our values for d, $\rm M_*$, and $\rm R_*$. The new estimates show a linear correlation with our results (Pearson's coefficient 0.65) with slope 1.0 ± 0.3, and displaced in the ordinate axis by a factor ~ 0.4. This agrees with the analysis in the following section. It must be noted that the stellar temperature for several objects in Garcia Lopez et al. (2006) falls well above the upper limit from which the Brγ relation in Calvet et al. (2004) was obtained -around 6100 K-.

Donehew & Brittain (2011) have derived mass accretion rates for a sample of HAeBe stars from the calibration with the Balmer excess provided by Muzerolle et al. (2004). The

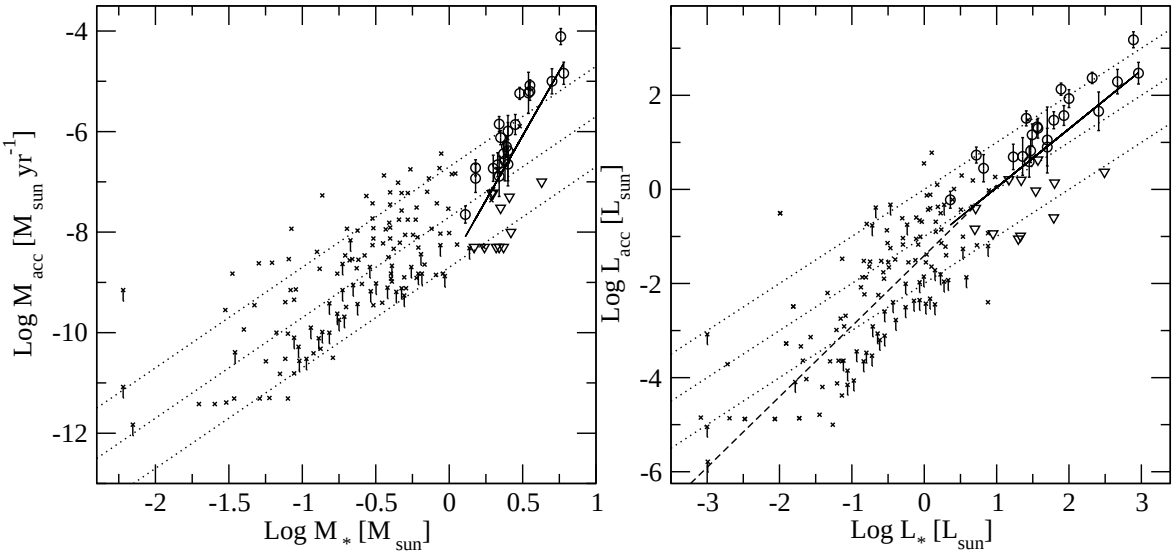

Figure 4.3: Mass accretion rate vs stellar mass (left) and accretion luminosity vs stellar luminosity (right). Our data are indicated with circles, and triangles for the upper limits on the accretion rates. Crosses are data from the literature (those with vertical bars are upper limits), including low-mass stars from different star-forming regions (see Natta et al. 2006, and references therein). Dotted lines indicate $\dot{M}_{\rm acc} \propto {\rm M}_*^2 \pm 1$ dex (left) and $L_{\rm acc}/{\rm L}_* = 0.01$, 0.1, 1 (right). The dashed line on the right side is the best fit for low-mass stars ($L_{\rm acc} \propto {\rm L}_*^{1.5}$), and the solid lines are the best fits for our sample ($\dot{M}_{\rm acc} \propto {\rm M}_*^5$ and $L_{\rm acc} \propto {\rm L}_*^{1.2}$).

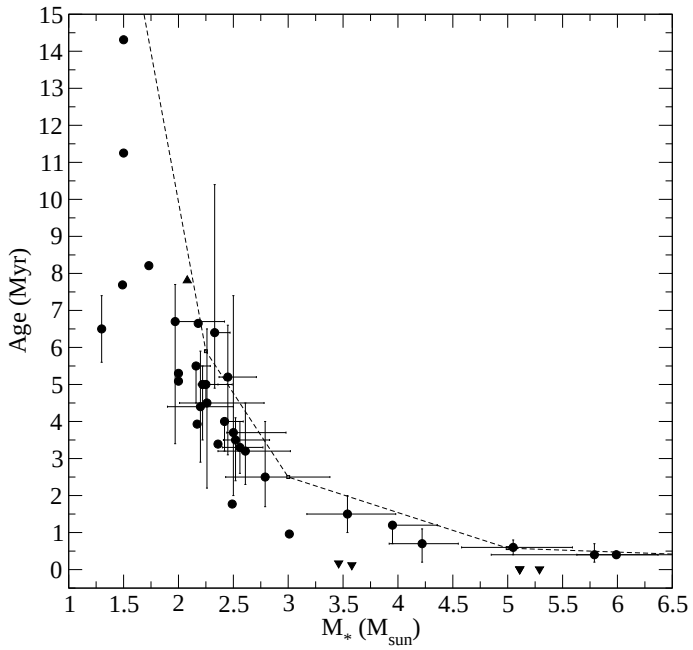

Figure 4.4: Stellar age versus stellar mass for the stars in the sample. Error bars are plotted when provided in the references of Table 4.1. The dashed line indicates the theoretical time to reach the main sequence (Tayler 1994).

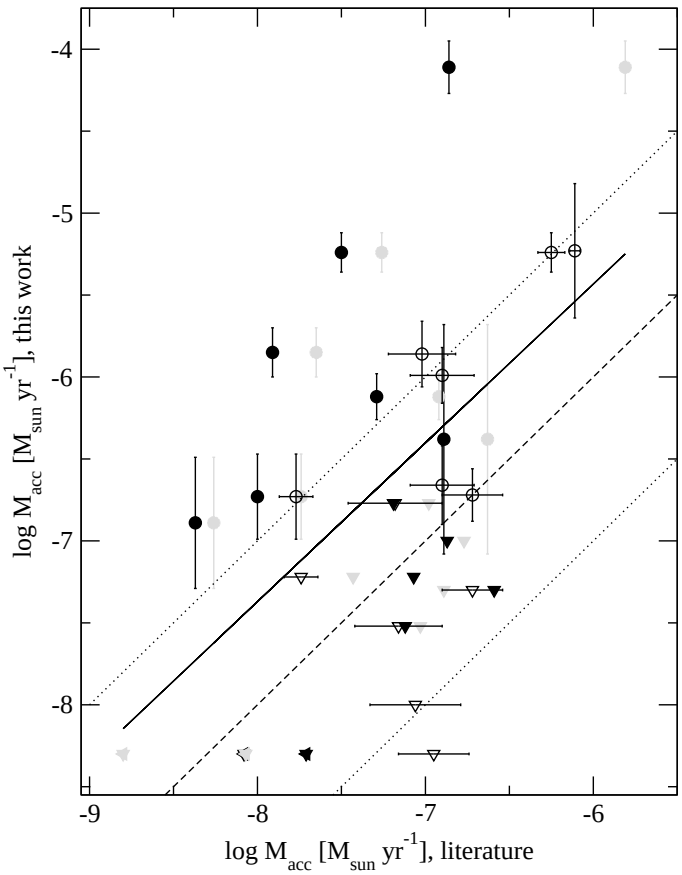

Figure 4.5: Mass accretion rates derived in this work against those derived by Garcia Lopez et al. (2006) (filled symbols) and Donehew & Brittain (2011) (open symbols). The dashed line indicates equal values and the dotted lines ±1 dex. The typical minimum uncertainty for the estimates in Garcia Lopez et al. (2006) is ± 0.5 dex. Triangles are upper limits. Grey symbols represent the estimates using the method in Garcia Lopez et al. (2006) from our distances and stellar parameters, and the solid line is the best fit.

Balmer excesses were obtained fitting both Kurucz and standard main-sequence spectra to UV-optical spectra. Figure 4.5 shows our mass accretion rates versus the ones from Donehew & Brittain (2011) for the stars included in both samples. Both estimates are equal within ± 1 dex for almost all objects in common. Variability could account for differences up to ∼ 0.5 dex (see Sect. 4.5), but the scatter can be explained also from other factors. First, the method used to derive the Balmer excess is different in both papers. Second, the stellar parameters differ significantly for several stars (e.g. $\Delta T_* > 10000$ K for V1686 Cyg). Finally, the calibration used by Donehew & Brittain (2011) was in many cases applied to stars with stellar parameters significantly different than those from which the calibration was made (spectral type A2, $M_* = 3$ M$_\odot$ and $R_* = 3$ R$_\odot$ Muzerolle et al. 2004). As discussed in Sect. 4.3.1, the ΔD_B–$\dot{M}_{\rm acc}$ calibration differs strongly depending on the stellar parameters considered (right panel in Fig. 4.1).

The mass accretion rate provided for CO Ori in Calvet et al. (2004) was derived from a similar method to the one used in this paper, but it was a factor ∼ 70 lower. This is explained mainly from differences in the stellar parameters adopted. Both L_* and M_* are higher in the present work by a factor ∼ 45 and 1.4, respectively. From L_* and T_* (see below), our R_* is a factor 2 larger. The values adopted for R_* and M_* affect those for the filling factor and the

blackbody temperature representing the accretion shock. The values for the surface gravities and effective temperatures are log g = 3.6 against our 3.2, and $T_* = 6030$ K against our 6310 K. This difference of almost 300 K in that range of stellar temperatures, along with the slight differences in the $U-B$ and $B-V$ colours -around 0.05 magnitudes-, translates into a significant change in the Balmer excess -0.24 magnitudes from the data in Calvet et al. (2004) against our 0.38 magnitudes; see the discussion in Sect. 4.3.1-. The higher mass accretion rate we provide agrees with the one expected for a star that here is considered hotter, with a lower value for log g and with more Balmer excess (see right panel in Fig. 4.1), but our model yields the same $\dot{M}_{\rm acc} \sim 10^{-7}$–$10^{-8}$ $M_\odot$ yr^{-1} for CO Ori using the parameters in Calvet et al. (2004). The different extinction treatment is also relevant, but other factors such as the use of different values for $\mathcal{F}$ and R_i have less influence. The mass accretion rate for the other object in common with Calvet et al. (2004), RY Tau, is a factor ~ 3 higher than our estimate, but the values overlap ($\sim 10^{-8}$ $M_\odot$ yr^{-1}) if considering the uncertainties from both papers. Apart from the practically equal values for $U-B$ and $B-V$, again within 0.05 magnitudes, the stellar parameters adopted in both works are more similar than for CO Ori.

Given the relevance of the stellar characterization to derive the accretion rates, we notice that most of the stellar parameters in Table 4.1 were carefully obtained by Montesinos et al. (2009) in a paper specifically devoted to that task, which takes much of the photometry used in this work into account.

4.4 Accretion tracers

Figure 4.6 shows our accretion luminosities in Table 4.2 against the Hα, [OI]6300 and Brγ luminosities in Table 4.1. The best least-squares fits provide the following empirical calibrations for our sample ($1 \leq M_*/M_\odot \leq 6$; $6000 \leq T_*(K) \leq 11000$):

$$\log\left(\frac{L_{\rm acc}}{L_\odot}\right) = 2.28(\pm0.25) + 1.09(\pm0.16) \times \log\left(\frac{L_{\rm H\alpha}}{L_\odot}\right) \tag{4.6}$$

$$\log\left(\frac{L_{\rm acc}}{L_\odot}\right) = 4.80(\pm0.50) + 1.13(\pm0.14) \times \log\left(\frac{L_{\rm [OI]6300}}{L_\odot}\right) \tag{4.7}$$

$$\log\left(\frac{L_{\rm acc}}{L_\odot}\right) = 3.55(\pm0.80) + 0.91(\pm0.27) \times \log\left(\frac{L_{\rm Br\gamma}}{L_\odot}\right). \tag{4.8}$$

These empirical expressions are very similar to those provided for low-mass CTT stars (Muzerolle et al. 1998a; Dahm 2008; Herczeg & Hillenbrand 2008):

$$\log\left(\frac{L_{\rm acc}}{L_\odot}\right) = 2.27(\pm0.70) + 1.31(\pm0.16) \times \log\left(\frac{L_{\rm H\alpha}}{L_\odot}\right) \tag{4.9}$$

$$\log\left(\frac{L_{\rm acc}}{L_\odot}\right) = 6.50(\pm2.18) + 1.67(\pm0.28) \times \log\left(\frac{L_{\rm [OI]6300}}{L_\odot}\right) \tag{4.10}$$

$$\log\left(\frac{L_{\rm acc}}{L_\odot}\right) = 4.43(\pm0.79) + 1.26(\pm0.19) \times \log\left(\frac{L_{\rm Br\gamma}}{L_\odot}\right). \tag{4.11}$$

There is an apparent decrease in the slope of the calibrations for the HAeBe regime, but firm conclusions can only be stated for the [OI]6300 line; the slope in Eq. 4.7 is shallower than that in Eq. 4.10 above the uncertainties. However, the Hα and Brγ slopes for intermediate-mass T-Tauri stars are 1.18±0.26 (Dahm 2008) and 0.9 (Calvet et al. 2004), respectively, i.e. closer to our estimates (see also Donehew & Brittain 2011). This could be indicating that the

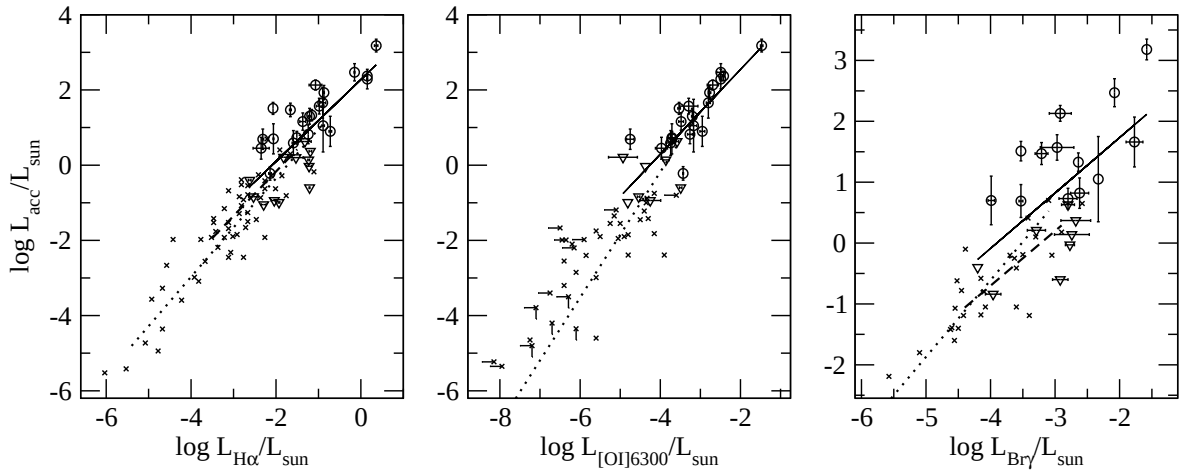

Figure 4.6: Accretion luminosity against the Hα (left), [OI]6300 (middle) and Brγ (right) luminosities . Our results are represented with circles and triangles for the upper limits on the accretion rates. Our accretion and Brγ luminosities were not derived from simultaneous measurements. Error bars for the line luminosities indicate the uncertainties for the non-variable objects and variability amplitudes for the variable ones. Our best fits are plotted with solid lines. Data for lower mass stars (crosses) were taken from Fang et al. (2009); Herczeg & Hillenbrand (2008), and Calvet et al. (2004), for the left, middle, and right panels, respectively. Upper limits are indicated with bars, when provided. Dotted and dashed lines are the empirical calibrations for Hα and Brγ in low and intermediate-mass CTT, respectively (see text).

slopes of the empirical calibrations decrease for higher stellar masses. The scatter for a given line luminosity is comparable for classical T-Tauri and HAeBe stars. The slightly higher dispersion for the Brγ line could likely be diminished using simultaneous measurements for the accretion and line luminosities.

As introduced in Sect. 4.2, a different value for the total-to-selective extinction ratio would influence only the Balmer excesses of the most heavily extincted sources in our sample. These tend to be the early-type HAeBe stars, which are the strongest accretors (see Fig. 4.2 and Sect. 4.3.2). Using $R_V < 5$ would make their accretion rate estimates lower. Therefore, the L_{acc}–L_* and L_{acc}–L_{line} trends for our sample in the right-hand panel of Fig. 4.3 and in Fig. 4.6 would flatten slightly. This would enhance the difference between the relations for the low-mass and the HAeBe regimes. In addition, The $\dot{M}_{acc}$–M_* relation in the left-hand panel of Fig. 4.3 would show a flatter slope, but the trend would be still steeper than for low-mass stars, even when using $R_V = 3.1$.

4.4.1 Accretion and the Hα 10% width

The Hα width at 10% of peak intensity is widely used as an empirical accretion tracer for low-mass stars (White & Basri 2003; Natta et al. 2004; Jayawardhana et al. 2006). Figure 4.7 shows the mass accretion rates against the Hα 10% widths. The trend followed by low-mass objects (Natta et al. 2004) breaks for HAeBe stars, whose $<W_{10}(H\alpha)>$ values show no correlation with log $\dot{M}_{acc}$. This was expected since the mean values and the relative variabilities of the Hα equivalent and 10% widths are not correlated in our sample (see Paper I). We conclude that $<W_{10}(H\alpha)>$ can usually not be used as a direct tracer of accretion for HAeBe stars, unlike in the lower mass regime. We argue in the following that one main reason for this discrepancy is that the typically high rotation rates of massive stars (Finkenzeller 1985; Mora et al. 2001) influence their $<W_{10}(H\alpha)>$ values. We suggest that this influence

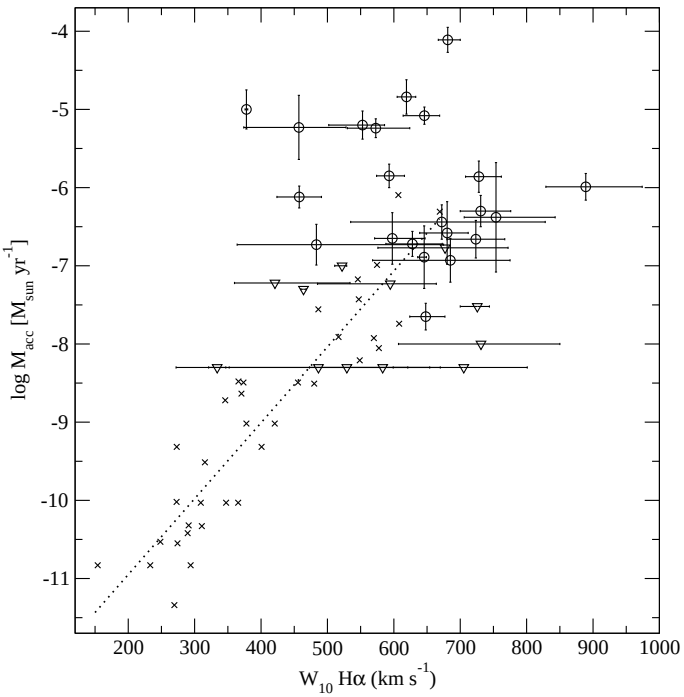

Figure 4.7: Mass accretion rate against the Hα 10% width. Our results are represented by circles, and triangles for the upper limits on the accretion rates. Error bars for the line widths indicate the uncertainties for the non-variable objects and variability amplitudes for the variable ones. Data for lower mass stars are also included (crosses; from the compilation of Natta et al. 2004), as well as the empirical expression relating both parameters in that stellar regime; log $\dot{M}_{\rm acc} \sim$ -12.9 + 9.7$\times$ 10^{-3}W$_{10}$(Hα) (dotted line; Natta et al. 2004).

can be interpreted in the context of the MA scenario.

Figure 4.8 relates $<$W$_{10}$(Hα)$>$ and $v \sin i$ for the stars in the sample (see also Jayawardhana et al. 2006). Although there is a scatter at low velocities, all the rapid HAe rotators ($v \sin i > 150$ km s^{-1}) have large Hα widths ($<$W$_{10}$$>$ $>$ 600 km s^{-1}). Our spectroscopic measurements refer to the non-photospheric contribution (see Paper I). Therefore the maximum Hα width must be influenced by the circumstellar gas rotating at the maximum speed, which, for Keplerian rotation, is located in the inner disk. The trend in Fig. 4.8 suggests that the inner disk gas traced by Hα is coupled to the rotating stellar photosphere. Magnetospheric channels could be the origin of this link.

The influence of the stellar rotation on the Hα line broadening can be qualitatively modelled from MA. The MA model described in Muzerolle et al. (2001) was successfully used to reproduce several spectral lines of accreting stars with different masses (MDCH04; Calvet et al. 2004; Muzerolle et al. 2005). That assumes a simple dipole geometry, where the Hα line is generated from free-falling gas that follows the magnetic lines connecting the magnetosphere in the inner disk and the stellar surface. We applied the model from Muzerolle et al. (2001) with input parameters of a typical HAe star. Apart from other effects described in that paper, the Hα line broadens whenever the stellar rotation is increased. The strength of the line broadening also depends on additional parameters such as the size of the magnetosphere, the gas temperature, the mass accretion rate, and the inclination to the line of sight. The top panel of Fig. 4.9 shows the synthetic profile best fitting the mean Hα line shown by BF Ori. This fit adds to that for UX Ori in MDCH04, again exemplifying that MA modelling is able to reproduce the line profiles of HAe stars with reasonable accuracy. The modelled profile for

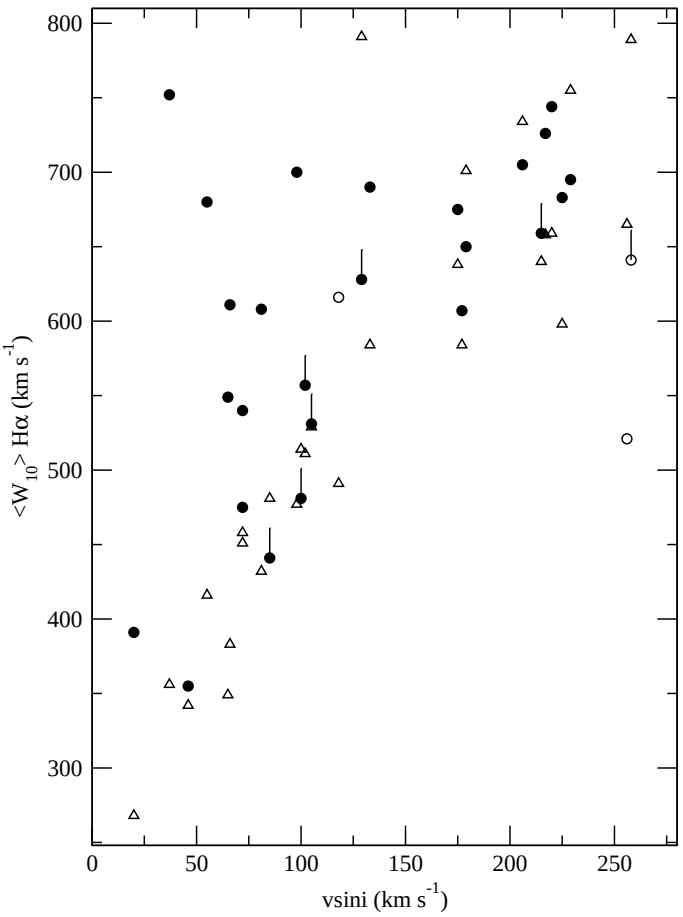

Figure 4.8: Hα mean line width at 10% of peak intensity (from Paper I) vs the projected rotational velocities (circles). Lower limits for $<W_{10}(H\alpha)>$ are marked with vertical bars. Open circles indicate HBe stars -51 Oph the object with the highest value of $v \sin i$-. Filled circles represent the stars in our sample with later spectral types. The theoretical lower limit estimates for each object are derived from Eq. 4.14, and are plotted as open triangles (see text).

BF Ori includes the corresponding rotation rate ($v \sin i = 37$ km s^{-1}, Mora et al. 2001), and is broadened with respect to the same synthetic profile that does not include rotation. The bottom panel of Fig. 4.9 plots some other examples of MA synthetic Hα profiles showing line broadening as the stellar rotation increases. All profiles were modelled from the same parameters as in the top panel, a magnetosphere size of 2.8–3 R$_*$ and different inclinations to the line of sight, as indicated (closer to pole-on for the strongest lines and closer to edge-on for the weakest).

In addition, the trend in Fig. 4.8 is quantitatively consistent with MA operating in HAe stars. When assuming this scenario, the region where the gas is channeled through the magnetic accretion flows has to be located between the stellar photosphere and the co-rotation radius (e.g. Shu et al. 1994). At this point the stellar and the disk angular velocities (assuming Keplerian rotation) are equal, deriving:

$$\mathrm{R_{cor}} \sim \frac{v_{\mathrm{gas}} \mathrm{R_*}}{v_*} \tag{4.12}$$

with v_{gas} the azimuthal velocity of the gas at the co-rotation radius. Since $v_* \geq v \sin i$, and assuming that the non-photospheric Hα line width reflects the velocity of the gas at some

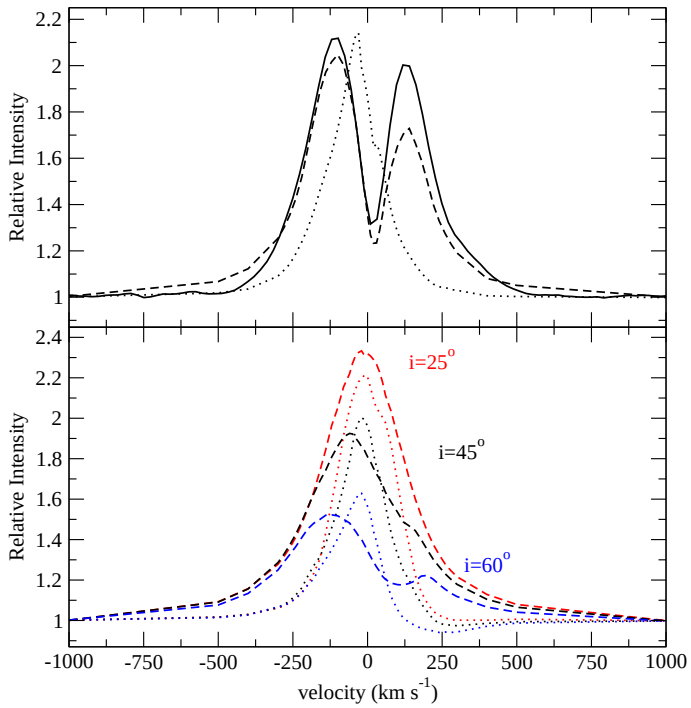

Figure 4.9: (Top): Mean Hα profile of BF Ori from the October campaign in Paper I (solid line) and magnetospheric accretion synthetic profile that best reproduces it (dashed line; $M_* = 2.5$ $M_\odot$, $R_* = 2.5$ $R_\odot$, $T_* = 9000$ K, magnetosphere size 4.2–5R_*, $\dot{M}_{acc} = 10^{-8}$ $M_\odot$ yr^{-1}, $i = 75$ deg, and $v \sin i = 37$ km s^{-1}). The dotted line is the same synthetic profile with no rotation. (Bottom): magnetospheric accretion synthetic Hα profiles with a stellar rotation rate of 75 km s^{-1} (dashed lines) and with no rotation (dotted lines).

point between R_* and R_{cor}, in the sense that $v_{gas} \leq <W_{10}(H\alpha)>/2$, we obtain

$$R_{cor} \leq \frac{< W_{10}(H\alpha) > R_*}{2v \sin i}. \quad (4.13)$$

For the $<W_{10}(H\alpha)>$ and $v \sin i$ values plotted in Fig. 4.8, R_{cor} of HAeBe stars is typically in the range $\sim$ 1–5 R_*, which agrees with the values expected for these objects (see Eq. 4.5). We note that $R_{cor} \leq 2$ R_* for all objects with $v \sin i > 150$ km s^{-1}. Simple dipole geometries would need modifications for such small magnetospheric sizes, in order to reproduce the large line strengths of HAe stars from MA (see MDCH04).

Using Eqs. 4.5 and 4.13, a lower limit for $<W_{10}(H\alpha)>$ can be estimated as a function of the stellar parameters:

$$< W_{10}(H\alpha) >_{min} \sim 2 \left(\frac{GM_* v \sin i}{R_*} \right)^{1/3}. \quad (4.14)$$

We note that this expression is derived by assuming that the line broadening is determined by Keplerian gas located below the co-rotation radius, which is a major requirement in the MA scenario.

Figure 4.8 overplots our $<W_{10}(H\alpha)>_{min}$ estimates from Eq. 4.14. They reproduce the overall trend followed by our $<W_{10}(H\alpha)>$ measurements. The largest differences between the observed and the estimated values occur for the objects with the lowest values of $v \sin i$. This can be partly attributed to inclination effects, i.e., for pole-on sources $v_* >> v \sin i$, and those are expected to be located mainly in the region $v \sin i < 150$ km s^{-1}.

The stars 51 Oph, VV Ser, VX Cas, and SV Cep show $<W_{10}(H\alpha)>$ measurements that are lower than their corresponding $<W_{10}(H\alpha)>_{min}$ estimates. The reason could be uncertainties in the stellar parameters, introduced e.g. by close (unknown) companions or simply by the absence of Keplerian-rotating gas between the stellar surface and the co-rotation radius. In this case MA would hardly operate on these objects. Interestingly, all of them are again HBe stars according to their effective temperature ($> 10000\ K$). Besides, the B-type object 51 Oph clearly deviates from the general trend in Fig. 4.8, likely pointing to an inner disk gas decoupled from the central star. The nature of this object is not clear, since it could be a more evolved star or a β-Pictoris analogue surrounded by a gas-rich debris disk (see e.g. van den Ancker et al. 2001; Stark et al. 2009, and references therein).

In summary, we argue that the high rotational velocities of HAe stars mean that $<W_{10}(H\alpha)>$ cannot be used as tracer of accretion for those objects. At the same time, that the Hα line width reflects the stellar rotation can be interpreted as a consequence of MA operating in the late-type HAeBe sources.

4.5 Variability of accretion rates and accretion tracers

The multi-epoch photometry and simultaneous spectra on which this work is based lead us to analyse the accretion rate variability and its possible relation with the changes in the accretion tracers. The photometry and spectra were taken during four campaigns of several days each, on different months (see Oudmaijer et al. 2001, and Paper I). The multi-epoch values for the Balmer excess were derived from the individual $U-B$ and $B-V$ data taken on the same nights, using an expression analogous to that for $<\Delta D_B>$ in Sect. 4.3.1. The multi-epoch Hα and [OI]6300 luminosites were derived in paper I from line equivalent widths and the photometric measurements in the R band taken on the same nights. The line luminosities were dereddened using simultaneous values for $B-V$ and a procedure analogous to the one explained in Sect. 4.2 for the mean line luminosities.

Most stars in our sample tend to show a constant Balmer excess, within the uncertainties. The strongest variations are between 0.1 and 0.2 magnitudes, which are detected in some observations of $\sim 41\%$ of the stars. An upper limit for the accretion rate variability can be estimated from the stars showing the smallest mean Balmer excesses and the largest Balmer excess variations (see the right panel of Fig. 4.1). As extreme examples, V1686 Cyg shows an increase in the Balmer excess from 0.04 magnitudes on 1998 May 15 to 0.18 magnitudes on 1998 October 27. That change implies an accretion rate increase of a factor ≤ 5. The Balmer excess of WW Vul decreased from 0.14 magnitudes on 1998 May 15 to 0.04 magnitudes on 1998 October 24, which translates into an accretion rate decrease of a factor ≤ 4. Considering all the stars, our model yields a typical upper limit of ~ 0.5 dex for the accretion rate changes, on timescales of days to months. More accurate constraints on possible accretion rate variations below our detection limit would require UV spectra or narrow-band photometry.

The analysis of the simultaneous variability of the Balmer excesses and the line luminosities is not only limited by the error bars provided for our broad-band photometry and mid-resolution spectra, but also by the number of data sampled per object. There is a maximum of 7 simultaneous photometric and spectral points per star, being typically 3 (see Table 3 in Paper I). However, we find objects showing changes in the Balmer excess for which the corresponding Hα and [OI]6300 luminosities do not vary accordingly, as would be expected for an accretion tracer. As an example, V1686 Cyg shows a Balmer excess close to 0 magnitudes on 1998 May 15, which increased to the typical value from our averaged data (0.12

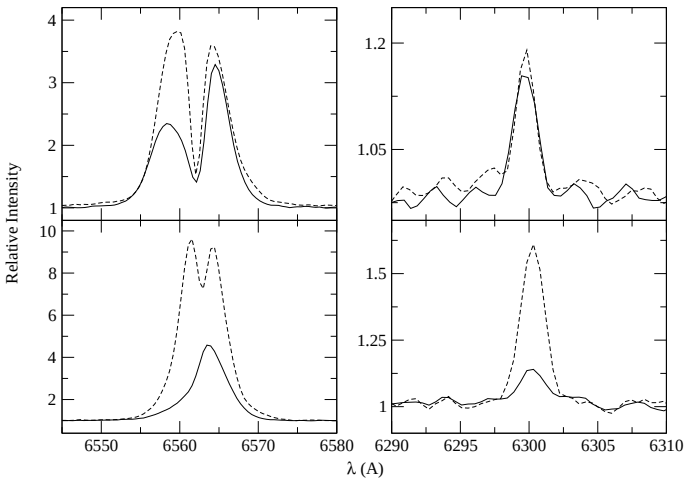

Figure 4.10: Hα (left panels) and [OI]6300 (right panels) normalized profiles for RR Tau (top) and HK Ori (bottom), with different scales depending on the panel. The dashed and solid lines represent the first and second observing dates (see text).

magnitudes) the following night. However, the corresponding Hα and [OI]6300 luminosities did not change. In contrast, there are stars showing variations in the line luminosities with a constant value of the Balmer excess. The one shown by BH Cep was ~ 0 magnitudes during all observations, but the Hα and [OI]6300 luminosities changed by a factor of almost 2. Two other stars showing a decoupled behaviour between the Balmer excess and the line luminosities are provided in Fig. 4.10. RR Tau increased the Balmer excess from ~ 0.32 magnitudes on 1998 October 27, to 0.45 magnitudes on 1999, January 30. Simultaneously, the Hα luminosity decreased by a factor 1.4 and the [OI]6300 luminosity remained constant within the uncertainties -note that the slight variation in the equivalent width was not accompanied by a change in the line luminosity (Paper I)-. HK Ori showed a constant Balmer excess of ~ 0.57 magnitudes at the same time that the Hα and [OI]6300 luminosities decreased by a factor ~ 2 from 1998 October 25 to the following night. The examples in this sense are not scarce, but the inverse case is not true; we do not detect stars in our sample for which a significant increase or decrease in the excess is reflected by the corresponding one in the line luminosities, but again, we note that most possible variations fall below our detection limit.

Even considering the limitations of our data to analyse such small changes, the results described above suggest that the Hα and [OI]6300 luminosities do not trace the accretion rate variability in several stars, unless they reflect the accretion rate changes with a certain lag not covered by our data. Night-to-night variations in the atmospheric transmission could contaminate the estimates of the variability in the Balmer excess. However, a careful photometric calibration was made, especially in the U band, by observing standard stars with different spectral types and airmasses and making several tests after the calibrations (Oudmaijer et al. 2001). It is unknown whether the variations in other empirical tracers not analysed in this work could correlate with the accretion rate variability from the changes in the Balmer excess, or whether the variability could be affected by other factors such as stellar companions. These topics are the subject of ongoing investigation. Multi-epoch, high-resolution spectra covering simultaneously the wavelength range from the UV to the near-IR will be very valuable in this sense. Those can be taken with the X-Shooter spectrograph on the VLT.

4.6 Discussion

The origin of the empirical calibrations between accretion and line luminosities could be explained from the influence that accretion has on the line formation: Both the Hα and Brγ lines have been explained from MA models (Muzerolle et al. 1998b, 2001, MDCH04), although the influence of winds can be non-negligible (Kurosawa et al. 2006; Kraus et al. 2008). The latter contribution seems to be more important as the stellar mass increases (see Paper I and references therein), which would explain the possible decrease in the slope of the Hα calibration, when compared to that for lower mass stars (left panel in Fig. 4.6). Accretion-powered outflows could be the origin of the [OI]6300 feature (Corcoran & Ray 1997, 1998). They could therefore link the luminosity of this line with that of accretion (middle panel in Fig. 4.6). If the [OI]6300 emission is caused by the UV flux illuminating the disk surface (Acke et al. 2005), then the UV excess from the accretion shock would explain the trend with the [OI]6300 luminosity. However, several HAe stars with strong Balmer excesses do not show [OI]6300 emission, regardless of their different degrees of disk flaring according to the Meeus et al. (2001) groups (see e.g. the group II object HD 150193 and the group I star V346 Ori).

Although the mean Hα and [OI]6300 luminosities are related to the "typical" accretion rates (Sect. 4.4), the numerous cases for which the changes in the line luminosities and in the simultaneous Balmer excesses are decoupled suggest that those lines do not to trace the accretion rate variability. This could be the case for several other lines because the typically low accretion rate changes we have derived -less than 0.5 dex- contrast with the complex variability behaviour shown by the spectral tracers. Multi-epoch observations indicate that their variability amplitudes are not correlated: the HeI5876 line shows equivalent width variations over one order of magnitude for a given HAe star, at the same time that Hα varies typically by less than a factor 4 (Paper I). Nguyen et al. (2009) reports that the CaII fluxes provide typical accretion rate variations of 0.35 dex while the Hα 10% width suggests changes of 0.65 dex for the same sample of CTT stars. These differences could be extended to a wide number of empirical tracers of accretion covering a wide wavelength range, indicating that the origin and strength of several of these lines are most probably influenced by different processes apart from accretion.

These results make it reasonable to doubt that several empirical calibrations between the "typical" accretion and line luminosities could not be caused by the accretion contribution to the lines but by a different source. We tentatively suggest that a common dependence of both the accretion and the line luminosities on the stellar one could have strong influence, thereby driving the empirical calibrations. First, there seems to be a direct dependence of $L_{\rm acc}$ on L_* (Fig. 4.3, right). Second, it seems from the comparison between the data for low-mass stars and our results (see e.g. Herczeg & Hillenbrand 2008, and Fig. 4.6) that several line luminosities are also correlated with L_*; e.g., most low-mass stars show Hα luminosities in the range $-6 \leq \log(L_{H\alpha}/L_\odot) \leq -2$, orders of magnitude lower than those shown by our more luminous stars. In addition, the line luminosities of the objects for which the shock models are not able to reproduce the Balmer excesses (see Sect. 4.3.2) tend to be the highest in our sample, as are their stellar luminosities (see Table 4.1). From a statistical point of view, the Spearman's probability (see e.g. Conover 1980) that our accretion and Hα luminosities are uncorrelated in Fig. 4.6 is only p = 4.1×10^{-4}%. However, this value does not consider the possible common dependence of both luminosities on L_*. The partial correlations technique (e.g. Wall & Jenkins 2003) is useful for this task, since it measures the degree of correlation between two variables, nullifying the effect of a common dependence on a third one. Under the

hypothesis that both $L_{\rm acc}$ and L(Hα) depend on L_*, the Spearman's probability from partial correlations increases to 27%. This value is close to that obtained from the comparison of two sets of random variables. A similar conclusion is reached for the Brγ calibration and, to a lesser extent, for the [OI]6300 one. These results indicate that the $L_{\rm acc}$ – L_{line} relations become much less significant once the common dependence on L_* is removed. In this view, the apparent decrease in the slopes in the $L_{\rm acc}$ – L_{line} trends for the intermediate-mass regime (Fig. 4.6) would be reflecting the possible decrease in the $L_{\rm acc}$ – L_* correlation (right panel in Fig. 4.3).

4.7 Conclusions

We applied shock modelling within the context of MA to 38 HAeBe stars, reproducing the strength of the observed Balmer excesses and deriving accretion rate estimates. The typical mass accretion rate is 2×10^{-7} M$_\odot$ yr^{-1}, with scatter and a steep dependence on the stellar mass. The latter can be explained by the most massive HAeBe stars being the youngest, hence the strongest accretors. We obtained empirical expressions to relate accretion and the Hα, [OI]6300, and Brγ luminosities, which are similar to those for the lower mass regime. However, there could be a slight decrease in the slope of the trends relating the accretion luminosity with both the line and the stellar luminosities. In contrast, the Hα line width at 10% of peak intensity can usually not be used to estimate accretion rates for HAeBe stars, unlike in the lower mass regime. The Hα width of HAe objects broadens as the projected rotational velocities increase, which is also consistent with MA operating in these stars.

Although the "typical" accretion rates show clear trends with the mean line luminosities, the accretion-rate changes from the Balmer excess -typically lower than 0.5 dex- seem to be uncorrelated with the variability of the Hα and [OI]6300 lines. We tentatively suggested that the origin of the empirical calibrations between the accretion and line luminosities could not be driven by the influence of accretion on the emission lines, but by a common dependence on the stellar luminosity. The statistical level of significance of the empirical calibrations is strongly diminished once this dependence is considered.

The shock model used is not able to reproduce the strong Balmer excesses shown by the four hottest stars in our sample under reasonable input parameters. In addition, the Hα 10% width of four HBe objects is not consistent with the presence of Keplerian gas between the stellar surface and the co-rotation radius, which is a major requirement for MA to operate. These results give additional support for a change from magnetically driven accretion in HAe stars to some other kind of accretion in HBes (see e.g. Vink et al. 2002; Eisner et al. 2004; Mottram et al. 2007).

It is finally pointed out that, although our results were obtained and interpreted within the context of MA, this means neither that the authors found a way to test magnetospheric accretion onto HAeBe stars nor that the observational data could not be explained from a different scenario. In this respect, further observational and theoretical efforts on the magnetic fields necessary to drive MA in these objects are needed to establish firmer conclusions.

Acknowledgements: The authors thank the referee, Greg Herczeg, for his useful comments on the original manuscript, which helped us to improve the paper. C. Eiroa, I. Mendigutía, and B. Montesinos are partially supported by grant AYA-2008 01727. I. Mendigutía is grateful for financial support from the Space Telescope Science Institute during a two-month stay. This research made use of the SIMBAD database, operated at the CDS, Strasbourg, France

Chapter 5

Accretion-related properties of Herbig Ae/Be stars. Comparison with T Tauris

This chapter includes a paper to be submitted to A&A, by Mendigutía, I.; Mora, A; Montesinos, B.; Eiroa, C.; Meeus, G.; Merín, B. and Oudmaijer, R.D.

Abstract:
Context: The mass accretion rate ($\dot{M}_{\rm acc}$) is a key parameter that has not accurately been determined for a wide sample of Herbig Ae/Be (HAeBe) stars until recently.
Aims: We look for trends relating $\dot{M}_{\rm acc}$ and the stellar ages (t), spectral energy distributions (SEDs), and disk masses for a sample of 38 HAeBe stars, comparing them to analogous correlations found for classical T Tauri (CTT) stars. Our goal is ultimately to shed light on the timescale and physical processes driving the evolution of intermediate-mass pre-main sequence objects.
Methods: Mass accretion rates from a previous work are related to several stellar and disk parameters: the age of the stars was compiled from the literature, multi-wavelength SEDs are classified according to their shape and the wavelength where the IR excess starts, near and mid IR colour excesses were computed, and disk masses were estimated from mm fluxes.
Results: $\dot{M}_{\rm acc}$ decreases with t, showing a dissipation timescale $\tau = 1.3^{+1.0}_{-0.5}$ Myr from an exponential law fit, while a power law yields $\dot{M}_{\rm acc}(\rm t) \propto \rm t^{-\eta}$, with $\eta = 1.8^{+1.4}_{-0.7}$. The near IR excess is larger and starts at shorter wavelengths (J and H bands) for the strongest accretors. Active and passive disks are divided at $\sim 10^{-7}$ $\rm M_{\odot}$ $\rm yr^{-1}$. The mid IR excess and the SED shape from the Meeus et al. classification are not correlated with $\dot{M}_{\rm acc}$. Concerning disk masses, we find $\rm M_{\it disk} \propto \dot{M}_{acc}{}^{1.1\pm0.3}$. Most stars in our sample with signs of inner dust dissipation typically show accretion rates 10 times lower and disk masses 3 times smaller than the remaining objects.
Conclusions: The differences in the inner gas dissipation timescale, and the relative position of the stars with signs of inner dust clearing in the $\dot{M}_{\rm acc}$–$\rm M_{\it disk}$ plane, could be suggesting a slightly faster evolution, and a different process -such as photoevaporation- playing a more relevant role dissipating disks in the HAeBe regime, when compared to lower-mass T Tauri stars.

keywords: Stars: pre-main sequence - Accretion, accretion disks - circumstellar matter - protoplanetary disks - Infrared: stars -

5.1 Introduction

Nowadays there is consensus that practically all stars are formed from accretion disks, even if these have sometimes very short dissipation timescales. The mass accretion rate ($\dot{M}_{\rm acc}$) is a major parameter driving the star-disk evolution, given that most of the stellar mass acquired during the pre-main sequence (PMS) phase is accreted from the disk. Circumstellar disks are also dissipated through other physical processes, including photo-evaporation, dust settling, and dynamical interactions with forming planets (see e.g. Cieza 2008; Williams & Cieza 2011). Their relative influence could in turn be estimated from the amount of gas

accreted by the star (Alexander & Armitage 2007; Najita et al. 2007).

Mass accretion rates in classical T Tauri (CTT) stars are mainly derived from the UV emission excess and spectroscopic veiling caused by the accretion shock, as well as from magnetospheric accretion line modelling and empirical correlations with the luminosity of several emission lines (see the review by Calvet et al. 2000, and references therein). CTTs show a decrease in $\dot{M}_{\rm acc}$ around one or two orders of magnitude on the first Myrs (e.g. Fang et al. 2009), which gives an estimate of the inner gas dissipation timescale. This is intimately related to that for the inner dust (Hartigan et al. 1995), indicating that both gas and dust close to the star vanish at a similar rate. Measurements of dust emission at longer wavelengths provide estimates of the disk mass (M_{disk}) and point to an inside-out dissipation of the circumstellar environment (see Cieza 2008, and references therein). The so-called transitional disks, where the IR emission is weak or negligible up to long wavelengths ($\lambda \sim 10$ μm), are particularly interesting. Stars with this type of spectral energy distribution (SED) are interpreted to be in a fast evolutionary stage that bridges the gap between the optically thick disk phase and the optically thin debris disk one (Wolk & Walter 1996; Cieza et al. 2007). An analysis of the M_{disk}–$\dot{M}_{\rm acc}$ plane can be useful to discern between the different physical processes driving disk dissipation, in particular, the region occupied by CTTs with transitional disks in that plane is compatible with the formation of Jovian planets (Najita et al. 2007).

Herbig Ae/Be (HAeBe) objects (see e.g. the review by Waters 2006) are the intermediate-mass ($\sim$ 1–10 $M_{\odot}$) counterparts of CTT stars. HAeBes are the most massive objects to experience an optically visible pre-main sequence phase, bridging the transition between low and high-mass stars. Despite of their interest -e.g., planet formation could be more efficient in stars more massive than the Sun (Kennedy & Kenyon 2008; Boss 2011)-, our knowledge about the properties of the HAeBe regime is much more limited than that for lower-mass objects. The main reason is the comparatively smaller sample, caused by the faster evolution of massive stars to the main-sequence, and by the fact that star formation shows favour for the less-massive objects, as the shape of the initial-mass function suggests (Salpeter 1995).

The multi epoch optical photometry in Oudmaijer et al. (2001) and the simultaneous optical spectra in Mendigutía et al. (2011a, Paper I hereafter) were recently used to derive accretion rate estimates and empirical relations with emission lines for 38 HAeBe stars (Mendigutía et al. 2011b, Paper II hereafter). The accretion rates in Paper II are the first ones obtained for a wide sample of HAeBe stars from a detailed modelling of the UV Balmer excess, constituting the most reliable estimates for this regime to date. The present work closes this series of papers. We analyse possible relationships between the mass accretion rates and several stellar and disk parameters of the 38 HAeBes studied in Papers I and II, and compare them to the widely known properties for CTTs. In particular, we look for trends with the stellar ages, properties of the spectral energy distributions (SEDs), and disk masses. The final aim is to contribute to the knowledge of circumstellar disk dissipation in HAeBe stars.

Sect. 5.2 describes some general properties of the sample. The SED properties and disk masses are treated separately in Sects. 5.2.1 and 5.2.2, respectively. The correlations with the mass accretion rate are presented and analysed in Sect. 5.3. The discussion is included in Sect. 5.4, and the summary and conclusions are in Sect. 5.5.

5.2 Sample properties and data

The sample is that analysed in Papers I and II, containing 38 HAeBe stars covering almost all such objects in the northern hemisphere from the catalogue of Thé et al. (1994). All stars show IR excess and variable emission lines (Merín 2004, Paper I). Table 5.1 includes the ages, distances, accretion rates, spectral types and information on possible stellar companions, in Cols 2 to 8. The parameters in Cols. 9 to 16 are described in following sections. Additional stellar parameters can be consulted in Papers I and II. The stellar age covers the pre-main sequence phase for our sample, between a few kyr and $\sim$ 15 Myr. Most ages were determined by Montesinos et al. (2009), with a typical uncertainty of 35%. The range in stellar mass and mass accretion rate is $\sim$ 1–6 $M_\odot$ and 10^{-9}–10^{-5} $M_\odot$ yr^{-1}, with a typical -median- value of 2.4×10^{-7} $M_\odot$ yr^{-1}. The mass accretion rates are those reproducing the observed Balmer excesses from a magnetospheric accretion shock model (Paper II). The accretion rates for R Mon, VY Mon, VV Ser and LkHa 234 were estimated extrapolating the calibrations with the emission luminosities provided in that work, and should be taken with caution. Their large uncertainties reflect the difficulty to model the strong Balmer excess of these stars. The spectral types cover the Ae and late-type Be regime, including 10 intermediate-mass F and G stars. In the case of multiplicity, most of the stellar and accretion parameters provided are in principle referred to the bright component, but some contamination cannot be discarded for objects with close companions (d < 1"; see references in Table 5.1). The large fraction of binaries is typical for HAeBe stars (see e.g. Wheelwright et al. 2010).

5.2.1 Spectral energy distributions

Appendix D shows the SEDs of the stars in the sample. The best fits obtained using the online SED fitting tool from the 2-D radiative transfer models in Robitaille et al. (2006, 2007)[1] are overplotted. The photometry has been compiled from the literature and is listed in Tables C.1, C.2 and C.3. We used simultaneous $UBVRIJHK$ photometry taken at the brightest V state from the available multi-epoch data in Oudmaijer et al. (2001) and Eiroa et al. (2002), which minimizes the influence of obscuring effects from circumstellar material and guarantees the best possible photospheric-inner disk fitting. This allows to derive accurate estimates for the wavelength where the IR excess becomes apparent in each object (Sect. 5.2.1). Since Robitaille's models were originally optimized for the 1 to 100 μm region, photometry at wavelengths longer than 160 μm was not used if its inclusion makes worse the stellar and inner-mid disk fitting. Photometry at wavelengths shorter than 0.14 μm or longer than 1.3 mm is not used in any case, since models become noisy at those wavelengths (Robitaille et al. 2006) and may be missing the coolest dust at long wavelength bands (Robitaille, priv. comm.). The stars are classified according to the shape of their SEDs and the properties of their IR excesses, as it is described in the two following sections.

[1] http://caravan.astro.wisc.edu/protostars/

Table 5.1: Sample of stars and parameters.

Star	Age (Myr)	d (pc)	$\dot{M}_{\rm acc}$ [$M_\odot$ yr^{-1}]	Spt	d(Spt') (")	δK (mag)	Ref	M01	IR$_{start}$ (band)	E$(H-K)_0$ (mag)	[12]-[25] (mag)	[25]-[60] (mag)	T$_D$ (K)	β	M$_{disk}$ [$M_\odot$]
[1]	[2]	[3]	[4]	[5]	[6]	[7]	[8]	[9]	[10]	[11]	[12]	[13]	[14]	[15]	[16]
HD 31648	6.7	146	<-7.23	A5 Vep	...	...	...	II	H	0.71	-0.18	0.08	21	0.9	-1.27±0.03
HD 34282	$> 7.8^A$	164^A	<-8.30	A3 Vne	...	...	...	I	K	0.57	0.92	2.01	38	1.4	-1.94±0.04
HD 34700	3.4^B	336^E	<-8.30	G0 IVe	5.2(M1-2)	3.3	(1)	I	>K	0.18	2.17	1.26	16	1.5	-1.86±0.04
					9.2(M2-3)	4.2	(1)								
HD 58647	0.4	543	-4.84±0.22	B9 IVep	>0.5(?)	?	(2)	II	H	0.65	-0.59	-1.96	...	...	...
HD 141569	6.7^A	99^A	-6.89±0.40	B9.5 Vev	7.6(M2)	1.8^{*1}	(3)	II	>K	0.04	1.33	1.18	33	1.2	-3.41±0.19
					9.0(M4)	2.4^{*1}	(4)								
HD 142666	5.1^A	145^A	-6.73±0.26	A8 Ve	...	...	...	II	K	0.56	0.29	-0.48	21	0.6	-1.73±0.03
HD 144432	5.3^A	145^A	<-7.22	A9 IVev	1.4(K5Ve)	2.4	(4,5)	II	H	0.61	0.24	-0.53	16	1.0	-2.15±0.04
HD 150193	5.0	203	-6.12±0.14	A2 IVe	1.1(F9Ve)	2.2	(4,6)	II	J	0.67	0.03	-0.87	26	0.2	-1.98±0.04
HD 163296	5.0	130	<-7.52	A1 Vepv	...	...	...	II	H	0.76	0.15	0.32	29	0.5	-1.18±0.02
HD 179218	3.3	201	<-7.30	A0 IVe	2.5(?)	6.6	(7,8)	I	K	0.64	0.67	-0.41	29	1.3	-1.84±0.04
HD 190073	0.6	767	-5.00±0.25	A2 IVev	...	...	...	II	H	0.74	-0.28	-1.15	...	...	...
AS 442	1.5	826	-5.08±0.11	B8 Ve	?(?)	?	(9)	I	J	0.86	-0.71	1.38	...	...	...
VX Cas	6.4	619	-6.44±0.22	A0 Vep	5.3(?)	4.8	(8)	II	K	0.91	0.59	-0.69	28	1.0	<-1.92
BH Cep	8.2^A	450^A	<-8.30	F5 IIIev	...	...	...	II	K	0.55	-1.53	0.19	...	...	...
BO Cep	11.2^A	400^A	-6.93±0.28	F5 Ve	...	...	...	I	$> K$	0.19	1.52	1.75	...	...	...
SV Cep	5.2	596	-6.30±0.20	A2 IVe	...	...	...	II	H	0.72	0.23	-0.73	24	1.0	-1.82±0.12
V1686 Cyg	$< 0.2^A$	980^A	-5.23±0.41	A4 Ve	...	...	...	I	K	1.05	0.53	1.50	16	1.0	<-0.42
R Mon	$< 0.01^A$	800^A	(-4±1)	B8 IIIev	0.7(K1V)	6.0^{*2}	(10)	I	H	1.49	0.96	-0.09	56	0.7	-0.78±0.04
VY Mon	$< 0.01^A$	800^A	(-4±1)	A5 Vep	...	...	...	I	J	0.97	0.67	0.57	32	2.4	-0.45±0.04
51 Oph	0.7	142	<-7.00	B9.5 IIIe	...	...	...	II	>K	0.42	-0.47	-2.46	...	...	...
KK Oph	3.9^A	160^A	-5.85±0.15	A8 Vev	1.5(G6Ve)	2.5	(4,6)	II	K	1.33	-0.03	-0.48	16	0.1	-1.91±0.04
T Ori	4.0	472	-6.58±0.40	A3 IVev	7.7	>4.5	(11)	I	>K	0.86	...	...	30	1.0	-0.85±0.09
BF Ori	3.2	603	<-8.00	A2 IVev	...	...	...	II	K	0.60	-0.20	1.22	24	1.0	-1.88±0.14
CO Ori	$< 0.1^A$	450^A	-5.20±0.18	F7 Vev	2.0(?)	3.2^{*3}	(12)	II	H	0.65	-0.13	0.40	15	1.0	<-2.11
HK Ori	1.0^A	460^A	-5.24±0.12	G1 Ve	0.4(K3)	2.30	(11,13)	II	>K	0.86	0.08	-0.99	20	1.0	<-0.81
NV Ori	4.4^C	450^F	<-8.30	F6 IIIeV	...	...	...	II	K	0.51	...	...	...	...	...
RY Ori	1.8^A	460^A	-6.65±0.33	F6 Vev	...	...	...	II	H	0.49	-0.06	1.27	...	...	...
UX Ori	4.5	517	<-6.77	A4 IVe	$\geq$ 0.02(?)	?	(12)	II	H	0.72	0.35	-0.28	28	0.6	-1.49±0.04
V346 Ori	3.5	586	-5.99±0.17	A2 IV	...	...	...	I	K	0.47	1.51	1.63	...	...	...
V350 Ori	5.5	735	-6.66±0.24	A2 IVe	0.3(?)	3.2	(8)	II	>K	0.71	0.67	-0.42	...	...	...
XY Per	2.5	347	-5.86±0.20	A2 IV	1.2(?)	0.0	(6)	II	H	0.73	0.06	0.21	...	...	...
VV Ser	1.2	614	(-5.2±0.8)	A0 Vevp	...	...	...	II	H	0.93	-0.22	0.56	45	1.0	<-1.61
CQ Tau	7.7^B	130^G	<-8.30	F5 IVe	...	...	...	I	K	0.73	1.31	0.06	14	0.6	-1.60±0.03
RR Tau	0.4	2103	-4.11±0.16	A0 IVev	?(?)	?	(7)	II	H	0.88	0.25	0.77	28	1.0	<-0.33
RY Tau	6.5^D	134^F	-7.65±0.17	F8 IIIev	...	...	...	II	H	0.68	0.43	-0.58	14	1.0	-1.50±0.04
PX Vul	14^A	420^A	-6.72±0.16	F3 Ve	...	...	...	II	K	0.57	0.49	-0.68	...	...	...
WW Vul	3.7	696	-6.38±0.70	A2 IVe	...	...	...	II	H	0.83	0.31	-0.38	24	1.0	-1.51±0.04
LkHa 234	$< 0.01^A$	1250^A	(-4.1±0.4)	B5 Vev	2.7(?)	> 5.20	(11)	I	H	0.88	1.82	2.35	65	2.5	0.31±0.04

Notes. Unless otherwise indicated, the ages and distances are from Montesinos et al. (2009). ^{A}Manoj et al. (2006), ^{B}Alonso-Albi et al. (2009), ^{C}Merín (2004), ^{D}Siess et al. (1999) ^{E}Acke et al. (2005), ^{F}Blondel et al. (2006), ^{G}Garcia Lopez et al. (2006). The mass accretion rates (on log scale) are from Paper II. The spectral types in Col. 5 are from Mora et al. (2001). The angular distances, spectral types and differences in K magnitude (K_s for ^{*1}, K' for ^{*2} and Hipparcos H$_p$ for ^{*3}) are shown in Cols. 6 and 7 for the companions, when available from the references in Col. 8. (1): Sterzik et al. (2005), (2): Baines et al. (2006), (3): Weinberger et al. (2000), (4): Carmona et al. (2007), (5): Pérez et al. (2004), (6): Pirzkal et al. (1997), (7): Wheelwright et al. (2010), (8): Thomas et al. (2007), (9): Corporon & Lagrange (1999), (10): Close et al. (1997), (11): Leinert et al. (1997), (12): Bertout et al. (1999), (13): Smith et al. (2005). HD 34700 is a triple visual system, being the brightest object a spectroscopic binary (1). HD 141569 is a triple system (3). Disk masses (in log scale) were obtained from the fluxes at 1.3 mm, except for HD 34700, V1686 Cyg, RY Tau and LkHa 234 (see Table C.2)

Classification from the SED shape

Column 9 in Table 5.1 shows the SED group according to the Meeus et al. (2001) classification scheme. The Meeus group I and group II (M01 groups hereafter) SEDs have been associated with geometrical differences in the structure of the disks (flared and self-shadowed respectively, see Meeus et al. 2001; Dullemond 2002; Dullemond & Dominik 2004), and show differences regarding the photopolarimetric behaviour (Dullemond et al. 2003), presence and strength of the polycyclic aromatic hydrocarbons (PAHs) features (Acke & van den Ancker 2004), and grain growth as observed from sub-mm data (Acke et al. 2004). The classification in M01 groups was made following the colour criterium in van Boekel et al. (2003). This is based on the ratio L(nIR) (the integrated luminosity obtained from broad-band $JHKLM$ photometry) to L(IR) (the equivalent parameter, obtained from the IRAS 12, 25 and 60 micron fluxes), and on the non-colour corrected IRAS [12] – [60] colour. The M01 classification agrees with previous ones reported for many of the stars in our sample (Meeus et al. 2001; Acke et al. 2004; Acke & van den Ancker 2004; Acke et al. 2010). A direct visual inspection of the corresponding panels in Appendix D allows to classify HD 58647, BH Cep and NV Ori as M01 group II sources, and AS 442, VY Mon as group I. T Ori is provisionally classified as a group I source, but mid-IR photometry is necessary to confirm this result. Summarizing, 12 sources in our sample are classified as group I stars, being the remaining 26 group II objects.

IR excess

The sample was divided into two groups according to the shortest wavelength where the IR excess is apparent from the SED fits in Appendix D. Half the stars show an IR excess starting at wavelengths corresponding to the J or H bands (1.3 and 1.7 μm), and are included in the first group (group JH hereafter). The objects in the second group (group K) show an IR excess starting at $\lambda \geq 2.2$ μm (filter K), implying blackbody temperatures colder by $\sim$ 400 K or more than the corresponding ones for group JH sources. The SEDs in group K suggest some inner dust dissipation, which is more clear for the four stars showing transition disks with no or very small excess up to $\sim$ 10 μm (HD 34700, HD 141569, BO Cep and 51 Oph). The photometric band where the IR excess starts for each object is shown in Col. 10 of Table 5.1.

Almost all the stars in the sample have measurements in H, K and the IRAS bands, which are used to quantify the IR excess at different parts of the circumstellar environment. Column 11 in Table 5.1 shows the intrinsic colour excess $E(H-K)_0 = (H-K)_{dered}$ - $(H-K)_0$. This parameter measures the colour excess without the extinction contribution (Meyer et al. 1997), reflecting the properties of the inner disk dust. The deredenned colour $(H-K)_{dered}$ is derived considering the extinction law compiled in Robitaille et al. (2007) from Kim et al. (1994) and Indebetouw et al. (2005), a total-to-selective extinction ratio $R_V = 5$ (Hernández et al. 2004), and the B-V colour excesses from Paper II. The intrinsic colours $(H-K)_0$ are from Kenyon & Hartmann (1995). Columns 12 and 13 of Table 5.1 shows the IRAS [12]-[25] and [25]-[26] colours, reflecting the mid-disk dust. Note that in this case the uncertainty in the IRAS colours -typically 0.15 magnitudes- is significantly larger than the redenning and intrinsic colour corrections (see e.g. Patten & Willson 1991), which are therefore not applied for these bands.

5.2.2 Disk masses

Column 16 in Table 5.1 shows the total (dust + gas) disk masses for the stars having mm photometry (see Table C.3). Estimates of the disk masses were derived following Beckwith et al. (1990), assuming that the emission is optically thin at mm wavelengths, and a gas-to-dust ratio of 100. The following expression, valid under the Rayleigh-Jeans regime, has been used:

$$M_{disk} \sim F_\nu \frac{\mathrm{d}^2}{2\mathrm{kT_D}} \frac{c^2}{\nu^2 k_\nu} \tag{5.1}$$

where F_ν is the flux measured at 1.3 mm for most stars in the sample, d is the distance, k is the Boltzmann constant, $\mathrm{T_D}$ is the dust temperature, and k_ν the opacity at the observed frequency. We adopted the standard $\mathrm{k_{1.3mm}} = 0.02$ cm^{-2}gr^{-1} and a wavelength dependence $\mathrm{k_{mm}} \propto \lambda^{-\beta}$ (Beckwith et al. 1990), with $0 < \beta \leq 2.5$. The value of β is representative of the maximum dust grain size, being $\sim$ 2–2.5 for the IS medium and smaller for larger grains (Pollack & Hollenbach 1994; Draine 2006). The parameters $\mathrm{T_D}$ and β are those best fitting the available fluxes longward 350 μm from a graybody (see e.g. André et at. 1993; Sandell 2000), where an input range of ~ 15 K for $\mathrm{T_D}$ was selected taking the relation with the spectral type in Natta et al. (2000) into account. The figures at the end of Appendix D show the results from these fits. The typical β value obtained from them is ~ 1.0 (mean and median), pointing to grain growth with respect the interstellar medium. Several stars in the sample have one single mm measurement. For these objects we followed Natta et al. (2000), fixing β to 1 and $\mathrm{T_D}$ to the corresponding value from the spectral type, according to their Table II. The final values for $\mathrm{T_D}$ and β are listed in Cols. 14 and 15 of Table 5.1.

M_{disk} ranges between 10^{-4} and 0.4 $\mathrm{M}_\odot$, being typically 0.02 $\mathrm{M}_\odot$ (median). Considering the stellar masses, the median value for the $\mathrm{M}_{disk}/\mathrm{M}_*$ ratio is 1 % (i.e. the same one as for lower-mass T Tauri stars; see Andrews & Williams 2007). The extremely high disk mass for LkHa 234 comes from the flux data set in Pezzuto & Strafella (1997) (see Table C.3) which are most probably contaminated by environment emission, given that the object is deeply embedded. Fuente et al. (2001) reports a flux of less than 20 mJy at 1.3 mm from a 1.2" $\times$ 1.3" beam, deriving a disk mass < 0.1 $\mathrm{M}_\odot$ for LkHa 234, whereas Alonso-Albi et al. (2009) reports $\mathrm{M}_{disk} < 0.2$ $\mathrm{M}_\odot$ from the same flux. It is finally noted that the uncertainties for M_{disk} listed in Table 5.1 were computed taking the ones in the mm fluxes into account. Therefore, they should be considered as lower limits, since additional error sources are most probably coming from the $\mathrm{T_D}$ and β values used in the fits, and specially from the uncertainty in the opacity (See Section 5.4 and references therein).

5.3 Correlations analysis

In this section we analyse possible correlations between the mass accretion rates from Paper II (Col. 4 in Table 5.1) and several properties of the stars in the sample, described in previous sections.

5.3.1 Accretion rate and stellar age

The mass accretion rates are plotted against the stellar ages in Fig. 5.1. The accretion rate declines as the age increases following a trend that can be fitted to an exponential expression $\dot{M}_{\rm acc}(t) = \dot{M}_{\rm acc}(0) \times \exp(-t/\tau)$, being t the age of the star and τ the dissipation timescale (Manoj et al. 2006; Fedele et al. 2010). Apart from intrinsic scatter, the final value for τ will

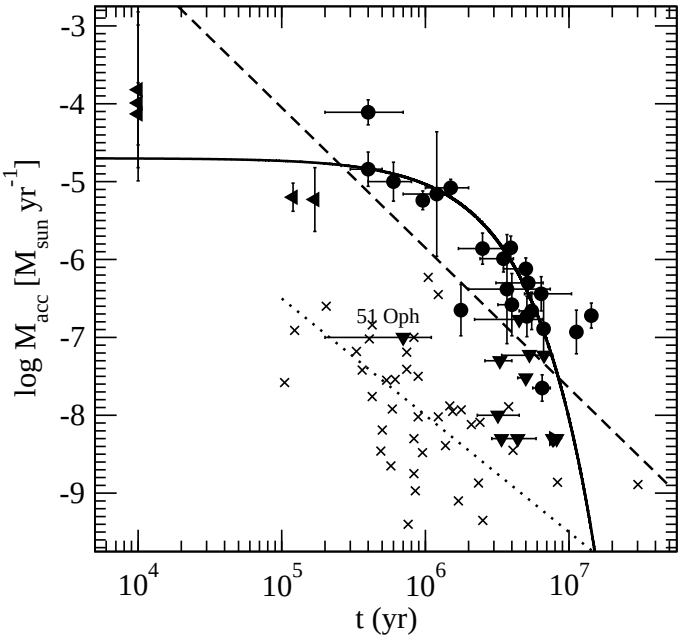

Figure 5.1: Mass accretion rates versus stellar age for our HAeBes (solid symbols, upper and lower limits are represented with triangles) and T Tauri stars from Hartmann et al. (1998) (crosses). The best fits for our sample are represented with solid and dashed lines, for the exponential ($\tau = 1.3^{+1.0}_{-0.5}$ Myr) and power-law ($\eta = 1.8^{+1.4}_{-0.7}$) expressions, respectively. 51 Oph was not considered for the fit. The dotted line is the best power-law fit for T Tauri stars ($\eta \sim 1.5$; see Hartmann et al. 1998; Calvet et al. 2000; Muzerolle et al. 2000).

be affected by uncertainties in the accretion rates and stellar ages, and also by upper and lower limits in both parameters for several stars. Both sources of error can be treated statistically in independent ways, i.e., there is no statistical technique able to deal with a sample that has simultaneosuly both uncertainties for detections and upper/lower limit estimates, to our knowledge. We used the method in York et al. (2004) to derive a fit assuming different ranges of reasonable error bars for both $\dot{M}_{\rm acc}$ and t, obtaining $\tau = 0.9^{+1.0}_{-0.2}$ Myr. On the other hand, the astronomical survival analysis methods discussed in Isobe et al. (1986) and Lavalley et al. (1992) are useful to deal with censored data that includes upper and lower limits. The `schmidttbin` task in the `iraf/stsdas` package is based on those works and provides a value of $\tau = 1.7 \pm 0.6$ Myr for our sample. Taking the average from both estimates, we will consider that $\tau = 1.3^{+1.0}_{-0.5}$ Myr is the accretion rate dissipation timescale for our sample.

The accretion rate decrease with the stellar age can also be fitted by a power-law expression $\dot{M}_{\rm acc}({\rm t}) \propto {\rm t}^{-\eta}$, which is the one used in viscous dissipation models (Hartmann et al. 1998). From the statistical methods explained above, our data can be reproduced with $\eta = 2.3^{+0.9}_{-1.0}$ taking the error-bars into account. If the upper and lower limits are considered, then $\eta = 1.2 \pm 0.1$. The average fit for our sample is $\eta = 1.8^{+1.4}_{-0.7}$, which is shown in Fig 5.1, along with the best fit obtained for CTT stars with K and M spectral types from Hartmann et al. (1998).

The exponential decay provides a better fit than the power-law one, in terms of a lower χ^2, and could reflect better the high but finite accretion rates of the youngest sources in the sample. This conclusion depends on the strong uncertainties for the accretion rates and ages of the youngest stars, which are also the most scarce in our sample. The stellar ages assigned for objects as V1686 Cyg, R Mon, VY Mon, and LkHa 234 are lower than 1 Myr (Manoj et

al. 2006), and our exponential fit provides a slower dissipation timescale than if their ages were larger than assumed here. The stellar ages derived by other authors are also ≤ 1 Myr for these stars (see e.g. Alonso-Albi et al. 2009; Tetzlaff et al. 2011), which are mainly early-type HAeBes. The fact that these objects are already optically visible at this ages could be understood from a very fast evolution (see below). In addition, 51 Oph stands apart from the trend, and was not considered in the fits. The evolutionary stage of this object is not clear, showing characteristics typical of both an HBe star and a MS star with a gas-rich debris disk (van den Ancker et al. 2001; Stark et al. 2009, Paper II).

The exponential expression fitting the accretion rate decline with age for our sample provides a timescale lower than that obtained for the Hα equivalent width of HAeBe stars ($\sim$ 3 Myr in Manoj et al. 2006). However, the equivalent width itself does not measure the gas content and is subject to strong variability (see Paper I). The difference with the estimate by Manoj et al. (2006) can be diminished transforming the line equivalent widths into line luminosities, and then translating these to accretion rates (See Paper I and II). CTT stars show a decrease of $\sim$ 1–2 dex in log $\dot{M}_{\rm acc}$ on the first Myr (Fang et al. 2009), as it is roughly shown by our sample. Although equal considering the large uncertainties, our value for τ is lower than the $\sim$ 2.3 Myr reported for K0–M5 pre-main sequence stars by Fedele et al. (2010). These authors made a statistical study of the objects showing signs of accretion in star forming regions at different ages, concluding that planet formation, and/or migration, in the inner disk might be a viable mechanism to halt further accretion onto the central star on such a short timescale. Indeed, core-accretion models (Pollack et al. 1996; Mordasini et al. 2008) require $\sim$ 3 Myr including planet migration (Alibert et al. 2004, 2005), while gravitational instability (Boss 1997, 1998; Durisen 2007) needs around 1 Myr to form planets. The fast accretion rate dissipation timescale we find for our sample contrasts with that required for the formation of planets from core-accretion models. Other processes apart from planet formation might contribute explaining the fast decrease of the accretion rate in our stars, as it is discussed in following sections.

The analysis of the accretion rate decline represented as a power-law also points to a slightly faster inner disk gas dissipation in HAeBes, compared to CTT stars. Despite the strong uncertainties, $\eta \sim 1.5$ seems to be more consistent for low-mass objects (Hartmann et al. 1998; Calvet et al. 2000; Muzerolle et al. 2000), which is lower than the mean value derived for our sample.

The discussion above considers the HAeBe sample as a whole. However, different evidences, mainly based on spectropolarimetric (Vink et al. 2002; Eisner et al. 2004; Mottram et al. 2007), spectroscopic, and shock modelling analysis (see Paper I, Paper II and references therein), suggest that the accretion paradigm could change at some point between the HBe and the HAe regime, this latter showing properties more similar to the CTT one. As it was previously mentioned, almost all the stars in our sample with $M_* > 2.5$ $M_\odot$ are younger than 1 Myr, which could be indicating that at longer ages most of these objects have already reached the MS phase. The faster evolution of HBe stars compared to HAes would be in agreement with recent observational works, in particular, Roccatagliata et al. (2011) reports that sources with masses > 2 $M_\odot$ in the OB association IC 1795 have a disk fraction of 20%, while lower mass objects (2–0.8 $M_\odot$) have a disk fraction of 50%.

5.3.2 Accretion rate and spectral energy distribution

Figure 5.2 shows the distribution of mass accretion rates for the whole sample, as well as for the M01 group I and group II sources. The typical -median- accretion rate for each group is

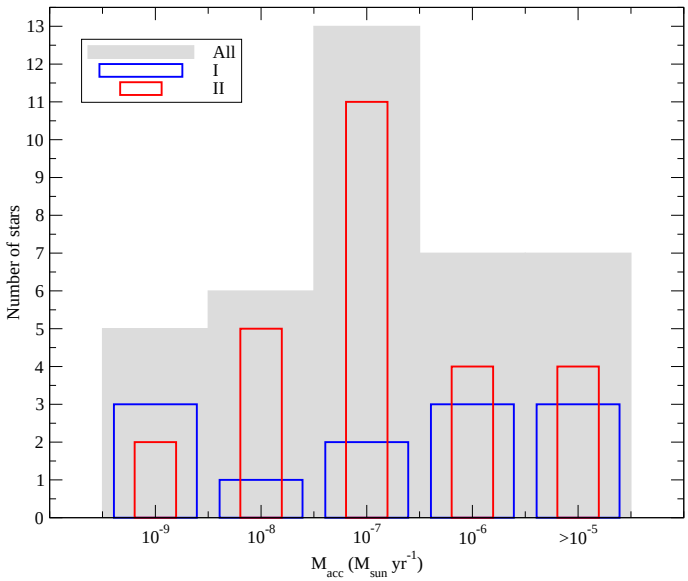

Figure 5.2: Bar diagram showing the mass accretion rates for the 38 stars in the sample (shaded bars), and the stars belonging to the groups I and II (12 and 26 objects; blue and red lines) from the classification of Meeus et al. (2001).

$\sim 10^{-7}$ $M_\odot$ yr^{-1}, as for the whole sample. Group II stars show accretion rates distributed roughly homogeneously around the median. Group I sources show more scatter, but their accretion rates also cover the full possible range for the HAeBe regime. Three Group I sources, namely R Mon, VY Mon and LkHa 234, are early type HAeBes with strong Balmer excesses most probably associated to strong accretion rates (Paper II). Despite of that, the null hypothesis that both M01 groups are drawn from the same accretion rate distribution is confirmed by a two-sample Kolmogorov-Smirnov test with a probability of 75%.

A larger number of M01 group II stars, compared to group I, is found in all works dealing with this classification (see Sect. 5.2.1 and references below). The origin of this division could be understood arguing that objects showing flared group I SEDs are in a younger, faster evolving stage than self-shadowed group II stars. This view pointing to an evolution from group I to group II sources has theoretical and observational support (Dullemond 2002; Dullemond & Dominik 2004; Acke et al. 2004). Therefore, in this scenario it could be expected that group I sources should show larger accretion rates than group II stars. This is not observed in our sample an the implications deserve further study. On the other hand, our data agree with previous works reporting larger dust grain sizes in group II stars (Acke et al. 2004) -our median β value obtained from the fits in Apppendix D is 0.6 for this group, against 1.4 for group I sources-, and with those reporting that UXOrs tend to be group II sources (Dullemond et al. 2003) -LkHa 234 is the only UXOr in our sample not belonging to that group (see Oudmaijer et al. 2001; Rodgers 2003), but this should be taken with caution given its deeply embedded nature-.

From the observational perspective, the absence of a clear correlation between the accretion rates and the M01 groups was somehow expected. The M01 classification scheme depends strongly on the shape of the SED at long wavelengths (in particular on the IRAS 12, 25 and 60 μm fluxes; see van Boekel et al. 2003, and Sect. 5.2.1), but Fig. 5.3 shows that the mass accretion rate is not correlated with the colours at these bands.

The contribution from the accretion shock is stronger at shorter wavelengths (see Paper

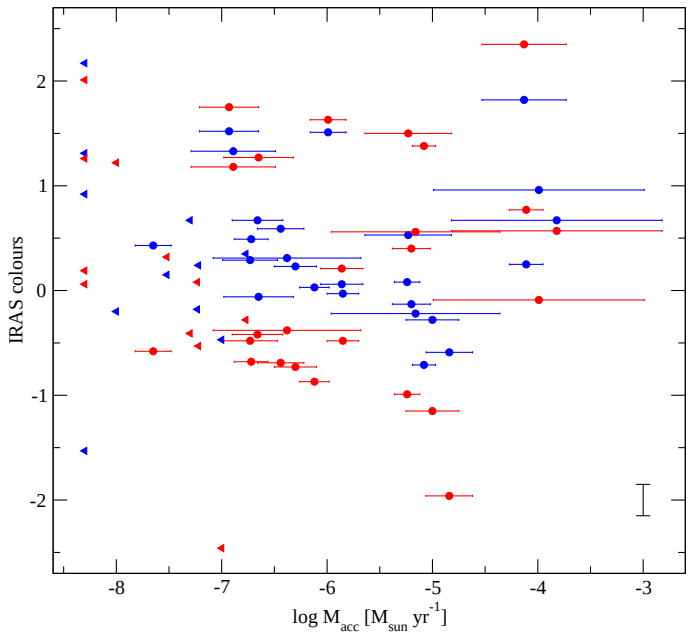

Figure 5.3: IRAS colours [12]-[25] (blue symbols) and [25]-[60] (red) versus the mass accretion rate. The typical uncertanty for the colours is plotted close to the right corner. Triangles are upper limits for the accretion rates.

II and references therein), and could be measurable up to nIR wavelengths (Muzerolle et al. 2004). Figure 5.4 shows the intrinsic colour excess $E(H-K)_0$ against the mass accretion rates for TTs and the stars in our sample. Both parameters are significantly correlated, with a Spearman's probability of false correlation of 1.5×10^{-5} % for our sample. However, this relation becomes non-significant for $\dot{M}_{\rm acc} < 1.5 \times 10^{-7}$ $M_\odot$ yr^{-1}. The slope for stronger accretion rates is 0.12 ± 0.05, equal within the uncertainties than the corresponding slope for CTT stars (0.10 ± 0.05; Meyer et al. 1997). Both samples can be fitted simultaneously with a linear expression with slope 0.15 ± 0.03.

The similar correlation between the mass accretion rates and the *H-K* colour excesses followed by both T Tauri and HAeBe stars point to a common origin, suggesting that the inner dust of HAeBe stars is not only heated by re-processing light from the central star, but also by the contribution of accretion. Giving that the relation between the mass accretion rate and the nIR colour breaks for $\dot{M}_{\rm acc} < 1.5 \times 10^{-7}$ $M_\odot$ yr^{-1}, this value can be considered as an approximate limit dividing passive and active disks in HAeBe stars (see also van den Ancker 2005). This is one order of magnitude larger than the corresponding accretion rate dividing weak and classical T Tauri stars (Fig. 5.4), as it can be estimated assuming viscous dissipation and stellar irradiation as the only heating sources of the disk (Calvet et al. 2000):

$$\dot{M}_{\rm pa} \sim 2 \times 10^{-8} M_\odot yr^{-1} \left(\frac{T_*}{4000K}\right)^4 \left(\frac{R_*}{2R_\odot}\right)^3 \left(\frac{M_*}{0.5M_\odot}\right)^{-1} \quad (5.2)$$

where $\dot{M}_{\rm pa}$, the accretion rate dividing passive and active disks, is derived matching the disk temperature that would result from viscous accretion as the only heating source to that for the case of only irradiation. It is assumed that the mass accretion rate through the inner disk is constant and equal to the rate at which mass is transferred onto the central object, regardless of whether this is channeled through magnetospheric accretion or not. Applying Eq. 5.2 to a typical HAe star (T_* =9000 K, $M_* = 3$ $M_\odot$, $R_* = 3R_\odot$), the observational value

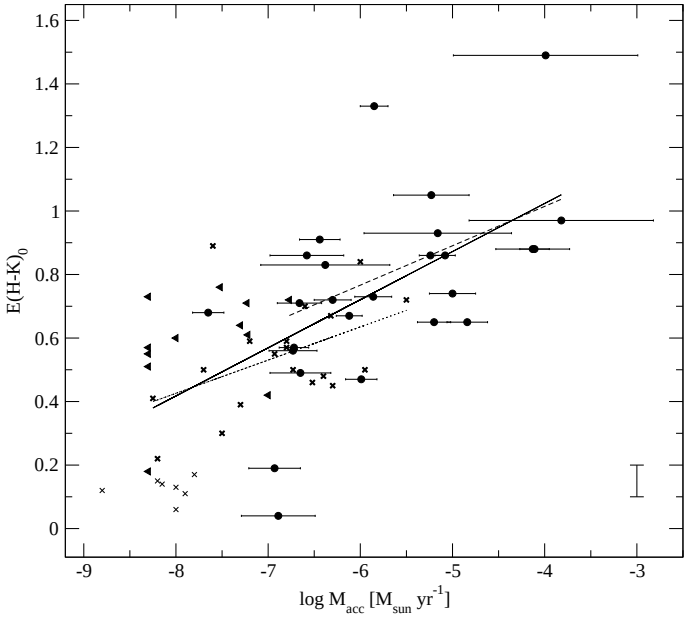

Figure 5.4: Intrinsic colour excess in $H-K$ versus the mass accretion rate. The typical uncertainty for the colour is plotted close to the right corner. Triangles are upper limits for the accretion rates. Crosses represent classical T-Tauri (strong crosses) and weak T Tauri (light crosses) stars from Meyer et al. (1997). The best fits are $E(H-K)_0 = 1.51(\pm0.26) + 0.12(\pm0.05) \times \log \dot{M}_{\rm acc}$ (dashed line, Pearson's correlation coefficient 0.50) for HAeBes with $\dot{M}_{\rm acc} > 1.5 \times 10^{-7}$ M$_\odot$ yr^{-1}, $E(H-K)_0 = 1.26(\pm0.34) + 0.10(\pm0.05) \times \log \dot{M}_{\rm acc}$ (dotted line, Pearson's correlation coefficient 0.50) for CTTs, and $E(H-K)_0 = 1.63(\pm0.17) + 0.15(\pm0.03) \times \log \dot{M}_{\rm acc}$ (solid line, Pearson's correlation coefficient 0.65) for both HAeBes showing high accretion rates and CTTs.

1.5×10^{-7} M$_\odot$ yr^{-1} is also recovered. This corresponds to log (L$_{acc}$/L$_\odot$) $\sim$ 0.60, which, along with the empirical relations with the emission line luminosities provided in Paper II, indicates that active disks around HAeBes tend to show observational thresholds log (L$_{H\alpha}$/L$_\odot$) > -1.5, log (L$_{[OI]6300}$/L$_\odot$) > -3.7, and log (L$_{Br\gamma}$/L$_\odot$) > -3.2.

Figure 5.5 shows the distribution of mass accretion rates according with the classification from the wavelength where the IR excess starts (groups JH and K). The K-S test provides a probability of only 1.8% that both groups follow the same accretion rate distribution (null-hypothesis), against the alternative that both groups show different accretion rate distributions. Moreover, if the alternative hypothesis is that the stars in the group JH have a smaller cumulative distribution function than the remaining objects, then the null hypothesis is rejected with a probability of 99.1 %. Therefore, we conclude that there is a significant trend for the stars with signs of inner dust dissipation to have smaller accretion rates ($\leq 10^{-7}$ M$_\odot$ yr^{-1}), being the objects with IR excesses starting at J or H the strongest accretors. The typical -median- mass accretion rate for these stars is $\sim 10^{-6}$ M$_\odot$ yr^{-1}, one order of magnitude larger than that for the group K objects. This difference reaches 2 orders of magnitude if mean values are adopted instead of medians. Some stars deviate from the general trend relating the accretion rates and the wavelength where the IR excess starts: for instance, HD 141569 shows an SED typical of a transitional disk (see the corresponding panel in Appendix D), indicating an important inner dust dissipation. At the same time, there are no signs of significant inner gas dissipation, since its mass accretion rate is only slightly lower than the median value for the sample (1.3×10^{-7} against 2.4×10^{-7} M$_\odot$ yr^{-1}).

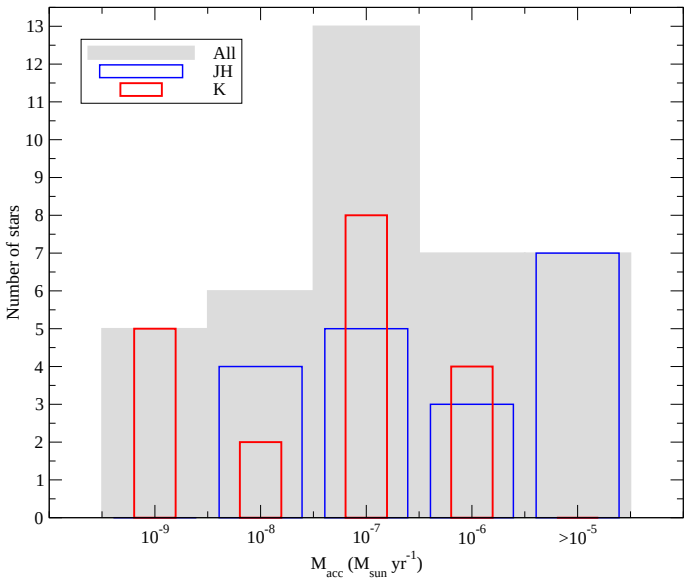

Figure 5.5: Same caption as in Fig. 5.2, but considering the objects with apparent IR excess at bands J–H, or at K or longer wavelengths. Half of the stars in the sample belong to each group.

Finally, the median β value obtained from the fits of the mm fluxes (Appendix D) has a similar value around 1.1 for both groups JH and K, which contrasts with the results mentioned above about the differences for the M01 groups. This suggests that the dust clearing in the inner disk is not necessarily linked to grain growth as determined by mm measurements; these sample the outer disk, and are more related to the decrease of the disk flaring angle associated to M01 group II sources.

5.3.3 Accretion rate and disk mass

Fig. 5.6 shows the mass accretion rate against the disk mass for the stars in our sample, as well as for T Tauris. The Spearman's probability of false correlation between log $\dot{M}_{\rm acc}$ and log M_{disk} is 2.9 % for our sample, which is best fitted from log $\dot{M}_{\rm acc} = 1.1(\pm0.3) \times$ log M_{disk} - 5.0($\pm$0.5), with a Pearson correlation coefficient of 0.60. Most stars in the sample deviate from that expression by less than one order of magnitude (dashed lines in Fig. 5.6). The slope for T-Tauris is also close to unity, once they are divided in transition and non-transition disks (Najita et al. 2007), which is the value expected from simple viscous dissipation models (see Hartmann et al. 1998; Dullemond et al. 2006; Najita et al. 2007). The trend could break for HBe stars more massive than studied here, given the uncertainty for their accretion rates, and that some of their disk masses are lower than for T Tauri stars (Alonso-Albi et al. 2009).

Our sample is divided in Fig. 5.6 according to the wavelength where the IR excess starts, and considering the close binaries -separated by less than 1000 AU from the distances in Table 5.1-, in analogy with the study in Najita et al. (2007) for lower-mass stars in Taurus. In this case it was reported that stars with transition disks, when compared with non-transitional ones, tend to show accretion rates 10 times lower for a given disk mass, and median disk masses $\sim$ 4 times larger. In addition, close binary stars were reported to show slightly lower median disk masses than non-binaries. Although most of our group K stars are far away to be classified as transitionals, two of the three mentioned conclusions from Najita et al. (2007) also apply to the HAeBes. First, the mass accretion rates tend to be lower by

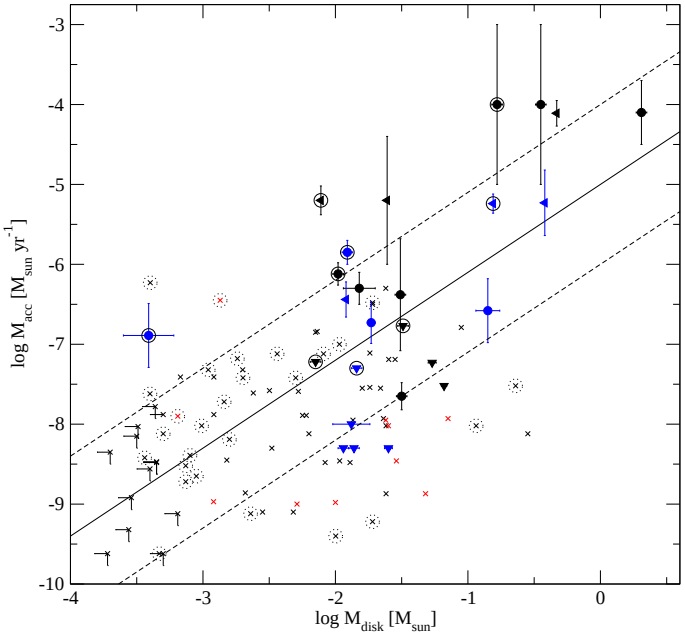

Figure 5.6: Mass accretion rate against disk mass. Crosses are T Tauri stars from Hartmann et al. (1998) and Najita et al. (2007). The latter sample is divided in transition (red) and non-transition disks (black). Our data is represented with solid symbols, triangles for the upper limits. The stars where the IR excess starts at wavelengths equal or larger than that represented by the K band are in blue, the remaining in black. The solid line represents the best fit to our sample and the dashed lines $\pm$ 1 dex. The close binaries in our sample and in T Tauri stars are surrounded by solid and dotted circles, respectively.

a factor $\sim$ 10 for our stars with IR excesses starting at longer wavelengths (Sect. 5.3.2). Second, the close binaries in our sample have lower median disk masses compared to systems without such companions (1.2×10^{-2} against 3.1×10^{-2} $M_{\odot}$). However, in contrast with the results in Najita et al. (2007), the disk masses of the HAeBes with signs of inner disk dissipation are lower than those with IR excesses measured at the J or H bands -median of 0.01 against 0.03 $M_{\odot}$, respectively-. This difference between TTs and HAeBes could be pointing to different physical mechanisms dominating inner disk clearing in both regimes (see the following section).

5.4 Discussion

Our data are consistent with a slightly faster inner gas dissipation timescale than that for lower-mass T Tauri stars (Sect. 5.3.1). However, the similarities found when the accretion rate is related to the nIR colours (Sect. 5.3.2), and disk masses (Sect. 5.3.3), point to a common origin explaining these trends for both the T Tauri and the intermediate-mass regime. The relation with the nIR colour excess extends the corresponding one from lower-mass to HAeBe stars (Fig. 5.4). Both trends are understood if the dust of the inner disk is heated not only by reprocessed stellar light, but also by the viscous accretion contribution (Calvet et al. 2000). The slope relating the accretion rate and the disk mass is close to unity (Fig. 5.6), which is also expected from simple viscous disk models (e.g. Dullemond et al. 2006).

In addition, the relative position of the stars in the $\dot{M}_{\rm acc}$–M_{disk} plane (Fig. 5.6), could

provide clues on the physical mechanisms dominating circumstellar disk dissipation. As an example (see Alexander & Armitage 2007; Najita et al. 2007, for more details), large disk masses and low mass accretion rates, compared to those typically shown by non-transitional disks, are expected if Jovian planets are formed around stars with signs of inner disk dissipation: a large reservoir of material is necessary to form such type of planets, at the same time that the inner gas content -and therefore the accretion rate- is strongly diminished. In contrast, photoevaporated disks are in principle more consistent with both low masses and accretion rates. As indicated in Sect. 5.3.3, most of our stars with signs of inner dust dissipation have mass accretion rates and disk masses lower than the corresponding median values for the remaining sources, by a typical factor of $\sim$ 10 and 3, respectively. Some examples are HD 34282, HD 34700, HD 142666 or BF Ori, as well as transition disks associated to non-close binary and binary stars (HD 34700 and HD 141569, respectively). The lower values for both $\dot{M}_{\rm acc}$ and M_{disk} could be expected from photoevaporation sweeping out both the circumstellar gas and dust content (Clarke et al. 2001; Alonso-Albi et al. 2009). Photoevaporation could in fact be more relevant dissipating disks in the HAeBe regime than in the T Tauri one, from the theoretical point of view (see e.g. Takeuchi et al. 2005). On the other hand, T Ori is the only star in our sample with signs of inner dust dissipation that shows a lower mass accretion rate and a higher disk mass than the corresponding median values for the stars with an IR excess starting at J or H bands. As argued by Najita et al. (2007) for the transition disks in Taurus, those properties are anticipated by several planet formation theories, suggesting that Jovian planets could be playing a significant role in explaining the inner disk dissipation of T Ori. The possible presence of a T-Tauri type stellar companion located at $\sim$ 3500 AU, considering a distance to the system of 470 pc (Leinert et al. 1997; Montesinos et al. 2009), could also be affecting the position of T Ori in the $\dot{M}_{\rm acc}$–M_{disk} plane. CQ Tau shows similar characteristics to T Ori, with signs of inner disk dissipation, a low value of $\dot{M}_{\rm acc}$ and a high M_{disk}, compared with the medians for the whole sample. Thus, the formation of Jovian planets could also be playing a role for this star. Grain growth is also apparent from the fitted value of β ($\sim$ 0.6).

Finally, the discussion above must take into account that disk masses estimated from mm measurements could be affected by strong uncertainties. Andrews & Williams (2007) found that disk masses from mm continuum emission underestimate those from accretion by roughly one order of magnitude, for a sample of T Tauri stars. Following a procedure similar to that in Hartmann et al. (1998), the amount of material accreted from t_0 to t_{MS} -with t_0 the age of the star and t_{MS} the time to reach the main sequence- is a lower limit for the disk mass at t_0, and is given by:

$$M_{disk} \geq \int_{t_0}^{t_{MS}} \dot{M}_{\rm acc}(t)dt. \tag{5.3}$$

Assuming $\dot{M}_{\rm acc}(t) = At^{-\eta} + B$, whith $\eta > 1$ and A, B constants that can be determined from a measurement of the mass accretion rate at a given t_0, and under the condition $\dot{M}_{\rm acc}(t_{MS}) \sim 0$, it is derived:

$$M_{disk} \geq \left(\frac{\dot{M}_{\rm acc}(t_0)}{t_0^{-\eta} - t_{MS}^{-\eta}}\right) \times \left(\frac{1}{\eta - 1}\right) \times \left(\frac{1}{t_0^{\eta-1}} - \frac{1}{t_{MS}^{\eta-1}} + \frac{t_0(\eta-1)}{t_{MS}^{\eta}}\right) \tag{5.4}$$

which, for $t_{MS} \gg t_0$, yields:

$$M_{disk} \geq \frac{\dot{M}_{\rm acc}(t_0)}{\eta - 1} \times t_0. \tag{5.5}$$

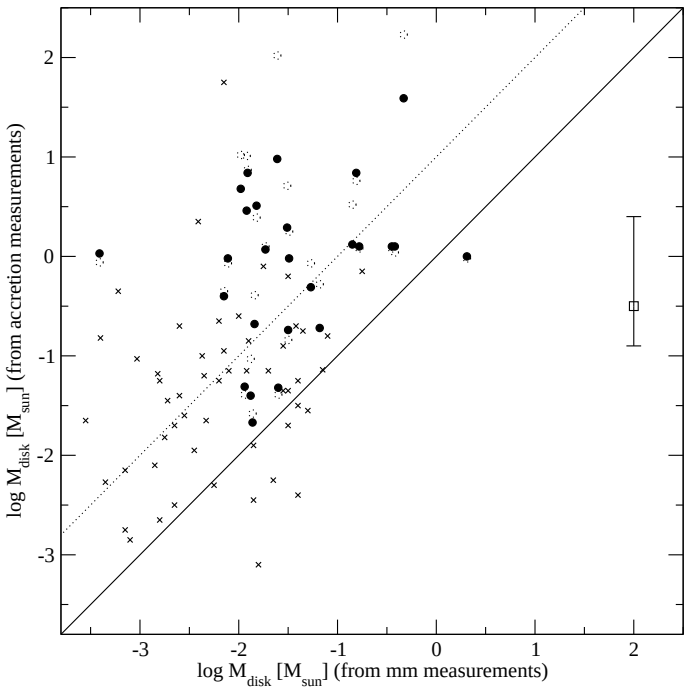

Figure 5.7: Disk masses from accretion versus those from dust emission at mm wavelengths. Crosses are T Tauri stars taken from Andrews & Williams (2007) and circles the estimates for our sample. The solid line represents equal values and the dotted line bisects both samples, indicating that disk masses from accretion are typically one order of magnitude larger than those from mm measurements. The filled circles are derived from Eq. 5.5 and $\eta = 1.8$ Myr. The error bar in the right side represents the uncertainty coming from using $\eta = 1.1$ Myr (upper limit) or 3.2 Myr (lower limit). The open-dotted circles are the estimates from Eq. 5.4, $\eta = 1.8$ Myr, and the theoretical times to reach the main sequence from Tayler (1994).

Equation 5.5 was applied by Hartmann et al. (1998) and Andrews & Williams (2007) for T-Tauri stars. It provides practically equal values than Eq. 5.4 for these objects, and for many of our stars, but Eq. 5.4 provides disk masses that can be one order of magnitude larger than those from Eq. 5.5 for the most massive stars in our sample. These objects are expected to evolve very fast and their ages are comparable to the theoretical times to reach the main sequence (i.e. $t_0 \sim t_{MS}$, see Fig. 4 in paper II and e.g. Tayler 1994). Figure 5.7 compares the disk masses derived from the mass accretion rate to those from the cold dust emission. The results for our sample extend the finding for T Tauri stars, indicating that disk masses from mm measurements are smaller than those from accretion by an order of magnitude on average. Following Andrews & Williams (2007), this may be the result of particle growth (up to approximately meter sizes), leading to an overestimate of the opacity used to compute M_{disk} from the millimeter luminosity. This view is supported by the low β values derived for most stars in our sample with SED fitting at mm and sub-mm wavelengths (Appendix D), which are similar to those for T Tauris (Ricci et al. 2010) and point to substantial grain growth in the CS environment of pre-main sequence stars (see Andrews & Williams 2007, and references therein).

5.5 Summary and conclusions

We looked for correlations between the mass accretion rates and several parameters for a sample of 38 F-G, HAe and late-type HBe PMS objects, comparing them to the corresponding for lower mass T Tauri stars. Our main results and conclusions are:

- The mass accretion rate decreases with the stellar age. This decline can be fitted to $\dot{M}_{\rm acc}(\rm t) \propto \exp(-t/\tau)$ or to $\dot{M}_{\rm acc}(\rm t) \propto \rm t^{-\eta}$. The first expression provides a dissipation timescale $\tau = 1.3^{+1.0}_{-0.5}$ Myr. The second expression is the same one as that used in simple viscous dissipation models for CTT stars, yielding $\eta = 1.8^{+1.4}_{-0.7}$. The large error bars reflect intrinsic scatter, uncertainties and upper-lower limit estimates for the accretion rates and stellar ages. However, both expressions point to a slightly faster dissipation of the inner gas in our sample, when compared to lower mass T Tauri stars.

- Our sample does not show any apparent correlation between $\dot{M}_{\rm acc}$ and the SED shape according to the Meeus et al. (2001) classification scheme. This is more related with the grain size or the UXOr behaviour, as it was previously reported.

- The correlation between the near IR excess and the accretion rate extends from the CTT to the intermediate-mass regime. The mass accretion rate dividing active and passive disks rises one order of magnitude for our sample (10^{-7} $\rm M_\odot$ $\rm yr^{-1}$), as can be inferred assuming viscous accretion and stellar irradiation as the only heating sources of the inner disk.

- In agreement with simple viscous disk models, the mass accretion rate correlates with the disk mass as $\dot{M}_{\rm acc} \propto {\rm M_{\it disk}}^{1.1(\pm0.3)}$, with a scatter lower than $\pm$ 1 dex for most of the stars, as it is roughly followed by CTT stars once classified in transition and non-transition disks (Najita et al. 2007).

- Most stars in our sample with signs of inner dust disk clearing (IR excesses starting at the K band or longer wavelengths) show lower accretion rates and disk masses than those for the remaining objects. This contrasts with previous results for transitional T Tauri stars, and could be suggesting that a different physical process -such as photoevaporation- plays a major role dissipating disks in HAeBes.

Finally, we extended to the HAeBe regime the previously reported mismatch between the accretion rates derived from cold dust emission and accretion. Further efforts are necessary to break that inconsistency, most probably related to the way that disk masses are estimated from mm measurements.

Chapter 6

Conclusions and future work

This chapter closes this thesis. The main results and conclusions are summarized in Sect. 6.1 (translated into Spanish in Sect. 6.2). Future research lines that could be conducted, motivated by the latter results, are described in Sect. 6.3.

6.1 Summary and conclusions

This thesis presents a study of the circumstellar and accretion properties of a sample of 38 HAe, late-type HBe and intermediate-mass F-G PMS stars, representative of the HAeBe regime. It is mainly based on multi-epoch optical spectra and simultaneous optical and near infrared photometry, as well as on well-known stellar parameters and on the analysis of the SEDs. The main results and conclusions are:

- Chapter 3 includes the most complete characterization to date of the circumstellar atomic gas of HAeBe stars in the optical, analysing multi-epoch (intervals of hours-days-months) and averaged spectra in Hα, [OI]6300, NaID and HeI5876. These spectra, and the simultaneous photometry, have allowed us to estimate line fluxes and to soundly assess whether the observed EW variations are caused by changes in the stellar continuum or by variations of the circumstellar gas itself. These data constitute one of the largest existing data bases to study some of the variability properties in intermediate-mass PMS stars. Specific results in this respect are:
  - The EW variability of the different lines depends on the timescale and is independent of the mean line strength. The HeI5876 and NaID lines show the largest EW variations and can be seen either in absorption or in emission. In contrast, [OI]6300 is the only line without variations on timescales of hours and is also the line showing variability in a smaller percentage of the stars in the sample.
  - There is a correlation between the Hα and [OI]6300 relative variabilities, which suggests a common origin. In some stars the EW variability of both lines are due to variations of the continuum, but in other objects the EW variability reflects variations of the line luminosities and, consequently, of the CS gas properties.
  - Mean values and relative variabilities of the Hα line widths W_{10} and EW are uncorrelated in our sample. The lack of correlation between both parameters suggests that the Hα broadening does not depend on the column density of hydrogen atoms. Thus, estimates of gas properties, such as accretion rates, based on the Hα W_{10} or EW would differ significantly, unlike in lower mass stars.

  - The Hα behaviour differs depending on the stellar mass, which suggests different physical processes for Herbig Ae and Herbig Be stars. The massive stars tend to show stable Hα profiles, mainly dominated by blueshifted self-absorptions. In addition, stars with $M_* \geq 3.0$ $M_\odot$ show very low W_{10}(Hα) relative variabilities ($\leq$ 0.06).

- We applied magnetospheric-accretion shock modelling to reproduce the observed Balmer excess from the multi-epoch Johnson's UB photometry in chapter 4, deriving the most reliable estimates of the accretion rates for a wide sample of HAeBe stars to date. The accretion rates were related to both Hα luminosities, Hα 10% widths, and [OI]6300 luminosities from simultaneous spectra, and to Brγ luminosities from the literature, obtaining the following results:

  - The typical -median- mass accretion rate is 2×10^{-7} $M_\odot$ yr^{-1} in our sample, 36 % of the stars showing values $\leq 10^{-7}$ $M_\odot$ yr^{-1}, 35% between 10^{-7} and 10^{-6}, and 29% $> 10^{-6}$ $M_\odot$ yr^{-1}.
  - When accretion is related to the stellar masses and luminosities ($1 \leq M_*/M_\odot \leq 6$; $2 \leq L_*/L_\odot \leq 10^3$), we derive $\dot{M}_{\rm acc} \propto M_*^5$ and $L_{\rm acc} \propto L_*^{1.2}$, with scatter. The steeper trend relating $\dot{M}_{\rm acc}$ and M_*, when compared to that for lower mass objects, can be explained from the mass-age distribution characterizing HAeBe stars.
  - Empirical calibrations relating the accretion and the Hα, [OI]6300, and Brγ luminosities were provided. The slopes in our expressions are slightly shallower than those for lower mass stars, but the difference is within the uncertainties, except for the [OI]6300 line.
  - Although the "typical" accretion rates show clear trends with the mean line luminosities, the accretion rate variations from the Balmer excess -typically lower than 0.5 dex- seem to be uncorrelated with the variability of the Hα and [OI]6300 lines. We tentatively suggested that the origin of the empirical calibrations between the accretion and line luminosities could not be driven by the influence of accretion on the emission lines, but by a common dependence on the stellar luminosity. The statistical level of significance of the empirical calibrations is strongly diminished once this dependence is considered.
  - The W_{10}(Hα) is uncorrelated with $\dot{M}_{\rm acc}$, unlike for the lower mass regime. The mean Hα 10% width shows higher values as the projected rotational velocities of HAe stars increase, which agrees with MA.
  - The shock model used is not able to reproduce the strong Balmer excesses shown by the four hottest stars in our sample under reasonable input parameters. In addition, the W_{10}(Hα) of four HBe objects is not consistent with the presence of Keplerian gas between the stellar surface and the co-rotation radius, which is a major requirement for MA to operate. These results give additional support for a change from magnetically driven accretion in HAe stars to some other kind of accretion in HBes.

- Finally, chapter 5 studied the timescale and physical processes driving the evolution of intermediate-mass pre-main sequence stars. We looked for trends relating $\dot{M}_{\rm acc}$ and the stellar ages, properties of the SEDs, and disk masses for our sample. The correlations found were compared to better known empirical laws for CTT stars. The main results are:

– The mass accretion rate decreases with the stellar age. This decline can be fitted to $\dot{M}_{\rm acc}(\rm t) \propto \exp(-t/\tau)$ or to $\dot{M}_{\rm acc}(\rm t) \propto \rm t^{-\eta}$. The first expression provides a dissipation timescale $\tau = 1.3^{+1.0}_{-0.5}$ Myr. The second expression is the same one than that used in simple viscous dissipation models for CTT stars, yielding $\eta = 1.8^{+1.4}_{-0.7}$. The large error bars reflect intrinsic scatter, uncertainties and upper and lower limit estimates for the accretion rates and stellar ages. However, both latter expressions point to a slightly faster dissipation of the inner gas in our sample, when compared to lower mass T Tauri stars.

– Our sample does not show any apparent correlation between $\dot{M}_{\rm acc}$ and the SED shape according to the Meeus et al. (2001) classification scheme. This is more related with the grain size or the UXOr behaviour, as it was previously reported.

– The correlation between the near IR excess and the accretion rate extends from the CTT to the intermediate-mass regime. The mass accretion rate dividing active and passive disks rises one order of magnitude for our sample (10^{-7} $\rm M_\odot$ $\rm yr^{-1}$), as can be inferred assuming viscous accretion and stellar irradiation as the only heating sources of the inner disk.

– In agreement with simple viscous disk models, the mass accretion rate correlates with the disk mass as $\dot{M}_{\rm acc} \propto {\rm M_{\it disk}}^{1.1(\pm0.3)}$, with a scatter lower than $\pm$ 1 dex for most of the stars, as it is roughly followed by CTT stars once classified in transition and non-transition disks (Najita et al. 2007).

– Most stars in our sample with signs of inner dust disk clearing (IR excesses starting at the K band or longer wavelengths) show lower accretion rates and disk masses than those for the remaining objects. This contrasts with previous results for transitional T Tauri stars, and could be suggesting that a different physical process -such as photoevaporation- plays a major role dissipating disks in HAeBes.

– We extended to the HAeBe regime the previously reported mismatch between the disk masses derived from cold dust emission and from accretion. Further efforts are necessary to break that inconsistency, most probably related to the way that disk masses are estimated from mm measurements.

6.2 Resumen y conclusiones

Esta tesis presenta un estudio de las propiedades circunestelares y de acreción de una muestra de 38 estrellas PMS de tipo HAe, HBe tardías y F-G de masa intermedia, representativa del régimen HAeBe. Está basada fundamentalmente en espectros óptico multi-época y fotometría simultánea óptica e infrarroja cercana, así como en parámetros estelares bien conocidos y en el análisis de las SEDs. Los resultados y conclusiones fundamentales son:

- El Capítulo 3 incluye la caracterización mas completa hasta la fecha del gas atómico circunestelar de estrellas HAeBe en el óptico, analizando espectros multi-época (intervalos de horas-dias-meses) y promediados en Hα, [OI]6300, NaID y HeI5876. Estos espectros, junto con la fotometría simultánea, nos han permitido estimar flujos de línea y evaluar de manera robusta en qué casos las variaciones de la EW son causadas por cambios en el contínuo estelar o por variaciones del propio gas circunestelar. Esta base de datos es una de las mas extensas para estudiar algunas de las propiedades de variabilidad en estrellas PMS de masa intermedia. Los resultados específicos relacionados son:

- La variabilidad en la EW de las diferentes líneas depende de la escala temporal y es independiente de la intensidad de línea promedio. Las líneas HeI5876 y NaID muestran las variaciones de EW mas intensas y pueden observarse tanto en absorción como en emisión. Como contraposición, la única línea sin variaciones en escalas de tiempo de horas es [OI]63000, siendo además la línea que muestra variabilidad en un porcentaje mas pequeño de las estrellas en la muestra.
- Existe una correlación entre las variabilidades relativas en Hα y [OI]6300, que sugiere un origen común. En algunas estrellas la variabilidad en la EW de ambas líneas es debida a variaciones del contínuo, pero en otros objetos la variabilidad en la EW refleja variaciones en la luminosidad de las líneas y, consecuentemente, en las propiedades del gas CS.
- Los valores promedios y las variabilidades relativas de las anchuras W_{10} y EW en Hα no están correlacionadas en nuestra muestra. La ausencia de correlación entre ambos parámetros sugiere que el ensanchamiento Hα no depende de la densidad de columna de átomos de hidrógeno. Por tanto, estimaciones de las propiedades del gas, como las tasas de acreción, basadas en la W_{10} o la EW de Hα diferirían de manera significativa, a diferencia de en las estrellas de menor masa.
- El comportamiento en Hα difiere dependiendo de la masa estelar, lo que sugiere procesos físicos diferentes en estrellas Herbig Ae y Herbig Be. Las estrellas masivas tienden a mostrar perfiles Hα estables, dominados fundamentalmente por autoabsorciones desplazadas al azul. Además, las estrellas con $M_* \geq 3.0$ $M_\odot$ muestran variabilidades relativas en W_{10}(Hα) muy bajas (≤ 0.06).

- En el Capítulo 4 hemos aplicado un modelado de acreción magnetosférica para reproducir los excesos de Balmer observados a partir de fotometría multi-época UB de Johnson, derivando las estimaciones mas fiables hasta la fecha de la tasa de acreción de una muestra amplia de estrellas HAeBe. Las tasas de acreción fueron relacionadas tanto con luminosidades Hα, anchuras Hα al 10%, y luminosidades [OI]6300 a partir de espectros simultáneos, como con luminosidades Brγ de la literatura, obteniendo los siguientes resultados:
  - La tasa de acreción de masa típica -mediana- es 2×10^{-7} $M_\odot$ yr^{-1} en nuestra muestra, el 36 % de las estrellas mostrando valores $\leq 10^{-7}$ $M_\odot$ yr^{-1}, el 35% entre 10^{-7} y 10^{-6}, y el 29% $> 10^{-6}$ $M_\odot$ yr^{-1}.
  - Cuando la acreción se relaciona con las masas y luminosidades estelares ($1 \leq M_*/M_\odot \leq 6$; $2 \leq L_*/L_\odot \leq 10^3$), obtenemos $\dot{M}_{\rm acc} \propto M_*^5$ y $L_{\rm acc} \propto L_*^{1.2}$, con dispersión. La tendencia que relaciona $\dot{M}_{\rm acc}$ y M_* es más pronunciada, comparada con la de los objetos de menor masa, y puede ser explicada a partir de la distribución masa-edad que caracteriza las estrellas HAeBe.
  - Se han proporcionado calibraciones empíricas relacionando las luminosidades de acreción con las de Hα, [OI]6300, y Brγ. Las pendientes en nuestras expresiones son ligeramente más planas que las de las estrellas de menor masa, aunque la diferencia cae dentro de las incertidumbres, excepto para la línea [OI]6300.
  - Aunque las tasas de acreción "típicas" muestran tendencias claras con las luminosidades promedio de las líneas, las variaciones de la tasa de acreción a partir del exceso de Balmer -típicamente menores que 0.5 dex- no parecen correlacionar con la variabilidad de las líneas Hα y [OI]6300. Sugerimos con precaución que

el origen de las calibraciones empíricas entre las luminosidades de acreción y de línea podrían no estar dirigidas por la influencia de la acreción en las líneas de emisión, sino por una dependencia común en la luminosidad estelar. El nivel de significancia estadística de las calibraciones empíricas disminuye fuertemente una vez esta dependencia es considerada.

- La $W_{10}(H\alpha)$ no correlaciona con $\dot{M}_{\rm acc}$, a diferencia del régimen de masas menores. El promedio de la anchura Hα al 10% muestra valores mayores según las velocidades de rotación proyectadas de las estrellas HAe aumentan, lo que está de acuerdo con la MA.
- El modelo de shock usado no es capaz de reproducir con parámetros de entrada razonables los fuertes excesos de Balmer mostrados por los cuatro objetos más calientes en nuestra muestra. Además, la $W_{10}(H\alpha)$ de cuatro objetos HBe no es consistente con la presencia de gas Kepleriano entre la superficie estelar y el radio de co-rotación, lo que es un requerimiento fundamental para que la MA opere. Estos resultados proporcionan un apoyo adicional al cambio desde la acreción dirigida magnéticamente en las estrellas HAe, a algún otro tipo de acreción en las HBe.

- Finalmente, en el Capítulo 5 se estudió la escala de tiempo y los procesos físicos que dirigen la evolución de las estrellas PMS de masa intermedia. Buscamos tendencias relacionando $\dot{M}_{\rm acc}$ y las edades estelares, la propiedades de las SEDs, y las masas de disco para nuestra muestra. Las correlaciones encontradas fueron comparadas con leyes empíricas para las estrellas CTT, mejor conocidas. Los resultados fundamentales son:

  - La tasa de acreción de masa decrece con la edad estelar. Esta decrecimiento puede ser ajustado a $\dot{M}_{\rm acc}({\rm t}) \propto \exp(-t/\tau)$ o a $\dot{M}_{\rm acc}({\rm t}) \propto {\rm t}^{-\eta}$. La primera expresión proporciona una escala temporal de disipación $\tau = 1.3^{+1.0}_{-0.5}$ Myr. La segunda expresión es la misma que la usada en modelos simples de disipación viscosa para estrellas CTT, dando lugar a $\eta = 1.8^{+1.4}_{-0.7}$. Las grandes barras de error reflejan dispersión intrínseca, incertidumbres y límites superiores e inferiores para las tasas de acreción y las edades estelares. Sin embargo, las dos expresiones anteriores apuntan a una disipación del gas interno ligeramente más rápida en nuestra muestra, cuando se compara con las estrellas T Tauri de menor masa.
  - En nuestra muestra, no hay correlación aparente entre $\dot{M}_{\rm acc}$ y la forma de la SED según el esquema de clasificación de Meeus et al. (2001). Este último está más relacionado con el tamaño de los granos o el comportamiento UXOr, tal como se ha documentado previamente.
  - La correlación entre el exceso en el IR cercano y la tasa de acreción se extiende desde el régimen CTT al de masa intermedia. La tasa de acreción de masa que divide los discos activos y pasivos crece un orden de magnitud para nuestra muestra (10^{-7} M$_\odot$ yr^{-1}), tal como se infiere asumiendo acreción viscosa e irradiación estelar como únicas fuentes de calentamiento del disco interno.
  - En acuerdo con los modelos simples de discos viscosos, la tasa de acreción de masa correlaciona con la masa del disco como $\dot{M}_{\rm acc} \propto {\rm M}_{disk}{}^{1.1(\pm0.3)}$, con una dispersión menor que 1 dex para la mayoría de estrellas, similar a lo que ocurre en las CTT una vez se las clasifica según muestren o no discos de transición (Najita et al. 2007).

– La mayoría de estrellas en nuestra muestra con signos de aclaramiento del polvo del disco interno (el exceso IR comienza en la banda K o a longitudes de onda más largas) muestra tasas de acreción y masas de disco menores que las del resto de objetos. Esto contrasta con resultados previos para estrellas T Tauri de transición, y podría estar sugiriendo que un proceso físico diferente -tal como la fotoevaporación- juega un papel fundamental disipando los discos en las HAeBes.

– Hemos extendido al régimen HAeBe el desacuerdo previamente publicado entre las masas de disco obtenidas a partir de la emisión del polvo frío y a partir de la acreción. Son necesarios esfuerzos adicionales para romper esta inconsistencia, muy probablemente en relación con el modo en que las masas de disco son estimadas a partir de medidas mm.

6.3 Future perspectives

Two future possible research lines related to -and somehow boosted by- the results of this thesis are summarized as follows:

- *Analysis of the accretion rate variability and its relation with the changes of the accretion rate tracers.* Although important achievements in this topic have been obtained in this thesis (chapter 4), those were limited by the sensitivity and wavelength coverage of the data. Multi-epoch, high resolution spectra covering simultaneously the Balmer excess region and the wavelengths where the accretion tracers are located (UV-optical-nIR) are necessary to find the best spectroscopic tracer of accretion among the different possibilities. This issue is better addresed by looking for correlations between the changes in the accretion rate from the Balmer excess and the simultaneous variations of the line luminosities, rather than relating single-epoch data for a sample of stars, since the latter approach could be affected by the influence of the stellar luminosity. The result from this research will unify criteria for accretion rate surveys, and is necessary to carry out future studies on the accretion rate variability over wide samples. The observing campaign "Multi-epoch observations of intermediate-mass pre-main sequence stars: accretion rates and accretion tracers." (088.C-0218, Mendigutía et al.) in the new spectrograph XShooter (VLT) has been awarded 18.5 hours with priority A, from October 2011 to March 2012. Multi epoch spectra with an unprecedented resolution and wavelength coverage will result from the observations, that will be devoted to analyse the problem outlined above. In addition, possible differences between the variability behaviour shown by HAe and HBe stars included in the sample could provide hints on the different accretion rate mechanisms pointed out in this thesis. The observations could be complemented in the future including lower mass stars.

- *Disk dissipation mechanisms in pre-main sequence stars: Looking for disks harbouring protoplanets.* Circumstellar disks can be dissipated through various physical processes including grain growth, dust settling or photoevaporation, planet formation being an additional mechanism may or may not happen (chapter 5). The relative importance of the different processes and their possible dependence on the stellar age and mass is object of active debate: does the dominant dissipating process change depending on the stellar age? do low-mass pre-main sequence stars clear their disks through processes different from those in their massive counterparts? Last but not least, what is the range of stellar ages and masses where disk dissipation is mainly caused by planet

formation?. Although these issues have been partially answered in this thesis, the questions raised have to be addressed comparing the accretion rates shown by transition and non-transition disks from a wide sample of pre-main sequence stars. In particular, the relative position of the stars in the mass accretion rate-disk mass plane is of great value, as discussed in section 1.3 and chapter 5.

Accretion rates over wide samples can easily and homogeneously be estimated from the Hα luminosity, not only for low-mass objects but now also for HAeBe stars (chapter 4). Accretion estimates will also benefit from the XShooter research described above. In this way, the full range of stellar masses where disks could be long-lived enough to form planets can be sampled for the first time. Disk masses can be estimated from millimetric measurements or from SED modelling. SED analysis is also necessary to classify the stars as having transition or non-transition disks, and the possible dependence of the clearing processes on the stellar age can be analysed from data of different star forming regions. This research therefore requires Hα measurements and multi-wavelength photometry for a wide sample of PMS stars. These can be collected from public surveys and published results, and could be complemented with additional observations.

The statistical analysis of the accretion rates and disk masses shown by transition and non-transition disks will lead to conclusions on mass-dependent disk dissipation, considering different objects in each star forming region, and on age-dependent disk clearing, comparing data from different star forming regions. It will answer the question of what stars are the best candidates to look for active planet formation in their disks, generating a sample in this sense. This information is important for an efficient use of the new generation of telescopes and instruments (e.g. ALMA, SPHERE at VLT), which will be able to make direct observations of planets in their formation sites (e.g. Huélamo et al. 2011). It will also provide the first relevant statistics on planet formation probabilities in circumstellar disks. Therefore, the project will be a first step for a future comparison between the growing statistics on exoplanets around MS stars (e.g. from data obtained with Corot or Kepler; see Traub 2011) and that on the probability of planet formation in disks around young stars. Our understanding of planetary formation and our own Solar System requires from such type of links between disks that are forming planets and stars surrounded by already formed planets.

Appendix A

Tables with multi-epoch line EWs and fluxes

Table A.1 shows the equivalent widths and their uncertainties (EW and δEW, respectively) for the indicated spectroscopic lines. For the Hα line, the profile shape according to the Reipurth et al. (1996) classification scheme, the width of the wings at 10% of peak intensity and its uncertainty (W_{10} and δW_{10}) are also given. "..." indicates that the spectroscopic line is not detected in any of the spectra of the star considered. When a line is measured only in several spectra of a given object, upper limits are shown for the non-detections.

Table A.2 shows the line fluxes and their uncertainties (F and δF, respectively, in erg cm^{-2} s^{-1}) derived from the equivalent widths in Table A.1 and the simultaneous V and R magnitudes from Oudmaijer et al. (2001). Flux uncertainties come from the propagation of the individual errors in the EWs and the magnitudes. Italic numbers refer to lines seen in absorption. "..." indicates that the line is not detected in any of the spectra of the corresponding star for which the fluxes can be derived. When a line is measured only in several spectra of a given object, upper limits are shown for the non-detections.

Table A.1: Equivalent widths, Hα widths at 10% of peak intensity and Hα profile types on different observing Julian Dates.

Star	JD (+2450000)	EW Hα (Å)	δEW Hα (Å)	W_{10} Hα (km/s)	δW_{10} Hα (km/s)	profile type Hα ...	EW [OI]6300 (Å)	δEW [OI]6300 (Å)	EW HeI5876 (Å)	δEW HeI5876 (Å)	EW $NaID_2$ (Å)	δEW $NaID_2$ (Å)	EW $NaID_1$ (Å)	δEW $NaID_1$ (Å)
HD 31648	1111.53	-17	1	>485	2	IIIB	...	...	-0.35	0.05	-0.61	0.03	-0.68	0.04
	1113.62	-20.6	0.5	635	7	IIIB	...	...	-0.58	0.07	-0.80	0.05	-0.73	0.02
	1114.60	-17.2	0.5	664	3	IIIB	...	...	-0.26	0.09	-0.58	0.02	-0.56	0.03
	1115.64	-19.7	0.1	632	4	IIIB	...	...	-0.52	0.05	-0.68	0.02	-0.70	0.03
	1208.43	-18.1	0.1	>440	2	IIIB	...	...	-0.30	0.05	-0.49	0.03	-0.58	0.03
	1209.44	-20.6	0.6	627	9	IIIB	...	...	-0.31	0.05	-0.63	0.02	-0.47	0.02
	1210.45	-22.6	0.5	>415	2	IIIB	...	...	-0.6	0.1	-0.68	0.03	-0.56	0.02
HD 34282	1111.64	-3.9	0.3	608	18	IIIR	...	...	0.15	0.04	0.12	0.02	0.08	0.02
	1112.68	-5.4	0.2	660	6	IIIR	...	...	0.13	0.03	0.10	0.02	0.06	0.02
	1113.67	-5.1	0.2	665	9	IIIR	...	...	0.25	0.05	0.09	0.02	0.04	0.02
	1114.65	-6	2	>352	15	IIIRm	...	...	0.19	0.06	0.09	0.02	0.05	0.02
	1115.77	-2.9	0.3	716	18	IIIRm	...	...	0.17	0.06	0.08	0.02	0.05	0.02
	1208.45	-5.3	0.5	678	37	IIB	...	...	0.12	0.03	0.09	0.02	0.06	0.02
	1209.46	-5.7	0.4	621	23	IIB	...	...	0.24	0.06	0.13	0.02	0.09	0.02
	1210.46	-5.2	0.2	720	12	IIB	...	...	0.18	0.06	0.10	0.02	0.06	0.02
HD 34700	1111.64	-2.5	0.1	351	11	I	...	...	...	...	0.09	0.02	0.09	0.03
	1112.19	-2.8	0.1	380	11	I	...	...	...	...	0.09	0.02	0.08	0.02
	1113.00	-2.0	0.1	353	10	I	...	...	...	...	0.05	0.02	0.06	0.02
	1114.65	-2.1	0.2	334	13	I	...	...	...	...	0.09	0.02	0.08	0.02
	1208.46	-2.6	0.1	373	9	I	...	...	...	...	0.10	0.02	0.08	0.02
	1209.46	-2.8	0.3	367	22	I	...	...	...	...	0.11	0.02	0.08	0.02
	1210.46	-2.3	0.1	327	7	I	...	...	...	...	0.08	0.02	0.07	0.02
HD 58647	1208.62	-11.3	0.4	610	10	IIR	-0.10	0.02	-0.12	0.05	0.14	0.02	0.12	0.02
	1209.54	-11.1	0.6	619	14	IIR	-0.05	0.02	-0.13	0.05	0.18	0.02	0.15	0.02
	1210.62	-11.8	0.4	619	6	IIR	-0.04	0.02	-0.13	0.05	0.12	0.02	0.11	0.02
HD 141569	0948.49	-6.2	0.3	658	11	IIR	-0.15	0.06	...	...	0.06	0.01	0.07	0.02
	0949.49	-6.0	0.3	649	14	IIR	-0.13	0.06	...	...	0.12	0.03	0.13	0.04
	0950.42	-6.0	0.3	649	14	IIR	-0.14	0.06	...	...	0.12	0.03	0.16	0.04
	0951.51	-6.0	0.5	638	17	IIR	-0.08	0.04	...	...	0.12	0.02	0.09	0.02
	1024.40	-6.2	0.4	636	14	IIR	-0.13	0.07	...	...	0.10	0.01	0.10	0.02
	1025.37	-6.1	0.5	641	25	IIR	-0.17	0.06	...	...	0.12	0.02	0.18	0.05
	1026.37	-6.1	0.2	632	10	IIR	-0.19	0.06	...	...	0.11	0.02	0.10	0.02
	1208.70	-5.3	0.6	623	13	IIR	-0.18	0.04	...	...	0.09	0.02	0.06	0.02
	1209.73	-5.9	0.3	649	14	IIR	-0.14	0.06	...	...	0.08	0.01	0.04	0.01
	1210.72	-5.7	0.3	636	14	IIR	-0.11	0.06	...	...	0.05	0.01	0.04	0.01
HD 142666	0948.50	-2.8	0.3	>399	11	IIIR	0	0.03	0.07	0.03	0.18	0.02	0.16	0.02
	0949.49	-2.7	0.3	>411	8	IIIR	0	0.03	0.14	0.06	0.18	0.03	0.16	0.03
	0950.58	-3.1	0.3	>364	10	IIIR	0	0.03	0.15	0.04	0.25	0.02	0.19	0.04
	0951.54	-5.0	0.3	>406	7	IIIR	0	0.03	0.30	0.05	0.21	0.03	0.21	0.05
	1023.39	-3.9	0.3	720	15	IIIRm	0	0.03	0.25	0.05	0.21	0.01	0.19	0.01
	1024.49	-3.3	0.3	675	18	IIIRm	0	0.03	0.22	0.06	0.22	0.02	0.21	0.02
	1025.38	-3.1	0.2	618	15	IIIRm	-0.04	0.02	0.25	0.07	0.26	0.02	0.24	0.02
	1026.38	-4.0	0.2	698	10	IIIRm	-0.04	0.02	0.37	0.06	0.28	0.02	0.25	0.03
	1208.74	-5.5	0.4	584	15	IIR	0	0.03	0.11	0.03	0.18	0.02	0.14	0.02
	1209.74	-4.8	0.2	544	11	IIB	-0.04	0.03	0.08	0.03	0.17	0.02	0.13	0.02
	1210.23	-5.2	0.4	517	16	IIB	0	0.03	0.18	0.05	0.14	0.02	0.13	0.02
HD 144432	0948.58	-13.9	0.4	>386	2	IIIB	0	0.02	-0.6	0.2	-0.53	0.08	-0.42	0.05

Table A.1: continued.

Star	JD (+2450000)	EW Hα (Å)	δEW Hα (Å)	W_{10} Hα (km/s)	δW_{10} Hα (km/s)	profile type Hα ...	EW [OI]6300 (Å)	δEW [OI]6300 (Å)	EW HeI5876 (Å)	δEW HeI5876 (Å)	EW $NaID_2$ (Å)	δEW $NaID_2$ (Å)	EW $NaID_1$ (Å)	δEW $NaID_1$ (Å)
	0949.52	-11.4	0.3	>360	1	IIIB	0	0.02	-0.19	0.07	-0.28	0.05	-0.25	0.05
	0950.59	-12.7	0.4	>369	1	IIIB	0	0.02	-0.4	0.1	-0.41	0.06	-0.31	0.06
	0951.55	-12.9	0.9	>343	4	IIIB	0	0.02	-0.4	0.1	-0.32	0.06	-0.25	0.06
	1023.42	-11.2	0.6	576	6	IIIB	-0.04	0.02	-0.16	0.07	-0.16	0.04	-0.45	0.09
	1024.40	-12	1	534	9	IIIB	-0.03	0.02	-0.16	0.07	-0.08	0.03	-0.31	0.09
	1025.39	-10.7	0.3	583	6	IIIB	-0.04	0.02	-0.2	0.1	-0.04	0.02	-0.17	0.05
	1026.38	-9.6	0.3	568	6	IIIB	-0.03	0.02	-0.11	0.08	0.08	0.02	0	0.09
	1208.76	-12.5	0.4	>381	3	IIIB	0	0.02	-0.2	0.1	-0.31	0.05	-0.25	0.05
	1209.75	-11.7	0.4	>352	3	IIIB	0	0.02	-0.4	0.1	-0.24	0.04	-0.23	0.05
	1210.74	-11.2	0.4	>395	3	IIIB	0	0.02	-0.21	0.07	-0.31	0.05	-0.22	0.05
HD 150193	0949.53	-13.1	0.1	>424	5	IIIB	...	...	-0.3	0.1	-0.33	0.08	-0.26	0.08
	0950.59	-14	1	491	8	IIIB	...	...	-0.22	0.08	-0.43	0.07	-0.32	0.08
	0951.56	-14.8	0.4	528	3	IIIB	...	...	-0.12	0.09	-0.32	0.06	-0.25	0.07
HD 163296	0948.59	-23	1	731	8	IIIB	0	0.02	0.70	0.05	-0.47	0.03	-0.54	0.05
	0949.59	-24.3	1	744	6	I	0	0.02	0.36	0.05	-0.43	0.04	-0.49	0.05
	0950.62	-22.0	0.8	700	4	I	0	0.02	0.84	0.07	-0.29	0.04	-0.29	0.05
	0951.60	-21.9	0.2	695	8	I	0	0.02	-0.30	0.06	-0.49	0.06	-0.49	0.06
	1023.46	-23.1	0.7	733	6	IIIB	-0.03	0.01	-0.4	0.1	-0.78	0.07	-0.54	0.06
	1024.46	-22.5	0.6	712	6	IIIB	-0.04	0.02	0.48	0.07	-0.40	0.04	-0.33	0.04
	1024.53	-23.2	0.8	733	6	IIIB	-0.05	0.02	0.57	0.05	-0.20	0.03	-0.19	0.03
	1025.43	-25	1	706	6	IIIB	-0.05	0.02	-0.6	0.1	-0.66	0.05	-0.73	0.04
	1025.49	-25.4	0.7	683	6	IIIB	-0.05	0.02	-0.32	0.06	-0.66	0.06	-0.58	0.06
	1026.42	-20.6	0.8	592	6	IIIB	-0.02	0.01	0.45	0.05	-0.39	0.04	-0.44	0.05
	1026.48	-19.7	0.5	557	2	IIIB	-0.04	0.01	0.35	0.04	-0.45	0.04	-0.47	0.04
HD 179218	0949.64	-12.8	0.8	464	4	I	-0.03	0.01	0.05	0.01	-0.04	0.01	-0.02	0.01
	0950.64	-14.0	0.2	484	3	I	-0.04	0.01	0.03	0.01	-0.06	0.01	-0.01	0.01
	0951.65	-14.0	0.2	478	3	I	-0.01	0.01	-0.08	0.03	-0.04	0.01	-0.06	0.01
HD 190073	0948.73	-25.3	0.9	411	2	I	0	0.02	-0.50	0.06	-1.09	0.05	-0.85	0.04
	0949.64	-25.1	0.9	407	1	I	0	0.02	-0.51	0.07	-1.02	0.05	-0.85	0.04
	0950.65	-24.4	0.8	397	2	I	0	0.02	-0.53	0.08	-1.00	0.04	-0.82	0.04
	0951.65	-23.6	0.6	379	2	IVB	0	0.02	-0.52	0.06	-1.02	0.05	-0.85	0.04
	1023.53	-26	1	381	2	IVB	-0.07	0.02	-0.37	0.04	-1.04	0.06	-0.92	0.07
	1024.55	-26.0	0.8	378	2	IVB	-0.06	0.01	-0.45	0.06	-0.96	0.04	-0.84	0.05
	1025.51	-27.0	0.8	389	2	IVB	-0.06	0.02	-0.44	0.06	-1.00	0.05	-0.83	0.04
	1026.51	-27.6	0.7	387	1	IVB	-0.06	0.02	-0.42	0.07	-1.01	0.04	-0.85	0.04
AS 442	0949.66	-36.1	0.7	669	5	IIIB	-0.08	0.04	0.11	0.03	0.88	0.02	0.70	0.02
	0950.66	-34.3	0.6	649	5	IIIB	-0.12	0.05	0.22	0.09	0.86	0.02	0.72	0.02
	0951.66	-36.2	0.7	680	5	IIIB	-0.08	0.04	0.29	0.06	0.89	0.02	0.74	0.02
	1023.56	-27.2	0.5	614	6	IIIB	-0.10	0.04	0.14	0.05	0.53	0.03	0.49	0.01
	1024.59	-30	1	616	5	IIIB	-0.06	0.04	0.20	0.06	0.62	0.03	0.52	0.02
VX Cas	1023.69	-50	4	559	8	IIR	-0.54	0.05	0.20	0.05	0.49	0.02	0.41	0.02
	1024.72	-37	3	554	6	IIR	-0.44	0.05	0.4	0.1	0.70	0.05	0.7	0.1
	1025.70	-24	2	638	11	IIR	-0.33	0.06	0.84	0.09	1.26	0.07	0.95	0.05
	1026.69	-20	1	635	5	IIR	-0.20	0.06	0.8	0.1	0.60	0.04	0.5	0.1
	1111.52	-16.7	0.6	738	4	IIB	-0.11	0.04	0.31	0.07	0.30	0.02	0.26	0.02
	1112.54	-18.0	0.7	671	7	IIB	-0.13	0.02	0.36	0.06	0.31	0.02	0.28	0.04
	1113.52	-16.0	0.8	707	9	IIR	-0.08	0.03	0.93	0.07	0.34	0.02	0.33	0.03
	1114.51	-15.9	0.4	828	17	IIB	-0.13	0.03	0.67	0.06	0.37	0.02	0.32	0.02

Table A.1: continued.

Star	JD (+2450000)	EW Hα (Å)	δEW Hα (Å)	W_{10} Hα (km/s)	δW_{10} Hα (km/s)	profile type Hα ...	EW [OI]6300 (Å)	δEW [OI]6300 (Å)	EW HeI5876 (Å)	δEW HeI5876 (Å)	EW $NaID_2$ (Å)	δEW $NaID_2$ (Å)	EW $NaID_1$ (Å)	δEW $NaID_1$ (Å)
	1115.50	-15.4	0.6	757	9	IIR	-0.14	0.02	0.70	0.08	0.36	0.02	0.32	0.02
	1209.36	-14.7	0.7	535	7	IIR	-0.15	0.02	0.9	0.1	0.67	0.03	0.61	0.05
	1210.36	-15.6	0.8	529	7	IIIR	-0.06	0.02	0.60	0.08	0.46	0.04	0.42	0.07
BH Cep	0949.70	-5.5	0.2	779	10	IIR	-0.04	0.02	0.20	0.09	0.42	0.03	0.41	0.09
	0950.70	-6.2	0.1	619	2	IIIR	0	0.03	0.4	0.1	0.52	0.04	0.41	0.04
	0951.73	-5	1	788	33	IIIR	0	0.03	0.3	0.2	0.60	0.05	0.5	0.2
	1023.60	-4.6	0.1	645	13	IIR	0	0.03	0.4	0.1	0.73	0.03	0.54	0.03
	1024.65	-5.6	0.5	599	23	IIIR	-0.02	0.01	0.6	0.1	0.64	0.04	0.7	0.3
	1025.59	-4.2	0.5	603	33	IIIR	-0.02	0.01	0.71	0.08	0.54	0.03	0.42	0.02
	1026.56	-4.0	0.3	678	9	IIIR	0	0.03	0.53	0.07	0.53	0.01	0.42	0.01
	1111.41	-11.1	0.6	650	6	IIR	-0.06	0.03	0.24	0.08	0.30	0.03	0.25	0.02
	1111.49	-12.6	0.4	665	7	IIR	-0.03	0.01	0.3	0.1	0.34	0.02	0.27	0.03
	1112.36	-6.6	0.2	766	9	IIRm	-0.04	0.02	0.60	0.09	0.57	0.03	0.44	0.07
	1112.46	-6.2	0.2	801	8	IIRm	-0.03	0.01	0.61	0.09	0.57	0.02	0.43	0.08
	1113.36	-4.7	0.3	720	6	IIIBm	-0.03	0.01	0.17	0.04	0.32	0.02	0.25	0.02
	1113.49	-4.5	0.2	692	7	IIIBm	-0.02	0.01	0.18	0.07	0.28	0.02	0.23	0.02
	1114.37	-6.5	0.2	709	9	IIBm	-0.07	0.02	0.10	0.03	0.26	0.02	0.21	0.02
	1114.49	-6.8	0.3	728	13	IIIBm	-0.05	0.02	0.07	0.03	0.24	0.01	0.20	0.01
	1115.37	-6.6	0.2	709	10	IIIBm	-0.05	0.02	0.31	0.05	0.22	0.01	0.20	0.01
	1209.33	-5.3	0.2	742	6	IIR	0	0.03	0.45	0.06	0.34	0.02	0.37	0.05
BO Cep	0949.71	-9.6	0.3	647	4	IIR	-0.21	0.09	0.16	0.04	0.30	0.05	0.22	0.02
	0950.71	-7.6	0.2	623	5	IIB	-0.19	0.08	0.26	0.09	0.29	0.05	0.22	0.03
	0951.72	-9.2	0.4	614	15	IIR	-0.15	0.07	0.05	0.03	0.23	0.03	0.18	0.03
	1023.61	-3.9	0.2	663	12	IIR	-0.15	0.08	0.22	0.07	0.28	0.04	0.23	0.03
	1024.67	-5.1	0.2	568	12	IIIRm	-0.11	0.07	0.22	0.09	0.41	0.05	0.33	0.09
	1025.60	-7.4	0.3	476	4	IIIR	-0.17	0.08	0.32	0.08	0.34	0.04	0.23	0.04
	1026.68	-7.4	0.1	562	3	IIR	-0.10	0.09	0.67	0.09	0.42	0.04	0.34	0.02
	1111.42	-8.5	0.2	658	9	IIR	-0.19	0.08	0.12	0.06	0.20	0.02	0.18	0.02
	1112.46	-9.2	0.3	775	7	IIR	-0.19	0.09	0.57	0.08	0.20	0.02	0.15	0.02
	1113.45	-8.9	0.3	729	7	IIR	-0.21	0.08	0.40	0.07	0.11	0.02	0.11	0.02
	1114.43	-6.8	0.3	696	11	IIIRm	-0.22	0.08	0.62	0.08	0.21	0.02	0.18	0.02
	1115.44	-6.9	0.3	660	7	IIIR	-0.16	0.07	0.24	0.06	0.19	0.02	0.16	0.02
	1210.32	-7.5	0.3	720	9	IIRm	-0.13	0.04	0.14	0.04	0.23	0.02	0.20	0.03
SV Cep	0948.71	-11.4	0.3	715	10	IIR	-0.16	0.04	0.16	0.05	0.22	0.02	0.19	0.02
	0949.73	-11.5	0.5	694	11	IIR	-0.14	0.04	0.31	0.07	0.23	0.02	0.2	0.02
	0950.72	-10.8	0.5	678	6	IIB	-0.16	0.05	0.25	0.07	0.23	0.02	0.16	0.03
	0951.71	-11.6	0.4	719	6	IIR	-0.11	0.05	0.34	0.04	0.23	0.02	0.16	0.02
	1023.63	-11.5	0.5	619	7	IIIR	-0.11	0.06	0.72	0.09	0.33	0.02	0.28	0.02
	1024.68	-11.4	0.6	708	14	IIIR	-0.14	0.04	0.20	0.05	0.53	0.03	0.41	0.02
	1025.62	-10.2	0.4	645	8	IIR	-0.12	0.04	0.67	0.09	0.55	0.03	0.50	0.06
	1026.60	-9.9	0.4	638	13	IIR	-0.16	0.05	0.45	0.07	0.45	0.03	0.37	0.03
	1111.44	-13.0	0.2	700	6	IIR	-0.14	0.05	0.52	0.07	0.22	0.02	0.19	0.02
	1112.49	-12.8	0.5	756	10	IIB	-0.13	0.04	0.84	0.09	0.22	0.02	0.21	0.02
	1113.47	-13.4	0.5	776	8	IIB	-0.12	0.05	0.55	0.07	0.21	0.02	0.18	0.02
	1114.45	-12.3	0.3	714	5	IIB	-0.12	0.04	0.61	0.07	0.42	0.02	0.32	0.02
	1115.46	-12.1	0.2	737	7	IIB	-0.11	0.04	0.28	0.05	0.28	0.02	0.24	0.02
	1208.32	-12.1	0.6	774	16	IIR	-0.08	0.04	0.61	0.07	0.28	0.02	0.22	0.02
V1686 Cyg	0948.69	-25.7	0.4	>473	6	IIIB	-0.5	0.2	0.19	0.09	1.74	0.09	0.81	0.06

Table A.1: continued.

Star	JD (+2450000)	EW Hα (Å)	δEW Hα (Å)	W_{10} Hα (km/s)	δW_{10} Hα (km/s)	profile type Hα ...	EW [OI]6300 (Å)	δEW [OI]6300 (Å)	EW HeI5876 (Å)	δEW HeI5876 (Å)	EW $NaID_2$ (Å)	δEW $NaID_2$ (Å)	EW $NaID_1$ (Å)	δEW $NaID_1$ (Å)
	0949.68	-28.0	0.5	>474	6	IIIB	-0.5	0.1	0.08	0.05	1.5	0.1	0.77	0.05
	0950.68	-41.3	0.7	>528	8	IIIB	-0.9	0.2	0	0.09	0.6	0.1	0.22	0.03
	1023.54	-25.4	0.4	>466	5	IIIBm	-0.20	0.09	-0.1	0.07	0.87	0.06	0.41	0.04
	1024.57	-25.5	0.4	>482	5	IIIB	-0.21	0.09	0.31	0.09	0.94	0.07	0.40	0.04
	1025.53	-25.8	0.4	>476	5	IIIB	-0.20	0.08	-0.10	0.06	0.94	0.07	0.33	0.05
	1026.52	-26.5	0.4	>502	12	IIIB	-0.13	0.06	0	0.09	1.15	0.06	0.45	0.05
	1111.36	-29.4	0.6	>476	8	IIIB	-0.22	0.09	-0.10	0.06	1.12	0.07	0.44	0.05
	1112.41	-13.8	0.2	>387	6	IIIBm	-0.26	0.08	0.40	0.07	2.46	0.07	1.61	0.08
	1113.38	-10.6	0.6	>374	10	IIIBm	-0.14	0.07	0.38	0.08	2.53	0.06	1.55	0.06
	1114.39	-10.3	0.2	>408	5	IIIBm	-0.14	0.08	0.53	0.03	2.7	0.1	1.67	0.07
	1115.40	-10.4	0.7	>444	10	IIIBm	-0.24	0.08	0.33	0.09	2.28	0.07	1.7	0.1
R Mon	1208.63	-115	3	824	1	Im	-5.1	0.2	1.2	0.2	-0.15	0.03	-0.46	0.07
	1209.65	-111	3	841	8	Im	-5.0	0.2	1.2	0.3	-0.16	0.02	-0.44	0.08
	1210.64	-115	3	832	10	Im	-4.9	0.2	1.2	0.2	-0.13	0.02	-0.51	0.07
VY Mon	1208.60	-42	1	726	3	IIIB	-2.0	0.1	...	...	2.24	0.09	1.44	0.04
	1209.63	-40	1	719	5	IIIB	-1.9	0.2	...	...	2.34	0.08	1.56	0.05
	1210.63	-41	1	688	6	IIIB	-1.9	0.2	...	...	2.39	0.09	1.6	0.05
51 Oph	0948.62	-3.3	0.1	537	11	IIB	...	...	-0.10	0.04	-0.08	0.03	-0.19	0.04
	0949.59	-3.2	0.2	529	14	IIB	...	...	-0.08	0.04	0	0.03	-0.08	0.04
	0950.61	-3.3	0.1	526	8	IIB	...	...	-0.11	0.06	-0.07	0.03	-0.14	0.04
	0951.59	-3.2	0.2	542	11	IIB	...	...	-0.12	0.04	-0.04	0.03	-0.12	0.04
	1023.45	-3.5	0.2	509	10	IIB	...	...	-0.14	0.04	-0.13	0.02	-0.24	0.05
	1024.45	-3.4	0.2	511	8	IIB	...	...	-0.12	0.05	-0.03	0.01	-0.10	0.02
	1025.42	-3.3	0.2	504	15	IIB	...	...	-0.06	0.02	0.04	0.01	0.03	0.01
	1026.41	-3.4	0.1	509	6	IIB	...	...	-0.08	0.04	-0.04	0.01	-0.11	0.02
KK Oph	0948.61	-69	4	627	6	I	-2.1	0.2	0.4	0.1	0.14	0.04	0.09	0.03
	0949.60	-67	4	616	4	I	-2.0	0.1	0.6	0.1	0.20	0.05	0.26	0.08
	0950.61	-72	3	589	2	Im	-2.8	0.2	-0.22	0.07	-0.32	0.07	-0.15	0.04
	0951.58	-76	5	594	3	Im	-2.7	0.2	0.29	0.09	-0.4	0.1	-0.21	0.06
	0951.64	-67	2	557	5	Im	-2.3	0.2	0.4	0.1	-0.4	0.2	-0.20	0.06
	0951.68	-79	3	611	2	I	-2.4	0.1	0.4	0.1	-0.3	0.1	-0.14	0.04
	1023.44	-96	3	537	3	IIR	-3.3	0.2	0.38	0.09	-0.5	0.1	-0.40	0.09
	1024.44	-89	6	574	1	IIR	-3.0	0.2	0.7	0.1	0.30	0.04	0.35	0.08
	1025.41	-67	5	702	5	IIR	-1.8	0.1	0.36	0.08	0.71	0.06	0.68	0.06
	1026.41	-61	5	664	11	IIB	-1.7	0.1	0.6	0.1	0.61	0.05	0.62	0.08
T Ori	1111.72	-23	1	712	6	IIR	-0.14	0.03	0.56	0.07	0.67	0.02	0.48	0.03
	1112.73	-34	2	690	6	IIR	-0.22	0.03	0.50	0.05	0.53	0.02	0.35	0.02
	1114.72	-20.7	0.8	639	7	IIR	-0.10	0.02	0.41	0.05	0.42	0.02	0.29	0.02
	1115.76	-23.0	0.3	626	9	IIR	-0.16	0.04	0.61	0.06	0.57	0.02	0.41	0.03
	1208.53	-16.0	0.2	711	6	IIR	-0.10	0.03	0.92	0.06	0.28	0.02	0.19	0.02
	1209.55	-17.1	0.5	687	5	IIR	-0.11	0.02	0.56	0.05	0.27	0.02	0.20	0.03
	1210.55	-17.9	0.4	659	4	IIR	-0.11	0.02	0.50	0.05	0.22	0.02	0.16	0.02
BF Ori	1111.71	-8.9	0.3	607	4	IIR	-0.05	0.02	1.13	0.06	0.24	0.02	0.56	0.04
	1112.64	-9.6	0.3	692	4	IIB	-0.05	0.01	0.53	0.05	0.74	0.01	0.65	0.02
	1113.69	-10.6	0.4	776	9	IIR	-0.07	0.02	0.42	0.07	0.58	0.02	0.46	0.01
	1114.67	-11	1	850	13	IIB	-0.04	0.01	0.47	0.03	0.99	0.01	0.78	0.01
	1115.66	-9	1	733	11	IIR	-0.05	0.02	0.72	0.08	0.66	0.02	0.48	0.03
	1208.53	-9.7	0.3	753	8	IIR	-0.04	0.01	0.76	0.08	0.51	0.02	0.35	0.02

Table A.1: continued.

Star	JD (+2450000)	EW Hα (Å)	δEW Hα (Å)	W_{10} Hα (km/s)	δW_{10} Hα (km/s)	profile type Hα ...	EW [OI]6300 (Å)	δEW [OI]6300 (Å)	EW HeI5876 (Å)	δEW HeI5876 (Å)	EW $NaID_2$ (Å)	δEW $NaID_2$ (Å)	EW $NaID_1$ (Å)	δEW $NaID_1$ (Å)
	1209.54	-9.9	0.2	815	8	IIR	-0.04	0.01	0.55	0.07	0.65	0.03	0.49	0.05
	1210.52	-10.6	0.3	786	4	IIR	-0.04	0.01	0.67	0.06	0.50	0.02	0.33	0.02
	1210.58	-10.0	0.3	758	7	IIR	-0.02	0.01	0.75	0.07	0.53	0.02	0.36	0.03
CO Ori	1111.57	-16.6	0.5	566	30	Im	-0.13	0.03	0	0.07	0.64	0.04	0.46	0.04
	1112.57	-21.0	0.6	548	6	Im	-0.26	0.04	0	0.07	0.22	0.02	0.18	0.02
	1113.56	-23	1	562	8	I	-0.34	0.06	0	0.07	0.09	0.02	0.11	0.02
	1114.54	-21	1	502	6	I	-0.29	0.04	0.22	0.07	0.17	0.01	0.21	0.02
	1115.55	-21	1	522	9	I	-0.35	0.05	0.11	0.07	0.22	0.02	0.21	0.02
	1208.48	-20.9	0.6	518	5	I	-0.33	0.05	0.13	0.06	0.37	0.04	0.32	0.06
	1209.49	-25.1	0.7	586	6	I	-0.34	0.07	0	0.07	0.37	0.04	0.34	0.05
	1210.48	-21.4	0.7	584	7	Im	-0.29	0.07	0.08	0.04	0.39	0.03	0.36	0.03
HK Ori	1111.68	-63	1	599	4	IIB	-1.4	0.1	0.53	0.05	0.53	0.04	0.52	0.05
	1112.74	-61	1	533	4	IIR	-1.4	0.1	0.58	0.05	0.47	0.04	0.44	0.06
	1113.66	-21	2	530	7	I	-0.5	0.1	0	0.09	-0.36	0.03	-0.19	0.06
	1114.71	-63	1	578	1	IIR	-1.4	0.1	0.53	0.05	0.35	0.03	0.41	0.04
	1115.68	-71	3	567	4	IIR	-1.5	0.1	0.30	0.09	0.30	0.05	0.27	0.06
	1208.49	-58	1	630	1	IIB	-1.33	0.09	0.4	0.1	0.14	0.02	0.16	0.03
	1209.50	-59	1	624	4	IIB	-1.4	0.1	0.48	0.06	0.22	0.03	0.21	0.04
	1210.51	-65	3	595	5	IIB	-1.29	0.08	0.36	0.09	0.41	0.05	0.39	0.05
NV Ori	1111.77	-4.4	0.2	473	10	Im	0	0.02	0.19	0.05	-0.27	0.03	-0.20	0.02
	1112.72	-4.0	0.3	546	10	IIIR	0	0.02	0	0.07	-0.26	0.04	-0.23	0.03
	1113.76	-3.9	0.1	616	8	IIR	0	0.02	0.13	0.05	-0.19	0.03	-0.28	0.06
	1114.74	-3.9	0.1	627	1	IIR	0	0.02	0.30	0.07	-0.20	0.03	-0.16	0.04
	1115.74	-3.8	0.1	633	7	IIIR	0	0.02	0.26	0.06	-0.16	0.03	-0.13	0.02
	1208.52	-3.8	0.2	697	16	IIB	-0.04	0.02	0.18	0.05	-0.18	0.02	-0.25	0.03
	1209.53	-4.3	0.1	654	7	IIR	-0.03	0.01	0.20	0.04	-0.24	0.02	-0.27	0.03
	1210.54	-3.8	0.2	618	13	IIIR	-0.03	0.01	0.30	0.06	0.28	0.02	0.22	0.04
RY Ori	1112.76	-19.4	0.6	585	4	IIR	-0.17	0.06	0.7	0.1	1.00	0.04	1.10	0.06
	1113.74	-14.3	0.4	588	8	IIB	-0.06	0.03	0.33	0.08	0.76	0.03	0.73	0.03
	1114.68	-11.0	0.3	571	6	IIR	-0.06	0.04	0.46	0.09	0.95	0.04	0.96	0.06
	1115.67	-21.4	0.7	606	6	IIR	-0.11	0.03	0.32	0.06	0.57	0.03	0.62	0.04
	1208.51	-13.8	0.5	616	7	IIR	-0.10	0.04	1.03	0.08	1.11	0.03	1.08	0.04
	1209.52	-13.2	0.4	647	10	IIR	-0.13	0.04	0.5	0.1	1.51	0.04	1.54	0.07
	1210.53	-17.4	0.5	662	6	IIR	-0.20	0.07	0.78	0.08	0.98	0.03	1.03	0.04
UX Ori	1111.61	-13.2	0.2	576	6	IIIB	-0.06	0.02	-0.14	0.05	0.15	0.03	0.27	0.05
	1112.60	-13.0	0.4	772	6	Im	-0.05	0.02	0.15	0.04	-0.29	0.07	-0.02	0.01
	1112.71	-12.8	0.4	740	6	Im	-0.07	0.04	0.24	0.04	-0.25	0.06	-0.04	0.03
	1113.61	-11.3	0.3	687	17	Im	-0.07	0.04	0.21	0.04	-0.29	0.06	-0.16	0.03
	1113.71	-11.8	0.2	744	9	Im	-0.05	0.02	-0.15	0.04	-0.36	0.07	-0.17	0.03
	1114.58	-11.8	0.6	735	6	Im	-0.06	0.02	0.21	0.04	0.22	0.01	0.15	0.02
	1114.70	-11.5	0.2	704	4	Im	-0.05	0.02	0.18	0.03	0.28	0.02	0.18	0.01
	1115.62	-10.7	0.3	777	7	IIBm	-0.04	0.02	0.48	0.04	0.28	0.02	0.19	0.02
	1208.44	-7.4	0.4	730	15	IIRm	-0.07	0.02	0.28	0.05	-0.24	0.05	-0.16	0.03
	1209.45	-6.6	0.3	616	9	IVRm	-0.06	0.02	0.54	0.07	-0.15	0.03	-0.14	0.04
	1209.57	-6.0	0.2	601	9	IVRm	-0.03	0.02	0.49	0.08	-0.14	0.03	-0.12	0.03
	1210.31	-5.5	0.5	532	21	IVR	-0.05	0.02	0.18	0.05	-0.23	0.04	-0.16	0.03
	1210.41	-5.8	0.3	537	14	IVR	-0.04	0.02	-0.07	0.04	-0.25	0.05	-0.16	0.03
	1210.49	-6.3	0.2	554	5	IIIRm	-0.05	0.02	0.06	0.03	-0.30	0.08	-0.15	0.03

Table A.1: continued.

Star	JD (+2450000)	EW Hα (Å)	δEW Hα (Å)	W_{10} Hα (km/s)	δW_{10} Hα (km/s)	profile type Hα ...	EW [OI]6300 (Å)	δEW [OI]6300 (Å)	EW HeI5876 (Å)	δEW HeI5876 (Å)	EW $NaID_2$ (Å)	δEW $NaID_2$ (Å)	EW $NaID_1$ (Å)	δEW $NaID_1$ (Å)
	1210.57	-5.9	0.4	>586	93	IIIRm	-0.03	0.02	0.16	0.05	-0.22	0.06	-0.10	0.03
V346 Ori	1111.66	-3.8	0.7	829	91	IIIRm	...	...	...	...	-0.13	0.04	-0.08	0.02
	1112.70	-4.4	0.8	1056	171	IIIRm	...	...	...	...	0.09	0.02	0.06	0.02
	1113.72	-5	1	972	109	IIIRm	...	...	...	...	0.08	0.02	0.07	0.02
	1114.69	-4.0	0.8	974	141	IIIBm	...	...	...	...	0.10	0.02	0.08	0.03
	1115.73	-4.1	0.6	880	80	IIIRm	...	...	...	...	0.12	0.03	0.09	0.03
	1208.47	-2.9	0.5	871	101	IIIRm	...	...	...	...	0.21	0.02	0.15	0.03
	1209.48	-2.8	0.5	864	145	IIIBm	...	...	...	...	0.23	0.02	0.17	0.03
	1210.47	-2.9	0.8	821	198	IIIBm	...	...	...	...	0.21	0.02	0.16	0.03
V350 Ori	1111.76	-11.8	0.6	729	10	IIR	-0.12	0.03	0.32	0.09	0.67	0.03	0.53	0.05
	1113.77	-11.4	0.5	767	8	IIR	-0.11	0.03	0.39	0.07	0.66	0.03	0.52	0.05
	1114.76	-12.8	0.7	680	10	IIR	-0.12	0.04	0.4	0.1	0.67	0.03	0.53	0.04
	1115.72	-15	1	645	7	IIIR	-0.14	0.02	0.40	0.08	0.63	0.04	0.54	0.07
	1208.54	-8.9	0.9	770	40	IIR	-0.20	0.06	0.23	0.08	0.56	0.04	0.45	0.07
	1209.58	-15	1	731	16	IIIR	-0.13	0.04	0.7	0.1	0.82	0.04	0.85	0.07
	1210.56	-11.3	0.8	730	14	IIIRm	-0.08	0.04	0.53	0.08	0.96	0.04	0.81	0.06
XY Per	1023.72	-10.7	0.7	733	6	IIRm	-0.02	0.01	0.17	0.02	0.46	0.01	0.38	0.01
	1024.73	-8.5	0.3	762	8	IIR	0	0.03	0.32	0.05	0.54	0.02	0.43	0.02
	1025.71	-9.0	0.3	744	6	IIB	-0.03	0.01	0.24	0.04	0.69	0.02	0.52	0.02
	1026.73	-10.7	0.1	704	4	IIBm	0	0.03	0.12	0.02	0.65	0.02	0.48	0.01
	1112.65	-10.1	0.8	713	12	IIR	-0.06	0.03	0.32	0.04	0.51	0.01	0.40	0.01
	1113.57	-11	1	729	12	IIR	-0.08	0.03	0.30	0.03	0.57	0.01	0.43	0.01
	1114.56	-11	1	729	15	IIB	-0.03	0.01	0.35	0.03	0.62	0.01	0.50	0.01
	1115.60	-11	1	706	12	IIB	-0.08	0.03	0.11	0.03	0.57	0.01	0.45	0.01
	1208.37	-8.2	0.7	743	14	IIB	-0.02	0.01	0.30	0.03	0.42	0.01	0.40	0.04
	1209.38	-8.5	0.7	708	11	IIB	-0.04	0.01	0.15	0.03	0.56	0.02	0.48	0.02
	1210.38	-9.4	0.6	720	7	IIB	-0.10	0.03	0.10	0.02	0.43	0.01	0.34	0.01
VV Ser	0949.56	-50.0	0.8	711	6	IIR	-0.6	0.1	0.8	0.1	0.65	0.04	0.47	0.04
	0950.62	-50.2	0.8	701	6	IIR	-0.46	0.07	0.5	0.2	0.79	0.06	0.8	0.1
	0951.61	-47	2	726	6	IIR	-0.43	0.07	0.9	0.1	0.75	0.04	0.61	0.04
	1023.47	-48.9	0.9	704	6	IIR	-0.6	0.1	0.47	0.08	0.68	0.04	0.53	0.04
	1024.48	-51.4	0.8	728	6	IIR	-0.50	0.08	0.6	0.1	0.98	0.05	0.93	0.09
	1024.54	-49	2	736	6	IIR	-0.58	0.09	0.8	0.2	0.86	0.06	0.8	0.1
	1024.61	-48	3	740	7	IIR	-0.59	0.05	0.81	0.08	0.98	0.05	0.87	0.08
	1025.44	-51.0	0.9	673	6	IIB	-0.54	0.08	0.44	0.09	1.08	0.05	0.90	0.08
	1025.50	-52.0	0.9	666	6	IIB	-0.52	0.08	0.3	0.1	1.07	0.05	0.94	0.08
	1025.57	-50.9	0.9	667	6	IIB	-0.56	0.08	0.42	0.06	1.07	0.05	0.95	0.09
	1026.44	-52.0	0.8	685	6	II	-0.51	0.07	0.48	0.05	0.81	0.05	0.69	0.08
	1026.49	-53.9	0.8	679	6	IIB	-0.56	0.06	0.45	0.06	0.82	0.05	0.68	0.09
	1026.56	-52.9	0.8	676	6	IIR	-0.53	0.06	-0.3	0.1	0.78	0.05	0.70	0.08
	1111.30	-48	3	671	6	IIB	-0.6	0.1	0.79	0.09	1.00	0.04	0.83	0.07
	1112.31	-50	3	706	6	IIB	-0.5	0.1	0.4	0.1	0.66	0.04	0.51	0.03
	1113.30	-46	3	673	5	IIB	-0.53	0.08	0.4	0.1	0.66	0.04	0.53	0.04
	1114.31	-44	3	646	5	II	-0.7	0.1	0.65	0.09	0.76	0.04	0.59	0.04
	1115.30	-49	1	727	6	IIB	-0.5	0.1	0.43	0.09	0.61	0.04	0.50	0.05
CQ Tau	1111.74	-3.3	0.1	>272	4	IIIR	-0.05	0.02	0.23	0.06	0.53	0.03	0.39	0.03
	1112.76	-5.1	0.1	670	4	IIIR	-0.04	0.02	0	0.08	0.52	0.03	0.39	0.03
	1113.75	-3.6	0.1	558	3	IIIR	-0.03	0.01	0	0.08	0.30	0.02	0.22	0.02

Table A.1: continued.

Star	JD (+2450000)	EW Hα (Å)	δEW Hα (Å)	W_{10} Hα (km/s)	δW_{10} Hα (km/s)	profile type Hα ...	EW [OI]6300 (Å)	δEW [OI]6300 (Å)	EW HeI5876 (Å)	δEW HeI5876 (Å)	EW $NaID_2$ (Å)	δEW $NaID_2$ (Å)	EW $NaID_1$ (Å)	δEW $NaID_1$ (Å)
	1114.73	-3.7	0.1	577	6	IIR	-0.03	0.01	0.11	0.06	0.32	0.02	0.24	0.02
	1115.69	-4.3	0.1	636	1	IIR	-0.05	0.02	0	0.08	0.32	0.04	0.25	0.02
	1208.56	-7.7	0.2	519	7	IIIR	-0.10	0.02	0.08	0.04	0.35	0.02	0.33	0.04
	1209.60	-6.1	0.2	569	6	IIIR	-0.07	0.02	0.26	0.08	0.48	0.02	0.45	0.04
	1210.59	-4.4	0.2	445	6	Im	-0.08	0.02	0.15	0.07	0.33	0.01	0.34	0.04
RR Tau	1111.73	-32.5	0.6	667	3	IIR	-0.46	0.06	0.20	0.03	0.70	0.02	0.64	0.04
	1112.77	-41.2	0.6	685	4	IIR	-0.56	0.05	0.69	0.03	0.64	0.02	0.60	0.04
	1113.78	-26	1	672	3	IIR	-0.44	0.06	0.40	0.04	1.00	0.03	0.92	0.05
	1114.75	-25.6	0.3	700	5	IIR	-0.34	0.05	0.64	0.04	0.88	0.02	0.76	0.04
	1115.71	-28.5	0.3	660	1	IIR	-0.38	0.05	0.27	0.04	0.66	0.03	0.55	0.04
	1208.57	-18.0	0.2	703	1	IIB	-0.36	0.07	0.31	0.05	0.71	0.05	0.53	0.04
	1209.61	-16.6	0.6	682	5	IIB	-0.30	0.03	0.42	0.05	0.71	0.03	0.60	0.07
	1210.60	-16.6	0.4	694	5	IIB	-0.30	0.03	0.54	0.06	0.77	0.05	0.68	0.07
RY Tau	1111.62	-14.1	0.4	634	2	IIIB	-0.7	0.1	0.25	0.06	0.50	0.04	0.41	0.05
	1112.59	-12.0	0.1	641	2	IIBm	-0.7	0.1	0.30	0.06	0.49	0.04	0.41	0.04
	1113.60	-13.0	0.3	624	4	IIB	-0.7	0.1	-0.19	0.06	-0.18	0.03	-0.19	0.03
	1114.59	-16.2	0.8	664	7	IIB	-0.7	0.1	-0.22	0.06	-0.32	0.06	-0.37	0.05
	1208.40	-19.9	0.4	837	18	IIR	-0.8	0.1	-0.33	0.06	0.44	0.02	0.42	0.02
	1209.41	-16.6	0.2	677	2	IIB	-0.9	0.1	-0.20	0.04	-0.39	0.05	-0.36	0.05
PX Vul	1023.51	-15.8	0.2	598	4	IIIB	-0.08	0.02	0	0.09	0.13	0.01	0.15	0.01
	1024.51	-15.1	0.3	588	4	IIIB	-0.06	0.02	0.24	0.05	0.25	0.02	0.23	0.01
	1025.47	-15.1	0.2	613	2	IIIB	-0.05	0.02	0.39	0.05	0.18	0.01	0.18	0.01
	1026.47	-14.0	0.9	671	7	Im	-0.06	0.02	0.38	0.04	0.16	0.02	0.15	0.02
	1111.34	-13	1	651	9	IIB	-0.11	0.03	0.09	0.02	0.13	0.01	0.14	0.01
	1112.34	-13	1	673	9	IIB	-0.07	0.02	0.14	0.03	0.14	0.01	0.14	0.01
	1113.34	-14.0	0.4	630	6	IIIB	-0.10	0.03	0.27	0.09	0.19	0.01	0.17	0.01
	1114.35	-15	1	598	10	IIIB	-0.09	0.03	0.04	0.02	0.13	0.01	0.13	0.01
	1115.35	15	1	616	7	Im	-0.10	0.02	0.18	0.04	0.21	0.01	0.18	0.01
WW Vul	0948.54	-21.2	0.2	749	6	IIB	-0.05	0.03	0.85	0.06	0.50	0.02	0.32	0.02
	0949.53	-20.8	0.2	713	6	IIB	-0.07	0.01	0.88	0.04	0.69	0.02	0.42	0.02
	0950.54	-19.8	0.2	706	6	IIB	-0.08	0.01	0.52	0.06	0.49	0.02	0.34	0.02
	0951.62	-20.0	0.2	769	8	IIB	-0.07	0.02	0.76	0.05	0.75	0.02	0.48	0.02
	1023.49	-16.5	0.1	747	6	IIB	-0.10	0.03	0.20	0.03	0.50	0.01	0.36	0.01
	1024.50	-17.9	0.4	720	6	IIR	-0.06	0.03	0.66	0.05	0.51	0.01	0.39	0.01
	1025.46	-17.6	0.8	707	9	IIR	-0.12	0.03	0.64	0.05	0.51	0.02	0.38	0.01
	1026.45	-19.2	0.4	742	9	IIR	-0.09	0.03	0.71	0.05	0.39	0.01	0.29	0.01
	1111.32	-17.8	0.7	843	9	IIR	-0.10	0.03	0.97	0.04	1.23	0.01	1.05	0.02
	1112.33	-17.4	0.3	721	5	IIB	-0.11	0.02	0.58	0.04	0.91	0.01	0.76	0.03
	1113.32	-22.8	0.3	728	6	IIB	-0.13	0.02	0.96	0.03	0.79	0.01	0.73	0.02
	1114.33	-17.0	0.1	812	6	IIB	-0.12	0.02	0.90	0.02	0.75	0.01	0.57	0.01
	1115.33	-19.5	0.2	711	8	IIB	-0.09	0.03	0.32	0.04	0.50	0.01	0.40	0.02
LkHa 234	1023.50	-70	1	749	7	IIB	-0.60	0.08	0.58	0.06	1.15	0.05	1.00	0.04
	1024.50	-69	1	812	7	IIB	-0.61	0.08	0.91	0.06	1.08	0.05	0.91	0.05
	1025.50	-61.4	0.9	762	5	IIB	-0.39	0.05	0.82	0.07	2.14	0.07	1.60	0.06
	1026.50	-74	2	776	5	IIB	-0.64	0.09	1.19	0.07	0.97	0.06	0.83	0.07
	1111.39	-64	1	804	5	IIIB	-0.60	0.08	0.81	0.07	-0.2	0.1	-0.25	0.09
	1112.44	-71	2	745	4	IIIB	-0.54	0.08	0.74	0.06	-0.09	0.05	-0.13	0.07
	1113.44	-75	2	722	8	IIB	-0.58	0.08	0.83	0.08	-0.5	0.1	-0.23	0.09

Table A.1: continued.

Star	JD (+2450000)	EW Hα (Å)	δEW Hα (Å)	W_{10} Hα (km/s)	δW_{10} Hα (km/s)	profile type Hα ...	EW [OI]6300 (Å)	δEW [OI]6300 (Å)	EW HeI5876 (Å)	δEW HeI5876 (Å)	EW $NaID_2$ (Å)	δEW $NaID_2$ (Å)	EW $NaID_1$ (Å)	δEW $NaID_1$ (Å)
	1114.42	-73	2	718	6	IIB	-0.57	0.07	0.54	0.07	-0.5	0.1	-0.24	0.07
	1115.43	-72	2	773	5	IIIB	-0.58	0.08	0.87	0.06	-0.7	0.1	-0.3	0.1

Table A.2: Line fluxes on several observing Julian Dates for a subsample of the stars.

Star	JD (+2450000)	F Hα ($\times10^{-12}$)	δF Hα ($\times10^{-12}$)	F [OI]6300 ($\times10^{-14}$)	δF [OI]6300 ($\times10^{-14}$)	F HeI5876 ($\times10^{-14}$)	δF HeI5876 ($\times10^{-14}$)	F $NaID_2$ ($\times10^{-14}$)	δF $NaID_2$ ($\times10^{-14}$)	F $NaID_1$ ($\times10^{-14}$)	δF $NaID_1$ ($\times10^{-14}$)
HD 31648	1111.53	37	3	...	...	78	13	136	14	152	17
	1113.62	48	1	...	...	138	17	191	13	174	7
	1114.60	38	1	...	...	59	21	132	6	128	8
HD 34282	1114.65	1.5	0.5	...	...	*5*	2	2.3	0.5	*1.3*	0.5
	1209.46	1.6	0.1	...	...	*7*	2	3.9	0.6	*2.7*	0.6
HD 34700	1114.65	1.4	0.2	...	...	...	...	*5*	1	*5*	1
HD 58647	1209.54	51	3	23	9	63	24	*87*	10	*73*	10
HD 141569	0949.49	21	2	46	20	...	...	*45*	11	*49*	15
	0950.42	21	2	50	20	...	...	*45*	12	*61*	15
	1024.40	22	2	46	30	...	...	*39*	5	*39*	8
	1209.73	21	1	49	20	...	...	*31*	4	*15*	4
HD 142666	0949.49	2.9	0.5	...	...	*13*	5	*16*	3	*14*	3
	0950.58	3.3	0.5	...	...	*13*	4	*22*	2	*17*	4
	1024.49	3.4	0.5	...	...	*18*	5	*18*	2	*17*	2
HD 144432	0949.52	17.5	0.6	0	3	27	10	40	7	35	7
	0950.59	21.3	0.9	0	3	55	15	61	9	46	9
	1024.40	18	2	4	3	21	9	11	4	41	12
HD 150193	0949.53	12.2	0.4	...	...	22	7	24	6	19	6
	0950.59	13	1	...	...	16	6	32	5	24	6
HD 163296	0949.59	111	5	0	9	*173*	24	206	20	235	25
	0950.62	102	4	0	9	*404*	37	139	20	139	25
	1024.53	103	4	22	9	*266*	29	93	15	89	15
HD 179218	0949.64	36	2	8	3	*15*	3	11	3	6	3
HD 190073	1024.55	51	2	12	2	97	14	207	14	181	15
VX Cas	1024.72	0.76	0.06	0.9	0.1	*0.7*	0.2	*1.2*	0.1	*1.2*	0.2
	1111.52	1.22	0.05	0.8	0.3	*2.2*	0.5	*2.1*	0.2	*1.8*	0.1
	1112.54	1.21	0.08	0.9	0.2	*2.4*	0.4	*2.0*	0.2	*1.8*	0.3
	1113.52	1.16	0.07	0.6	0.2	*6.6*	0.6	*2.4*	0.2	*2.3*	0.2
	1114.51	1.12	0.04	0.9	0.2	*4.7*	0.4	*2.6*	0.2	*2.2*	0.2
	1209.36	0.90	0.04	0.92	0.1	*5.6*	0.6	*4.2*	0.2	*3.8*	0.3
BH Cep	1024.65	0.48	0.07	0.17	0.09	*3.9*	0.8	*4.4*	0.5	*5*	2
	1111.41	0.57	0.04	0.3	0.2	*0.9*	0.3	*1.1*	0.1	*0.9*	0.1
	1112.36	0.46	0.07	0.3	0.1	*3.2*	0.5	*3.0*	0.3	*2.3*	0.4
	1112.46	0.48	0.07	0.23	0.08	*3.7*	0.6	*3.5*	0.3	*2.6*	0.5
	1113.36	0.50	0.06	0.3	0.1	*1.5*	0.3	*2.7*	0.2	*2.1*	0.2
	1113.49	0.46	0.06	0.2	0.1	*1.5*	0.6	*2.3*	0.2	*1.9*	0.2
	1114.37	0.70	0.05	0.8	0.2	*0.9*	0.3	*2.2*	0.2	*1.8*	0.2
BO Cep	1024.67	0.38	0.04	0.8	0.5	*1.4*	0.6	*2.7*	0.4	*2.1*	0.6
	1111.42	0.68	0.04	1.5	0.6	*0.8*	0.4	*1.3*	0.1	*1.2*	0.1
	1112.46	0.69	0.07	1.4	0.7	*3.6*	0.6	*1.3*	0.2	*1.0*	0.1
	1113.45	0.65	0.06	1.5	0.6	*2.4*	0.4	*0.7*	0.1	*0.7*	0.1
	1114.43	0.50	0.03	1.6	0.6	*3.8*	0.5	*1.3*	0.1	*1.1*	0.1
SV Cep	1024.68	1.4	0.1	1.7	0.5	*2.3*	0.6	*6.1*	0.5	*4.7*	0.4
	1111.44	1.70	0.06	1.8	0.7	*5.7*	0.8	*2.4*	0.2	*2.1*	0.2
	1112.49	1.5	0.1	1.6	0.5	*9*	1	*2.3*	0.3	*2.2*	0.3
	1113.47	1.60	0.09	1.4	0.6	*5.8*	0.8	*2.2*	0.2	*1.9*	0.2
	1114.45	1.44	0.05	1.4	0.5	*6.3*	0.7	*4.3*	0.2	*3.3*	0.2
V1686 Cyg	0949.68	0.47	0.01	0.9	0.2	*0.06*	0.04	*1.2*	0.1	*0.60*	0.05

Table A.2: continued.

Star	JD (+2450000)	F Hα ($\times10^{-12}$)	δF Hα ($\times10^{-12}$)	F [OI]6300 ($\times10^{-14}$)	δF [OI]6300 ($\times10^{-14}$)	F HeI5876 ($\times10^{-14}$)	δF HeI5876 ($\times10^{-14}$)	F $NaID_2$ ($\times10^{-14}$)	δF $NaID_2$ ($\times10^{-14}$)	F $NaID_1$ ($\times10^{-14}$)	δF $NaID_1$ ($\times10^{-14}$)
	0950.68	0.47	0.01	1.0	0.2	0	0.1	*0.3*	0.1	*0.12*	0.02
	1024.57	0.60	0.02	0.5	0.2	*0.4*	0.1	*1.2*	0.1	*0.49*	0.06
	1111.36	0.98	0.02	0.7	0.3	0.2	0.1	*1.9*	0.1	*0.76*	0.09
	1113.38	0.36	0.03	0.5	0.2	*0.7*	0.1	*4.5*	0.2	*2.8*	0.1
	1114.39	0.34	0.01	0.5	0.3	*0.9*	0.1	*4.7*	0.2	*2.9*	0.1
VY Mon	1209.63	1.07	0.03	5.1	0.5	...	...	*2.0*	0.2	*1.3*	0.1
51 Oph	0949.00	92	10	...	...	249	127	0	96	249	127
	0950.00	96	10	...	...	343	190	218	96	436	131
	1024.00	95	10	...	...	367	157	92	32	306	67
KK Oph	0949.60	3.6	0.2	10.7	0.7	*2.5*	0.4	*0.8*	0.2	*1.0*	0.3
	0950.61	3.2	0.1	13	1	0.8	0.2	1.1	0.3	0.5	0.1
	1024.44	3.3	0.2	11.2	0.9	*1.6*	0.3	*0.7*	0.1	*0.8*	0.2
T Ori	1111.72	4.7	0.2	2.9	0.6	*9.2*	1	*11.1*	0.4	*7.9*	0.5
	1112.73	5.4	0.3	3.5	0.6	*6.3*	0.7	*6.6*	0.5	*4.4*	0.4
	1114.72	4.1	0.2	2.0	0.4	*6.7*	0.8	*6.9*	0.4	*4.7*	0.4
BF Ori	1111.71	3.2	0.2	1.8	0.7	*42*	3	*8.8*	0.8	*21*	2
	1112.64	3.4	0.3	1.8	0.4	*19*	2	*27*	2	*24*	2
	1113.69	3.4	0.2	2.2	0.6	*14*	2	*18.7*	0.9	*15.0*	0.6
	1114.67	3.6	0.3	1.3	0.3	*16*	1	*34*	1	*26.6*	0.8
CO Ori	1111.57	2.21	0.08	1.7	0.4	0	0.4	*5.1*	0.3	*3.6*	0.3
	1112.57	2.3	0.1	2.9	0.5	0	0.4	*1.4*	0.2	*1.1*	0.1
	1113.56	2.3	0.1	3.4	0.6	0	0.4	*0.5*	0.1	*0.6*	0.1
	1114.54	2.0	0.1	2.8	0.4	*1.2*	0.4	*0.9*	0.1	*1.1*	0.1
	1209.49	2.11	0.06	2.9	0.6	0.0	0.4	*1.8*	0.2	*1.7*	0.2
HK Ori	1111.68	4.61	0.08	10.3	0.8	*3.0*	0.3	*3.0*	0.2	*2.9*	0.3
	1112.74	4.6	0.1	11	1	*3.2*	0.3	*2.6*	0.3	*2.4*	0.4
	1113.66	1.6	0.2	3.8	0.8	0.0	0.4	2.0	0.2	1.1	0.3
	1114.71	4.38	0.07	10.1	0.8	*2.7*	0.3	*1.8*	0.2	*2.1*	0.2
	1209.50	5.19	0.09	12.1	0.9	*3.4*	0.4	*1.6*	0.2	*1.5*	0.3
NV Ori	1111.77	1.6	0.2	0	0.3	*6*	2	9	1	6.3	0.7
	1112.72	1.4	0.3	0	0.3	0	2	8	1	7	1
	1113.76	1.4	0.2	0	0.3	*4*	2	6	1	9	2
	1114.74	1.4	0.1	0	0.3	*9*	2	6	1	5	1
	1209.53	1.4	0.1	0.9	0.3	*6*	1	6.7	0.6	7.5	0.9
RY Ori	1112.76	0.91	0.05	0.8	0.3	*2*	0.3	*3.1*	0.2	*3.4*	0.3
	1113.74	0.79	0.04	0.3	0.2	*1*	0.3	*2.8*	0.2	*2.7*	0.2
	1114.68	0.68	0.03	0.4	0.2	*2*	0.4	*4.0*	0.2	*4.1*	0.3
	1209.52	0.76	0.03	0.8	0.2	*2*	0.4	*5.7*	0.2	*5.8*	0.3
UX Ori	1111.61	3.7	0.1	1.7	0.6	4	1	*3.9*	0.8	*7*	1
	1112.60	3.8	0.3	1.5	0.6	*4*	1	8	2	0.6	0.3
	1113.61	3.6	0.2	2	1	*7*	1	9	2	5	1
	1114.58	3.5	0.2	1.8	0.6	*6*	1	*6.4*	0.3	*4.3*	0.6
	1209.45	2.1	0.1	1.9	0.6	*17*	2	5	1	4	1
V346 Ori	1111.66	0.8	0.2	...	...	...	...	2.9	0.9	1.8	0.4
	1114.69	0.9	0.2	...	...	...	...	*2.3*	0.5	*1.8*	0.7
	1209.48	0.6	0.1	...	...	...	...	*5.3*	0.5	*3.9*	0.7
V350 Ori	1113.77	0.72	0.05	0.7	0.2	*2.1*	0.4	*3.5*	0.2	*2.7*	0.3
	1114.76	0.77	0.05	0.7	0.2	*2.1*	0.5	*3.4*	0.2	*2.7*	0.2

Table A.2: continued.

Star	JD (+2450000)	F Hα ($\times10^{-12}$)	δF Hα ($\times10^{-12}$)	F [OI]6300 ($\times10^{-14}$)	δF [OI]6300 ($\times10^{-14}$)	F HeI5876 ($\times10^{-14}$)	δF HeI5876 ($\times10^{-14}$)	F $NaID_2$ ($\times10^{-14}$)	δF $NaID_2$ ($\times10^{-14}$)	F $NaID_1$ ($\times10^{-14}$)	δF $NaID_1$ ($\times10^{-14}$)
XY Per	1024.73	5.8	0.4	0	2	*21*	4	*35*	3	*28*	2
	1112.65	7.2	0.8	4	2	*19*	3	*31*	2	*24*	2
	1113.57	8.0	0.9	6	2	*19*	2	*36*	1	*28*	1
	1209.38	4.0	0.3	1.9	0.5	*6*	1	*23.4*	0.9	*20.1*	0.9
VV Ser	0949.56	3.87	0.07	4.6	0.8	*3.5*	0.5	*3.0*	0.2	*2.2*	0.2
	0950.62	3.89	0.07	3.6	0.6	*2.5*	0.9	*3.7*	0.3	*3.6*	0.5
	1024.48	3.73	0.07	3.6	0.6	*2.6*	0.5	*4.4*	0.4	*4.1*	0.5
	1111.30	4.3	0.3	5.4	0.9	*3.9*	0.5	*5.0*	0.2	*4.1*	0.4
	1112.31	3.8	0.2	3.8	0.8	*2.1*	0.5	*3.1*	0.3	*2.4*	0.2
	1113.30	3.7	0.2	4.3	0.7	*2.1*	0.5	*3.2*	0.2	*2.5*	0.2
	1114.31	3.6	0.2	5.4	0.8	*3.2*	0.5	*3.7*	0.2	*2.9*	0.2
CQ Tau	1111.74	1.7	0.2	3	1	*10*	3	*23*	2	*17*	1
	1112.76	2.8	0.4	2	1	0	4	*23*	2	*17*	2
	1113.75	2.9	0.3	2.4	0.8	0	4	*20*	2	*15*	1
	1114.73	2.6	0.2	2.1	0.7	*7*	4	*20*	1	*15*	1
	1209.60	2.3	0.1	2.6	0.8	*8*	2	*14.5*	0.7	*14*	1
RR Tau	1111.73	3.51	0.08	5.0	0.7	*1.8*	0.3	*6.5*	0.3	*5.9*	0.4
	1112.77	3.53	0.09	4.8	0.6	*4.8*	0.4	*4.4*	0.3	*4.2*	0.4
	1113.78	3.4	0.1	5.8	0.8	*4.4*	0.5	*11.1*	0.5	*10.2*	0.6
	1114.75	3.32	0.05	4.4	0.7	*7.2*	0.5	*9.9*	0.4	*8.5*	0.5
	1209.61	2.19	0.08	4.0	0.4	*4.8*	0.6	*8.1*	0.4	*6.8*	0.8
RY Tau	1111.62	3.9	0.1	20	3	*4*	1	*8.2*	0.7	*6.7*	0.8
	1112.59	3.5	0.2	20	3	*5*	1	*8.2*	0.8	*6.8*	0.8
	1113.60	3.8	0.2	21	3	3	1	3.1	0.5	3.2	0.5
	1114.59	4.5	0.2	19	3	4	1	5	1	6.0	0.8
	1209.41	4.10	0.07	21	3	2.9	0.6	5.6	0.7	5.2	0.7
PX Vul	1024.51	1.33	0.05	0.5	0.2	*1.5*	0.3	*1.5*	0.2	*1.4*	0.1
	1111.34	1.3	0.1	1.1	0.3	*0.6*	0.1	*0.9*	0.1	*0.9*	0.1
	1112.34	1.2	0.1	0.6	0.2	*0.9*	0.2	*0.9*	0.1	*0.9*	0.1
	1113.34	1.34	0.06	1.0	0.3	*1.8*	0.6	*1.2*	0.1	*1.1*	0.1
	1114.35	1.4	0.1	0.8	0.3	*0.3*	0.1	*0.8*	0.1	*0.8*	0.1
WW Vul	0949.53	2.88	0.07	1.0	0.1	*10.5*	0.6	*8.2*	0.4	*5.0*	0.3
	0950.54	2.59	0.08	1.1	0.1	*6.1*	0.8	*5.8*	0.4	*4.0*	0.3
	1111.32	2.8	0.1	1.6	0.5	*14.3*	0.7	*18.2*	0.5	*15.5*	0.5
	1112.33	2.5	0.1	1.6	0.3	*7.6*	0.7	*11.9*	0.8	*10.0*	0.8
	1113.32	2.65	0.07	1.5	0.2	*9.9*	0.4	*8.2*	0.2	*7.5*	0.3
	1114.33	2.44	0.04	1.7	0.3	*11.8*	0.4	*9.9*	0.3	*7.5*	0.2
LkHa 234	1111.39	2.33	0.04	2.2	0.3	*1.7*	0.2	0.4	0.2	0.5	0.2
	1112.44	2.42	0.08	1.8	0.3	*1.5*	0.2	0.2	0.1	0.3	0.1
	1113.44	2.23	0.06	1.7	0.3	*1.4*	0.1	0.9	0.2	0.4	0.2
	1114.42	2.41	0.07	1.9	0.2	*1.1*	0.1	1.0	0.2	0.5	0.1

Appendix B

Mean spectra and relative variability distributions

For each star and observing campaign, the mean spectra and relative variability distributions are plotted on the left side. The HeI5876, NaID, [OI]6300 and Hα regions are enlarged on the right side, for a better visualization. The mean spectrum is given by $I_{rel,k} = \frac{1}{N} \cdot \sum_{i=1}^{N} I_{i,k}$, and the relative variability by $\sigma_k / I_{rel,k}$, being $\sigma_k = [\frac{1}{(N-1)} \cdot \sum_{i=1}^{N} (I_{i,k} - I_{rel,k})^2]^{1/2}$. The subindex k refers to each spectral bin and the subindex i to each one of the N spectra per observing campaign. The relative variability plots provide information on the strength and wavelength position of the changes in the line intensity (Johns & Basri 1995). Following, it is included the individual spectra taken within a time span of hours (i.e. during the same night) for the five objects monitored on this timescale.

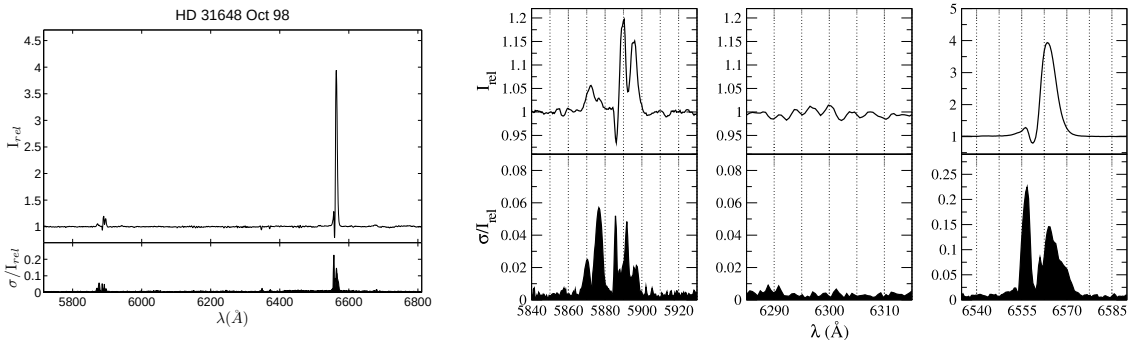
HD 31648 Oct 98
I_{rel}
σ/I_{rel}
$\lambda(\AA)$
I_{rel}
σ/I_{rel}
λ (Å)

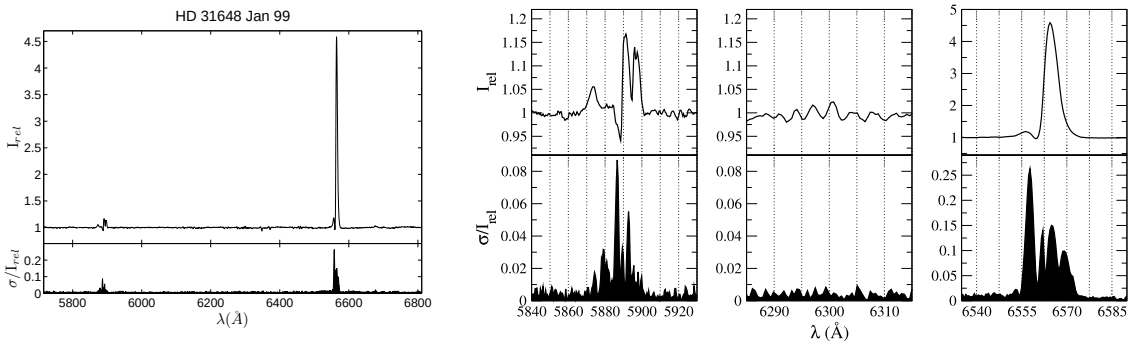
HD 31648 Jan 99
I_{rel}
σ/I_{rel}
$\lambda(\AA)$
I_{rel}
σ/I_{rel}
λ (Å)

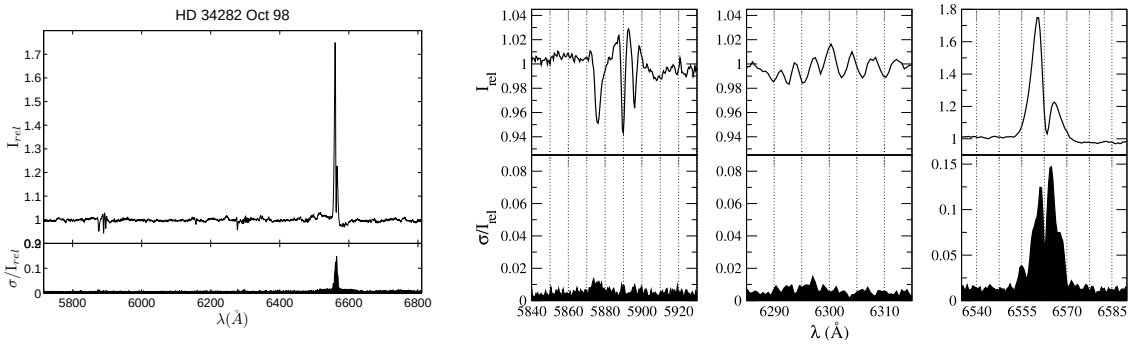
HD 34282 Oct 98
I_{rel}
σ/I_{rel}
$\lambda(\AA)$
I_{rel}
σ/I_{rel}
λ (Å)

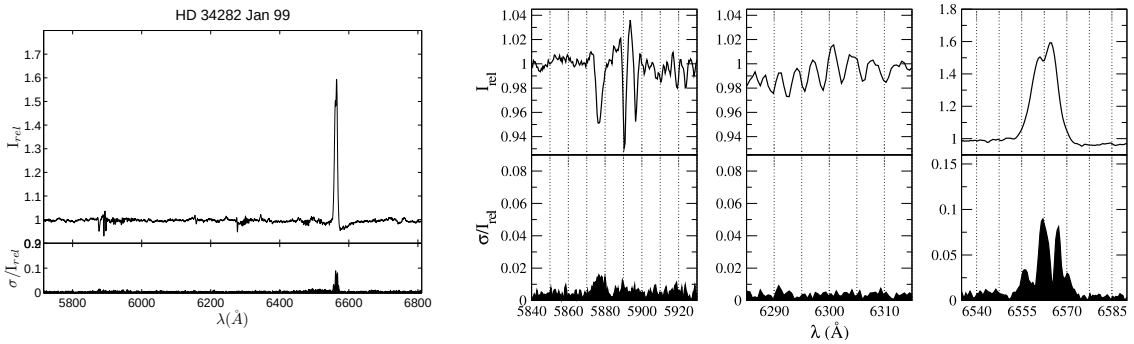
HD 34282 Jan 99
I_{rel}
σ/I_{rel}
$\lambda(\AA)$
I_{rel}
σ/I_{rel}
λ (Å)

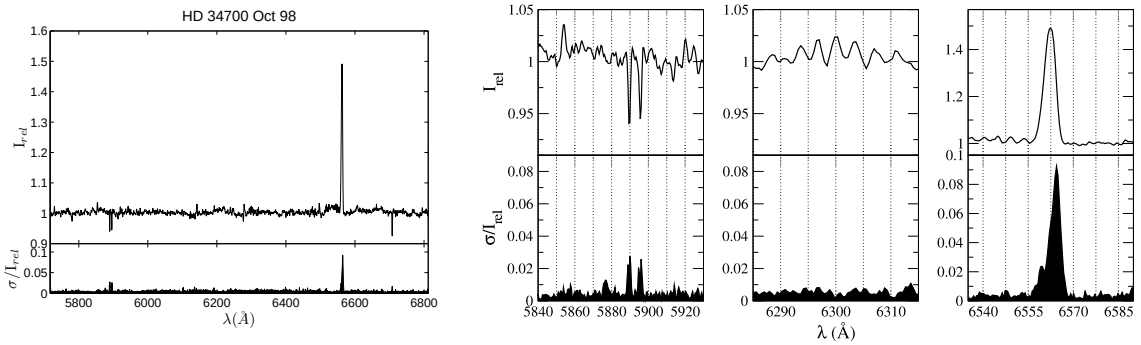
HD 34700 Oct 98
I_{rel}
σ/I_{rel}
$\lambda(\AA)$
I_{rel}
σ/I_{rel}
λ (Å)

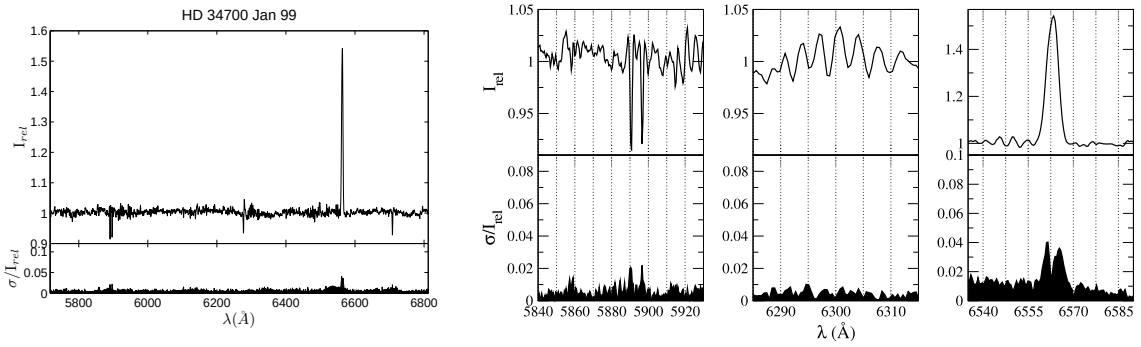
HD 34700 Jan 99
I_{rel}
σ/I_{rel}
$\lambda(\AA)$
I_{rel}
σ/I_{rel}
λ (Å)

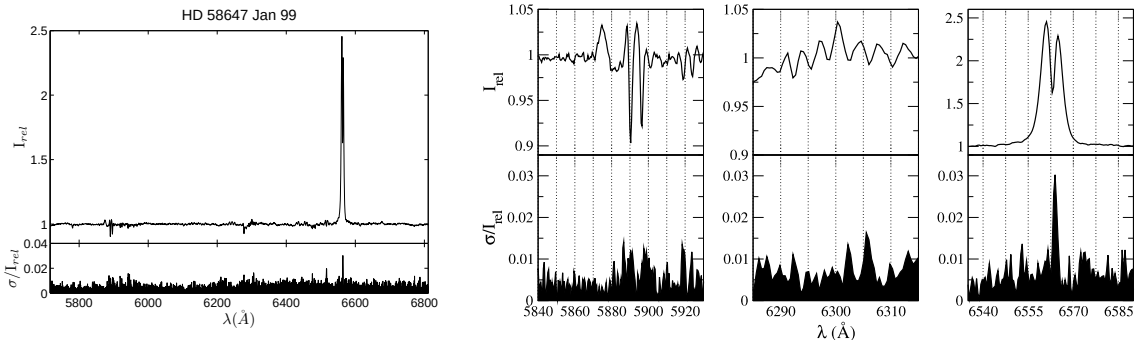
HD 58647 Jan 99
I_{rel}
σ/I_{rel}
$\lambda(\AA)$
I_{rel}
σ/I_{rel}
λ (Å)

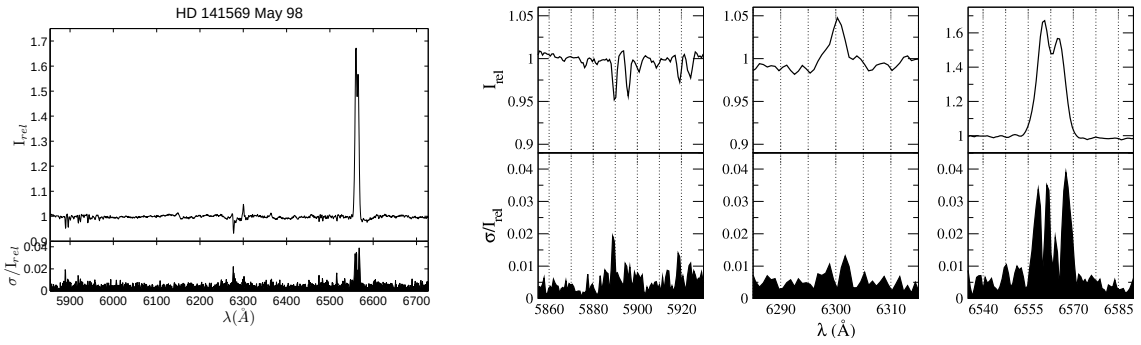
HD 141569 May 98
I_{rel}
σ/I_{rel}
$\lambda(\AA)$
I_{rel}
σ/I_{rel}
λ (Å)

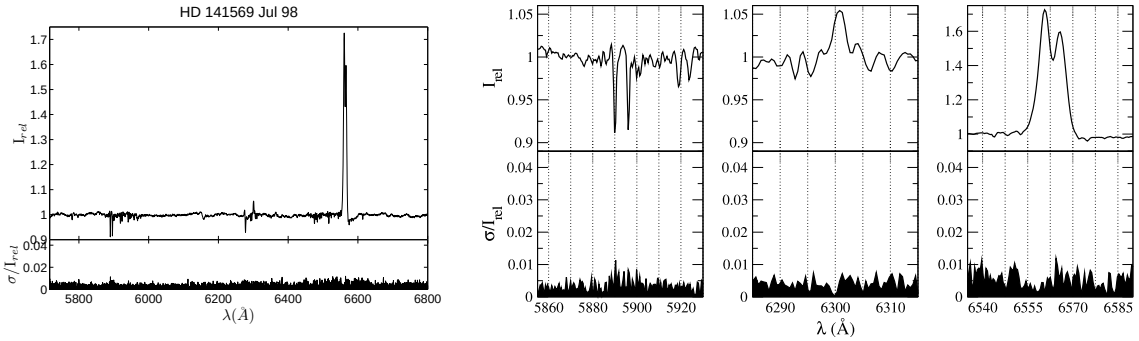
HD 141569 Jul 98
I_{rel}
σ/I_{rel}
$\lambda(\AA)$
I_{rel}
σ/I_{rel}
λ (Å)

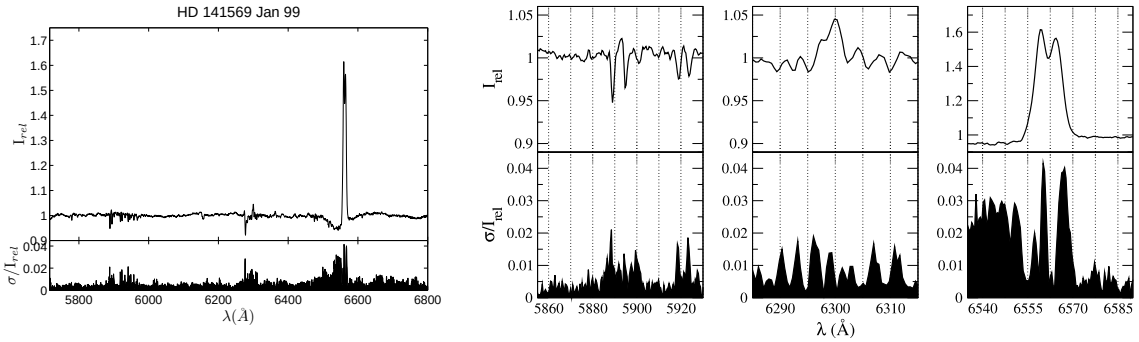
HD 141569 Jan 99
I_{rel}
σ/I_{rel}
$\lambda(\AA)$
I_{rel}
σ/I_{rel}
λ (Å)

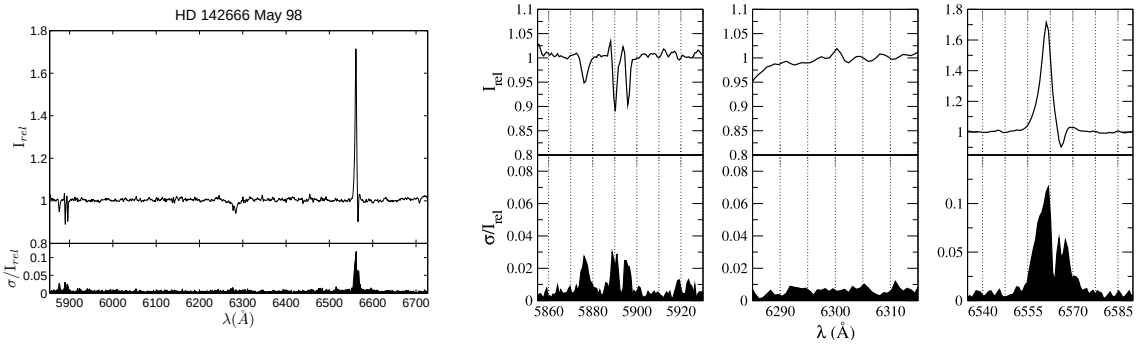
HD 142666 May 98
I_{rel}
σ/I_{rel}
$\lambda(\AA)$
I_{rel}
σ/I_{rel}
λ (Å)

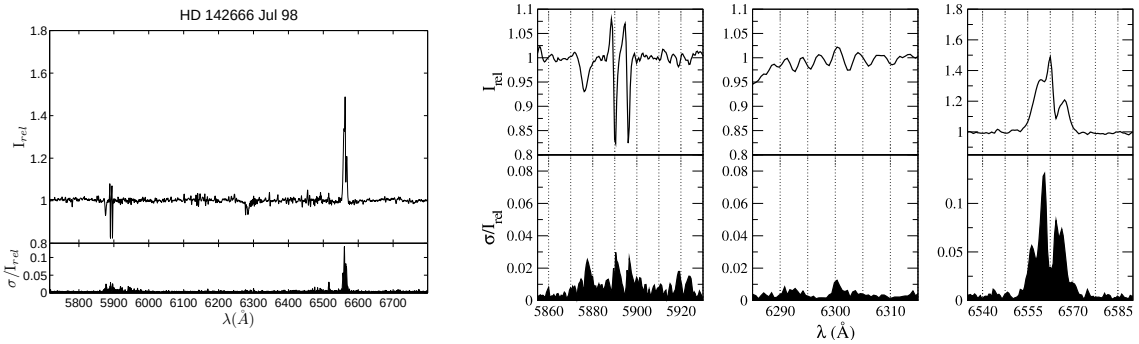
HD 142666 Jul 98
I_{rel}
σ/I_{rel}
$\lambda(\AA)$
I_{rel}
σ/I_{rel}
λ (Å)

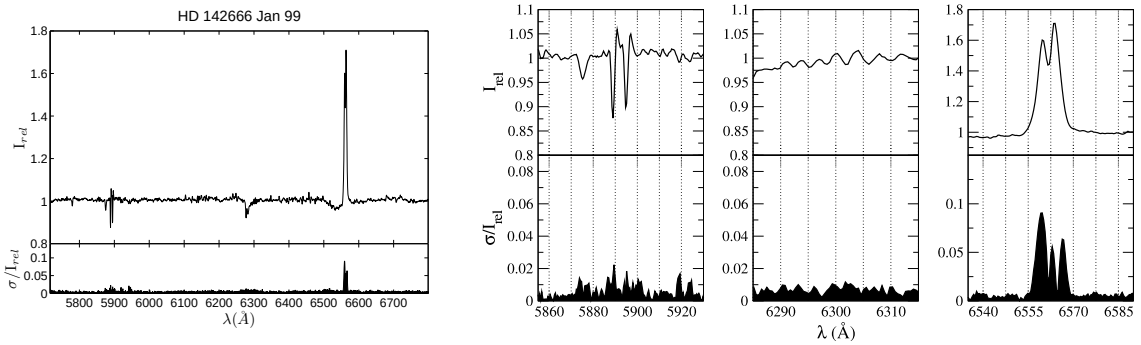
HD 142666 Jan 99
I_{rel}
σ/I_{rel}
$\lambda(\AA)$
I_{rel}
σ/I_{rel}
λ (Å)

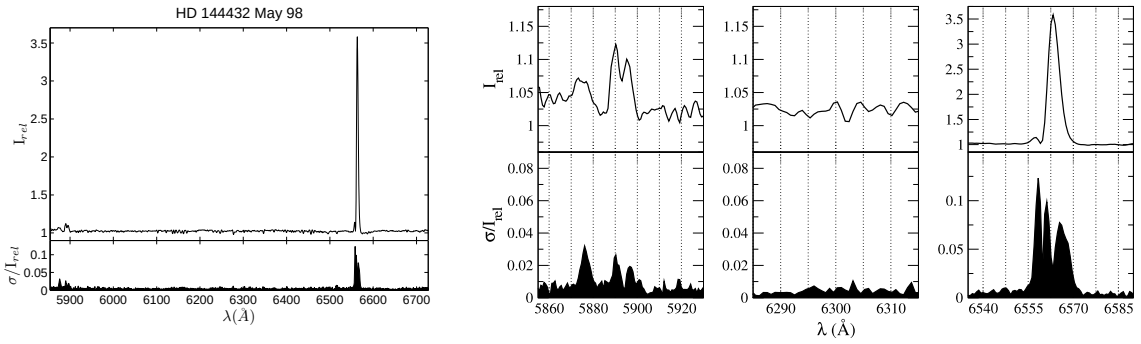
HD 144432 May 98
I_{rel}
σ/I_{rel}
$\lambda(\AA)$
I_{rel}
σ/I_{rel}
λ (Å)

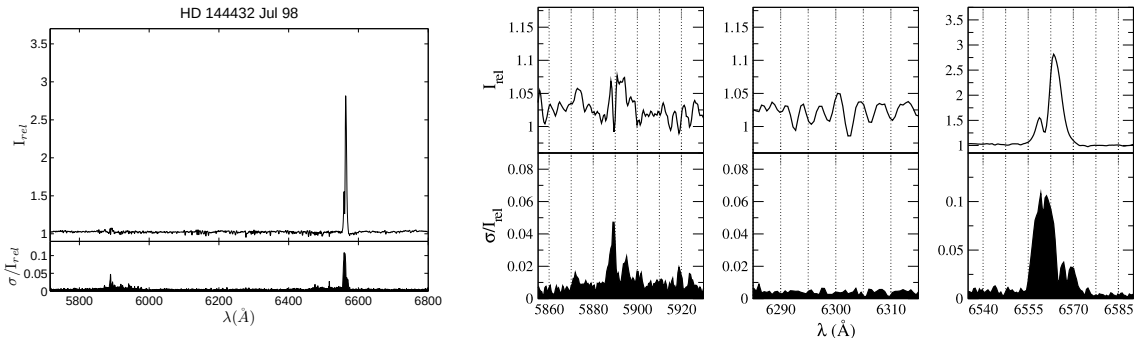
HD 144432 Jul 98
I_{rel}
σ/I_{rel}
$\lambda(\AA)$
I_{rel}
σ/I_{rel}
λ (Å)

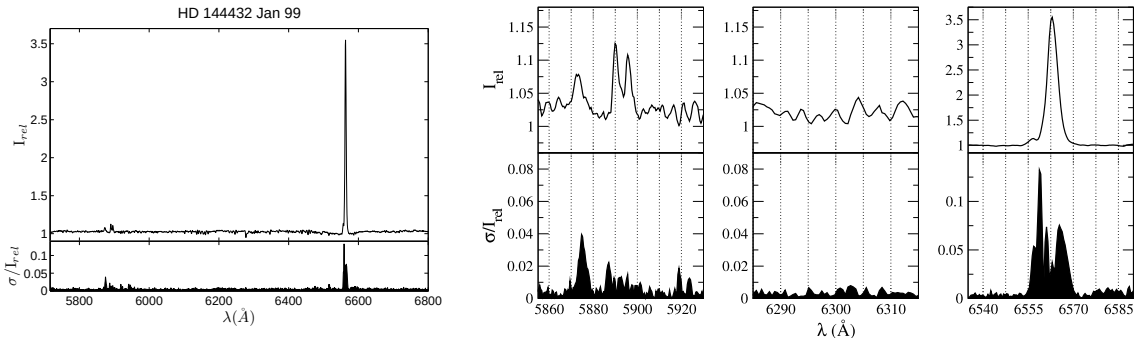
HD 144432 Jan 99
I_{rel}
σ/I_{rel}
$\lambda(\AA)$
I_{rel}
σ/I_{rel}
λ (Å)

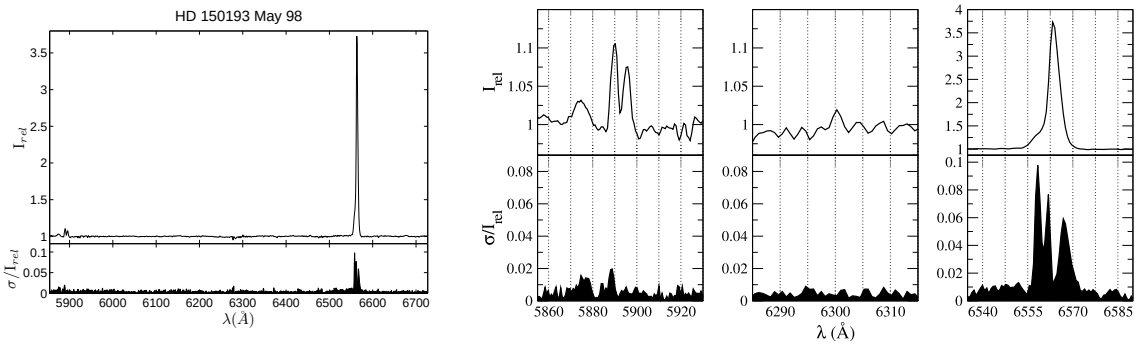
HD 150193 May 98
I_{rel}
σ/I_{rel}
$\lambda(\AA)$
I_{rel}
σ/I_{rel}
λ (Å)

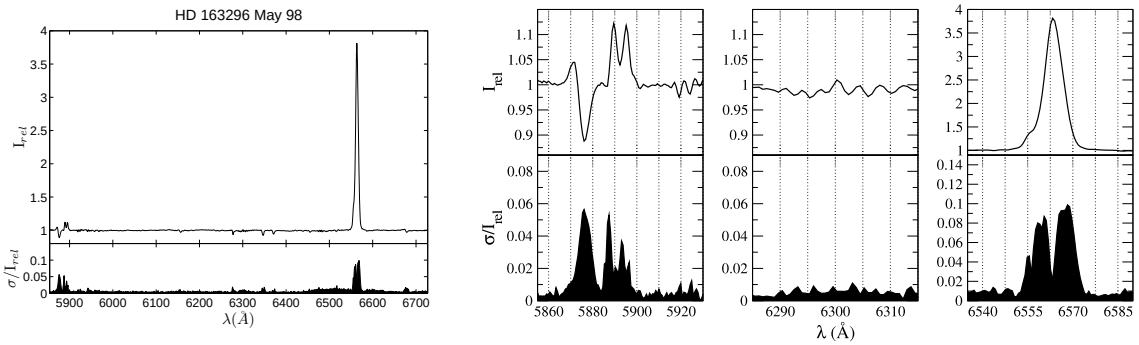
HD 163296 May 98
I_{rel}
σ/I_{rel}
$\lambda(\AA)$
I_{rel}
σ/I_{rel}
λ (Å)

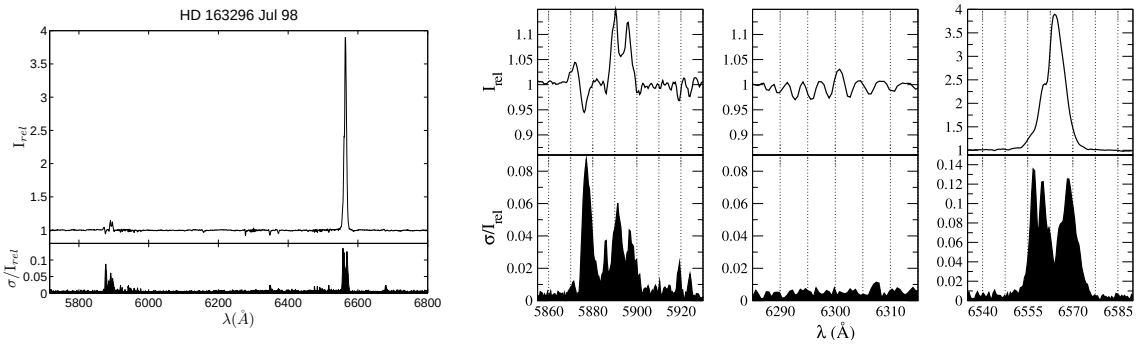
HD 163296 Jul 98
I_{rel}
σ/I_{rel}
$\lambda(\AA)$
I_{rel}
σ/I_{rel}
λ (Å)

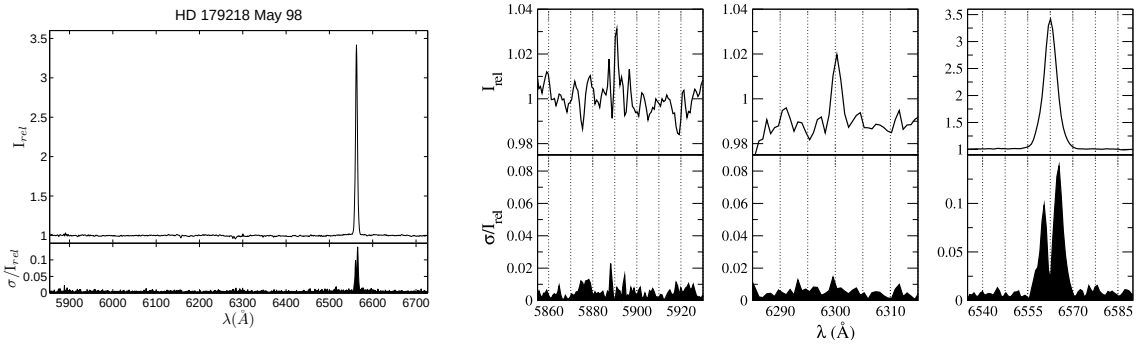
HD 179218 May 98
I_{rel}
σ/I_{rel}
$\lambda(\AA)$
I_{rel}
σ/I_{rel}
λ (Å)

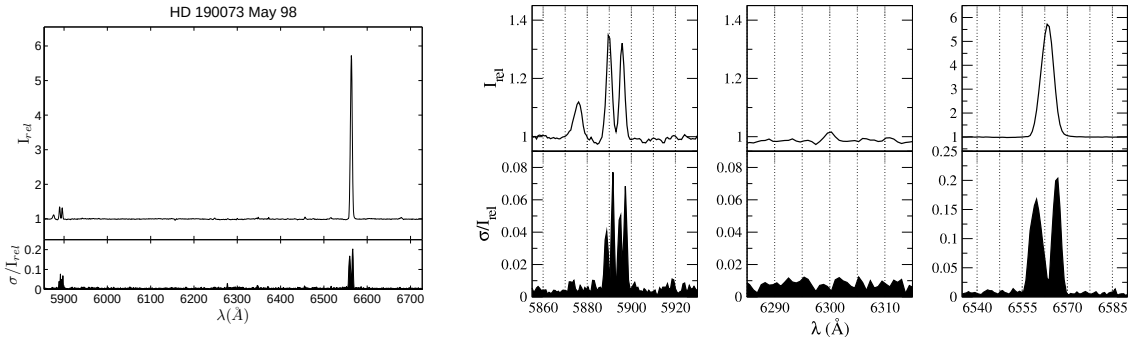
HD 190073 May 98
I_{rel}
σ/I_{rel}
$\lambda(\AA)$
I_{rel}
σ/I_{rel}
λ (Å)

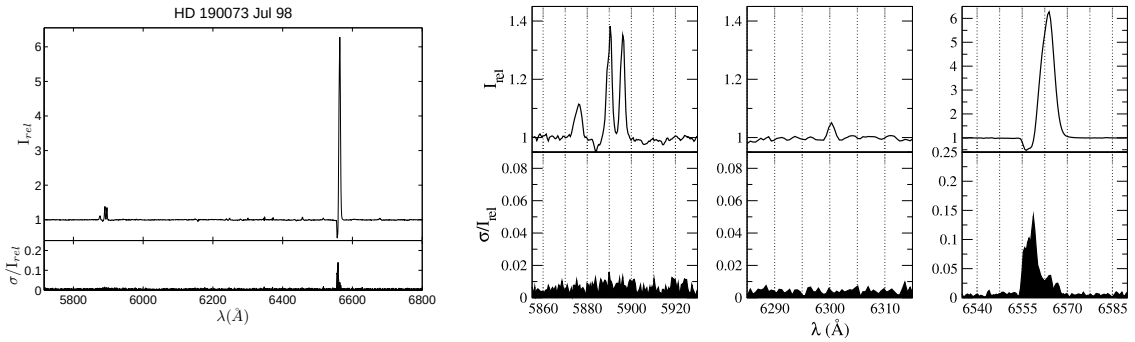
HD 190073 Jul 98
I_{rel}
σ/I_{rel}
$\lambda(\AA)$
I_{rel}
σ/I_{rel}
λ (Å)

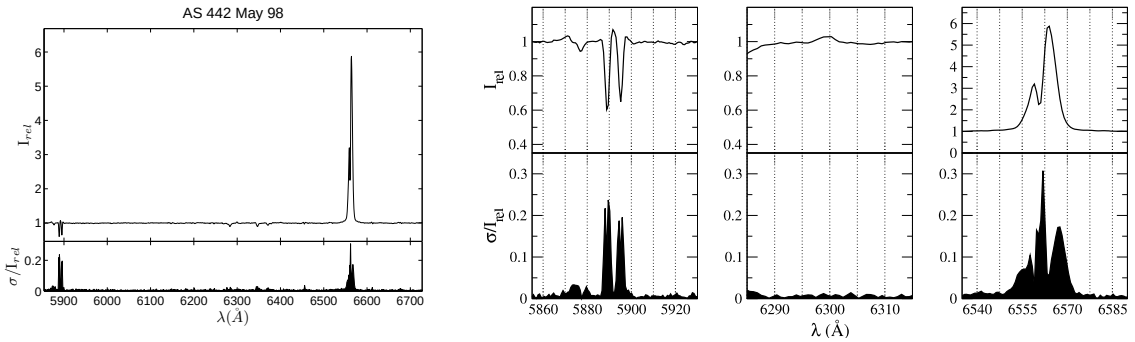
AS 442 May 98
I_{rel}
σ/I_{rel}
$\lambda(\AA)$
I_{rel}
σ/I_{rel}
λ (Å)

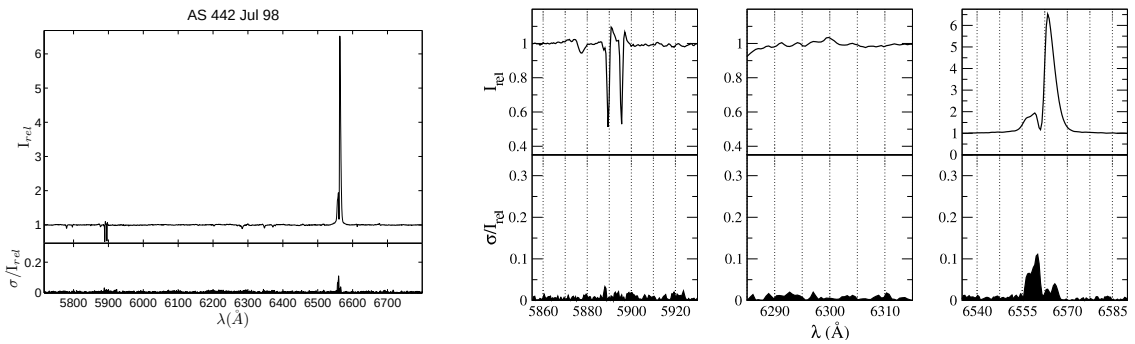
AS 442 Jul 98
I_{rel}
σ/I_{rel}
$\lambda(\AA)$
I_{rel}
σ/I_{rel}
λ (Å)

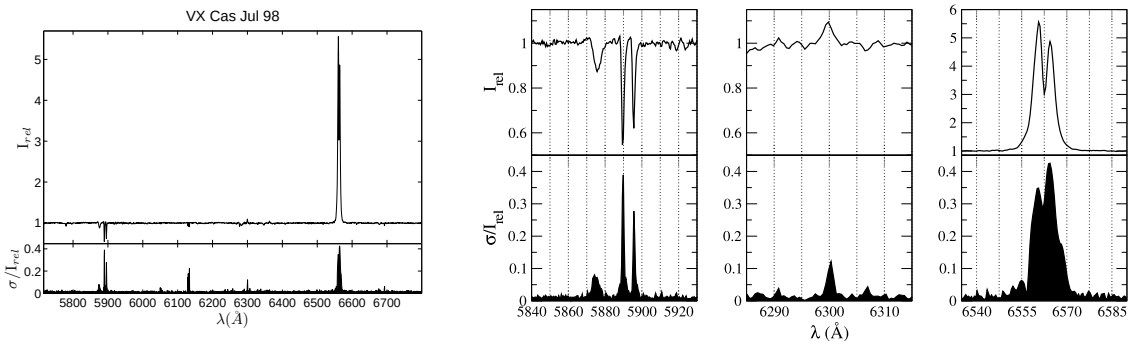
VX Cas Jul 98
I_{rel}
σ/I_{rel}
$\lambda(\AA)$
I_{rel}
σ/I_{rel}
λ (Å)

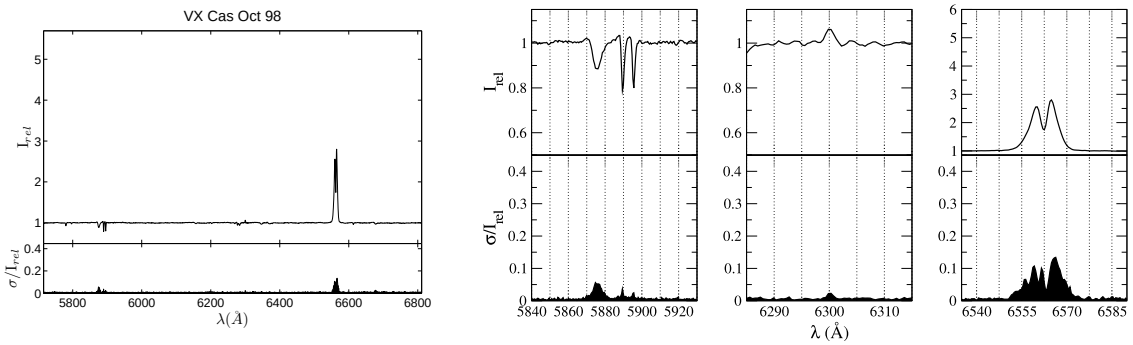
VX Cas Oct 98
I_{rel}
σ/I_{rel}
$\lambda(\AA)$
I_{rel}
σ/I_{rel}
λ (Å)

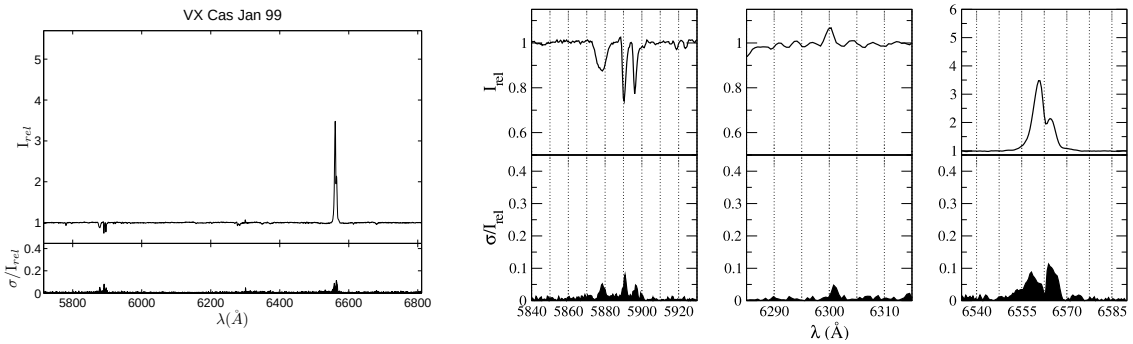
VX Cas Jan 99
I_{rel}
σ/I_{rel}
$\lambda(\AA)$
I_{rel}
σ/I_{rel}
λ (Å)

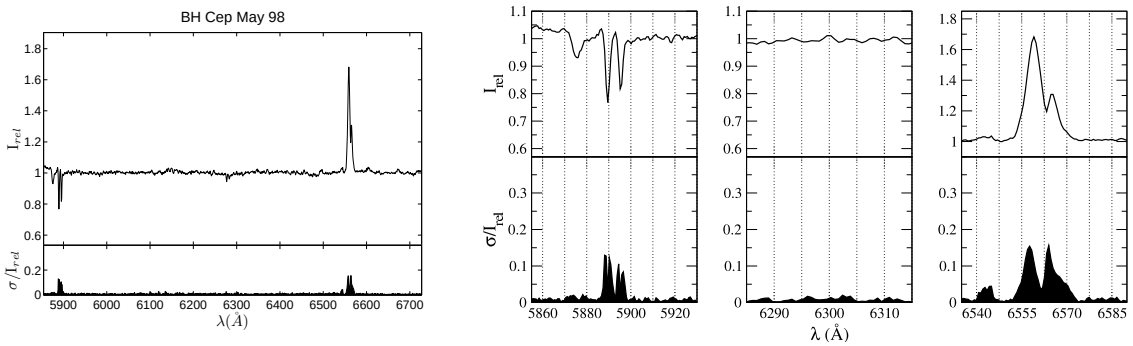
BH Cep May 98
I_{rel}
σ/I_{rel}
$\lambda(\AA)$
I_{rel}
σ/I_{rel}
λ (Å)

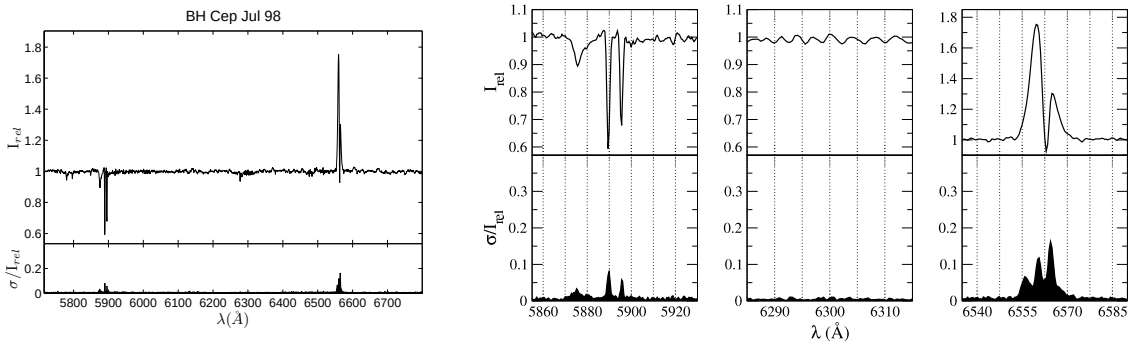
BH Cep Jul 98
I_{rel}
σ/I_{rel}
$\lambda(\AA)$
I_{rel}
σ/I_{rel}
λ (Å)

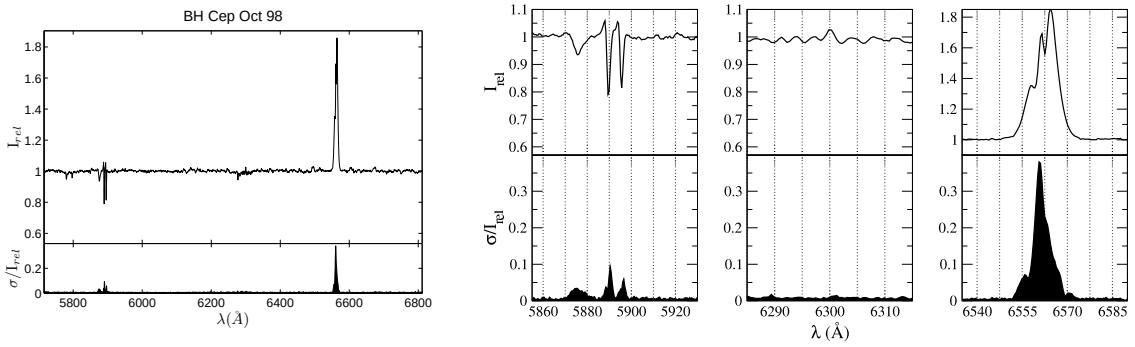
BH Cep Oct 98
I_{rel}
σ/I_{rel}
$\lambda(\AA)$
I_{rel}
σ/I_{rel}
λ (Å)

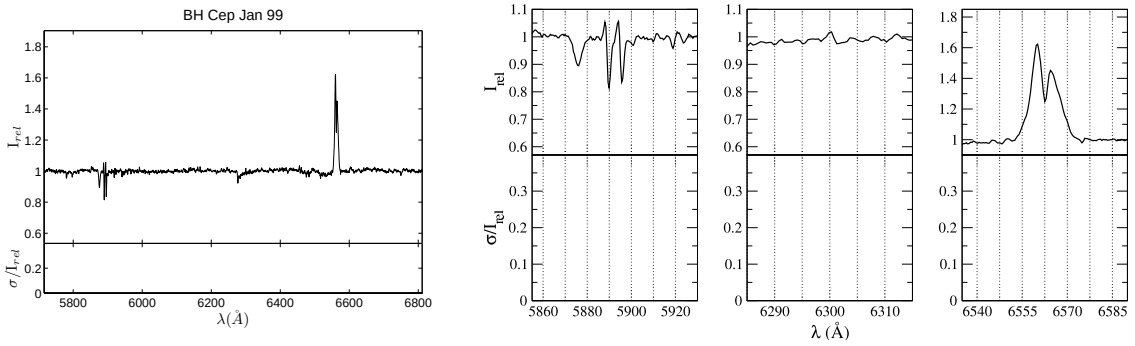
BH Cep Jan 99
I_{rel}
σ/I_{rel}
$\lambda(\AA)$
I_{rel}
σ/I_{rel}
λ (Å)

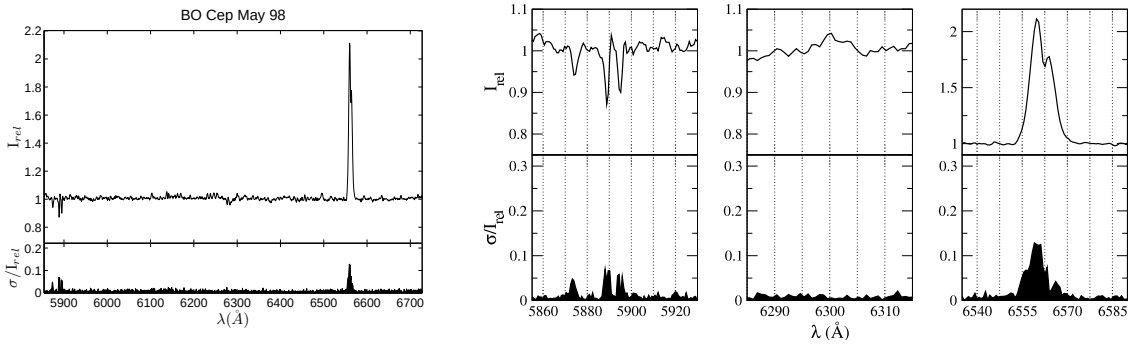
BO Cep May 98
I_{rel}
σ/I_{rel}
$\lambda(\AA)$
I_{rel}
σ/I_{rel}
λ (Å)

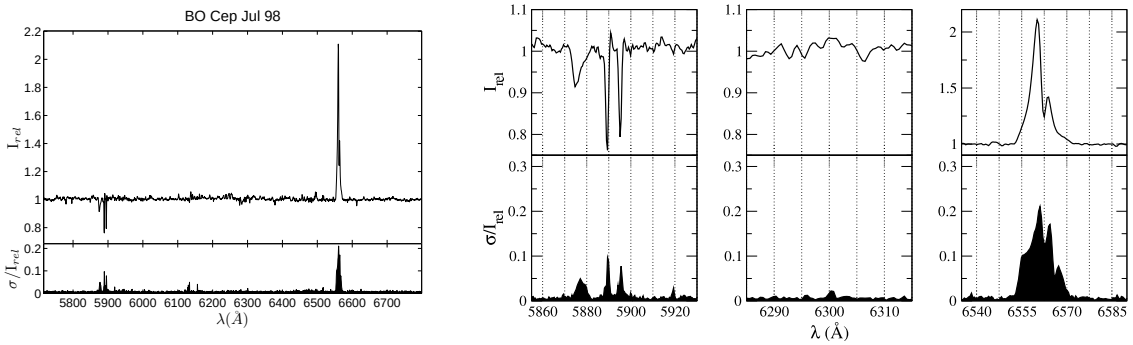
BO Cep Jul 98
I_{rel}
σ/I_{rel}
$\lambda(\AA)$
I_{rel}
σ/I_{rel}
λ (Å)

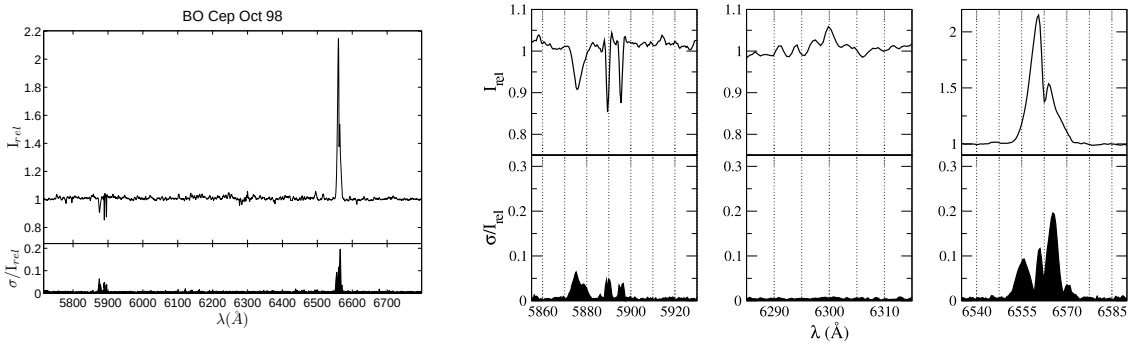
BO Cep Oct 98
I_{rel}
σ/I_{rel}
$\lambda(\AA)$
I_{rel}
σ/I_{rel}
λ (Å)

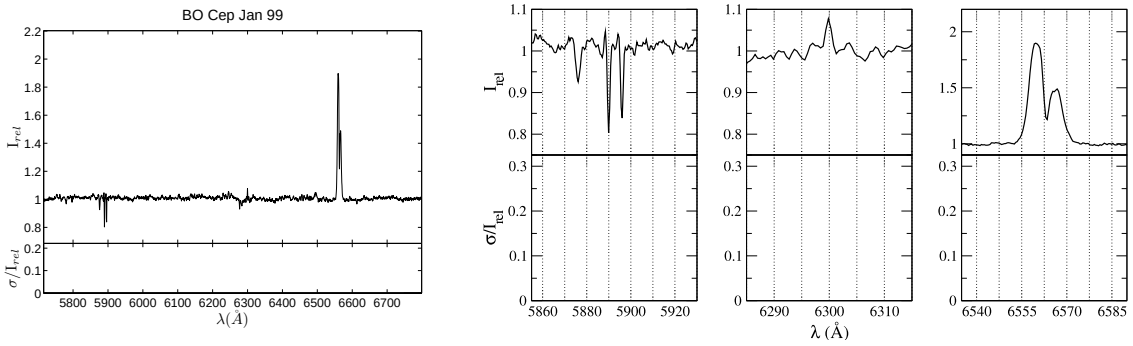
BO Cep Jan 99
I_{rel}
σ/I_{rel}
$\lambda(\AA)$
I_{rel}
σ/I_{rel}
λ (Å)

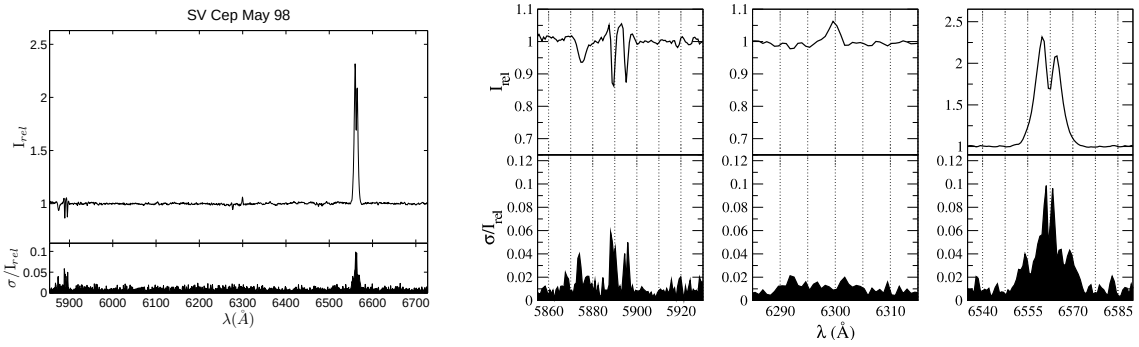
SV Cep May 98
I_{rel}
σ/I_{rel}
$\lambda(\AA)$
I_{rel}
σ/I_{rel}
λ (Å)

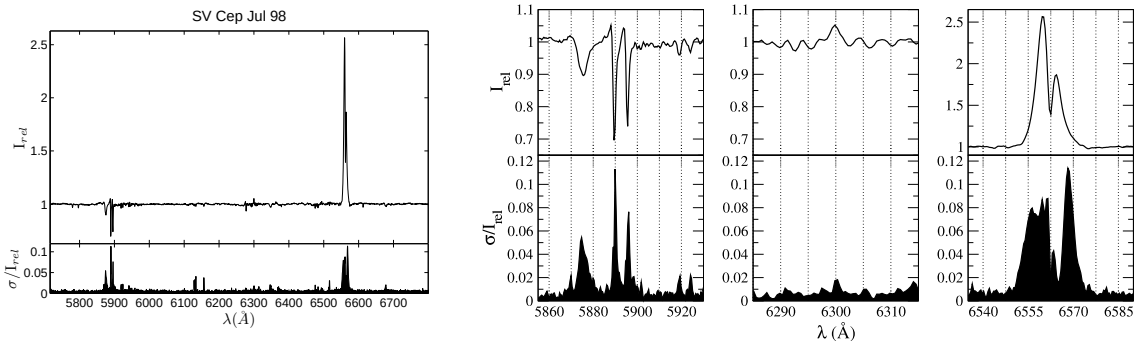
SV Cep Jul 98
I_{rel}
σ/I_{rel}
$\lambda(\AA)$
I_{rel}
σ/I_{rel}
λ (Å)

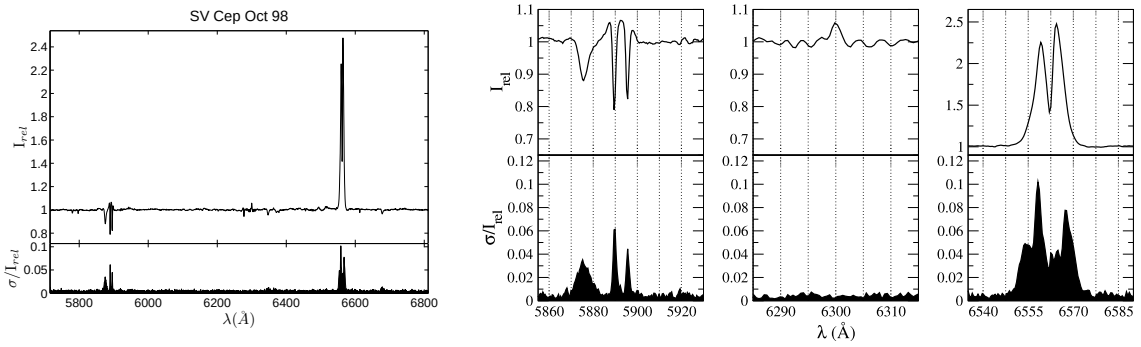
SV Cep Oct 98
I_{rel}
σ/I_{rel}
$\lambda(\AA)$
I_{rel}
σ/I_{rel}
λ (Å)

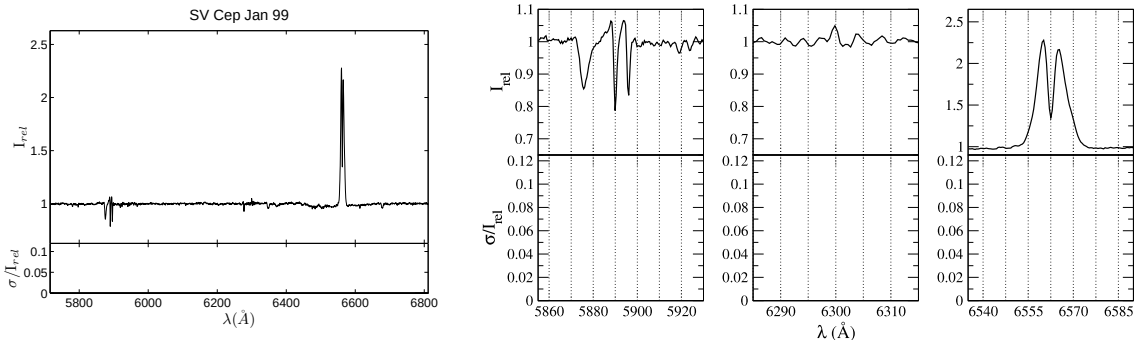
SV Cep Jan 99
I_{rel}
σ/I_{rel}
$\lambda(\AA)$
I_{rel}
σ/I_{rel}
λ (Å)

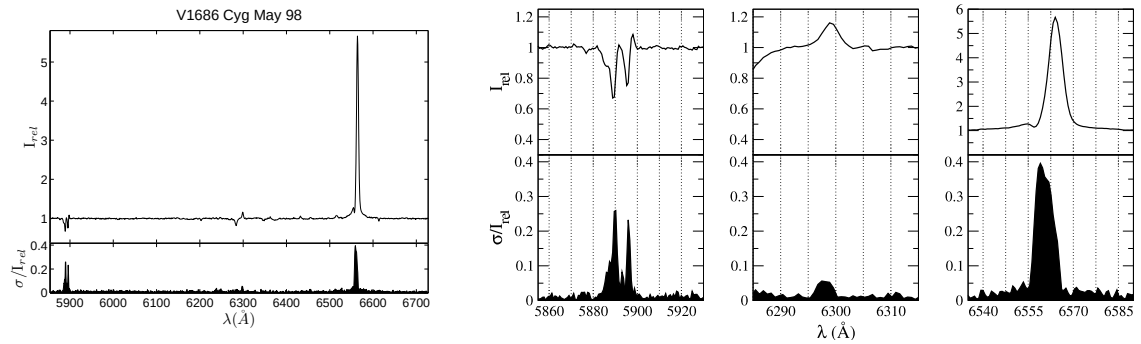
V1686 Cyg May 98
I_{rel}
σ/I_{rel}
$\lambda(\AA)$
I_{rel}
σ/I_{rel}
λ (Å)

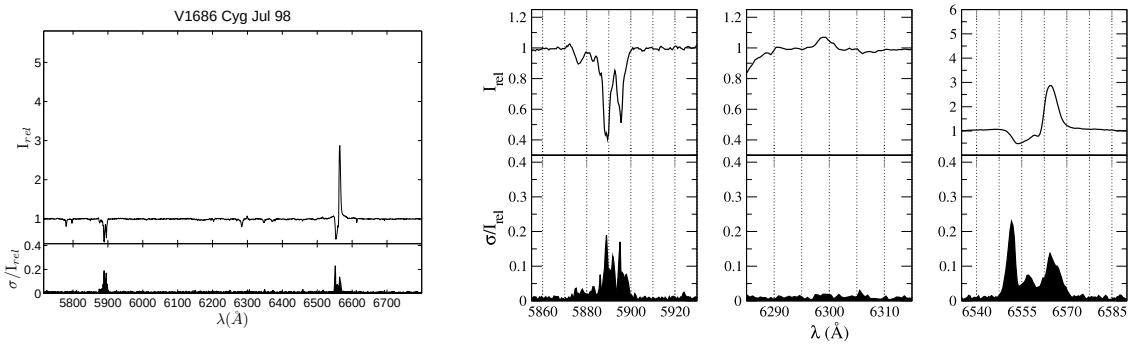
V1686 Cyg Jul 98
I_{rel}
σ/I_{rel}
$\lambda(\AA)$
I_{rel}
σ/I_{rel}
λ (Å)

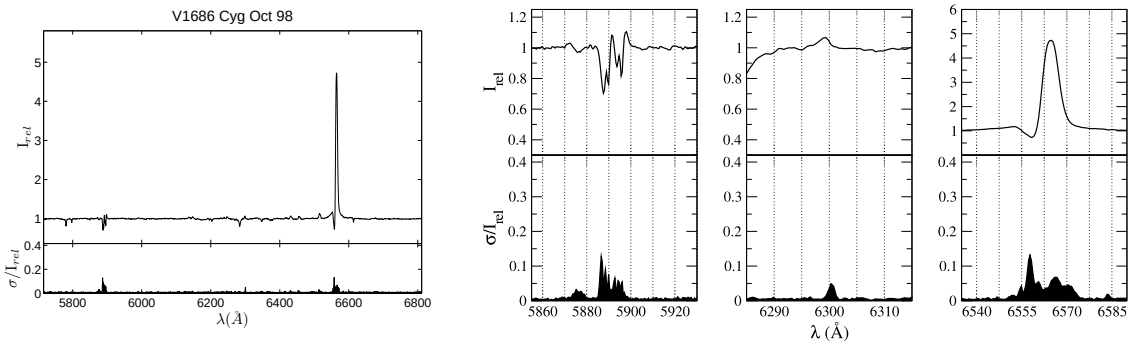
V1686 Cyg Oct 98
I_{rel}
σ/I_{rel}
$\lambda(\AA)$
I_{rel}
σ/I_{rel}
λ (Å)

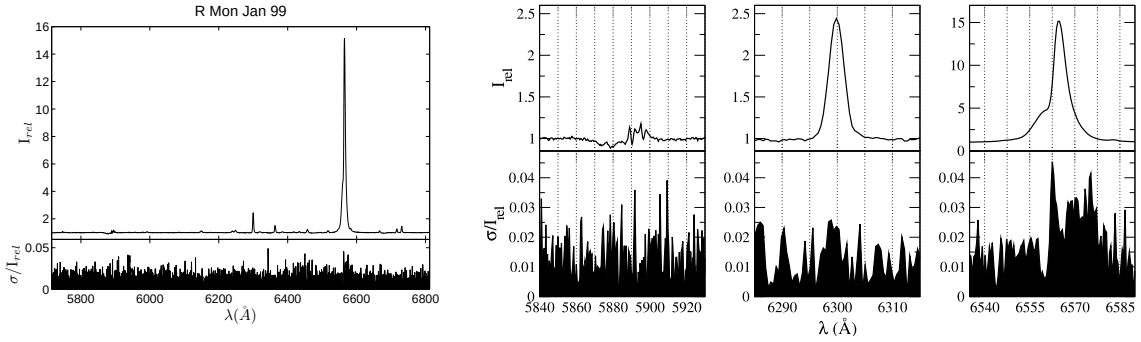
R Mon Jan 99
I_{rel}
σ/I_{rel}
$\lambda(\AA)$
I_{rel}
σ/I_{rel}
λ (Å)

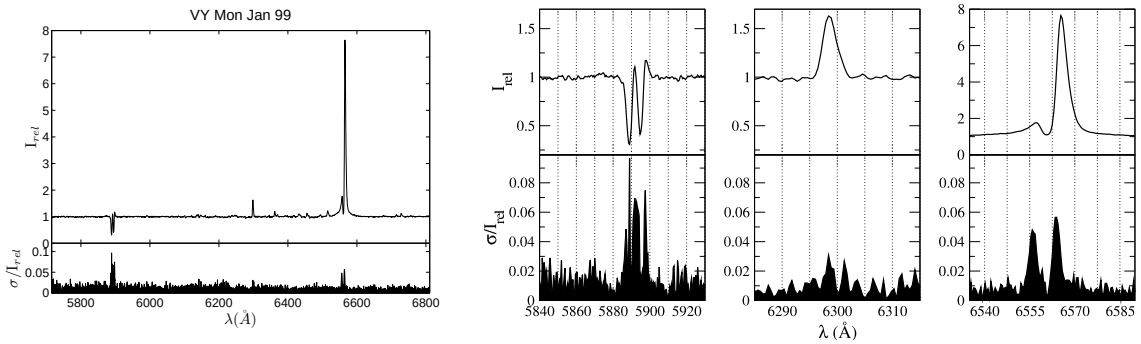
VY Mon Jan 99
I_{rel}
σ/I_{rel}
$\lambda(\AA)$
I_{rel}
σ/I_{rel}
λ (Å)

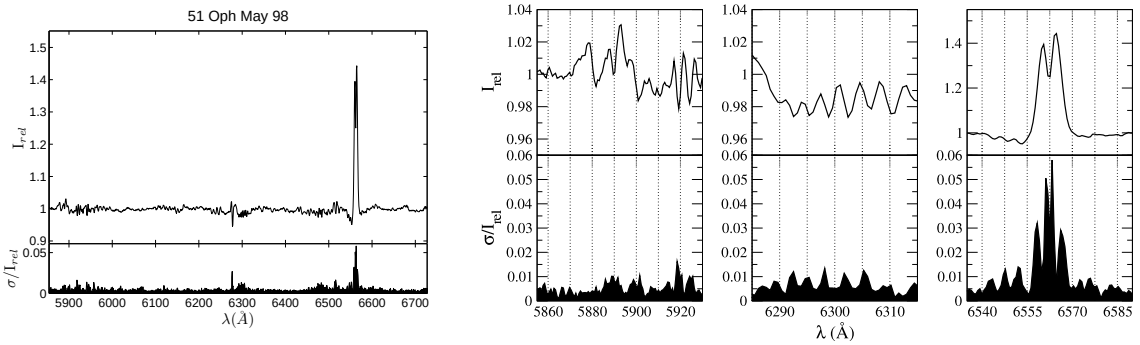
51 Oph May 98
I_{rel}
σ/I_{rel}
$\lambda(\AA)$
I_{rel}
σ/I_{rel}
λ (Å)

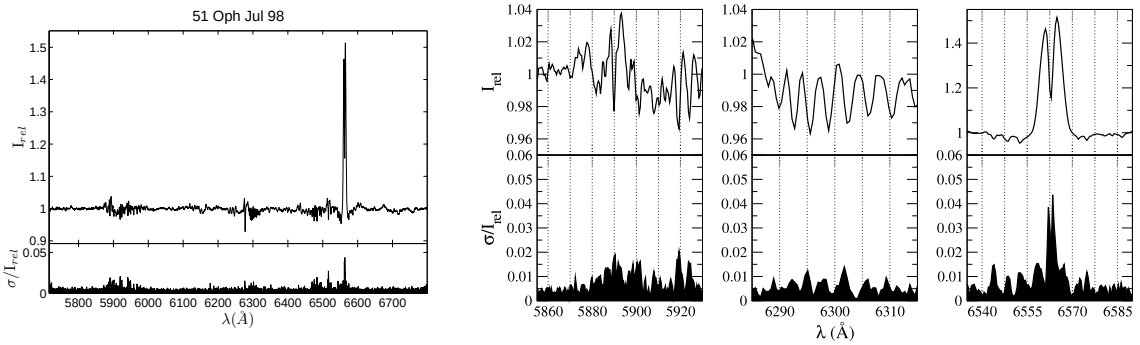
51 Oph Jul 98
I_{rel}
σ/I_{rel}
$\lambda(\AA)$
I_{rel}
σ/I_{rel}
λ (Å)

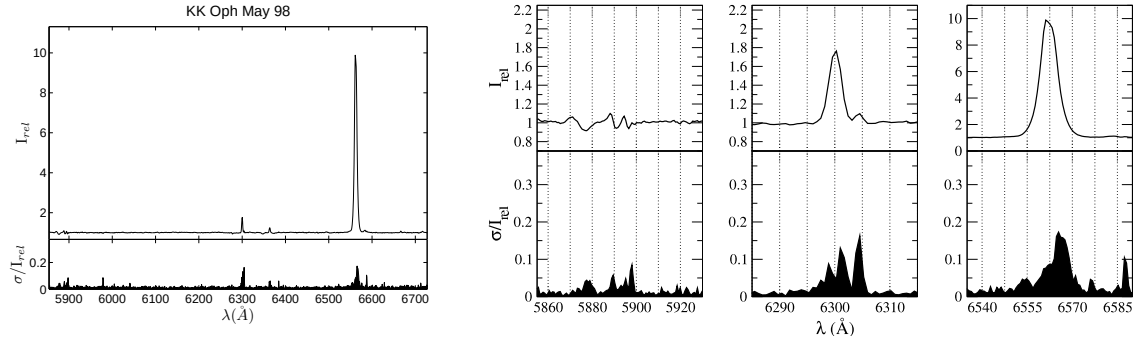
KK Oph May 98
I_{rel}
σ/I_{rel}
$\lambda(\AA)$
I_{rel}
σ/I_{rel}
λ (Å)

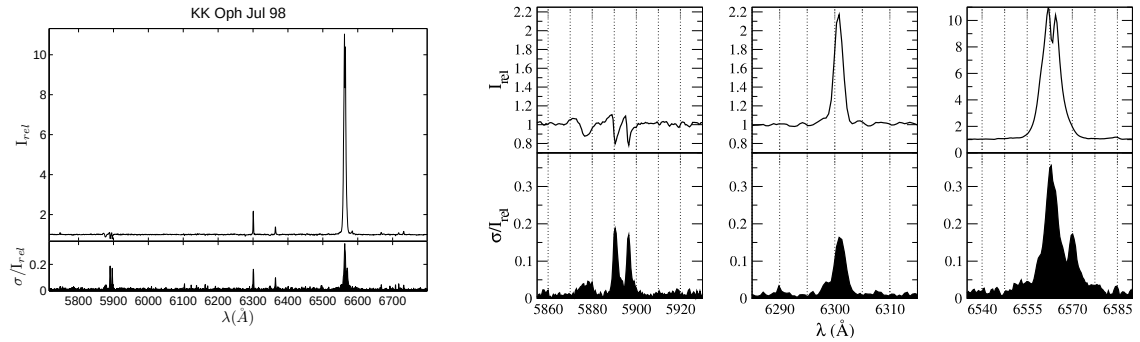
KK Oph Jul 98
I_{rel}
σ/I_{rel}
$\lambda(\AA)$
I_{rel}
σ/I_{rel}
λ (Å)

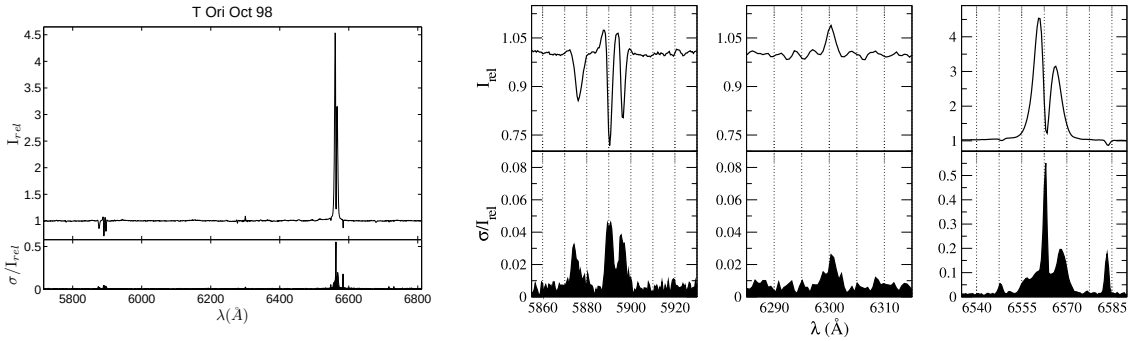
T Ori Oct 98
I_{rel}
σ/I_{rel}
$\lambda(\AA)$
I_{rel}
σ/I_{rel}
λ (Å)

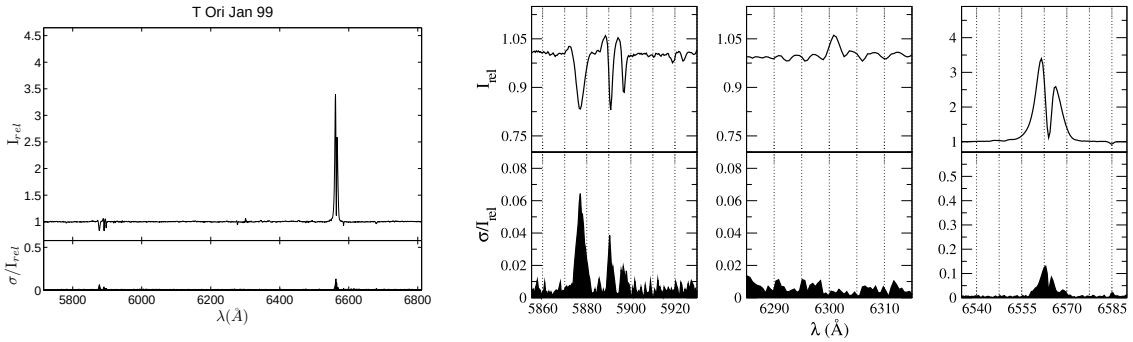
T Ori Jan 99
I_{rel}
σ/I_{rel}
$\lambda(\AA)$
I_{rel}
σ/I_{rel}
λ (Å)

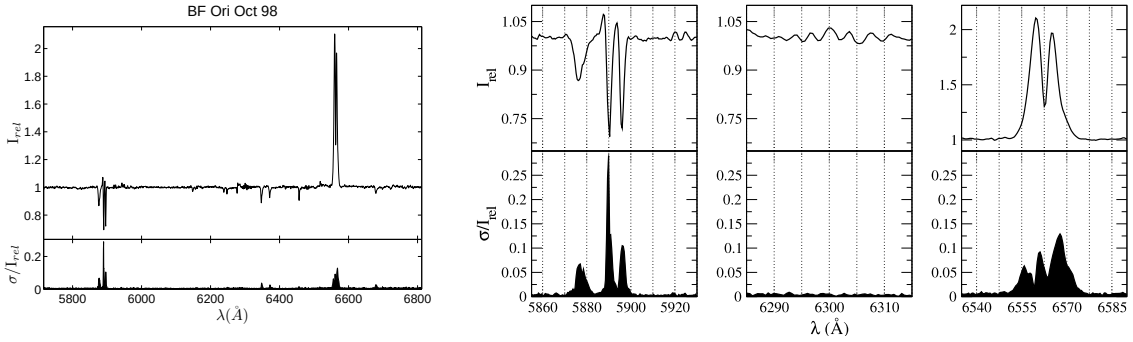
BF Ori Oct 98
I_{rel}
σ/I_{rel}
$\lambda(\AA)$
I_{rel}
σ/I_{rel}
λ (Å)

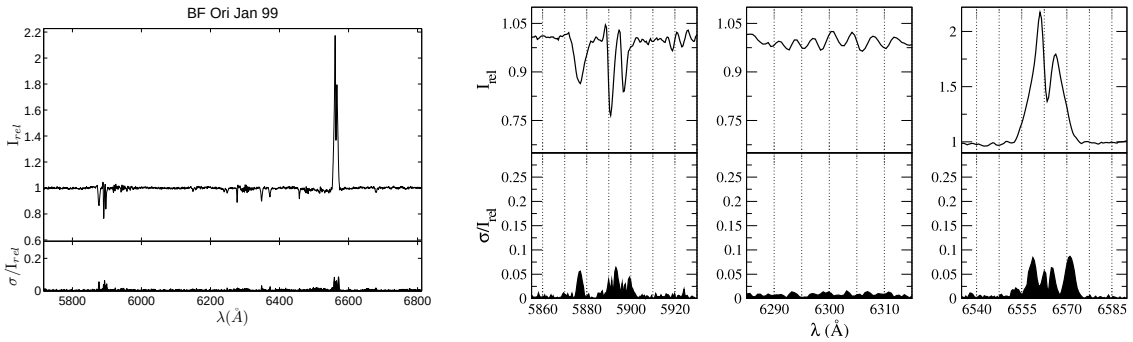
BF Ori Jan 99
I_{rel}
σ/I_{rel}
$\lambda(\AA)$
I_{rel}
σ/I_{rel}
λ (Å)

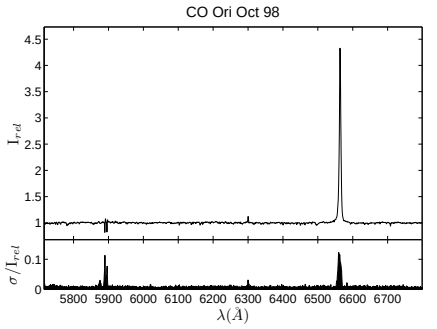
CO Ori Oct 98
I_{rel}
σ/I_{rel}
$\lambda(\AA)$

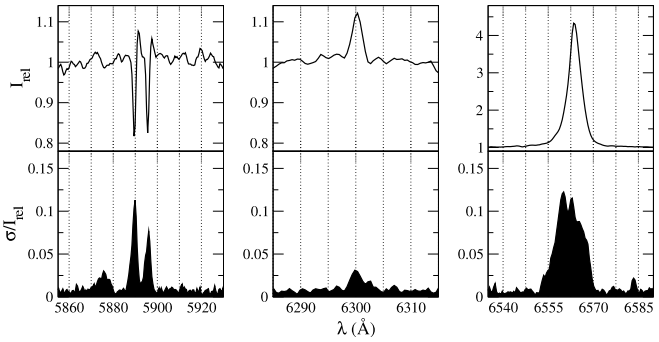
I_{rel}
σ/I_{rel}
λ (Å)

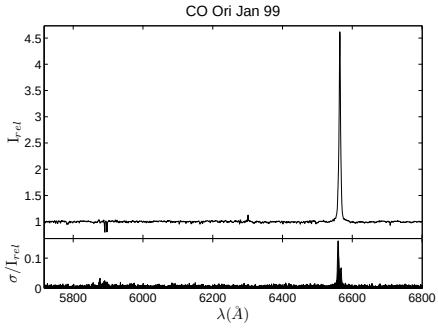
CO Ori Jan 99
I_{rel}
σ/I_{rel}
$\lambda(\AA)$

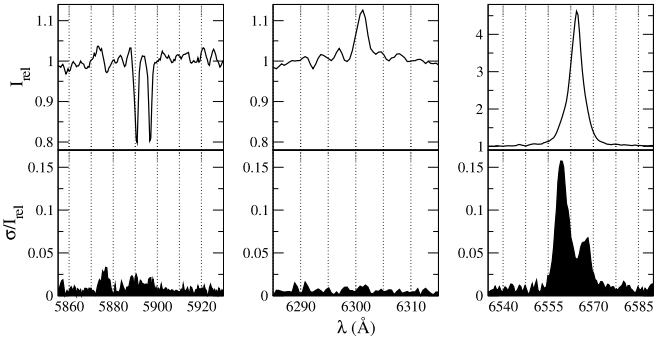
I_{rel}
σ/I_{rel}
λ (Å)

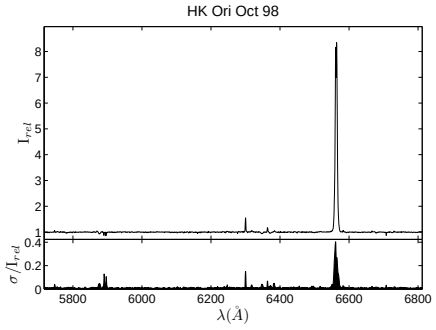
HK Ori Oct 98
I_{rel}
σ/I_{rel}
$\lambda(\AA)$

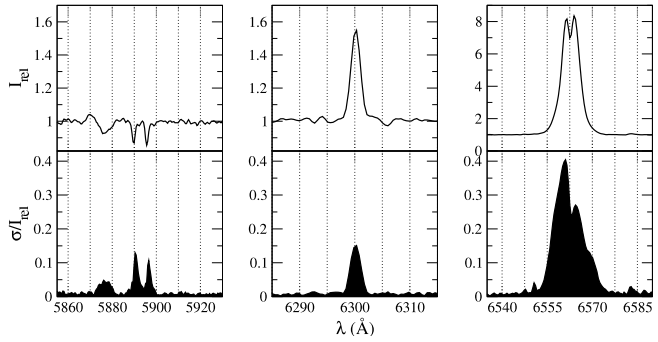
I_{rel}
σ/I_{rel}
λ (Å)

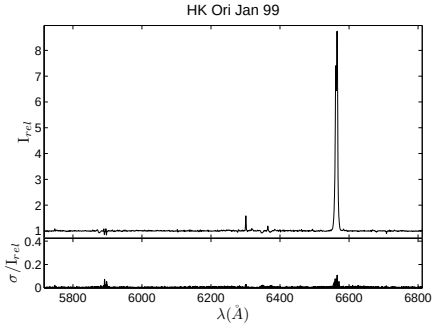
HK Ori Jan 99
I_{rel}
σ/I_{rel}
$\lambda(\AA)$

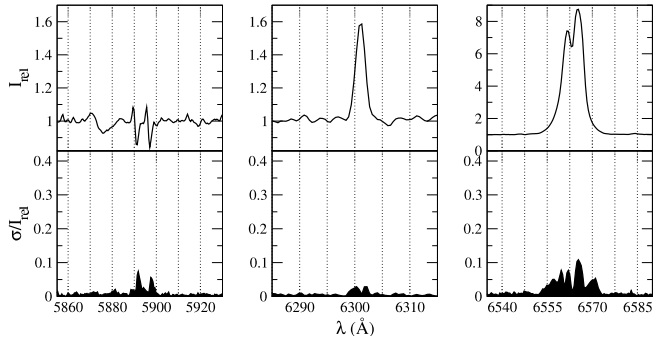
I_{rel}
σ/I_{rel}
λ (Å)

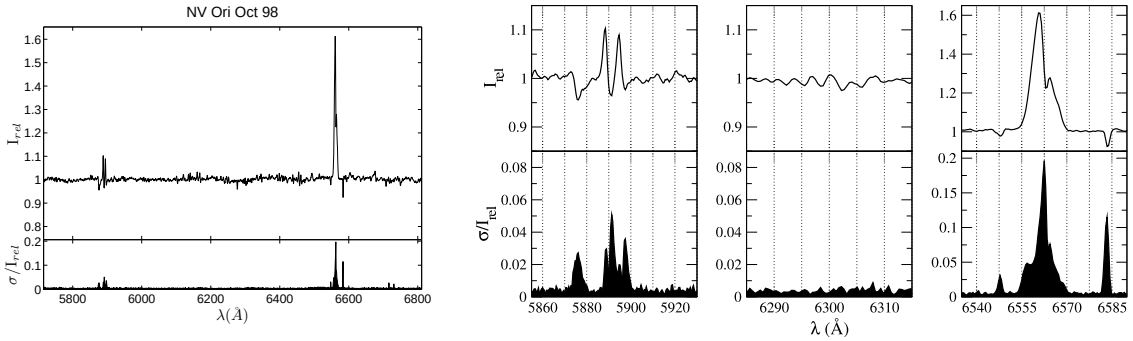
NV Ori Oct 98
I_{rel}
σ/I_{rel}
$\lambda(\AA)$
I_{rel}
σ/I_{rel}
λ (Å)

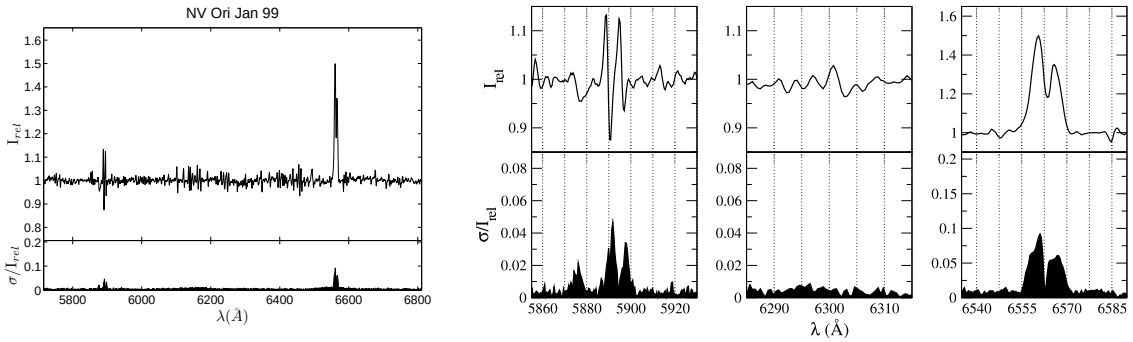
NV Ori Jan 99
I_{rel}
σ/I_{rel}
$\lambda(\AA)$
I_{rel}
σ/I_{rel}
λ (Å)

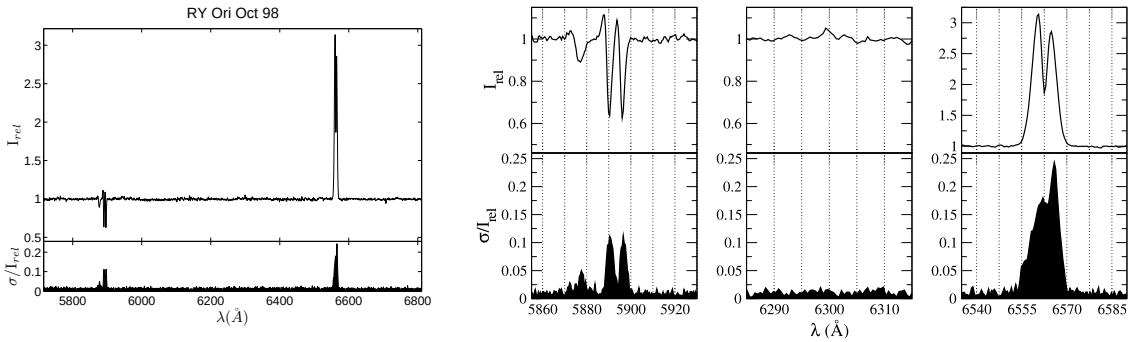
RY Ori Oct 98
I_{rel}
σ/I_{rel}
$\lambda(\AA)$
I_{rel}
σ/I_{rel}
λ (Å)

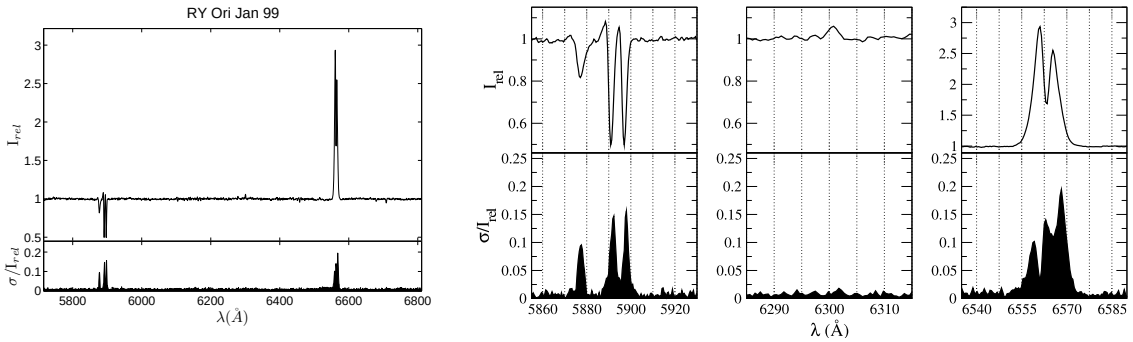
RY Ori Jan 99
I_{rel}
σ/I_{rel}
$\lambda(\AA)$
I_{rel}
σ/I_{rel}
λ (Å)

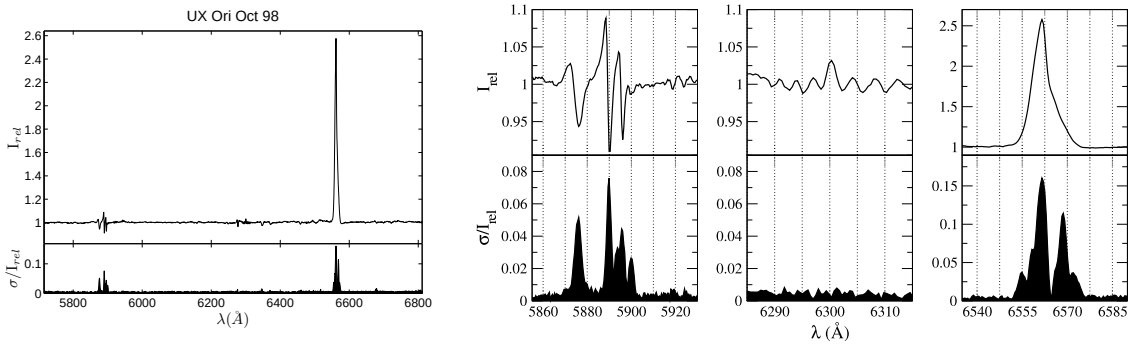
UX Ori Oct 98
I_{rel}
σ/I_{rel}
$\lambda(\AA)$
I_{rel}
σ/I_{rel}
λ (Å)

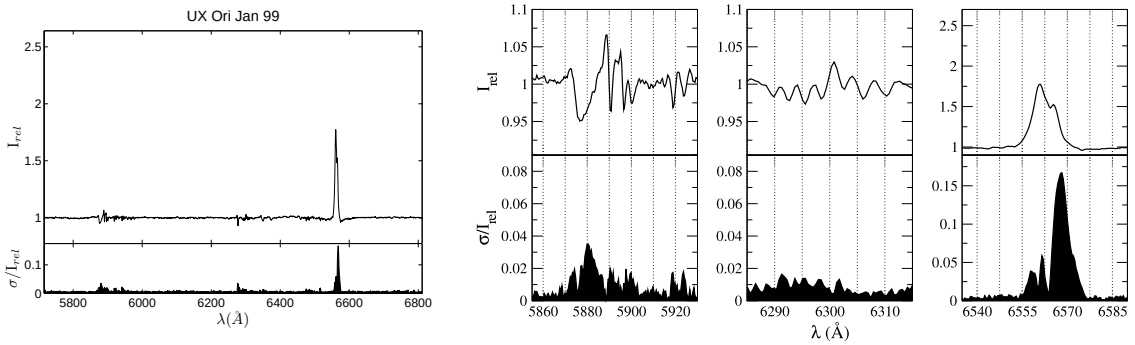
UX Ori Jan 99
I_{rel}
σ/I_{rel}
$\lambda(\AA)$
I_{rel}
σ/I_{rel}
λ (Å)

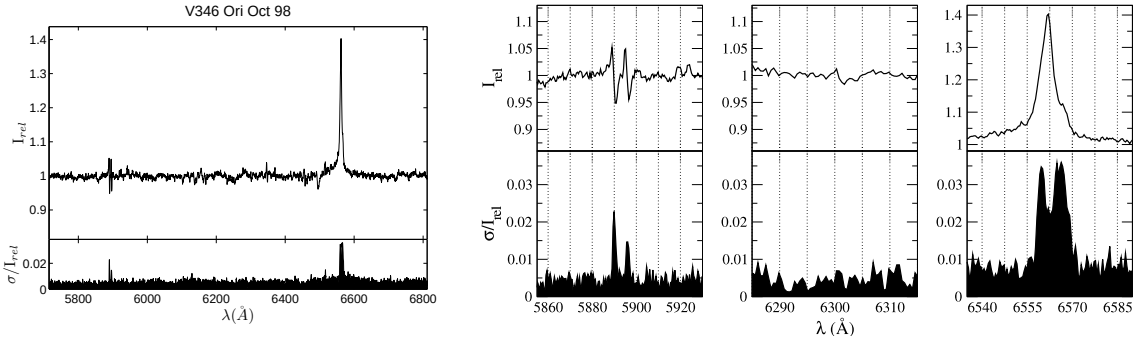
V346 Ori Oct 98
I_{rel}
σ/I_{rel}
$\lambda(\AA)$
I_{rel}
σ/I_{rel}
λ (Å)

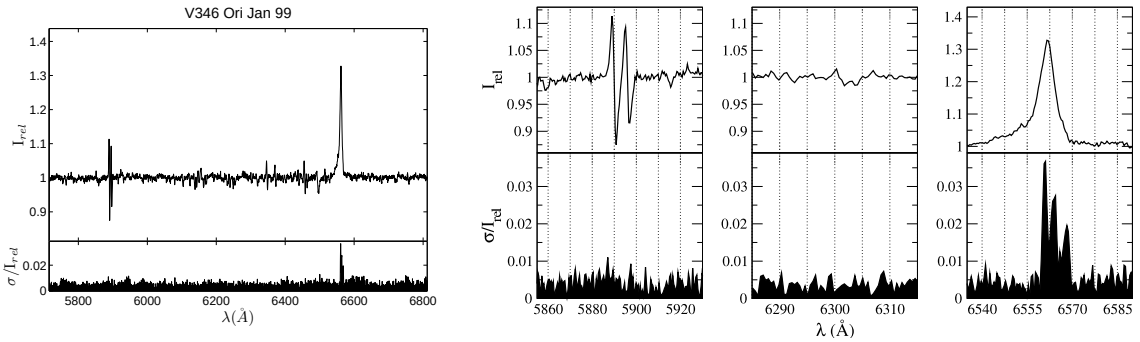
V346 Ori Jan 99
I_{rel}
σ/I_{rel}
$\lambda(\AA)$
I_{rel}
σ/I_{rel}
λ (Å)

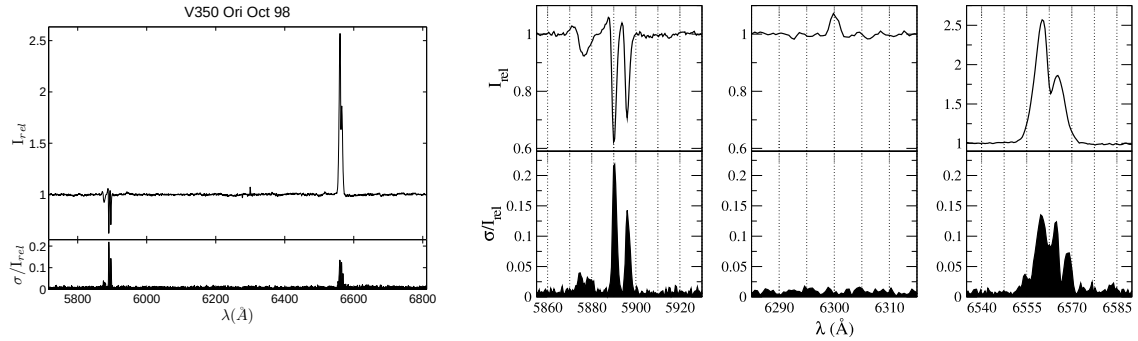
V350 Ori Oct 98
I_{rel}
σ/I_{rel}
$\lambda(\AA)$
I_{rel}
σ/I_{rel}
λ (Å)

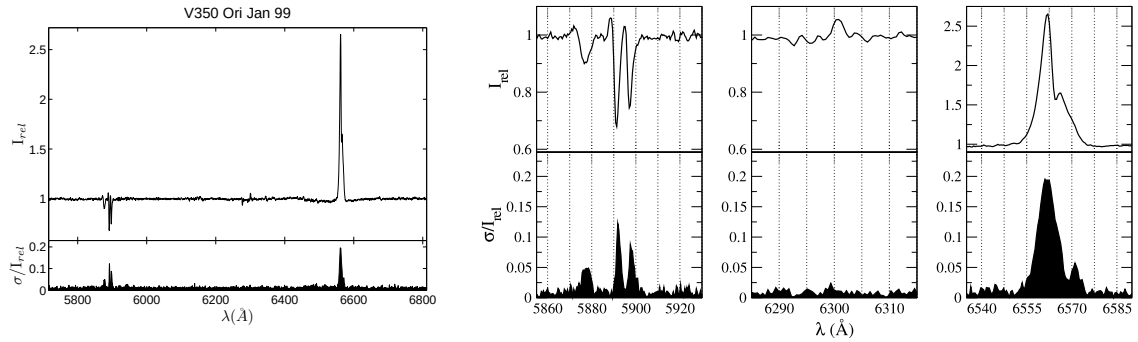
V350 Ori Jan 99
I_{rel}
σ/I_{rel}
$\lambda(\AA)$
I_{rel}
σ/I_{rel}
λ (Å)

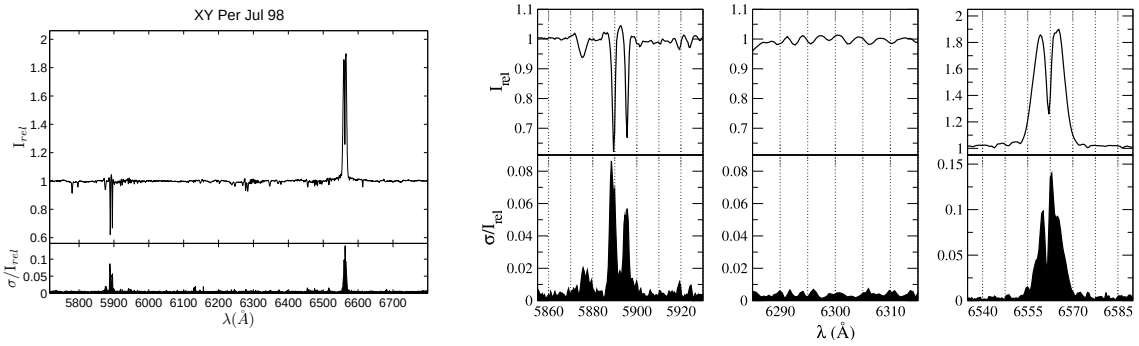
XY Per Jul 98
I_{rel}
σ/I_{rel}
$\lambda(\AA)$
I_{rel}
σ/I_{rel}
λ (Å)

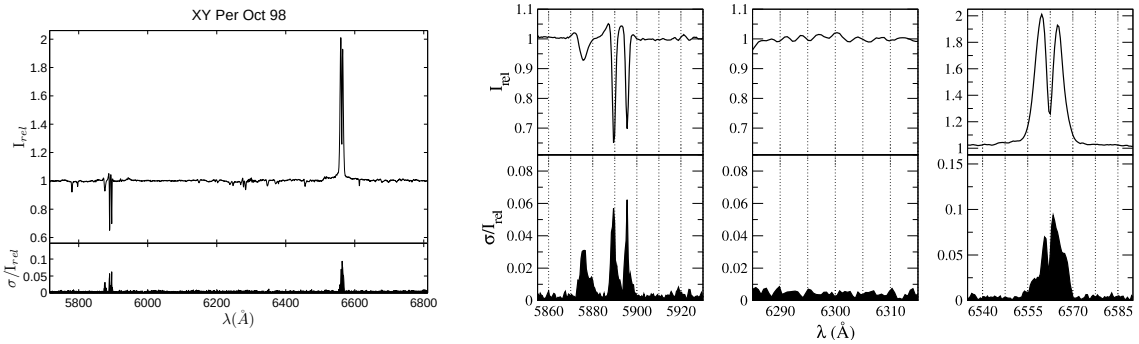
XY Per Oct 98
I_{rel}
σ/I_{rel}
$\lambda(\AA)$
I_{rel}
σ/I_{rel}
λ (Å)

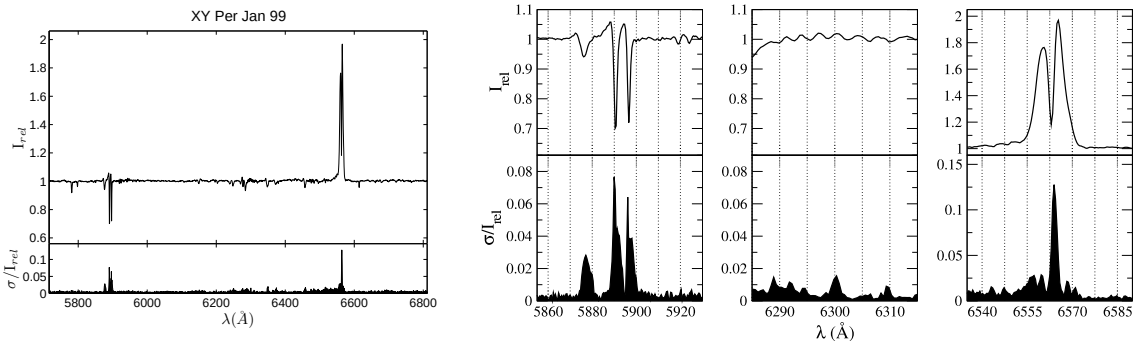
XY Per Jan 99
I_{rel}
σ/I_{rel}
$\lambda(\AA)$
I_{rel}
σ/I_{rel}
λ (Å)

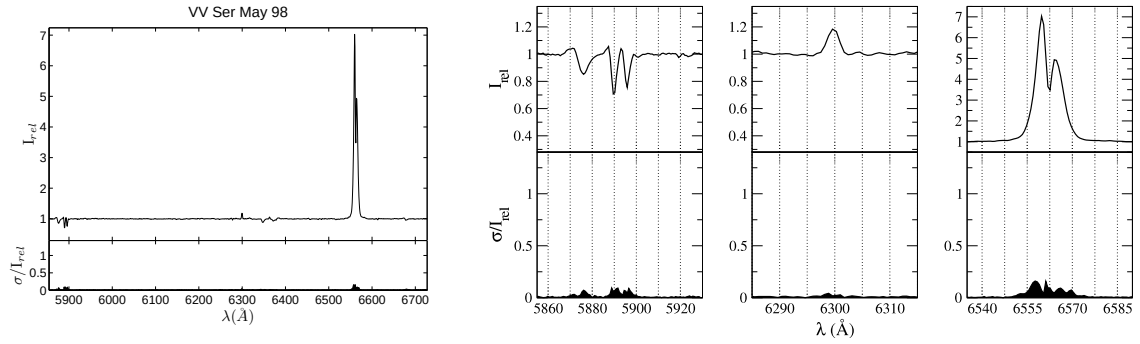
VV Ser May 98
I_{rel}
σ/I_{rel}
$\lambda(\AA)$
I_{rel}
σ/I_{rel}
λ (Å)

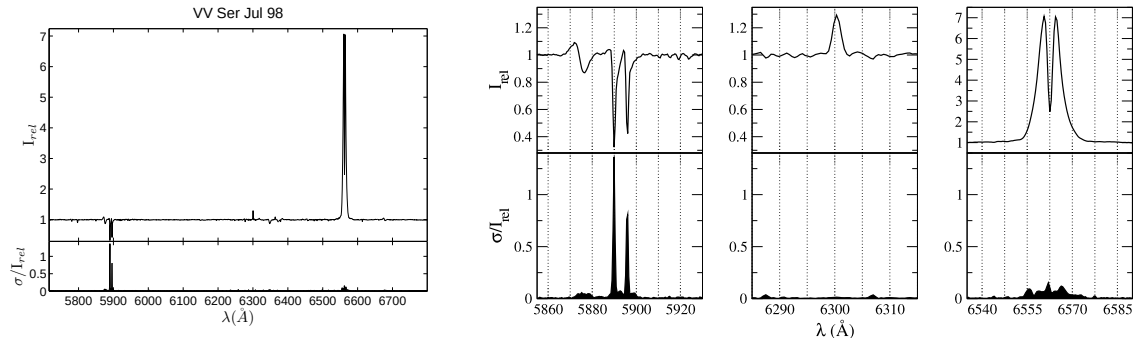
VV Ser Jul 98
I_{rel}
σ/I_{rel}
$\lambda(\AA)$
I_{rel}
σ/I_{rel}
λ (Å)

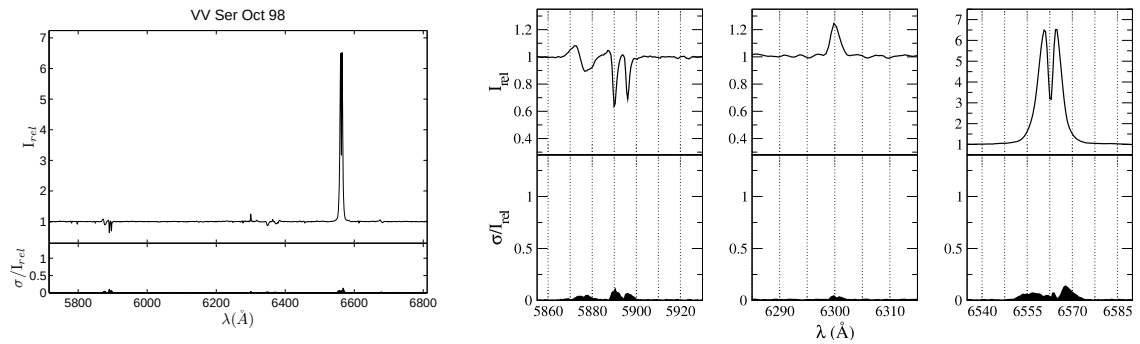
VV Ser Oct 98
I_{rel}
σ/I_{rel}
$\lambda(\AA)$
I_{rel}
σ/I_{rel}
λ (Å)

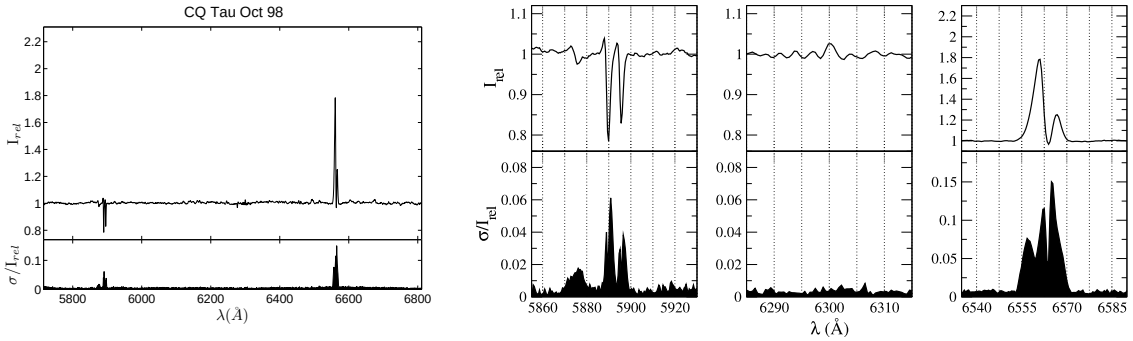
CQ Tau Oct 98
I_{rel}
σ/I_{rel}
$\lambda(\AA)$
I_{rel}
σ/I_{rel}
λ (Å)

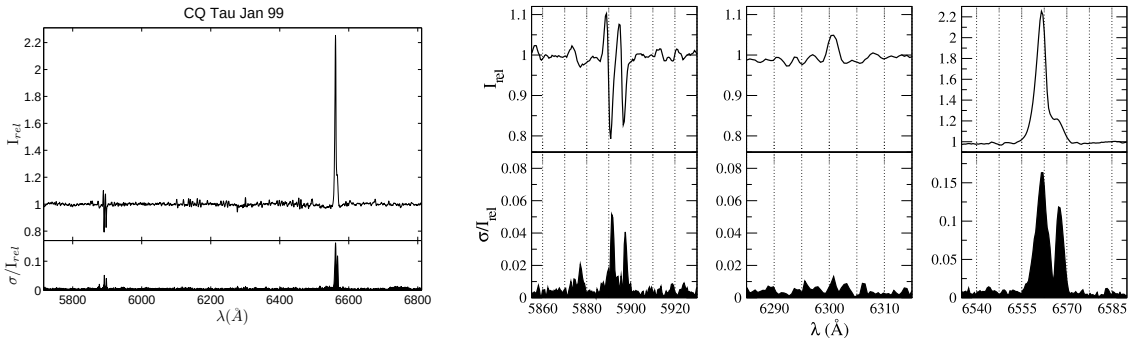
CQ Tau Jan 99
I_{rel}
σ/I_{rel}
$\lambda(\AA)$
I_{rel}
σ/I_{rel}
λ (Å)

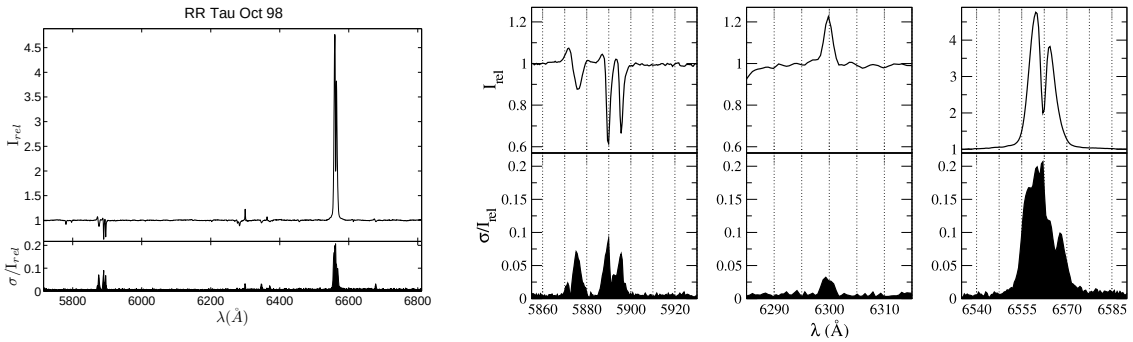
RR Tau Oct 98
I_{rel}
σ/I_{rel}
$\lambda(\AA)$
I_{rel}
σ/I_{rel}
λ (Å)

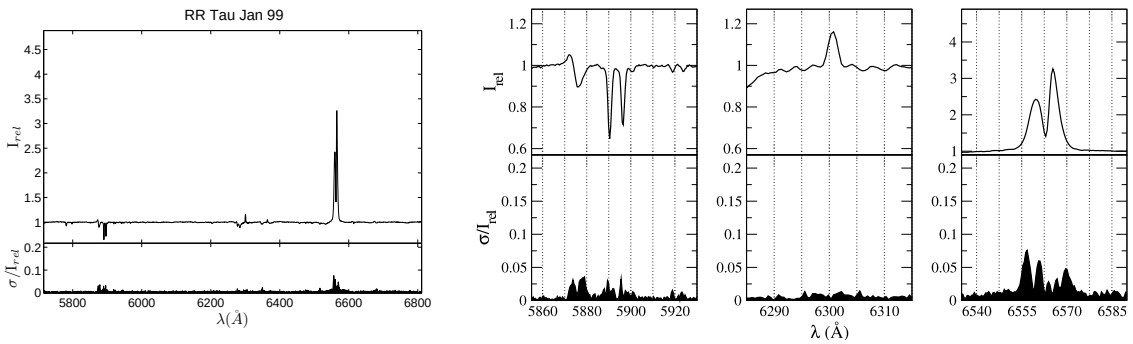
RR Tau Jan 99
I_{rel}
σ/I_{rel}
$\lambda(\AA)$
I_{rel}
σ/I_{rel}
λ (Å)

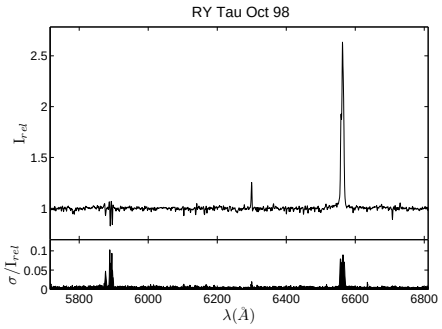
RY Tau Oct 98
I_{rel}
σ/I_{rel}
$\lambda(\AA)$

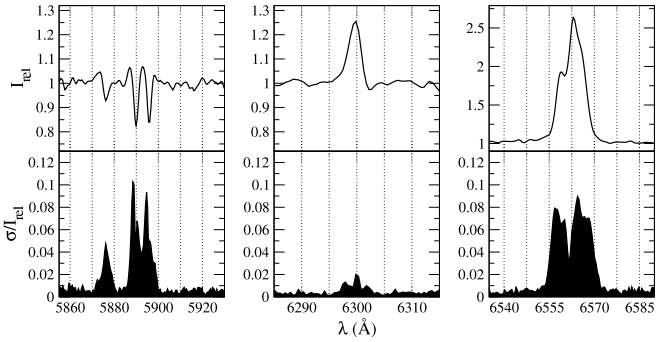
I_{rel}
σ/I_{rel}
λ (Å)

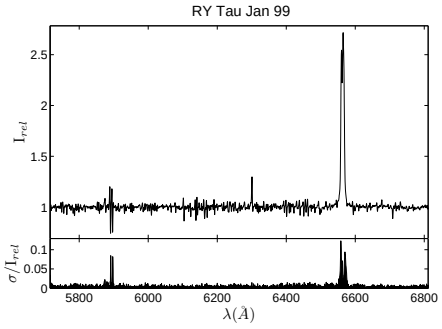
RY Tau Jan 99
I_{rel}
σ/I_{rel}
$\lambda(\AA)$

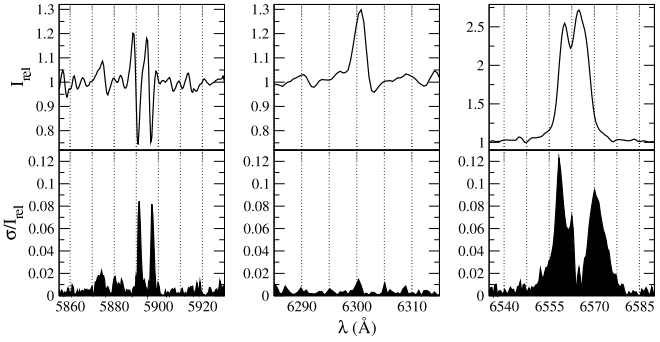
I_{rel}
σ/I_{rel}
λ (Å)

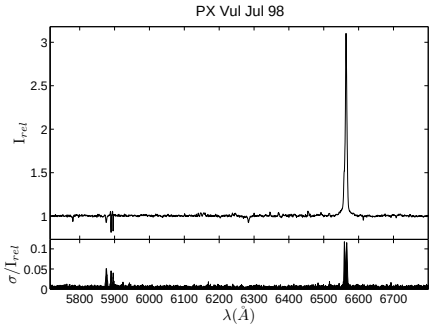
PX Vul Jul 98
I_{rel}
σ/I_{rel}
$\lambda(\AA)$

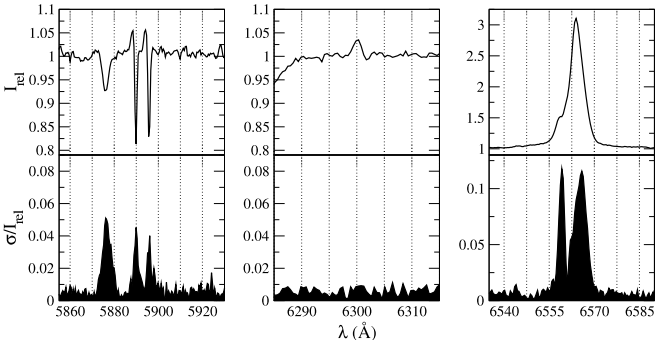
I_{rel}
σ/I_{rel}
λ (Å)

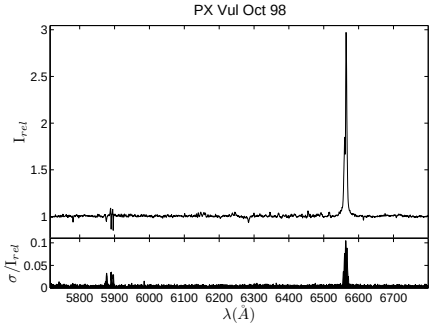
PX Vul Oct 98
I_{rel}
σ/I_{rel}
$\lambda(\AA)$

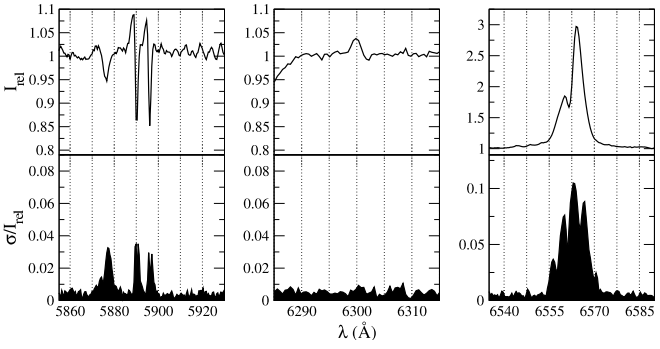
I_{rel}
σ/I_{rel}
λ (Å)

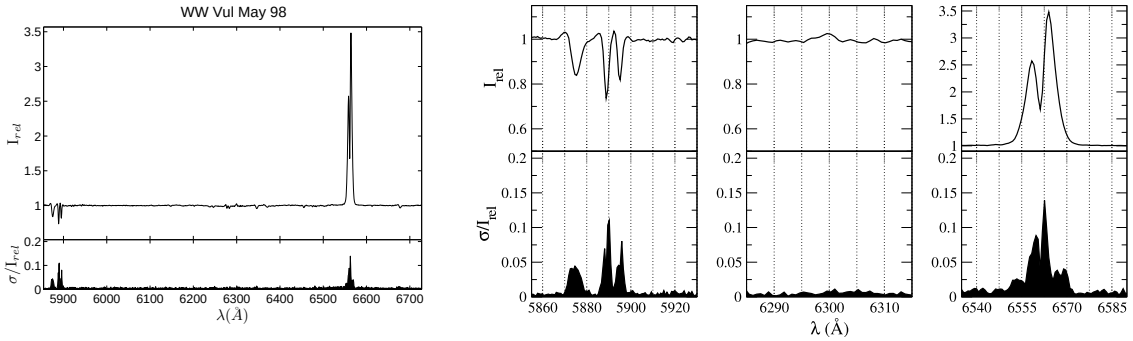
WW Vul May 98
I_{rel}
σ/I_{rel}
$\lambda(\AA)$
I_{rel}
σ/I_{rel}
λ (Å)

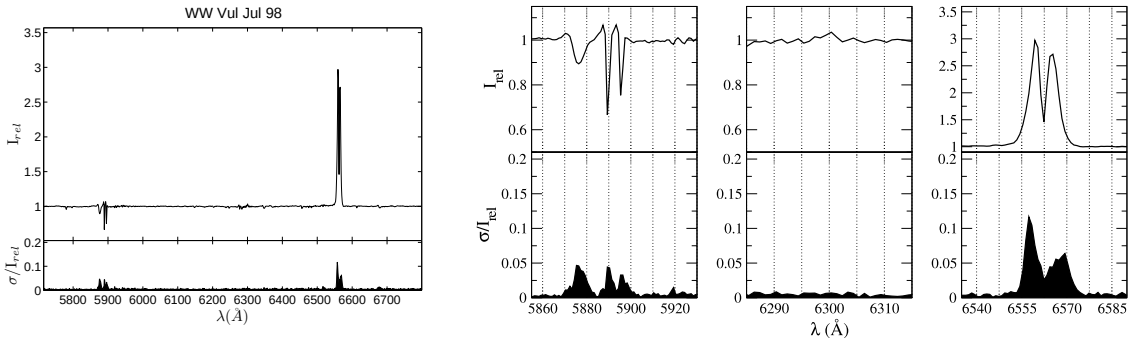
WW Vul Jul 98
I_{rel}
σ/I_{rel}
$\lambda(\AA)$
I_{rel}
σ/I_{rel}
λ (Å)

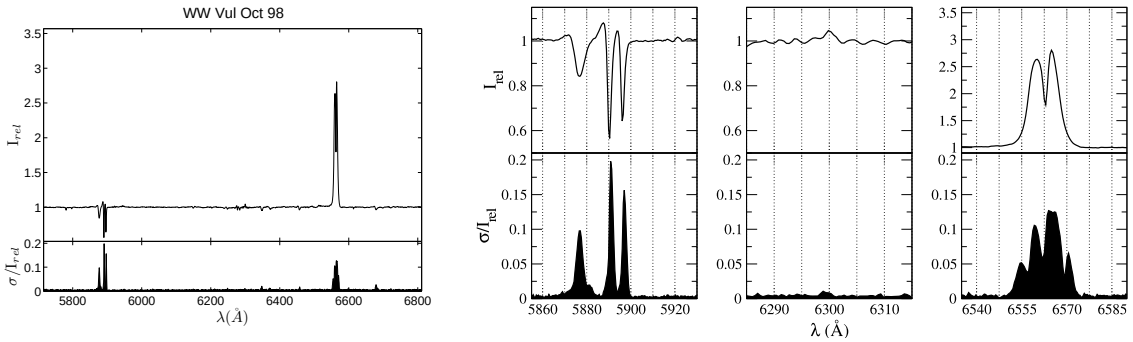
WW Vul Oct 98
I_{rel}
σ/I_{rel}
$\lambda(\AA)$
I_{rel}
σ/I_{rel}
λ (Å)

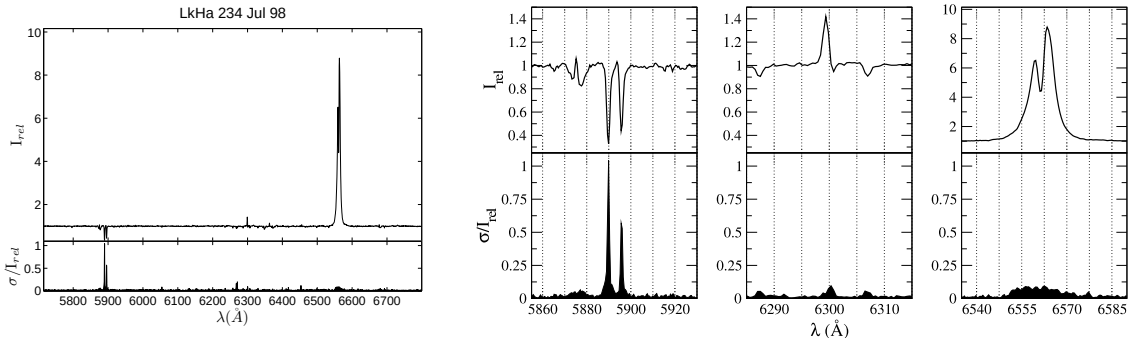
LkHa 234 Jul 98
I_{rel}
σ/I_{rel}
$\lambda(\AA)$
I_{rel}
σ/I_{rel}
λ (Å)

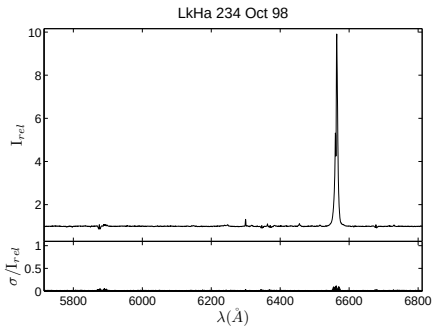
LkHa 234 Oct 98
I_{rel}
σ/I_{rel}
$\lambda(\AA)$

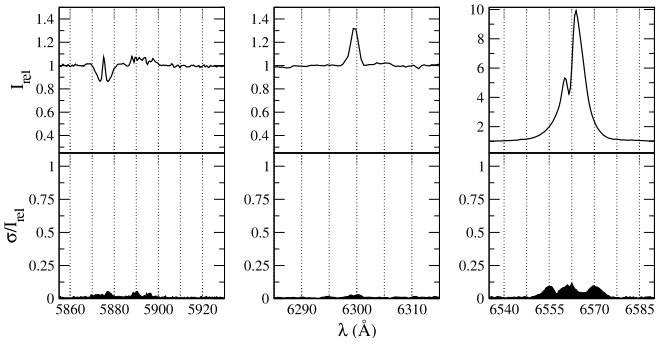
I_{rel}
σ/I_{rel}
λ (Å)

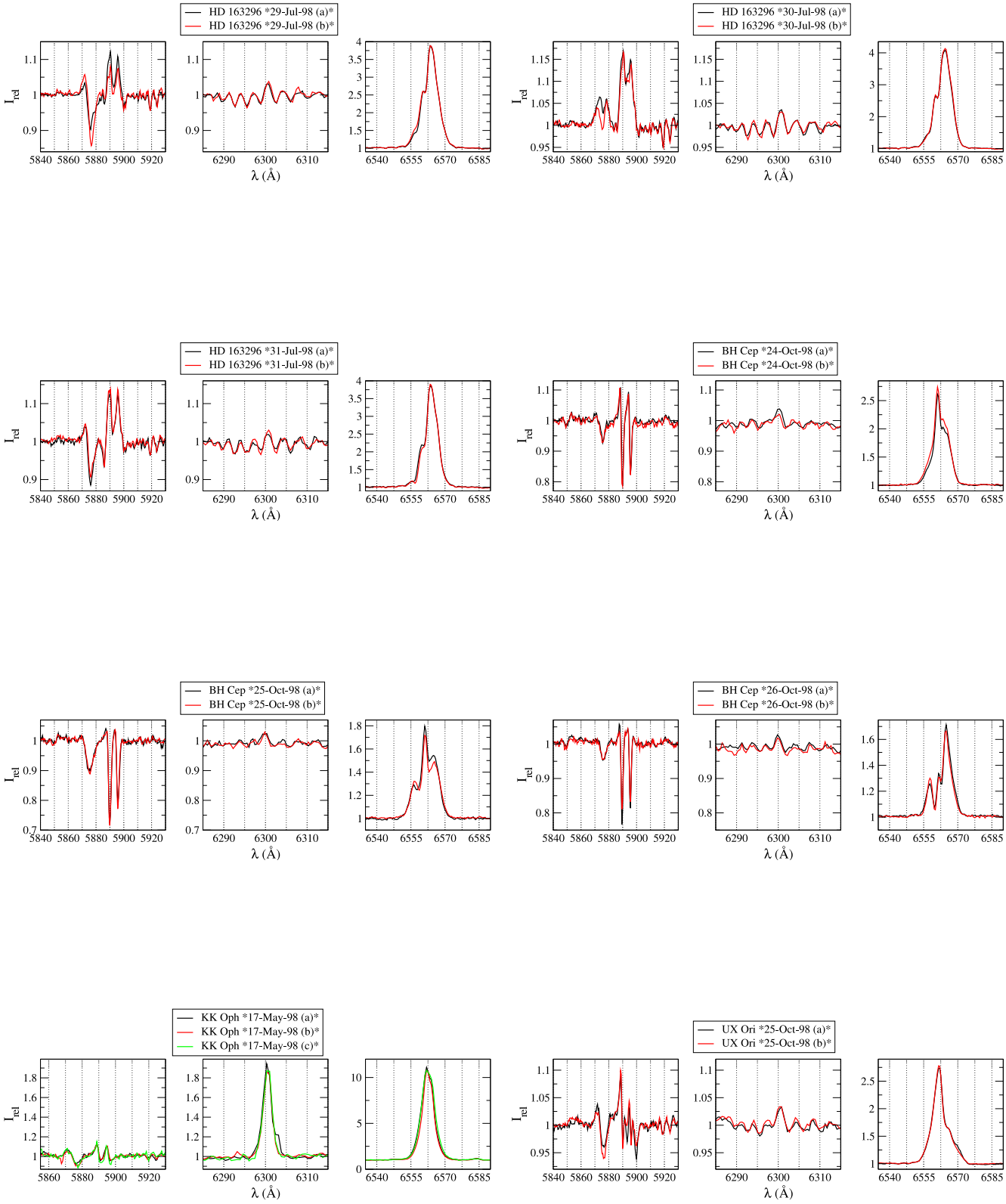
HD 163296 *29-Jul-98 (a)*
HD 163296 *29-Jul-98 (b)*
HD 163296 *30-Jul-98 (a)*
HD 163296 *30-Jul-98 (b)*
HD 163296 *31-Jul-98 (a)*
HD 163296 *31-Jul-98 (b)*
BH Cep *24-Oct-98 (a)*
BH Cep *24-Oct-98 (b)*
BH Cep *25-Oct-98 (a)*
BH Cep *25-Oct-98 (b)*
BH Cep *26-Oct-98 (a)*
BH Cep *26-Oct-98 (b)*
KK Oph *17-May-98 (a)*
KK Oph *17-May-98 (b)*
KK Oph *17-May-98 (c)*
UX Ori *25-Oct-98 (a)*
UX Ori *25-Oct-98 (b)*
I_rel
λ (Å)

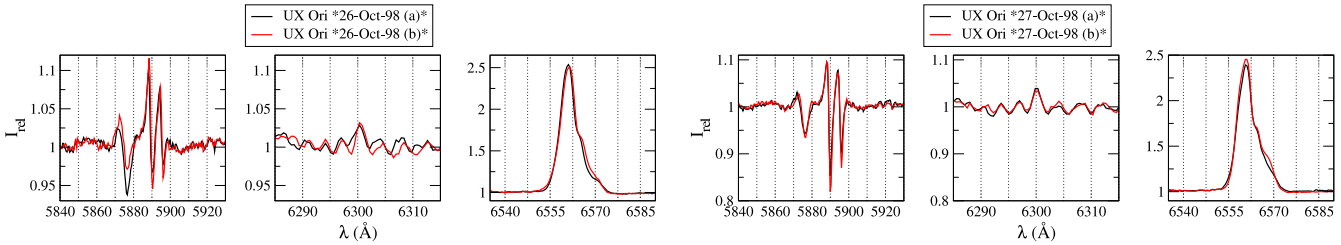
UX Ori *26-Oct-98 (a)*
UX Ori *26-Oct-98 (b)*
UX Ori *27-Oct-98 (a)*
UX Ori *27-Oct-98 (b)*
I_rel
λ (Å)

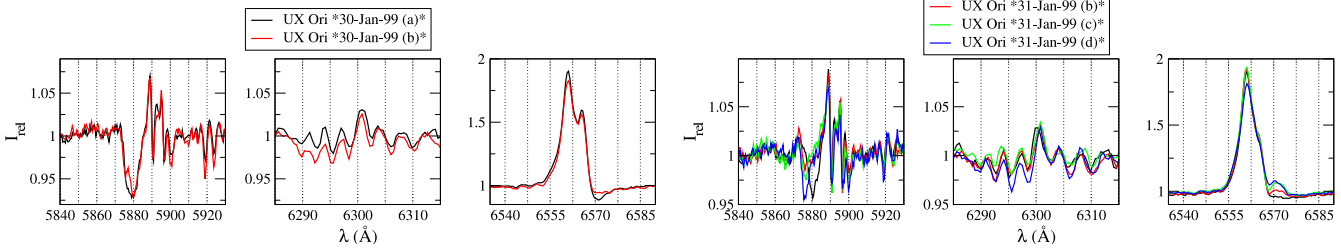
UX Ori *30-Jan-99 (a)*
UX Ori *30-Jan-99 (b)*
UX Ori *31-Jan-99 (a)*
UX Ori *31-Jan-99 (b)*
UX Ori *31-Jan-99 (c)*
UX Ori *31-Jan-99 (d)*
I_rel
λ (Å)

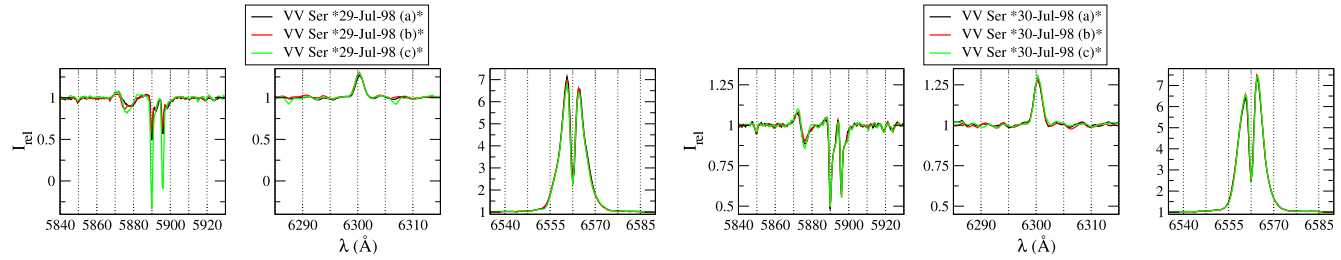
VV Ser *29-Jul-98 (a)*
VV Ser *29-Jul-98 (b)*
VV Ser *29-Jul-98 (c)*
VV Ser *30-Jul-98 (a)*
VV Ser *30-Jul-98 (b)*
VV Ser *30-Jul-98 (c)*
I_rel
λ (Å)

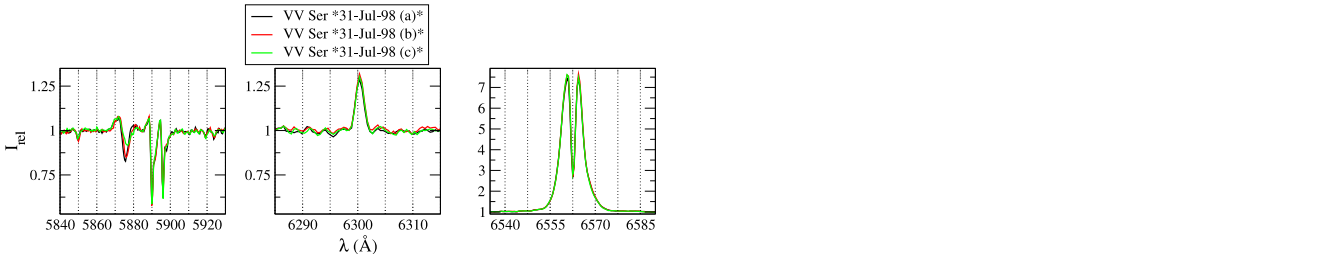
VV Ser *31-Jul-98 (a)*
VV Ser *31-Jul-98 (b)*
VV Ser *31-Jul-98 (c)*
I_rel
λ (Å)

Appendix C

Tables with multiwavelength photometry

Tables C.1, C.2 and C.3 show the compiled photometry for the stars in the sample. That has been divided according to the wavelength range-spatial region in the star-disk system.

Table C.1: Ultraviolet, optical and near-IR photometry

Star	IUE	U	B	V	R	I	J	H	K	L	M
HD 31648	√	7.84	7.78	7.62	7.46	7.43	6.98	6.41	5.67	4.61[1]	...
HD 34282	...	10.19	10.03	9.87	9.77	9.63	9.13	8.55	7.93	6.25[1]	6.16[1]
HD 34700	√	9.75	9.67	9.09	8.70	8.51	7.96	7.63	7.40	6.89[2]	...
HD 58647	√	*6.81**	6.92	6.85	6.73	6.73	*6.44**	*6.11**	*5.44**	...	...
HD 141569	√	7.22	7.20	7.09	7.00	7.04	6.66	6.58	6.51	6.69[3]	6.50[3]
HD 142666	√	9.41	9.16	8.68	8.31	8.01	7.30	6.74	6.09	5.05[3]	4.85[3]
HD 144432	√	8.47	8.46	8.14	7.82	7.53	*7.07*	*6.53*	*5.93*	5.00[3]	4.52[3]
HD150193	√	9.71	9.39	8.89	8.41	7.81	*6.89*	*6.14*	*5.33*	4.19[4]	3.76[4]
HD163296	√	6.95	6.92	6.86	6.73	6.67	6.17	5.49	4.71	3.51[4]	3.13[4]
HD 179218	√	7.55	7.46	7.38	7.25	7.21	6.99	6.61	5.95	4.68[1]	4.18[1]
HD 190073	...	*8.46*[1]	7.86	7.73	7.66	7.65	7.22	6.63	5.85	4.58[1]	...
AS 442	...	*11.90*[5]	11.56*	10.90*	*10.18*[5]	*9.95*[6]	8.65*	7.70*	6.62*	...	...
VX Cas	√	11.83	11.65	11.39	11.19	10.94	10.08	9.12	8.15	...	...
BH Cep	...	12.18	11.91	11.23	10.81	10.34	*9.69**	*8.99**	*8.31**	...	...
BO Cep	...	11.86	11.97	11.52	11.12	10.71	*10.32**	*9.85**	*9.58**	...	...
SV Cep	√	11.40	11.23	10.97	10.59	10.14	*9.35**	*8.56**	*7.74**	...	...
V1686Cyg	√	14.82	14.08	12.93	12.05	11.08	*9.45*[4]	*7.60*[4]	*6.17*[4]	4.57[4]	3.60[4]
R Mon	...	12.22*	12.46*	11.85*	10.96*	10.25*	*9.24*[4]	*7.60*[4]	*5.83*[4]	3.46[4]	2.55[4]
VY Mon	...	16.58	15.66	13.92	12.49	11.00	8.35	6.77	5.34[7]	3.16[7]	2.09[7]
51 Oph	√	4.78	4.82	4.83	4.72	4.61	*4.90**	*4.70**	*4.30**	...	...
KK Oph	...	12.86	12.58	12.06	11.56	10.82	8.77	7.19	5.78	3.98[4]	2.51[4]
T Ori	√	11.63	11.01	10.52	10.09	9.63	8.37	7.33	6.34	5.05[4]	4.60[4]
BF Ori	√	10.16	9.83	9.65	9.48	9.31	8.92	8.45	7.81	6.60[4]	5.80[4]
CO Ori	...	12.96	12.33	11.13	10.33	9.63	8.36	7.45	6.62	...	...
HK Ori	...	11.82	11.83	11.44	11.02	10.56	9.22	8.18	7.26	5.87[4]	5.10[4]
NV Ori	√	10.36	10.21	9.78	9.48	9.22	8.71	8.22	7.64	...	...
RY Ori	...	12.62	12.18	11.36	10.82	10.34	9.51	8.90	8.29	...	...
UX Ori	√	10.25	10.04	9.80	9.62	9.43	8.92	8.31	7.62	6.10[4]	5.51[4]
V346 Ori	...	10.55	10.42	10.16	9.99	9.80	9.50	9.03	8.55	6.80[8]	...
V350 Ori	...	12.74	12.27	11.76	11.38	10.96	9.88	9.13	8.28	...	...
XY Per	...	9.91	9.47	9.05	8.70	8.40	7.59	6.83	5.99	...	...
VV Ser	√	12.99	12.63	11.82	11.01	10.24	8.72	7.48	6.31	4.51[4]	4.40[4]
CQ Tau	√	9.75	9.50	8.98	8.63	8.33	7.76	7.09	6.31	...	...
RR Tau	√	11.64	11.42	10.92	10.58	10.17	8.99	7.97	7.07	5.80[4]	5.50[4]
RY Tau	...	11.87	11.48	10.47	9.67	8.87	7.23	6.22	5.34	4.29[9]	3.38[9]
PX Vul	...	12.56	12.29	11.51	10.90	10.30	9.31	8.52	7.77	...	...
WW Vul	√	11.46	11.02	10.64	10.38	10.12	9.24	8.40	7.46	...	...
LkHa 234	√	13.65	13.61	12.73	11.98	11.20	*9.50*[10]	*8.18*[10]	*7.09*[10]	...	...

Notes and references to Table C.1: Numbers are in magnitudes. Most UBVRIJHK photometry is from the simultaneous EXPORT multi-epoch observations (Oudmaijer et al. 2001; Eiroa et al. 2002), selecting the data at the brightest V-magnitude (italic numbers for the magnitudes not measured simultaneously to V). *SIMBAD (http://simbad.u-strasbg.fr/simbad/), [1]Malfait et al. (1998), [2]Coulson et al. (1998), [3]Sylvester et al. (1996) (includes L' magnitudes for HD 141569, HD 142666 and HD 144432), [4]Hillenbrand et al. (1992), [5]Bigay & Garnier (1970), [6]Merín (2004), [7]Herbst et al. (1982), [8]Glass & Penston (1974), [9]Kenyon & Hartmann (1995), [10]Monnier et al. (2009). Good quality IUE spectra are available for the stars indicated in Col. 2, which were used to derive synthetic UV photometry to fit the SEDs. Uncertainties are available in the references, being typically not larger than 0.05 magnitudes for the EXPORT data.

Table C.2: Mid-infrared photometry

Star	ISO	F_9	F_{12}	F_{18}	F_{25}	F_{60}	F_{65}	F_{90}	F_{100}	$F_{140}(F_{160})$	Add. Refs
HD 31648	...	9.118	12.25	8.070	10.34	11.11	10.17	11.73	12.52	11.85	(1)
HD 34282	...	0.736	0.700	...	1.630	10.40	10.04	...	10.72	9.745(9.353)	...
HD 34700	√	...	0.600	...	4.420	14.06	...	...	9.380	...	...
HD 58647	...	5.068	4.950	2.774	2.870	0.470	...	...	<7.360	...	...
HD 141569	√	0.518	0.550	0.866	1.870	5.530	6.52	3.917	3.470	3.915	...
HD 142666	√	5.152	8.570	6.578	11.21	7.230	5.259	5.729	5.460	5.966	...
HD 144432	√	...	7.530	7.326	9.360	5.760	5.290	4.916	3.290	...	(2)
HD150193	√	13.00	17.61	...	18.10	8.130	5.839	6.019	<16.25	...	(1,2)
HD163296	√	15.02	18.20	...	20.99	28.24	...	....	<40.62	...	(1,2,3)
HD 179218	√	14.74	23.44	27.88	43.63	29.92	19.43	16.80	17.35	9.263	(1)
HD 190073	...	5.734	7.160	4.457	5.530	1.920	...	1.119	<1.000	...	(1)
AS 442	...	...	<5.188	...	2.690	<9.620	...	...	<7.215	...	...
VX Cas	...	0.7554	1.540	1.327	2.640	1.400	...	0.7453	<15.17	...	...
BH Cep	...	0.481	0.475	0.767	0.116	0.138	...	0.117	<0.257	...	...
BO Cep	...	0.084	<0.070	0.118	0.285	1.430	...	1.566	<3.770	...	...
SV Cep	√	2.527	4.220	3.459	5.220	2.660	...	1.858	1.760	...	...
V1686Cyg	√	38.73	72.80	79.53	119.0	474.0	...	...	880.0	...	(2,4)
R Mon	...	34.07	54.65	79.24	132.1	121.3	129.5	78.13	148.5	66.37(62.26)	(1,2)
VY Mon	...	...	42.20	56.22	78.50	133.0	129.0	115.1	260.0	100.1	(4,5)
51 Oph	√	...	15.67	9.241	10.19	1.060	...	...	<5.970	...	(1)
KK Oph	...	9.100	9.870	8.276	9.560	6.140	3.905	4.431	<17.75	...	(2)
T Ori	...	...	...	...	...	...	...	...	...	...	(2)
BF Ori	√	...	0.960	...	0.800	<2.460	...	....	<29.81	...	(2)
CO Ori	...	1.677	1.580	1.537	1.400	<2.030	...	...	<10.88	...	...
HK Ori	...	2.708	3.800	2.882	4.080	<1.640	...	...	<70.37	...	(2)
NV Ori	...	1.247	...	...	...	...	...	...	...	...	...
RY Ori	...	0.665	0.750	0.788	0.710	<2.280	...	...	<19.09	...	...
UX Ori	√	...	2.680	3.112	3.690	2.850	2.736	2.129	3.760	4.282	(2,6)
V346 Ori	...	...	0.310	0.590	1.250	5.630	4.054	3.793	3.470	3.917	(7)
V350 Ori	...	0.556	0.940	1.008	1.750	1.190	...	...	<21.94	...	...
XY Per	...	4.302	3.850	3.404	4.060	4.910	3.958	4.367	<10.27	5.323	...
VV Ser	√	4.261	4.610	3.259	3.770	6.340	...	...	24.29	...	(2,8)
CQ Tau	√	4.855	6.210	12.88	20.66	21.88	15.89	16.25	13.65	10.30	(6)
RR Tau	√	1.365	1.740	1.367	2.200	4.460	...	...	36.68	...	(2)
RY Tau	...	12.28	17.47	15.43	26.07	15.29	...	...	13.65	...	(2,6,9)
PX Vul	...	0.433	0.550	0.569	0.860	<0.460	...	...	<5.060	...	
WW Vul	√	1.502	1.660	1.786	2.210	1.560	...	1.357	<9.590	...	(6)
LkHa 234	√	5.844	14.78	18.72	78.96	687.7	...	...	1215	757.2(880.6)	(1,4)

Notes and references to Table C.2: Fluxes are in Jy. IRAS fluxes at 12, 25, 60 and 100 μm are from SIMBAD (http://simbad.u-strasbg.fr/simbad/) by default, and from the IRAS Faint Source Reject Catalog (IPAC 1992) for AS 442, IRAS Faint Source Catalog, $|b| > 10$, Version 2.0 for BH Cep and BO Cep, and from Casey & Harper (1990) for VY Mon. AKARI fluxes at 9, 18, 65, 90, 140 and 160 μm are from AKARI/IRC All-Sky Survey Point Source Catalogue (Version 1.0) and AKARI/FIS All-Sky Survey Bright Source Catalogue (Version 1.0). Additional references are given in Col. 12 for photometry in the following wavelengths: (1): 10.7 μm from Monnier et al. (2009); (2): 10.5(N) and 20.1(Q) μm from Hillenbrand et al. (1992); (3): Spitzer IRAC 5.8 μm from the GLIMPSE catalogue; (4): Spitzer IRAC 3.6, 4.5, 5.8 and 8.0 μm from the "Spitzer survey of young stellar clusters" (Gutermuth et al. 2009); (5): 10.5(N) and 20.1(Q) μm from Herbst et al. (1982); (6): ISO photometry at 6.9, 9.6, 17, and 28.2 μm from Thi et al. (2001); (7): Spitzer IRAC 5.8, 8.0 and MIPs 24 μm from Hernández et al. (2006); (8,9): Spitzer IRAC 3.6, 4.5, 5.8, 8.0 and MIPs 24, 70 μm from the "Spitzer survey of Serpens YSO population" (Harvey et al. 2007) and from Robitaille et al. (2007), respectively. Photometry extracted from ISO data is available in Merín (2004) for the stars indicated in Col. 2. The typical uncertainty is not larger than 10 % for IRAS and 5 % for AKARI data.

Table C.3: Sub-mm and mm photometry for a sub-sample of stars

Star	F(1.3mm) (mJy)	F(λ) (mJy)((mm))	Ref.
HD 31648	360±24	3300(0.45); 780(0.85); 235(1.4); 39.9(2.7); 35.2(2.8)	(1,2,3)
HD 34282	110±10	2700(0.45); 409(0.80); 360(0.85); 183(1.1); 24(2.6); 5.0(3.4)	(4,5,6)
HD 34700	11.7±1.1*	218(0.45); 41(0.85); 39(1.1)	(6,7,8)
HD 141569	9.0±4.0	65(0.45); 11(0.85)	(5,9)
HD 142666	127±9	1090(0.45); 351(0.80); 180(1.1); <63(2.0)	(6)
HD 144432	37±3	103(0.80); 129(0.85); 69(1.1)	(5.6.9)
HD150193	45±4.5	101(0.85)	(5,10)
HD163296	780±31	10660(0.35); 5560(0.45); 3380(0.60); 2650(0.75); 2320(0.80); 1920(0.85); 1020(1.1)	(11)
HD 179218	71±7	7.6(2.6)	(12)
VX Cas	<6	...	(13)
SV Cep	7±2	...	(13)
V1686Cyg	<4.8*	...	(14)
R Mon	100±10	1980(0.35); 1560(0.45); 217(0.80); 77(1.1); 1.17(20); 0.37(36); 0.29(60)	(11,15,16)
VY Mon	120±12	18000(0.37); 1.5(60)	(10,17)
KK Oph	52±5.2	109(0.80); 36(1.1); 0.24(36)	(5,16)
T Ori	130±28	...	(15)
BF Ori	6±2	...	(13)
CO Ori	<4.0	...	(13)
HK Ori	<100	...	(15)
UX Ori	23±2	3.8(2.6); 0.8(7.0)	(13,18,19)
VV Ser	<20	...	(15)
CQ Tau	143±8.4	2.6(7.0)	(12,19)
RR Tau	<20	...	(15)
RY Tau	212±21*	2439(0.35); 1920(0.45); 560(0.85)	(20,21)
WW Vul	10.5±1.0	...	(13)
LkHa 234	827±82.7*	60000(0.45); 4200(0.80); 3400(0.85); 2.67(20); 1.82(36); 1.65(60)	(16)

Notes. The second column shows the fluxes used to compute the disk masses in Table 5.1. Those tagged with * were measured at 1.35 mm (HD 34700), 2.70 mm (V1686 Cyg) and 1.20 mm (RY Tau and LkHa 234). An uncertainty of 10% is assigned when that is not provided in the reference. (1): Mannings & Sargent (1997), (2): Sandell & Weintraub (2003), (3): Piétu et al. (2006),(4): Piétu et al. (2003), (5): Sandell et al. (2011), (6): Sylvester et al. (1996),(7): Sylvester et al. (2001), (8): Sheret et al. (2004), (9): Walker & Butner (1995), (10): Alonso-Albi et al. (2009), (11): Mannings (1994), (12): Mannings & Sargent (2000), (13): Natta et al. (1997), (14): Natta et al. (2000), (15): Hillenbrand et al. (1992), (16): Pezzuto & Strafella (1997), (17): Casey & Harper (1990), (18): Acke & van den Ancker (2006), (19): Testi et al. (2001), (20): Robitaille et al. (2007), (21): Altenhoff et al. (1994)

Appendix D

Spectral energy distributions

The first figures show the UV-optical-IR SEDs (see Tables C.1 and C.2) of the stars in the sample. Triangles are photometric upper limits. For each panel, the best fit is the black-solid line and the models fitting with χ^2 - $\chi^2_{best} \leq 3n$ are the grey-solid lines, being n the number of datapoints per star (see Robitaille et al. 2007). The best stellar (deredenned) photosphere is indicated with a dashed line.

The remaining figures show the submm and mm SEDs for a subsample of stars with fluxes available at $\lambda \geq 0.35$ mm ($\log \nu$ [GHz] ≤ 2.9, see Table C.2). The best graybody fits yielding the indicated values for T_D and β are shown. Fluxes at $\lambda \leq 2.0$ mm ($\log \nu$ [GHz] ≥ 2.1) are weighted stronger in the fits.

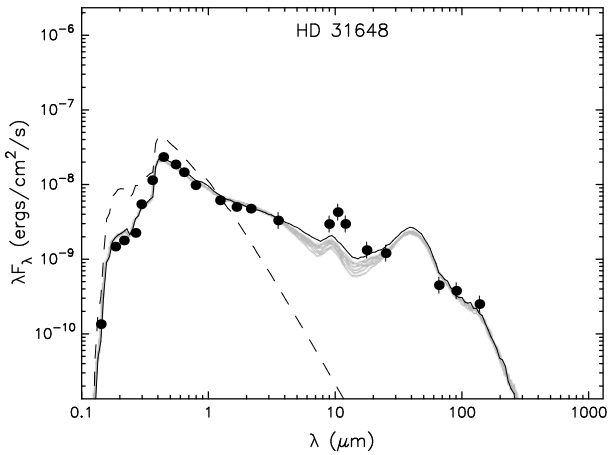
HD 31648
λF_λ (ergs/cm²/s)
λ (μm)

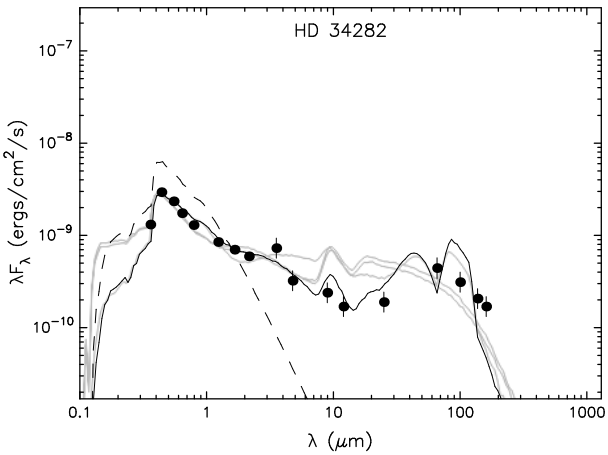
HD 34282
λF_λ (ergs/cm²/s)
λ (μm)

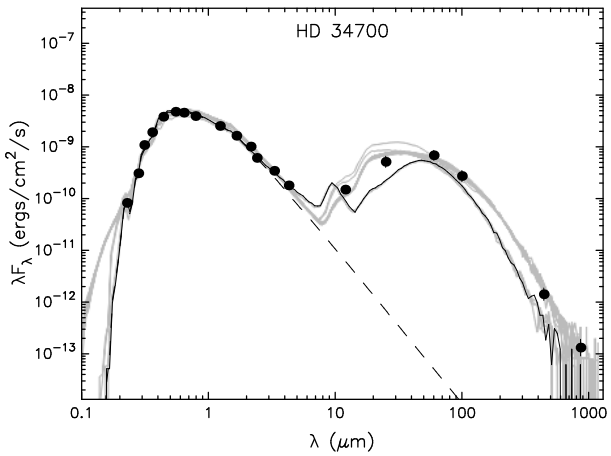
HD 34700
λF_λ (ergs/cm²/s)
λ (μm)

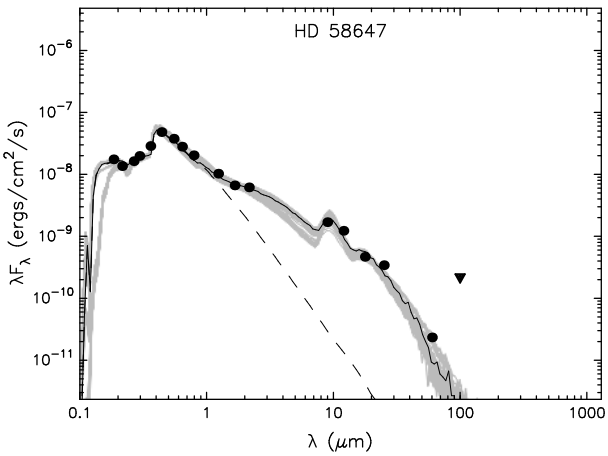
HD 58647
λF_λ (ergs/cm²/s)
λ (μm)

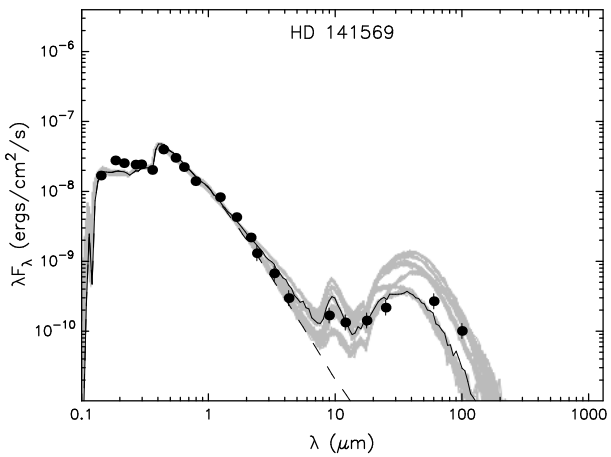
HD 141569
λF_λ (ergs/cm²/s)
λ (μm)

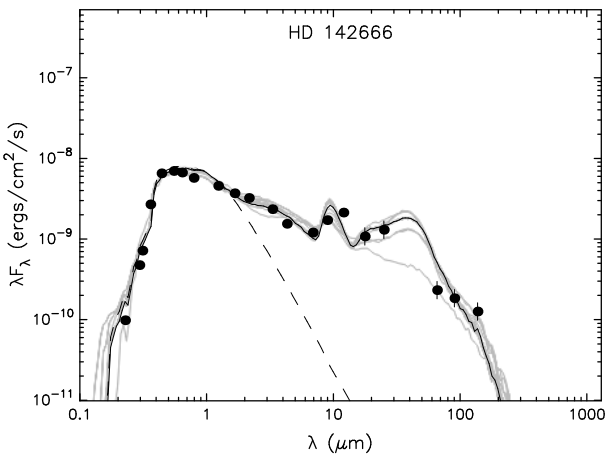
HD 142666
λF_λ (ergs/cm²/s)
λ (μm)

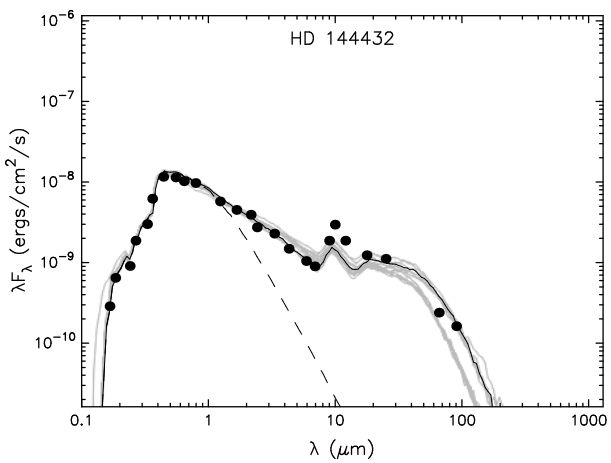
HD 144432
λF_λ (ergs/cm²/s)
λ (μm)

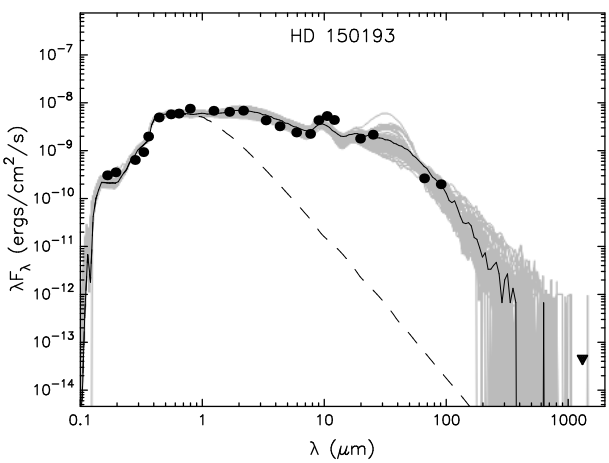
HD 150193
λF_λ (ergs/cm²/s)
λ (μm)

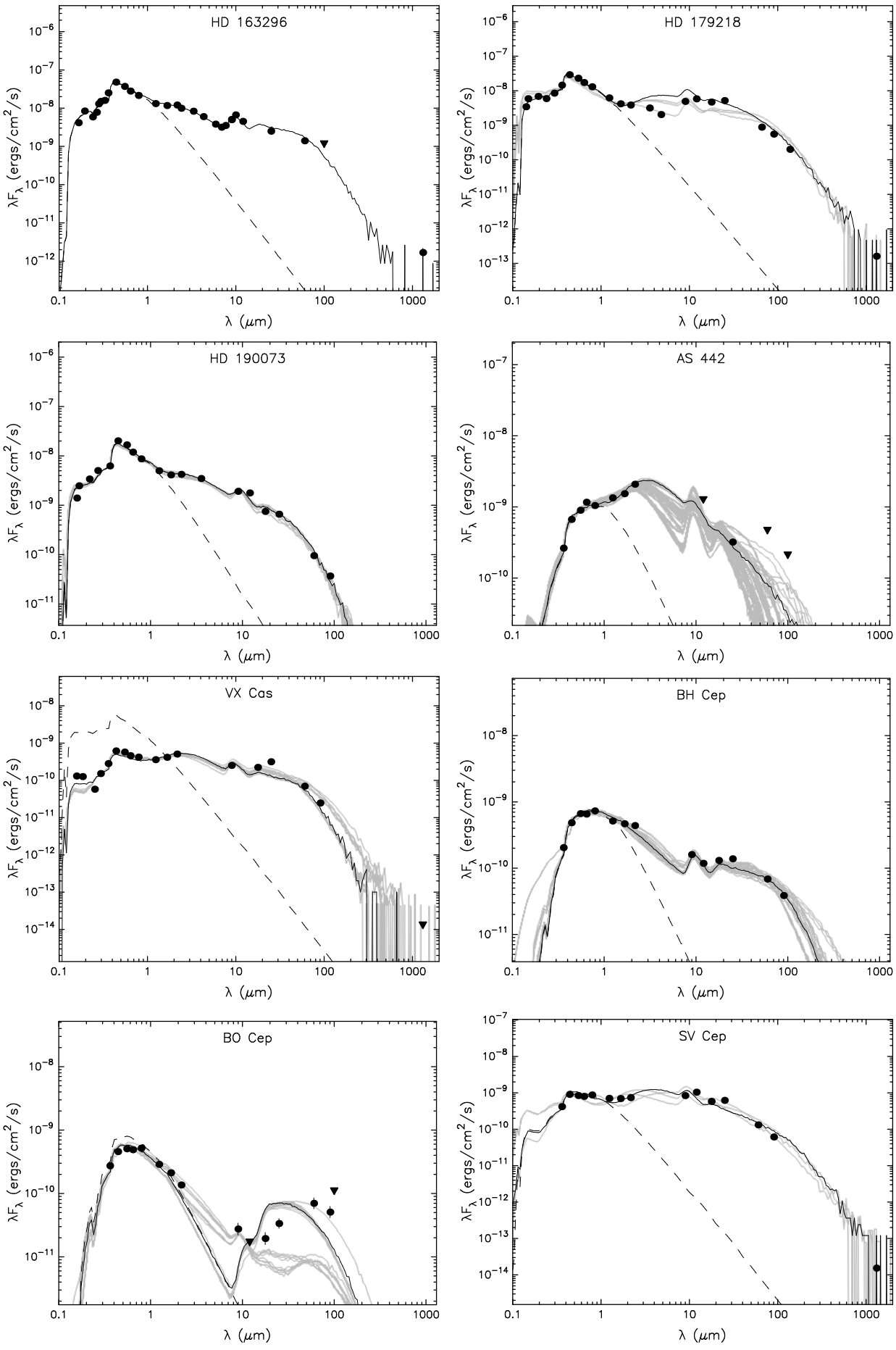
HD 163296
HD 179218
HD 190073
AS 442
VX Cas
BH Cep
BO Cep
SV Cep
λF_λ (ergs/cm²/s)
λ (μm)

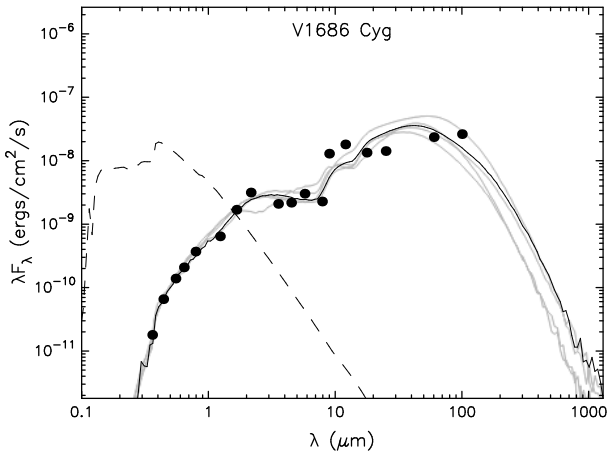
V1686 Cyg
λF_λ (ergs/cm²/s)
λ (μm)

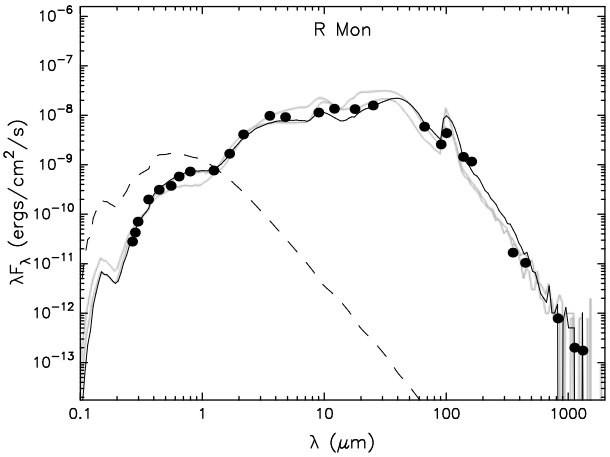
R Mon
λF_λ (ergs/cm²/s)
λ (μm)

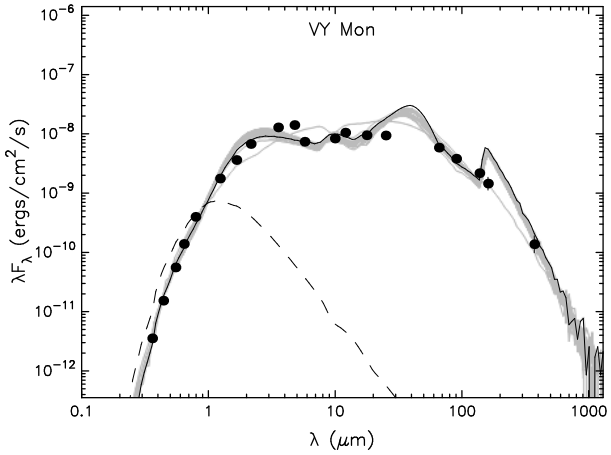
VY Mon
λF_λ (ergs/cm²/s)
λ (μm)

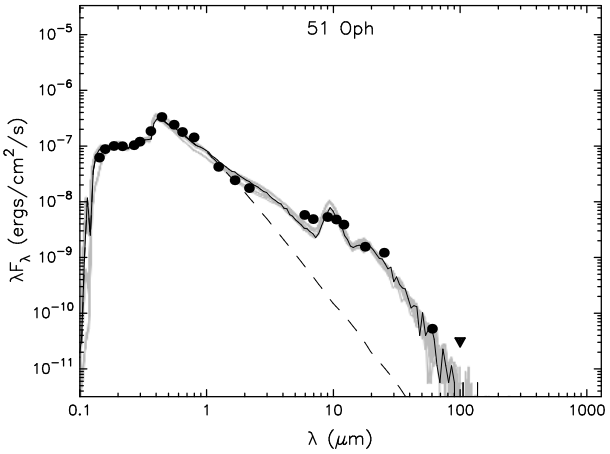
51 Oph
λF_λ (ergs/cm²/s)
λ (μm)

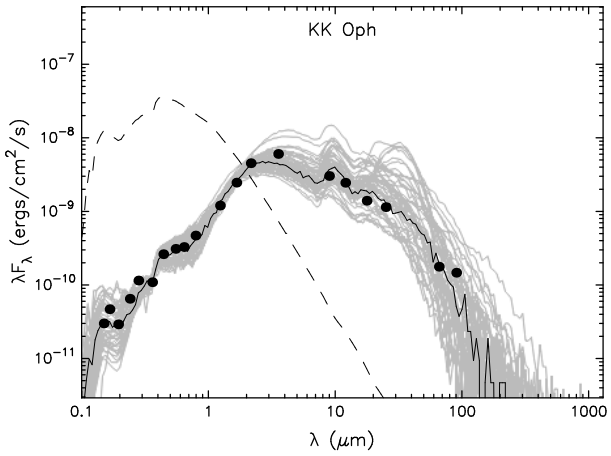
KK Oph
λF_λ (ergs/cm²/s)
λ (μm)

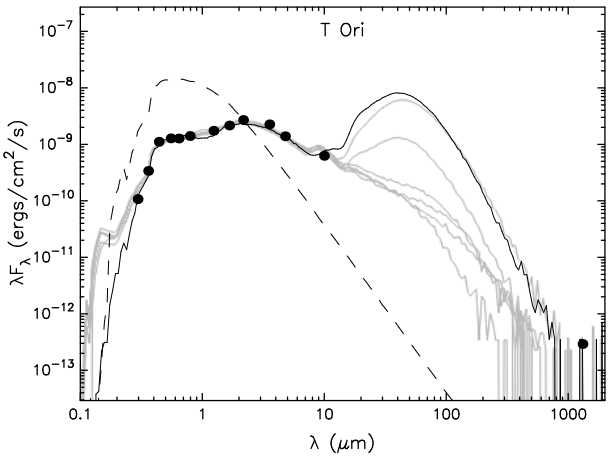
T Ori
λF_λ (ergs/cm²/s)
λ (μm)

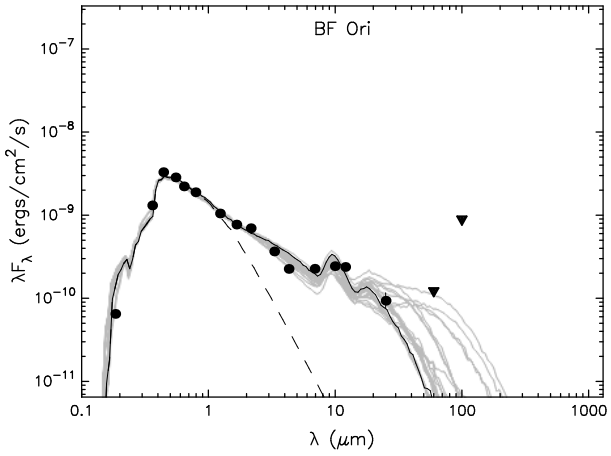
BF Ori
λF_λ (ergs/cm²/s)
λ (μm)

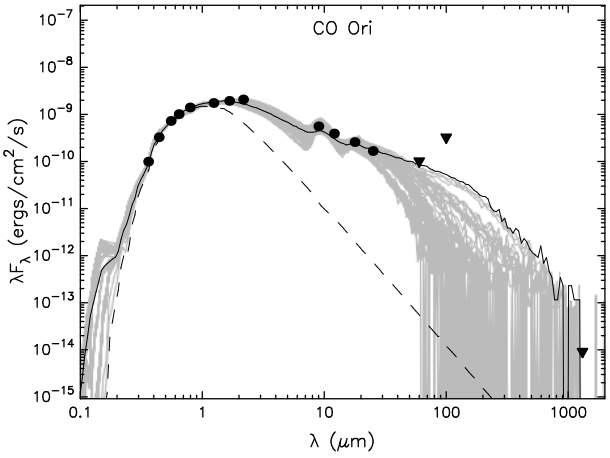
CO Ori
λF_λ (ergs/cm²/s)
λ (μm)

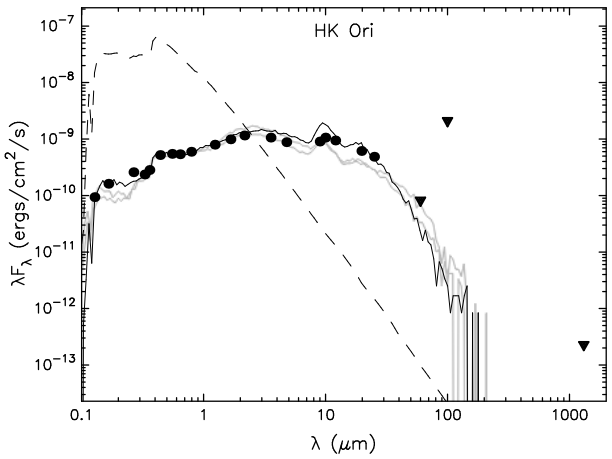
HK Ori
λF_λ (ergs/cm²/s)
λ (μm)

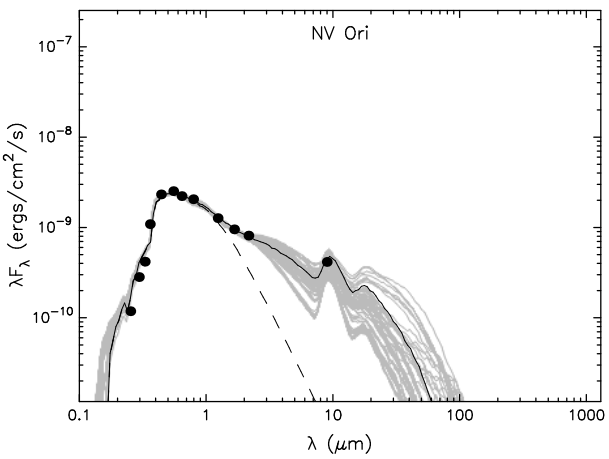
NV Ori
λF_λ (ergs/cm²/s)
λ (μm)

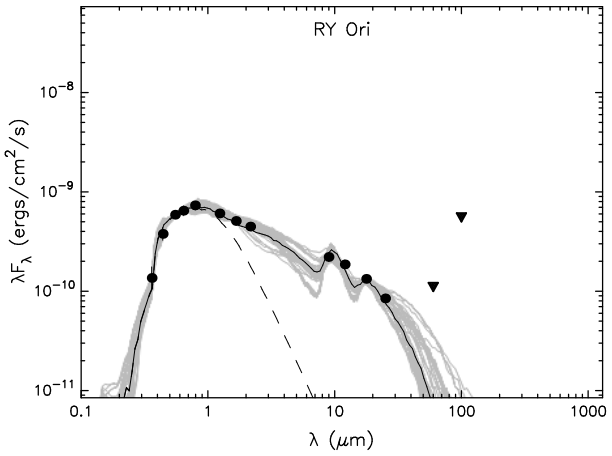
RY Ori
λF_λ (ergs/cm²/s)
λ (μm)

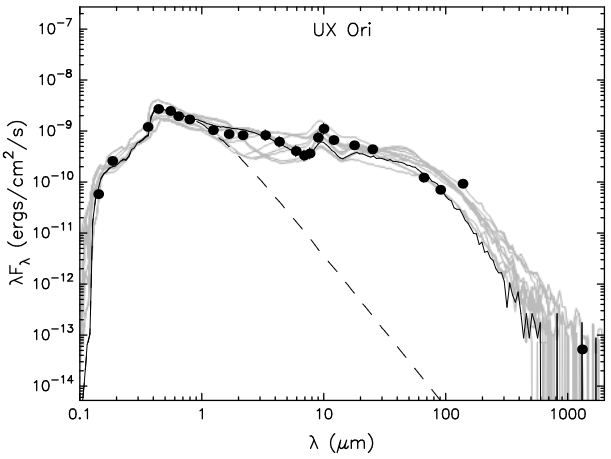
UX Ori
λF_λ (ergs/cm²/s)
λ (μm)

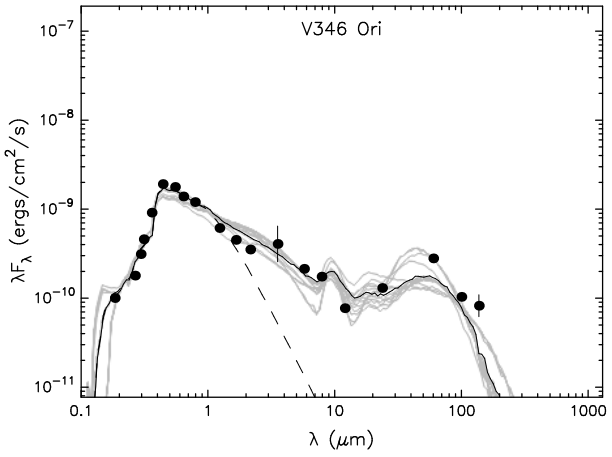
V346 Ori
λF_λ (ergs/cm²/s)
λ (μm)

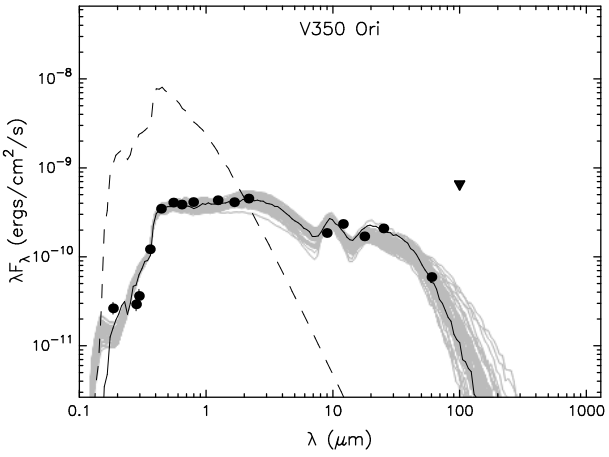
V350 Ori
λF_λ (ergs/cm²/s)
λ (μm)

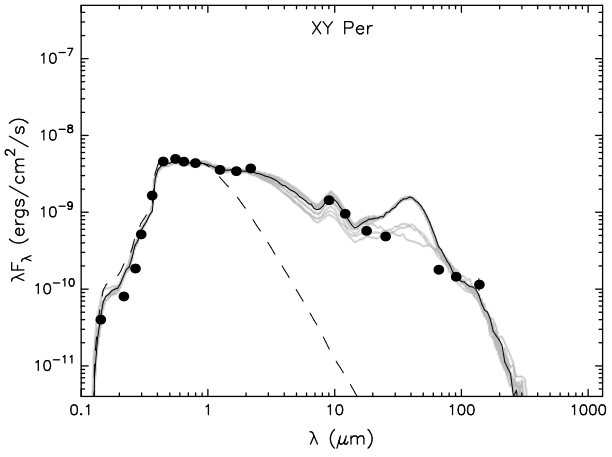
XY Per
λF_λ (ergs/cm²/s)
λ (μm)

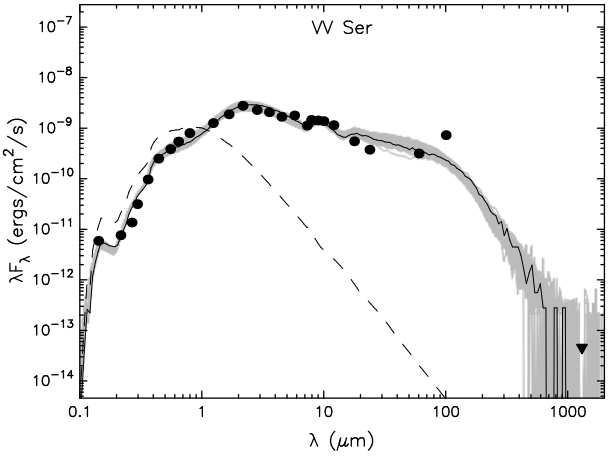
VV Ser
λF_λ (ergs/cm²/s)
λ (μm)

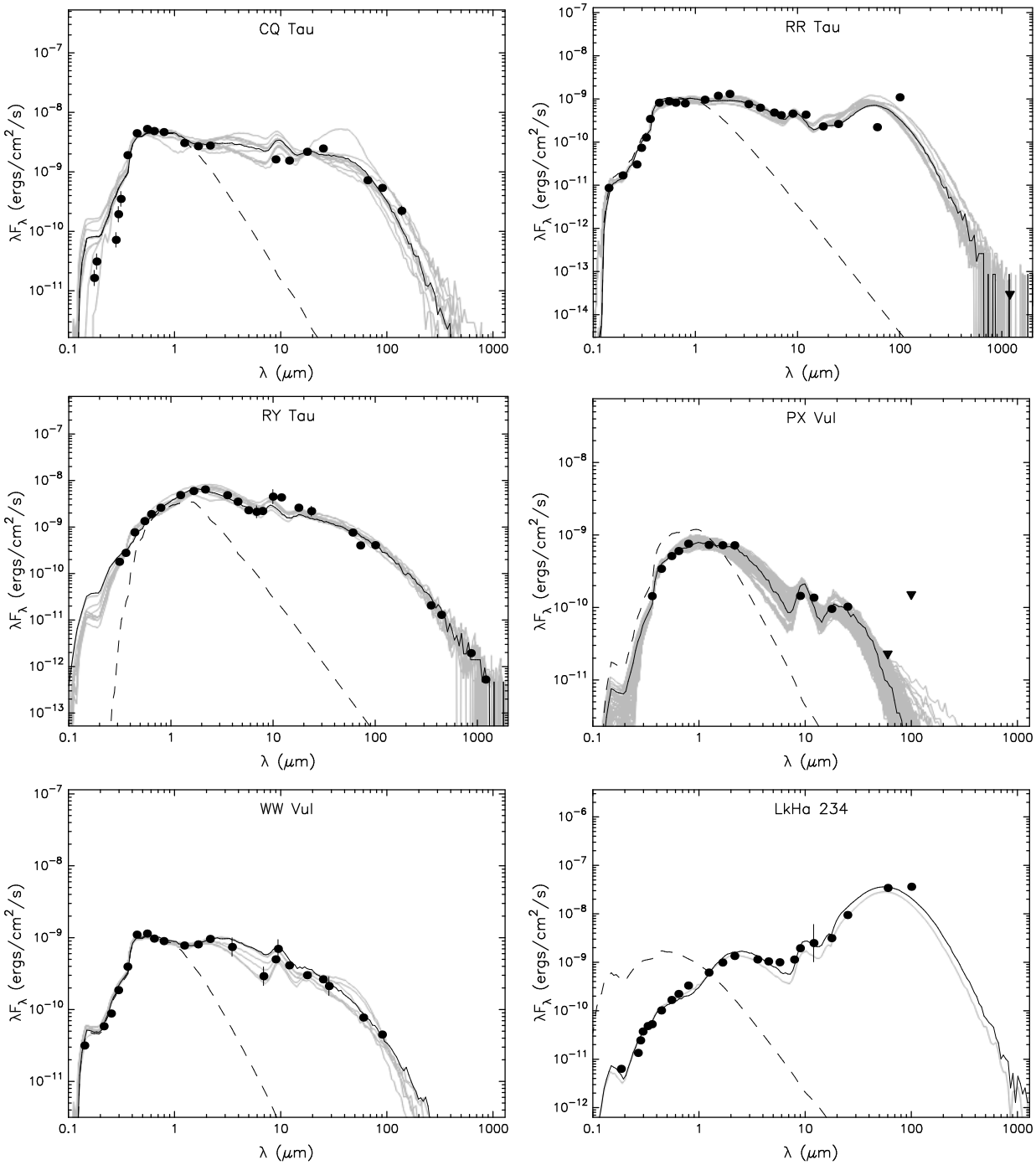
CQ Tau
RR Tau
RY Tau
PX Vul
WW Vul
LkHa 234
λF_λ (ergs/cm²/s)
λ (μm)

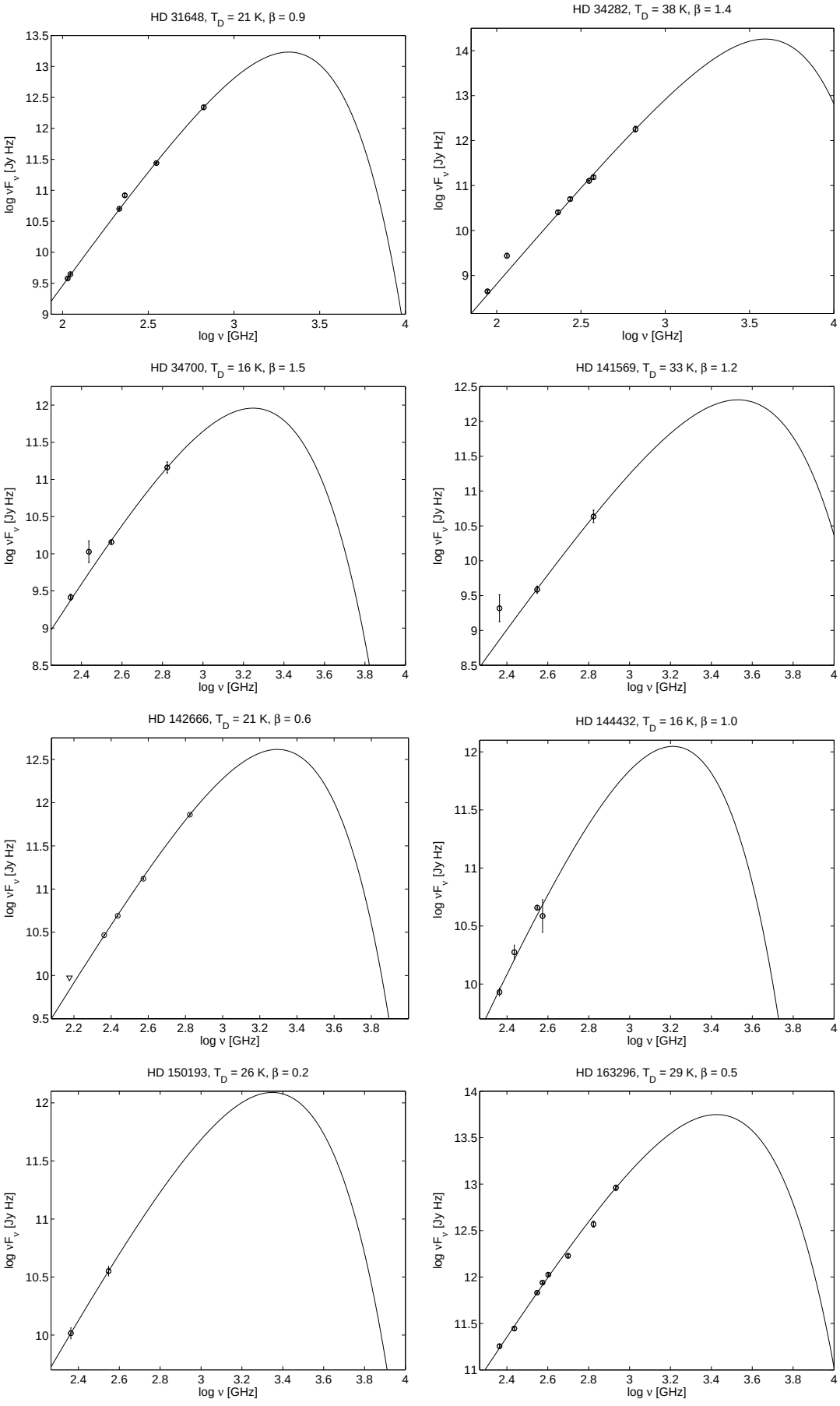
HD 31648, T_D = 21 K, β = 0.9
HD 34282, T_D = 38 K, β = 1.4
HD 34700, T_D = 16 K, β = 1.5
HD 141569, T_D = 33 K, β = 1.2
HD 142666, T_D = 21 K, β = 0.6
HD 144432, T_D = 16 K, β = 1.0
HD 150193, T_D = 26 K, β = 0.2
HD 163296, T_D = 29 K, β = 0.5
log νF_ν [Jy Hz]
log ν [GHz]

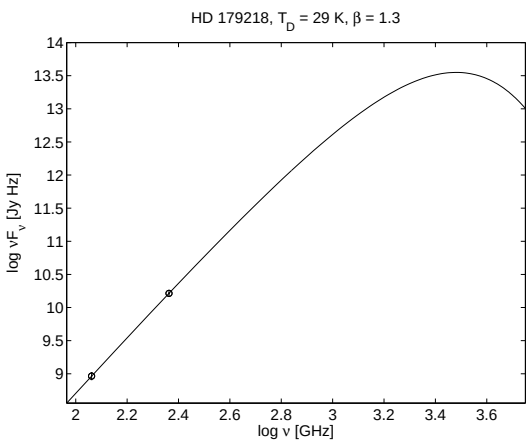
HD 179218, T_D = 29 K, β = 1.3
log νF_ν [Jy Hz]
log ν [GHz]

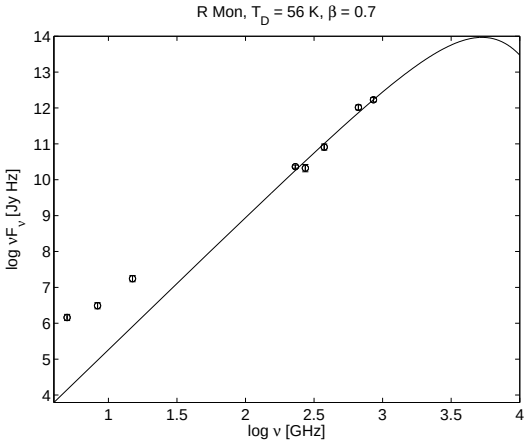
R Mon, T_D = 56 K, β = 0.7
log νF_ν [Jy Hz]
log ν [GHz]

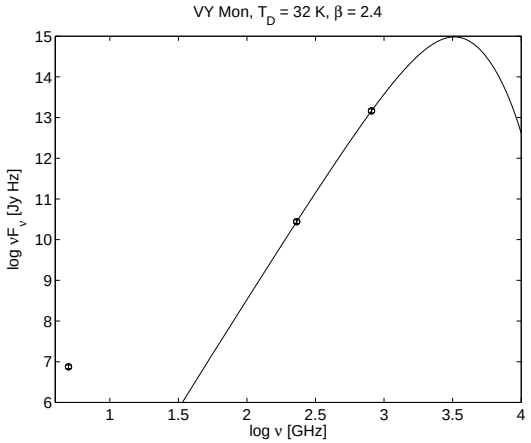
VY Mon, T_D = 32 K, β = 2.4
log νF_ν [Jy Hz]
log ν [GHz]

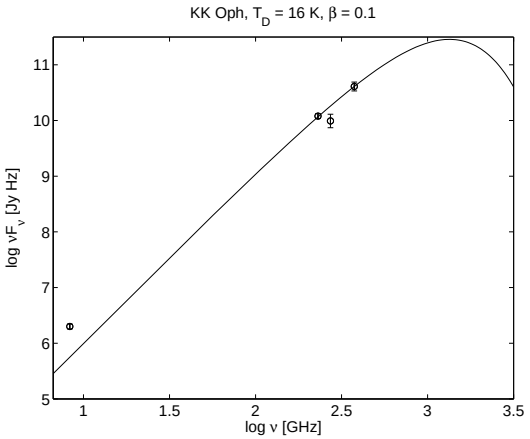
KK Oph, T_D = 16 K, β = 0.1
log νF_ν [Jy Hz]
log ν [GHz]

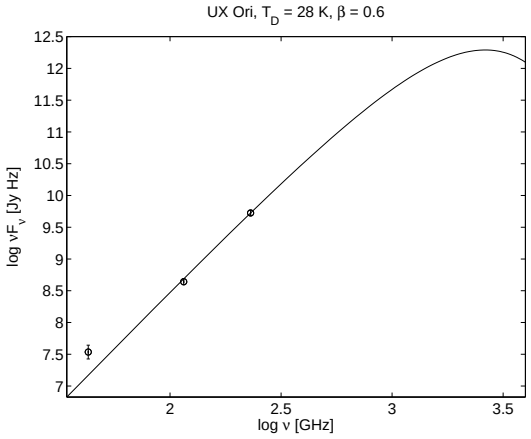
UX Ori, T_D = 28 K, β = 0.6
log νF_ν [Jy Hz]
log ν [GHz]

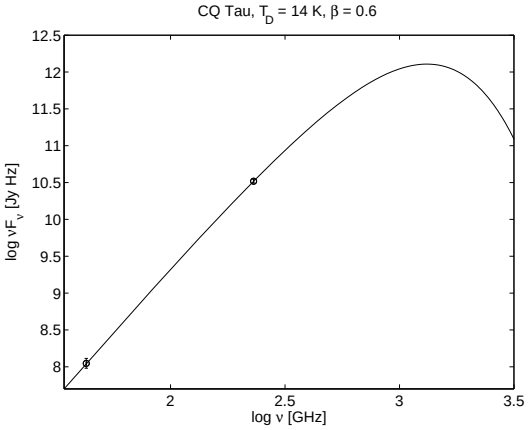
CQ Tau, T_D = 14 K, β = 0.6
log νF_ν [Jy Hz]
log ν [GHz]

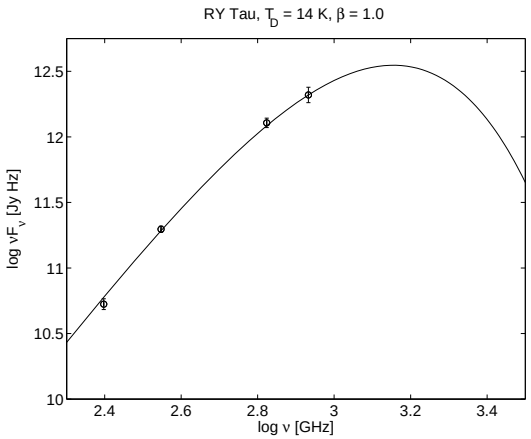
RY Tau, T_D = 14 K, β = 1.0
log νF_ν [Jy Hz]
log ν [GHz]

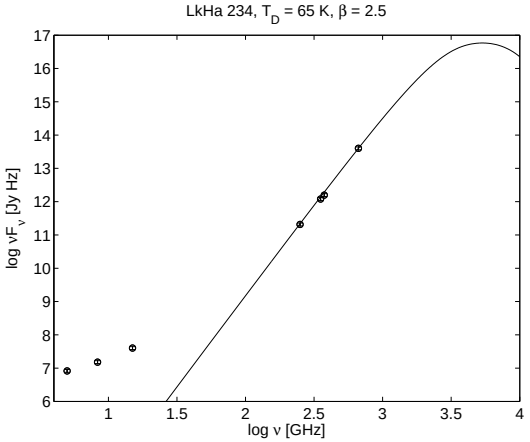
LkHa 234, T_D = 65 K, β = 2.5
log νF_ν [Jy Hz]
log ν [GHz]

Appendix E

List of Accronyms

CS: CircumStellar
CST: Carlos Sanchez Telescope
CTT: Classical T-Tauri
EW: Equivalent Width
HAeBe: Herbig Ae/Be
HAe: Herbig Ae
HBe: Herbig Be
IDS: Intermediate Dispersion Spectrograph
IMTT: Intermediate-Mass T-Tauri
INT: Isaac Newton Telescope
IR: InfraRed
MA: Magnetospheric Accretion
MS: Main Sequence
nIR: near-InfraRed
NOT: Nordic Optical Telescope
PAH: Polycyclic Aromatic Hydrocarbon
PMS: Pre-Main Sequence
SED: Spectral Energy Distribution.
UV: UltraViolet
WTT: Weak T-Tauri

Bibliography

Acke, B., van den Ancker, M.E., Dullemond, C.P., van Boekel, R., Waters, L.B.F.M. 2004, A&A, 422, 621

Acke, B. & van den Ancker, M.E. 2004, A&A, 426, 151

Acke, B., van den Ancker, M.E., Dullemond, C.P. 2005, A&A, 436, 209

Acke, B. & van den Ancker, M.E. 2006, A&A, 457, 171

Acke, B., Bouwman, J., Juhász, A. et al. 2010, ApJ, 718, 558

Alecian, E., Wade, G.A., Catala, C. et al. 2007, IAUS, 243, 43

Alencar, S. Star-disk Interaction in Classical T Tauri Stars, Lecture Notes in Physics, 2007, Volume 723/2007, 55-73

Alexander, R.D. & Armitage, P.J. 2007, MNRAS, 375, 500

Alibert, Y., Mordasini, C., Benz, W. 2004, A&A, 417, L25

Alibert, Y., Mordasini, C., Benz, W., Winisdoerffer, C. 2005, A&A, 434, 343

Alonso-Albi, T., Fuente, A., Bachiller, R. et al. 2009, A&A, 117, 136

Altenhoff, W.J., Thum, C., Wendker, H.J. 1994, A&A 281, 161

André, P., Ward-Thompson, D., Barsony, M. 1993, ApJ, 406, 122

Andrews, S.M. & Williams, J.P. 2007, ApJ, 671, 1800

Antoci, V., Handler, G., Campante, T.L. et al. The excitation of solar-like oscillations in a delta Scuti star by efficient envelope convection. to appear as a Letter to Nature; doi:10.1038/nature10389; see eprint arXiv:1109.4285.

Baines D., Oudmaijer R.D., Porter J.M., Pozzo M. 2006, MNRAS, 367, 737

Barrado y Navascués, D., Stauffer, J.R., Song, I., Caillault, J.P. 1999, ApJ, 520, L123

Beckwith, S.V.W., Sargent, A.I., Chini, R.S., Guesten, R. 1990, AJ, 99, 924

Bertout, C., Bouvier, J., Duschl, W.J., Tscharnuter, W.M. 1993, A&A, 275, 236

Bertout, C., Robichon, N., Arenou, F. 1999, A&A, 352, 574

Basri, G. & Bertout, C. 1989, ApJ, 341, 340

Bessell, M.S. 1979, PASP, 91, 589

Bigay J.H.& Garnier R. 1970, A&AS, 1, 15

Blondel, P.F.C., Djie, H.R.E., Tjin A. 2006, A&A, 456, 1045B

Böhm, T. & Catala, C. 1994, A&A, 290, 167

Böhm, T. & Hirth, G.A. 1997, A&A, 324, 177

Boss, A.P. 1997, Science, 276, 1836

Boss, A.P. 1998, ApJ, 503, 923

Boss, A.P. 2011, ApJ, 731, 74

Bouvier, J., Covino, E., Kovo, E. et al. 1995, A&A, 299, 89

Brittain, S.D., Simon, T., Najita, J.R., Rettig, T.W. 2007, ApJ, 659, 685

Brittain, S.D., Najita, J.R., Carr, J.S. 2009, ApJ, 702, 85

Cabrit, S., Edwards, S., Strom, S.E., Strom, K.M. 1990, ApJ, 354, 687

Caccin, B., Cavallini, F., Ceppatelli, G., Righini, A., Sambuco, A.M. 1985, A&A, 149, 357

Camenzind, M. 1990, Reviews of Modern Astronomy, 3, 234

Calvet, N. & Gullbring, E. 1998, ApJ, 509, 802

Calvet, N., Hartmann, L.. Strom, S.E. 2000, in Protostars and Planets IV, ed. V. Mannings, A.P. Boss, & S.S. Russell, p.377

Calvet, N., Muzerolle, J., Briceño, C. et al. 2004, AJ, 128, 1294

Carmona, A., van den Ancker, M.E., Henning, Th. 2007, A&A, 464, 687

Carmona, A., van den Ancker, M.E., Audard, M. et al. 2010, A&A, 517, A67

Casey, S.C. & Harper, D.A. 1990, ApJ, 362, 663

Cieza, L., Padgett, D.L., Stapelfeldt, K.R. et al. 2007, ApJ, 667, 308

Cieza, L.A. 2008, ASPC, 393, 35

Clarke, C.J., Gendrin, PA., Sotomayor, M. 2001, MNRAS, 328, 485

Clarke, C.J., & Pringle, J.E. 2006, MNRAS, 370, L10

Conover, W.J. 1980, Practical non-parametric statistics (2nd edition; New York: Wiley)

Corcoran, M. & Ray, T.P. 1997, A&A, 321, 189

Corcoran, M. & Ray, T.P. 1998, A&A, 331, 147

Corporon, P. & Lagrange, A.-M. 1999A&AS, 136, 429

Coulson, I.M., Walther, D.M., Dent, W.R.F. 1998, MNRAS, 296, 934

Close, L.M., Roddier, F., Hora, J.L. et al. 1997, ApJ, 489, 210

Dahm, S.E. 2008, AJ, 136, 521

de Winter, D., Grady, C.A., van den Ancker, M.E., Pérez, M.R., Eiroa, C. 1999, A&A, 343, 137

Donehew, B. & Brittain, S. 2011, AJ, 141, 46

Draine, B.T. 2006, ApJ, 636, 1114

Dullemond, C.P. 2002, A&A, 395, 853

Dullemond, C.P., van den Ancker, M.E., Acke, B., van Boekel, R. 2003, ApJ, 594, L47

Dullemond, C.P. & Dominik, C. 2004, A&A, 417, 159

Dullemond, C.P., Natta, A., Testi, L. 2006, ApJ, 645, L69

Durisen, R.H. e.a. 2007, in PPV, ed. B. Reipurth, D. Jewitt, K. Keil, 607-622

Edwards,S., Strom,S.E., Hartigan,P. et al. 1993, AJ, 106, 372

Edwards, S., Hartigan, P., Ghandour, L., Andrulis, C. 1994, AJ, 108, 1056

Eiroa, C., Alberdi, A., Camron, A. et al. 2000, ESASP, 451, 189

Eiroa, C., Garzón, F., Alberdi, A. et al. 2001, A&A, 365, 110E

Eiroa, C., Oudmaijer, R.D., Davies, J.K. et al. 2002, A&A, 384, 1038

Eisner, J.A., Lane, B.F., Hillenbrand, L.A., Akeson, R.L., Sargent, A.I. 2004, ApJ, 613, 1049

Fang, M., van Boekel, R., Wang, W. et al. 2009, A&A, 504, 461

Fedele, D., van den Ancker, M., Henning, Th., Jayawardhana, R., Oliveira, J.M. 2010, A&A, 510, 72

Finkenzeller, U. & Mundt, R. 1984, A&AS, 55, 109

Finkenzeller, U. 1985, A&A, 151, 340

Fuente, A., Neri, R., Martín-Pintado, J., Bachiller, R., Rodríguez-Franco, A., Palla, F. 2001, A&A, 366, 873

Garcia Lopez, R., Natta, A., Testi, L., Habart, E. 2006, A&A, 459, 837G

Garrison, L.M. 1978, ApJ, 224, 534

Glass, I.S. & Penston, M.V. 1974, MNRAS, 167, 237

Glebocki R., Gnacinski P., Stawikowski A. 2000, The Catalogue of Stellar Projected Rotational Velocities, Acta Astron., 50, 509

Grady, C.A., Pérez, M.R., Talavera, A. et al. 1996, A&AS, 120, 157

Grady, C.A., Sitko, M.L., Russell, R.W., et al. 2000, Protostars and Planets IV, 613

Grady, C.A., Hamaguchi, K., Schneider, G. et al. 2010, ApJ, 719, 1565

Grinin, V.P., Kiselev, N.N., Minikulov, N.Kh., Chernova, G.P. 1988, SvAL, 14, 219G

Grinin, V.P., The, P.S., de Winter, D. et al. 1994, A&A, 292, 165

Grinin, V.P., Kozlova, O.V., Natta, A. et al. 2001, A&A, 379, 482

Guimarães, M.M., Alencar, S.H.P., Corradi, W.J.B., Vieira, S.L.A. 2006, A&A, 457, 581

Gutermuth, R.A., Megeath, S.T., Myers, P.C. et al. 2009, ApJS, 184, 18

Hartigan, P., Edwards, S., Ghandour, L. 1995, ApJ, 452, 736

Hartmann, L., Hewett, R., Calvet, N. 1994, ApJ, 426, 669

Hartmann, L., Calvet, N., Gullbring, E., D'Alessio, P. 1998, ApJ, 495, 385

Hartmann, L. 2002, ApJ, 566, L29

Hartmann, L. 2009, Accretion processes in Star Formation, Cambridge Atrophysics Series, 2nd edition.

Harvey, P., Merín, B., Huard, T.L. et al. 2007, ApJ, 663, 1149

Hauschildt, P.H., Allard, F., Baron, E. 1999, ApJ, 512, 377

Herbig, G.H. 1960, ApJS, 4, 337

Herbig, G.H. & Bell, K.R. 1988, Third Catalogue of emission line stars of the Orion population, Lick Obs. Bull. 1111,1

Herbst, W., Miller, D.P., Warner, J.W., Herzog, A., 1982, AJ, 87, 98

Herbst, W., Herbst, D.K., Grossman, E.J., Weinstein, D. 1994, AJ, 108, 1906

Herbst, W. & Shevchenko, V.S. 1999, AJ, 118, 1043

Herczeg, G.J. & Hillenbrand, L.A. 2008, ApJ, 681, 594

Hernández, J., Calvet, N., Briceño, C.; Hartmann, L., Berlind, P. 2004, AJ, 127, 1682

Hernández, J., Briceo, C., Calvet, N. et al. 2006, ApJ, 652, 472

Hillenbrand, L.A., Strom, S.E., Vrba, F.J., Keene, J. 1992, ApJ, 397, 613

Hoffleit, D. & Jascheck, C. 1982, Bright Stars Catalogue, Yale University Observatory, New Haven.

Hollenbach, D. & Gorti, U. 2009, ApJ, 703, 1203

Huélamo, N., Lacour, S., Tuthill, P. et al. 2011, A&A, 528, L7

Hubrig, S., Stelzer, B., Schöller, M. et al. 2009, A&A, 502, 283

Indebetouw, R., Mathis, J.S., Babler, B.L. et al. 2005, ApJ, 619, 931

Isobe, T., Feigelson, E.D., Nelson, P.I. 1986, ApJ, 306, 490

Jayawardhana, R., Coffey, J., Scholz, A., Brandeker, A., van Kerkwijk, M.H. 2006, ApJ, 648, 1206

Johns, C.M. & Basri, G. 1995, AJ, 109, 2800

Johnson, J.A., Fischer, D.A., Marcy, G.W. 2007, ApJ, 665, 785

Kalas, P., Graham, J.R., Clampin, M. 2005, Nature, 435, 1067

Kennedy, G.M. & Kenyon, S.J. 2008, ApJ, 673, 502

Kenyon, S.J. & Hartmann, L. 1995, ApJS, 101, 117

Kim, S.-H., Martin, P.G., Hendry, P.D. 1994, ApJ, 422, 164

Königl, A. 1991, ApJ, 370, L39

Kraus, S., Hofmann, K.H., Benisty, M. et al. 2008, A&A 489, 1157

Kurosawa, R., Harries, T.J., Symington, N.H. 2006, MNRAS, 370, 580

Kurucz, R.L. 1993, ATLAS9 Stellar Atmosphere Programs and 2 km/s grid. CD-ROM No. 13. Cambridge, Massachusetts. Smithsonian Astrophysical Observatory

Lada, C.J. 1987, IAU Symp 115, Star Forming Regions, ed. M. Peimbert & J. Jugaku, 1-17

Lauroesch, J.T. & Meyer, D.M. 2003, ApJ, 591, L123

Lavalley, M., Isobe, T., Feigelson, E. 1992, Astronomical Data Analysis Software and Systems I, A.S.P. Conference Series, Vol. 25. p. 245

Leinert, C., Richichi, A., Haas, M. 1997, A&A, 318, 472

Lynden-Bell, D. & Pringle, J.E. 1974, MNRAS, 168, 603

Lundström, I., Arderberg, A., Maurice, E., Lindgren, H. 1991, A&AS, 91, 199

Malfait, K., Bogaert, E., Waelkens, C. 1998, A&A, 331, 211

Mannings, V. 1994, MNRAS, 271, 587

Mannings, V. & Sargent, A. 1997, ApJ, 490, 792

Mannings, V. & Sargent, A. 2000, ApJ, 529, 391

Manoj, P., Bhatt, H.C., Maheswar, G., Muneer, S. 2006, ApJ, 653, 657

Mathews, G.S., Dent, W.R.F., Williams, J.P. et al. 2010, A&A, 518, L127

Meeus, G., Waters, L.B.F.M., Bouwman, J. et al. 2001, A&A, 365, 476

Meeus, G., Pinte, C., Woitke, P. et al. 2010, A&A, 518, L124

Mendigutía, I., Montesinos, B., Eiroa, C., Mora, A. 2010, Highlights of Spanish Astrophysics, V, 425

Mendigutía, I., Eiroa, C., Montesinos, B. et al. 2011, A&A, 529, A34 (Paper I)

Mendigutía, I., Calvet, N., Montesinos, B. et al. 2011, A&A, 535, A99 (Paper II)

Mendigutía, I., Mora, A., Montesinos, B. et al. 2012, to be submitted to A&A (Paper III)

Merín, B. Study of envelopes and protoplanetary discs around young stars. PhD thesis, Universidad Autónoma de Madrid, 2004

Meyer, M.R., Calvet, N., Hillenbrand, L.A. 1997, AJ, 114, 288

Mohanty, S., Jayawardhana, R., Basri, G. 2005, ApJ, 626, 498

Monnier, J.D., Tuthill, P.G., Ireland, M. et al. 2009, ApJ, 700, 491

Montesinos, B., Eiroa, C., Merín, B., Mora, A. 2009, A&A, 495,901

Mora, A., Merín, B., Solano, E. et al. 2001, A&A, 378, 116

Mora, A., Natta, A., Eiroa, C. et al. 2002, A&A, 393, 259

Mora, A., Eiroa, C., Natta, A. et al. 2004, A&A, 419, 225

Mora, A. Kinematics of the circumstellar gas around UXOR stars. PhD thesis, Universidad Autónoma de Madrid, 2004

Mordasini, C., Alibert, Y., Benz, W., Naef, D. 2008, in ASPC series, ed. D. Fischer, F.A. Rasio, S.E. Thorsett, A. Wolszczan, Vol. 398, 235

Mottram, J.C., Vink, J.S., Oudmaijer, R.D., Patel, M. 2007, MNRAS, 377, 1363

Muzerolle, J., Hartmann, L., Calvet, N. 1998a, AJ, 116, 455

Muzerolle, J., Calvet, N., Hartmann, L. 1998b, ApJ, 492, 743

Muzerolle, J., Calvet, N., Briceño, C., Hartmann, L. and Hillenbrand, L. 2000, ApJ, 535, L47

Muzerolle, J., Calvet, N., Hartmann, L. 2001, ApJ, 550, 944

Muzerolle, J., Hillenbrand, L., Calvet, N.; Briceño, C., Hartmann, L. 2003, ApJ, 592, 266

Muzerolle, J., D'Alessio, P., Calvet, N., Hartmann, L. 2004, ApJ, 617, 406

Muzerolle, J., Luhman, K.L., Briceño, C., Hartmann, L., Calvet, N. 2005, ApJ, 625, 906

Najita, J.R., Strom, S.E., Muzerolle, J. 2007, MNRAS, 378, 369

Natta, A., Grinin, V.P., Mannings, V., Ungerechts, H. 1997, ApJ, 491, 885

Natta, A., Grinin, V., Mannings, V. 2000, Protostars and Planets IV, 559

Natta, A., Testi, L., Muzerolle, J. et al. 2004, A&A, 424, 603

Natta, A., Testi, L., Randich, S. 2006, A&A, 452, 245

Nguyen, D.C., Scholz, A., van Kerkwijk, M.H., Jayawardhana, R., Brandeker, A. 2009, ApJ, 694L, 153N

Oudmaijer, R.D., Palacios, J., Eiroa, C. et al. 2001, A&A, 379, 564.

Palla, F. & Stahler, S.W. 1999, ApJ, 525, 772

Patten, B.M. & Willson, L.A. 1991, AJ, 102, 323

Pérez, M.R., van den Ancker, M.E., de Winter, D., Bopp, B.W. 2004, A&A, 416, 647

Pezzuto, S. & Strafella, F. 1997, ApJ, 485, 290

Piétu, V., Dutrey, A., Kahane, C. 2003, A&A, 398, 565

Piétu, V., Dutrey, A., Guilloteau, S., Chapillon, E., Pety, J. 2006, A&A, 460, L43

Pinte, C., Woitke, P., Ménard, F. 2010, A&A, 518, L126

Pirzkal, N., Spillar, E.J., Dyck, H.M. 1997, ApJ, 481, 392

Pogodin, M.A., 1994, A&A, 282, 141

Pollack, J.B. & Hollenbach, D. 1994, ApJ, 421, 615

Pollack, J.B., Hubickyj, O., Bodenheimer, P. et al. 1996, Icarus, 124, 62

Praderie, F., Simon, T., Catala, C., Boesgaard, A.M., 1986, ApJ, 303, 311

Redfield, S. 2007, ApJ, 656, L97

Reipurth, B., Pedrosa, A., Lago, M.T.V.T. 1996, A&AS, 120, 229

Ricci, L., Testi, L., Natta, A. et al. 2010, A&A, 512, A15

Richter, M.J., Jaffe, D.T., Blake, G.A., Lacy, J.H. 2002, ApJ, 572, L161

Rigliaco, E., Natta, A., Randich, S. et al. 2011, A&A, 526, L6

Robitaille, T.P., Whitney, B.A., Indebetouw, R., Wood, K., Denzmore, P. 2006, ApJS, 167, 256

Robitaille, T.P., Whitney, B.A., Indebetouw, R., Wood, K. 2007, ApJS, 169, 328

Roccatagliata, V.; Bouwman, J.; Henning, T. et al. 2011, ApJ, 733, 113

Rodgers, B., Wooden, D.H., Grinin, V., Shakhovsky, D., Natta, A. 2002, ApJ, 564, 405

Rodgers, B. 2003, ASPC, 287, 180

Ruden, S.P. 1999, The formation of planets, in The origin of stars and planetary systems, 643-680, ed. C.J. Lada & N.D. Kylafis

Salpeter, E.E. 1995, ApJ, 121, 161

Sandell, G. 2000, A&A, 358, 242

Sandell, G. & Weintraub, D.A. 2003, AAS Poster

Sandell, G., Weintraub, D.A., Hamidouche, M. 2011, ApJ, 727, 26

Schisano, E., Covino, E., Alcalá, J.M. et al. 2009, A&A, 501, 1013

Sheret, I., Dent, W.R.F., Wyatt, M.C. 2004, MNRAS, 348, 1282

Shu, F.H., Adams, F.C., Lizano, S. 1987, ARA&A, 25, 23

Shu, F., Najita, J., Ostriker, E., Wilkin, F. 1994, ApJ, 429, 781

Siess, L., Forestini, M., Bertout, C. 1999, A&A, 342, 480

Simon, T., Ayres, T.R., Redfield, S., Linsky, J.L. 2002, ApJ, 579, 800

Smith, K.W., Balega, Y.Y., Duschl, W.J. et al. 2005, A&A, 431, 307

Stark, C.C., Kuchner, M.J., Traub, W.A. et al. 2009, ApJ, 703, 1188

Sterzik, M.F., Melo, C.H.F., Tokovinin, A.A., van der Bliek, N. 2005, A&A, 434, 671

Sylvester, R.J., Skinner, C.J., Barlow, M.J., Mannings, V. 1996, MNRAS, 279, 915

Sylvester, R.J., Dunkin, S.K., Barlow, M.J. 2001, MNRAS, 327, 133

Takeuchi, T., Clarke, C.J., Lin, D.N.C. 2005, ApJ, 627, 286

Tambovtseva, L.V., Grinin, V.P., Kozlova, O.V. 1999, Astrophysics, 42, 1

Tayler, R.J. The stars: their structure and evolution, Cambridge University Press, 1994

Terebey, S., Shu, F.H., Cassen, P.M. 1982, BAAS, 14, 639

Tetzlaff, N., Neuhäuser, R., Hohle, M.M. 2011, MNRAS, 410, 190

Testi, L., Natta, A., Shepherd, D.S., Wilner, D.J. 2001, ApJ, 554, 1087

Thé, P.S., de Winter D., Pérez, M.R. 1994, A&AS, 104, 315

Thi, W.F., van Dishoeck, E.F., Blake, G.A. et al. 2001, ApJ, 561, 1074

Thi, W.F., Mathews, G., Ménard, F. et al. 2010, A&A, 518, L125

Thomas, S.J., van der Bliek, N.S., Rodgers, B., Doppmann, G., Bouvier, J. 2007, IAUS, 240, 250

Tilling, I., Clarke, C.J., Pringle, J.E., Tout, C.A. 2008, MNRAS, 385, 1530

Tilling, I., Woitke, P., Meeus, G. et al. (2011). Accepted in A&A, see 2011arXiv1111.2549T

Uchida, Y. & Shibata, K. 1985, PASJ, 37, 515

Valenti, J.A., Basri, G., Johns, C.M. 1993, AJ, 106, 2024

Valenti, J.A. & Johns-Krull, C.M. 2004, Ap&SS, 292, 619

van Boekel, R., Waters, L.B.F.M., Dominik, C. et al. 2003, A&A, 400, L21-L24

van Boekel, R., Min, M., Waters, L.B.F.M. et al. 2005, A&A, 437, 189

van den Ancker, M.E., Meeus, G., Cami, J., Waters, L.B.F.M., Waelkens, C. 2001, A&A, 369, 17

van den Ancker, M.E. High Resolution Infrared Spectroscopy in Astronomy, Proceedings of an ESO Workshop held at Garching, Germany, 18-21 November 2003. Edited by H.U. Käufl, R. Siebenmorgen, and A. Moorwood. Garching, Germany, 2005., pp. 309-314

van der Plas, G., van den Ancker, M.E., Fedele, D. et al. 2008, A&A, 485, 487

Vieira, S.L.A., Corradi, W.J.B., Alencar, S.H.P. et al. 2003, AJ, 126, 2971

Vink, J.S., Drew, J.E., Harries, T.J., Oudmaijer, R.D., 2002, MNRAS, 337, 356

Vink, J.S., Drew, J.E., Harries, T.J., Oudmaijer, R.D., Unruh, Y.C. 2003, A&A, 406, 703

Wade, G.A., Drouin, D., Bagnulo, S. et al. 2005, A&A, 442L, 31

Wade, G.A., Bagnulo, S., Drouin, D., Landstreet, J.D., Monin, D. 2007, MNRAS, 376, 1145

Walker, H. J.& Butner, H. M. 1995, Ap&SS, 224, 389

Wall, J.V. & Jenkins, C.R. 2003, Practical statistics for astronomers, (Cambridge University Press)

Waters, L.B.F.M., & Waelkens, C., 1998, ARA&A, 36, 233

Waters L.B.F.M. 2006, ASPC, 355, 87

Weinberger, A.J., Rich, R.M., Becklin, E.E., Zuckerman, B., Matthews, K. 2000, ApJ, 544, 937

Wheelwright, H.E., Oudmaijer, R.D., Goodwin, S.P. 2010, MNRAS, 401, 1199

White, R.J. & Basri, G. 2003, ApJ, 582, 1109

Williams, J.P. & Cieza, L.A. 2011, ARA&A, 49, 67

Wolk, S.J. & Walter, F.M. 1996, AJ, 111, 2066

York, D.,Evensen, N., Martinez, M., Delgado, J. "Unified equations for the slope, intercept, and standard errors of the best straight line" Am. J. Phys. 72 (3) March 2004.